A SEARCH FOR VERY HIGH-ENERGY GAMMA-RAY EMISSION FROM PULSARS WITH VERITAS

A Dissertation
Presented to
The Academic Faculty

By

Gregory T. Richards

In Partial Fulfillment
of the Requirements for the Degree
Doctor of Philosophy in the
School of Physics

Georgia Institute of Technology

December 2017

A SEARCH FOR VERY HIGH-ENERGY GAMMA-RAY EMISSION FROM PULSARS WITH VERITAS

Approved by:

Dr. A. Nepomuk Otte, Advisor
School of Physics
Georgia Institute of Technology

Dr. Tamara Bogdonavić
School of Physics
Georgia Institute of Technology

Dr. Ignacio Taboada
School of Physics
Georgia Institute of Technology

Dr. Deirdre Shoemaker
School of Physics
Georgia Institute of Technology

Dr. Sven Simon
School of Earth and Atmospheric Science
Georgia Institute of Technology

Date Approved: October 25, 2017

In the beginning the Universe was created. This has made a lot of people very angry and been widely regarded as a bad move.

Douglas Adams

For my parents

ACKNOWLEDGEMENTS

I owe a debt of gratitude to too many people to name individually here. I'd be remiss not to single some out anyway.

I must first thank Mr. Helf, my high school physics teacher, for providing my first introduction to physics. His clear teaching style, perpetual availability, and irreverent sense of humor no doubt played a big role in shaping the path ahead for me.

Many thanks are also due to Prof. Duane Pontius, my advisor and primary physics instructor while I was an undergrad at BSC. That his love for physics was so palpable in his teaching played no small role in influencing my decision to pursue a doctorate.

I offer a big thank you to all the members of the VERITAS collaboration I've had the pleasure of working with and learning from over the years. I'd like to give a special thanks to my former colleague Andrew, with whom I had many educational discussions regarding analysis, hardware, and pulsar science during the long nights observing in Arizona.

Thank you to my friends, who helped keep me sane, distracted, and/or entertained during the past six-and-a-half years while working as a grad student. In particular (and in no particular order), I'd like to thank Sam, Geoffrey, Owen, Ted, Alan, Angel, Ham, and the Birmingham gang. Thanks also to the students who at some point made the brave choice of passing through Howey E-113 (Jacob and James, especially).

Lastly, I have to thank my Ph.D. supervisor Prof. Nepomuk Otte for all the guidance and support during my graduate studies.

TABLE OF CONTENTS

Acknowledgments v

List of Tables xii

List of Figures xiv

Chapter 1: Introduction 1

- 1.1 Very High-Energy Gamma-Ray Astronomy 1
- 1.2 Gamma-Ray Astronomy and Pulsars 2
- 1.3 Thesis Outline 3

Chapter 2: The Physics of Pulsars 6

- 2.1 Introduction to Pulsars 6
- 2.2 Properties of Pulsars 7
- 2.3 Mechanisms of Electromagnetic Radiation 9
  - 2.3.1 Synchrotron Radiation 10
  - 2.3.2 Curvature Radiation 12
  - 2.3.3 Inverse-Compton Scattering 13
- 2.4 Magnetospheric Emission Models 15
  - 2.4.1 Overall Structure of the Magnetosphere 15

2.4.2 The Polar Cap 17

2.4.3 The Slot Gap 20

2.4.4 The Outer Gap 20

2.4.5 The *Fermi*-LAT and the Gaps 23

Chapter 3: Review of Very High-Energy Pulsar Observations and Models 26

3.1 The Crab Pulsar 26

3.1.1 Past Results 26

3.1.2 Recent Results 28

3.2 Other Pulsars Observed by IACTs 30

3.2.1 The Geminga Pulsar 30

3.2.2 The Vela Pulsar 31

3.3 Status of Theory 33

3.4 Conclusion 36

Chapter 4: The Physics of Air Showers 38

4.1 Introduction 38

4.2 Cherenkov Radiation 39

4.3 Air Showers 42

4.3.1 Electromagnetic Showers 42

4.3.2 Hadronic Showers 44

Chapter 5: The VERITAS Detector 49

5.1 Overview 49

5.2 Structure and Optics 49

5.3 Cameras 50

5.4 Upgrades 52

5.5 Trigger System 53

5.6 Data Acquisition 54

5.7 Calibration 55

Chapter 6: Data Analysis 58

6.1 Pulsar Timing 58

 6.1.1 Barycentering 59

 6.1.2 Phase Folding 60

6.2 *Fermi*-LAT Data Analysis 61

6.3 VERITAS Data Analysis 62

 6.3.1 Introduction 62

 6.3.2 Calibration of Data 63

 6.3.3 Event Parametrization and Reconstruction 65

 6.3.4 Cosmic-Ray Rejection and Cut Selection 69

 6.3.5 Background Estimation 71

 6.3.6 Calculating Flux from Excess Counts 74

Chapter 7: Statistical Methods 77

7.1 Introduction 77

7.2 Significance from ON / OFF Counting 77

7.3 Periodicity Tests 78

7.3.1 The *H*-Test 79

7.4 Upper Limits from the *H*-Test Statistic 81

Chapter 8: The Geminga Pulsar 83

8.1 Abstract 83

8.2 Introduction 83

8.3 Observations 86

8.4 Data Analysis 87

8.4.1 Fermi-LAT Analysis 87

8.4.2 VERITAS Analysis 88

8.5 Results 91

8.5.1 Light curve 91

8.5.2 Spectrum 91

8.6 Discussion and Conclusion 93

Chapter 9: The Search for VHE Emission from the Missing Link Binary Pulsar J1023+0038 95

9.1 Abstract 95

9.2 Introduction 96

9.3 VHE Gamma-Ray Observations 100

9.4 VERITAS Analysis and Results 100

9.4.1 Analysis 100

9.4.2 Search for a Steady Signal 101

9.4.3 Search for Pulsations 101

9.5 Discussion and Conclusion 103
9.5.1 Millisecond Pulsar Phase 103
9.5.2 Accretion Phase 107

Chapter 10:The Fourteen Pulsars Appearing in Archival VERITAS Data 110

10.1 Introduction 110
10.2 Data Selection 114
10.3 Data Analysis 115
10.3.1 Pulsar Timing and Phase Gating for the VERITAS Analysis 115
10.3.2 VERITAS Data Analysis 117
10.4 Results 119
10.4.1 The PSR J2238+5903 Observation Campaign 121
10.4.2 Pulse Profiles from the VERITAS Data 124
10.4.3 *Fermi*-LAT Spectra with VERITAS Limits 139
10.5 Discussion and Conclusion 146

Chapter 11:Conclusion 151

Appendix A: A Search for Elevated Very High-Energy Gamma-Ray Flux During a Crab Nebula Flare with VERITAS 156

A.1 Abstract 156
A.2 Introduction 156
A.3 Observations and Analysis 158
A.3.1 VERITAS 158
A.3.2 *Fermi*-LAT 160

A.4 Results 161

A.5 Discussion 166

Appendix B: Measuring the Shapes of Pulses in the VERITAS Electronics . . . 170

B.1 Experimental Setup 170

B.2 Procedure 171

B.3 Results 172

References 216

LIST OF TABLES

6.1 Table of all relevant differences between the *Fermi*-LAT data analysis of the Geminga pulsar and the 15 archival pulsars. All differences are due solely to the fact that the LAT team refines the instrument IRFs, analysis software, and periodically reprocesses the data over time to improve the analysis. . . . 61

6.2 Definition of all cut values used in the analyses described in this thesis. . . . 71

8.1 Results from maximum-likelihood fits to the *Fermi*-LAT data. Between 100 MeV and 100 GeV the differential photon flux of Geminga was modeled as a power law multiplied by an exponential cut-off as defined in Equation 1. Between 10 GeV and 100 GeV, the differential photon flux of Geminga was modeled as a pure power law with the normalizing E_0 parameter fixed to 5 GeV. The quoted uncertainties are statistical only. The systematic uncertainty on the estimation of pulsar spectral values was studied by the *Fermi*-LAT collaboration in [6] and found to be, on average, 14% for Γ and 4% for $E_{\rm brk}$. 92

8.2 VERITAS event counts in the signal and background phase ranges. α is the ratio of the size of the signal phase gate to the background phase gate. The significance values were calculated using Equation 17 from [81]. 93

9.1 VERITAS analysis results for the location of PSR J1023+0038 for each of the two different binary states. The parameter α indicates the ratio of the ON- to OFF-source region exposure, and the LiMa significance is calculated using equation 17 in [81] (same as Equation 7.1 given in Section 7.2.). 100

9.2 *H* statistic and integral pulsed VHE flux upper limit computed with the VERITAS data for the radio MSP state of PSR J1023+0038. Due to the unavailability of a valid pulsar timing solution for the accretion/LMXB state, no *H* statistic or flux upper limit is given for VERITAS data collected during this state. 101

10.1 Table of the pulsar properties. The right ascension and declination (J2000) values given in columns 2 and 3 used in analysis are taken from the timing solutions. Columns 4 and 5 give the pulsar period P and time derivative of the period $\dot{P}$. The spin-down powers ($\dot{E}$) are given in column 6, and the pulsar distances or distance limits are given in column 7. Column 8 lists the ranking in $\dot{E}/d^2$ for the northern hemisphere, and the final column gives the VERITAS exposure time for the pulsar. Values for P, $\dot{P}$, and $\dot{E}$ have been taken from the 2PC [6], unless otherwise noted. Where a distance upper limit is quoted, the limit is the distance to the Galaxy's edge as calculated in [6]. 112

10.2 Table of the phase gate and phase offset definitions. Columns 2 and 3 give the gate definitions for the peak locations P1 and P2, respectively. Column 4 gives the background phase-gate definitions. Column 5 lists the phase offsets between the used timing solutions and those appearing in the 2PC, which were used to calculate the phase gates. 117

10.3 Results for the 14 pulsars appearing in archival VERITAS data. Each pulsar has three sets of results, one for each set of cuts applied to the data. Column 2 lists the exposure time for each pulsar, copied here from Table 10.1 for convenience. Column 3 specifies the set of cuts used in the analysis. Column 4 gives the lower energy threshold for the analysis in GeV. Columns 5 and 6 give the phase-gate test significance and *H* statistic, respectively. Integral flux upper limits at the 95% CL from the *H* test and the Rolke method are given in columns 7 and 8, respectively. 123

A.1 95% CL Bayesian upper limits on the VHE relative flux increase during the flare period for three energy thresholds. 166

LIST OF FIGURES

1.1 Map of all currently known very high-energy gamma-ray sources in galactic coordinates. The backdrop image is the high-energy gamma-ray sky seen by the *Fermi*-LAT. The fraction of the sky visible to VERITAS is indicated by the white shaded region. Figure from TeVCat [2] on September 25th, 2017. 1

2.1 A P-$\dot{P}$ diagram from the 2PC. Lines of surface magnetic field strengths are shown in green, while characteristic ages are shown in blue, and spin-down powers are shown in red. Pulsars not detected by the *Fermi*-LAT are represented by the gray and black dots. Figure from [6]. © AAS. Reproduced with permission. 9

2.2 The standard pulsar spectrum from radio to very high-energy gamma rays. The different components are labeled as follows: Sy–synchrotron emission, kT–blackbody radiation, CR–curvature radiation, and CS–inverse-Compton scattering. The dotted line is the curvature spectrum due to a monoenergetic primary for comparison. Figure from [16]. © AAS. Reproduced with permission. 10

2.3 An emission schematic for synchrotron emission. The radiation is produced in a cone-shaped beam of angular width $\alpha = \gamma^{-1}$, as shown by the blue cone. The path of the electron is shown as the green helix. Figure from [18]. 11

2.4 An emission schematic for curvature radiation. As a charged particle follows a magnetic field line to which it is bound, it emits photons in a cone due to the curved trajectory. Figure from [18]. 12

2.5 Two-panel diagram of Compton scattering. In the inverse-Compton scattering case (*right*), a high-energy charged particle collides with a lower-energy photon. The photon is “upscattered,” receiving a large amount of energy from the charged particle in the interaction. Figure from [18]. 13

2.6 Magnetic field lines for a pulsar with a 90° misalignment between the spin and magnetic dipole axes. The right panel is a zoom of the left, and the gray circle indicates the light cylinder. The axis units are multiples of the light cylinder radius. The blue spirals are meant to show the wave structure of the magnetic field as it flows away from the pulsar. Figure from [20]. . . 16

2.7 General structure of the pulsar mangetosphere and locations of the gap regions. The polar cap is just above the magnetic poles of the star and is shown in red. The slot gap is shown in blue, and the outer gap is shown in orange. The pulsar spin axis is indicated by the vertical light blue line, and the magnetic dipole axis is shown as a green line. Figure from [21]. 18

2.8 Diagram of particle cascades in the polar cap. Figure from [24]. © AAS. Reproduced with permission. 19

2.9 Diagram of the polar-cap and low-altitude slot-gap region in a pulsar magnetosphere. The curve labeled PFF refers to the pair-formation front—the propagation of the particle cascade in the polar cap. The gray hollow-cone beam shows the standard polar cap emission geometry. $\Delta\xi_{\mathrm{SG}}$ is the slot-gap thickness, and μ labels the magnetic dipole axis. Figure from [29]. © AAS. Reproduced with permission. 21

2.10 A pulsar magnetosphere diagram showing the outer gap (solid gray region). The null charge surface is indicated by the dashed line labelled $\Omega \cdot B = 0$. The magnetic dipole axis is labelled μ, and the rotation axis is labelled Ω. The angle between these two axes is given by α. The red squiggly lines depict gamma-ray emission from both the polar-cap and outer-gap regions. Figure from [32]. 22

2.11 A simulated intensity pattern for a pulsar with $\alpha = 65^\circ$. The rotation phase in degrees is given on the horizontal axis, while the vertical axis shows the viewing angle ζ. Emission from the three gap regions are shown with the polar cap in blue, slot gap in green, and the outer-gap component in orange. A horizontal slice through the pattern for a specific ζ would give a pulse profile. Figure from [34]. © AAS. Reproduced with permission. 24

3.1 Crab pulsar spectral energy distribution for the energy range from 100 MeV to 400 GeV. Spectral measurements from the *Fermi*-LAT (green squares), MAGIC (upside-down maroon triangle), and VERITAS (red circles) are shown along with various flux upper limits from other VHE gamma-ray instruments. The exponential cut-off fit to the *Fermi*-LAT data is clearly a poor description for the tail of the spectrum. Figure from [3]. 28

3.2 MAGIC and *Fermi*-LAT phase-resolved Crab pulsar spectra. The black and blue straight lines are power-law fits to the data above 10 GeV. The arrows represent 95% confidence level upper limits, with the slope of the line indicating the assumed spectral index for the upper limit calculation. The dashed lines are fits to the *Fermi*-LAT data of a power law with an exponential cut-off for P1 and P2. Figure from [4] 29

3.3 *Fermi*-LAT and H.E.S.S. II spectra for the dominant gamma-ray peak seen from the Vela pulsar, P2. The *Fermi*-LAT points are shown in blue; the H.E.S.S. detection bow tie is shown in red; a simple power-law fit to the LAT data is given by the purple solid and dashed lines; and the cyan line is a power-law-with-an-exponential-cut-off (denoted ECPL in the legend) fit to the LAT data above 100 MeV. Reproduced from [50], with the permission of AIP Publishing. 32

3.4 Crab pulsar spectrum between 1 GeV and 1 TeV with superposed model predictions from [55]. The *Fermi*-LAT data are shown as blue squares, while the VHE data are given as the gray circles and magenta diamonds (MAGIC) and the green hexagons (VERITAS). The gray dashed and solid lines are fits to the LAT data, while the dotted gray line is the sum of the red and gray solid lines. The colored lines give the predictions from the wind model as specified in the legend. The parameter Γ_{w} is the wind Lorentz factor, R_{w} is the distance from the neutron star to the center of the wind acceleration zone, and R_{L} is the light-cylinder radius ($\sim 10^6$ m). Figure from [55]. 35

4.1 Cartoon depicting the creation of a Cherenkov light pool due to a gamma-ray induced air shower. An IACT located within the light pool collects some of the Cherenkov photons and images the air shower, which is then used to reconstruct properties of the primary gamma ray. 38

4.2 Illustrations showing the polarization induced in nearby atoms due to a passing charged particle. In *(a)*, a subluminal particle is shown polarizing atoms in a symmetric fashion, which will not produce coherent depolarization. In *(b)*, a superluminal particle is shown leaving a wake of polarized atoms, which will depolarize coherently, producing Cherenkov radidation. The particles take the trajectory from A to B, as indicated by the vertical arrow. Figure from [59]. 40

4.3 The geometry of Cherenkov light emission showing how to find the Cherenkov angle θ. 41

4.4 Spectrum of Cherenkov light (red) at $\sim$2 km above sea level in arbitrary units, shown along with the spectrum of night-sky-background light (green). Figure from [61]. 42

4.5 Air shower diagrams for an electromagnetic cascade (*left*) and a hadronic cascade (*right*). Figure from [62]. 43

4.6 Structure of an electromagnetic cascade. The Cherenkov emission angle is seen to increase with decreasing altitude, which has the effect that the highest concentration of Cherenkov photons on the ground falls in an annulus of approximate radius 100 m. The locations of the shower maximum and shower core are also indicated. Figure adapted from [62]. 44

4.7 Simulated electron (green) and positron (red) tracks for an electromagnetic shower induced by a 700 GeV primary gamma ray. The vertical scale represents the altitude range from 20 km down to 1.3 km, and the horizontal scale spans a distance of 9.4 km. Figure courtesy of M. Kertzman. 45

4.8 Bird's-eye view of the distribution of Cherenkov photons on the ground produced by shower electrons (green) and positrons (red) for a 700 GeV gamma-ray. The vertical and horizontal scales represent distances of about 600 m each. The top of the image corresponds to north. Figure courtesy of M. Kertzman. 46

4.9 Side view of the photons in Figure 4.8 showing the time profile of the photons. The vertical scale is 20 ns, and the horizontal scale is 600 m. Figure courtesy of M. Kertzman. 46

4.10 Simulated tracks for a hadronic shower induced by a 900 GeV primary proton. The color scheme is as follows: e^+–red, e^-–green, μ^+–purple, μ^-–cyan, π^0–yellow, π^+–maroon, π^-–teal, p^+–orange. Distance scales are the same as in Figure 4.7. Figure courtesy of M. Kertzman. 47

4.11 Bird's-eye view of the distribution of Cherenkov photons on the ground produced in a hadronic shower initiated by a 900 GeV proton. The color scale for the Cherenkov photons indicates the particle that produced the photon and is the same as in Figure 4.10. Distance scales are the same as in Figure 4.8. Figure courtesy of M. Kertzman. 48

4.12 Side view of the photons in Figure 4.11 showing the time profiles. The vertical scale is 20 ns, and the horizontal scale is 600 m. Figure courtesy of M. Kertzman. 48

5.1 The basecamp and VERITAS telescopes at the Fred Lawrence Whipple Observatory in Arizona. 49

5.2 The reflector of T1 as imaged from the platform near the camera. Also pictured are the LED flasher and focal-plane camera, both mounted on the crossbeam, and the sky and reflectivity cameras, both situated in the reflector where there are missing facets. These components are discussed further in Section 5.7. A reflected image of the author in a green shirt can also be seen. 51

5.3 The pre- and post-upgrade photomultiplier tubes used in the VERITAS cameras. The Hamamatsu R10560-100-20 is shown in the bottom-left and the Photonis XP2970/02 in the top-right. 52

5.4 An example bias curve taken during the V6 era. The black points show the L3 rate, and the colored points are the L2 rate for a specific telescope as follows—T1: red, T2: green, T3: blue, T4: magenta. The vertical black line indicates the 45 mV CFD threshold that is currently used during observations. 54

5.5 Block diagram of the VERITAS signal chain for a single-pixel signal. The dashed blue lines indicate transitions between the telescope camera, telescope trailer, and control room. The other 498 PMTs and channels that comprise the T1 electronics are not pictured, though all channels connect to the L2 board as indicated in the diagram. After an L3 trigger, a read-out signal (dashed black line) is sent to all channels in the array. 56

6.1 Illustration of commonly used parameters for a Cherenkov shower imaged by an IACT. Figure from [75] 66

6.2 Illustration of the camera plane showing the direction reconstruction method. The intersection of the major axis of each ellipse gives the arrival direction. Note that in the general case and as pictured here, the major axes will not exactly intersect for $N_{\text{tel}} > 2$, so a weighting method is used to determine the arrival direction (shown as a gold star). 67

6.3 Image showing the impact distance and core location of a gamma-ray shower based on the intersection of the image major axes. 68

6.4 A drawing of the reflected region method. The largest circle represents the FoV of a telescope, with the two intersecting dashed lines showing the center. The expected source location is represented by the yellow star. The ON region is shown encircling the expected source location in green, and the "reflected" OFF regions are given by the gray circles, which are all the same distance from the center as the ON region. 73

6.5 An example θ^2 distribution derived from Crab Nebula data. The vertical black line indicates a θ^2 cut of 0.01. The event counts fall rapidly, leaving only background moving away from the source, though not instantaneously due to the nonzero gamma-ray PSF. 74

6.6 An example simulated effective area of the V6 configuration of VERITAS for $0°$ zenith and $0°$ azimuth with cuts $MSW = 1.1$, $MSL = 1.3$, and $\theta^2 = 0.03$. 75

8.1 The phase-folded light curve of the Geminga pulsar as measured by the *Fermi*-LAT. The *Fermi* light curve contains all events that fell within a $2°$ radius centered on the position of the Geminga pulsar. The energy-dependent evolution of the light curve is in clear agreement with the light curves presented in [87] and [88]. The P1 and P2 emission peaks were fitted with asymmetric Gaussian functions above 5 GeV and 10 GeV, respectively. These fits, which are plotted as smooth black curves in panel (b), were used to define the signal regions for the P1 and P2 spectral analyses. These phase regions, [0.072 - 0.125] for P1 and [0.575 - 0.617] for P2, are indicated as vertical dashed lines. The background-event sample for the VERITAS analysis was selected from the phase range [0.7 - 1.0]. There is no evidence of pulsed emission above 100 GeV at any phase in the VERITAS data plotted in panel (c). 89

8.2 Measured SEDs and flux upper limits for the Geminga pulsar. Measurements of the Crab Nebula and pulsar are plotted for comparison. The Geminga limits and fluxes shown for PACT, Crimea, HEGRA, Whipple and Ootacamund were derived from the integral values reported by those experiments, assuming a power law with index 2.5 in each case. 90

9.1 Light curve of events phase folded with the Jodrell Bank radio timing solution for the radio MSP state . The light curve shows two pulsar periods and contains 30 bins per period. The dashed and dotted red lines represent the average number of counts and error on the average, respectively. 102

9.2 Broadband spectrum of PSR J1023+0038 during the millisecond pulsar phase. Thick blue bars show the detection of the X-ray emission by *XMM*-Newton in 2008 [146] and the *Fermi*-LAT GeV detection [147]. The black solid line represents synchrotron emission in a 40 G magnetic field, and the black dashed line represents the component due to inverse-Compton scattering of optical photons. The solid and dashed green lines represent those same components in the case of a 2 G magnetic field. The red dashed line represents a typical power-law model with an exponential cut-off spectrum of a GeV millisecond pulsar. The arrow represents the VERITAS flux upper limit reported in this work. 104

9.3 Broadband spectrum of PSR J1023+0038 after the reappearance of the accretion disk. The thick blue bar shows the X-ray emission detected by *Swift* in November 2013 [157]. Black triangles represent the *Fermi*-LAT HE gamma-ray detection in 2013 [157]. The arrow shows the VERITAS upper limit for the accretion/LMXB state, as reported in this work. Solid and dashed lines correspond to the synchrotron and inverse-Compton emission coming from the shock for the case of a 10 G (green lines) and 80 G (black lines) magnetic field. The spectral signature of inverse-Compton scattering of photons emitted by the accretion disk on the unshocked electrons is shown with a red dash-dotted line. 107

10.1 Phase-gate definitions for all 14 pulsars appearing in archival VERITAS data. The ON-counting regions, corresponding to the locations of P1 and P2, are shown in green, and the OFF-counting background region is shown in blue. Figure created by J. Tyler (McGill University). 118

10.2 Significance distributions between $\pm 3\sigma$ from the phase-gate test for soft (*top*), moderate (*middle*), and hard (*bottom*) cuts. Each distribution is fitted with a Gaussian (red curve), and all are consistent with being normally distributed. 120

10.3 Pulse profiles of **PSR J0007+7303** from VERITAS data for soft cuts (top panel), moderate cuts (middle panel), and hard cuts (bottom panel). 125

10.4 Pulse profiles of **PSR J0205+6449** from VERITAS data for soft cuts (top panel), moderate cuts (middle panel), and hard cuts (bottom panel). 126

10.5 Pulse profiles of **PSR J0248+6021** from VERITAS data for soft cuts (top panel), moderate cuts (middle panel), and hard cuts (bottom panel). 127

10.6 Pulse profiles of **PSR J0357+3205** from VERITAS data for soft cuts (top panel), moderate cuts (middle panel), and hard cuts (bottom panel). 128

10.7 Pulse profiles of **PSR J0631+1036** from VERITAS data for soft cuts (top panel), moderate cuts (middle panel), and hard cuts (bottom panel). 129

10.8 Pulse profiles of **PSR J0633+0632** from VERITAS data for soft cuts (top panel), moderate cuts (middle panel), and hard cuts (bottom panel). 130

10.9 Pulse profiles of **PSR J1907+0602** from VERITAS data for soft cuts (top panel), moderate cuts (middle panel), and hard cuts (bottom panel). 131

10.10 Pulse profiles of **PSR J1954+2836** from VERITAS data for soft cuts (top panel), moderate cuts (middle panel), and hard cuts (bottom panel). 132

10.11 Pulse profiles of **PSR J1958+2846** from VERITAS data for soft cuts (top panel), moderate cuts (middle panel), and hard cuts (bottom panel). 133

10.12 Pulse profiles of **PSR J2021+3651** from VERITAS data for soft cuts (top panel), moderate cuts (middle panel), and hard cuts (bottom panel). 134

10.13 Pulse profiles of **PSR J2021+4026** from VERITAS data for soft cuts (top panel), moderate cuts (middle panel), and hard cuts (bottom panel). 135

10.14 Pulse profiles of **PSR J2032+4127** from VERITAS data for soft cuts (top panel), moderate cuts (middle panel), and hard cuts (bottom panel). 136

10.15 Pulse profiles of **PSR J2229+6114** from VERITAS data for soft cuts (top panel), moderate cuts (middle panel), and hard cuts (bottom panel). 137

10.16 Pulse profiles of **PSR J2238+5903** from VERITAS data for soft cuts (top panel), moderate cuts (middle panel), and hard cuts (bottom panel). 138

10.17 **PSR J0007+7303** *Fermi*-LAT spectrum (black squares) with VERITAS flux upper limits (red and blue arrows). A power-law fit to the *Fermi* data above 10 GeV is given by the black dashed line. 139

10.18 **PSR J0205+6449** *Fermi*-LAT spectrum (black squares) with VERITAS flux upper limits (red and blue arrows). 140

10.19 **PSR J0248+6021** *Fermi*-LAT spectrum (black squares) with VERITAS flux upper limits (red and blue arrows). 140

10.20 **PSR J0357+3205** *Fermi*-LAT spectrum (black squares) with VERITAS flux upper limits (red and blue arrows). 141

10.21 **PSR J0631+1036** *Fermi*-LAT spectrum (black squares) with VERITAS flux upper limits (red and blue arrows). 141

10.22 **PSR J0633+0632** *Fermi*-LAT spectrum (black squares) with VERITAS flux upper limits (red and blue arrows). 142

10.23 **PSR J1907+0602** *Fermi*-LAT spectrum (black squares) with VERITAS flux upper limits (red and blue arrows). 142

10.24 **PSR J1954+2836** *Fermi*-LAT spectrum (black squares) with VERITAS flux upper limits (red and blue arrows). 143

10.25 **PSR J1958+2846** *Fermi*-LAT spectrum (black squares) with VERITAS flux upper limits (red and blue arrows). 143

10.26 **PSR J2021+3651** *Fermi*-LAT spectrum (black squares) with VERITAS flux upper limits (red and blue arrows). 144

10.27 **PSR J2021+4026** *Fermi*-LAT spectrum (black squares) with VERITAS flux upper limits (red and blue arrows). A power-law fit to the *Fermi* data above 10 GeV is given by the black dashed line. 144

10.28 **PSR J2032+4127** *Fermi*-LAT spectrum (black squares) with VERITAS flux upper limits (red and blue arrows). 145

10.29 **PSR J2229+6114** *Fermi*-LAT spectrum (black squares) with VERITAS flux upper limits (red and blue arrows). 145

10.30 **PSR J2238+5903** *Fermi*-LAT spectrum (black squares) with VERITAS flux upper limits (red and blue arrows). 146

10.31 Flux upper limits from the phase-gate test versus $\sqrt{\dot{E}}/d^2$ for soft cuts. The VHE flux limits are shown by the black squares, and the right-pointing arrows indicate an upper limit on $\sqrt{\dot{E}}/d^2$ for pulsars where only a distance limit is available. Error bars come from propagation of the uncertainty on the distance as given in Table 10.1. The flux and $\sqrt{\dot{E}}/d^2$ for the Crab pulsar are represented by the red dot. Extrapolated fluxes (see text) for the Geminga and Vela pulsars are shown as a teal and olive circles, respectively. The teal triangle and arrow is a Geminga VHE flux upper limit from VERITAS at 135 GeV from [7]. The Crab pulsar flux shown here is calculated according to the method given in the text. The solid gray line corresponds to $F \propto \sqrt{\dot{E}}/d^2$, where the line has been drawn to intersect the Crab pulsar flux point. The gray dashed lines have the same proportionality but indicate a flux level of two and ten times the Crab pulsar flux. The blue dashed line corresponds to $F \propto \dot{E}/d^2$, which is equivalent to the prediction $L_\gamma \propto \dot{E}$ that has been made for the gamma-ray luminosity in some models (e.g., [46]). The brown solid line is the same as the solid gray line but instead drawn to intersect the Vela flux point. 147

10.32 Continuation of Figure 10.31 for moderate cuts (*top*) and hard cuts (*bottom*). 148

A.1 VHE Crab Nebula spectral energy distributions for the flare and non-flare data sets. The SEDs are fit with power-law functions (§ A.3.1). From the limits on the relative flux change above 1 TeV, 4 TeV, and 6 TeV (§ A.4), upper limits on an extra flux component in the flare are computed assuming a spectral index of -2.4. 160

A.2 Combined SED of the Crab Nebula. The baseline *Fermi*-LAT spectrum (black squares) is averaged over ~5 years of observations, while the baseline VHE spectrum (blue circles) includes all good data taken outside of the FTW in the $2012 - 2013$ VERITAS observing season. The FTW VHE spectrum (red diamonds) shows no significant deviation from the baseline, while the synchrotron spectrum during this period (magenta triangles) exhibits spectral hardening. All spectral parameters given in § A.3.1, A.3.2. . . 162

A.3 *Fermi*-LAT and VERITAS light curves for the March 2013 Crab Nebula flare. The 12-hour binned *Fermi*-LAT light curve (square markers) spans MJD $56330 - 56370$. The VERITAS light curves (triangle and diamond markers) span ten nights during the FTW where weather permitted observations. The baseline Crab Nebula synchrotron flux above 100 MeV and average VHE flux above 0.15 TeV and 1 TeV are aligned and are indicated by the solid black line. The vertical scales of the three light curves have been adjusted such that the zero points and baseline fluxes are coincident. . 163

A.4 Relative flux changes for simultaneous *Fermi*-LAT (square markers) and VERITAS (triangle markers) observations during the FTW. The zero line corresponds to an observed flux equal to the average. Note that the vertical scale for the VERITAS points is a factor of ten smaller than the vertical scale for the *Fermi*-LAT points. 165

B.1 Laser setup in J. Buckley's lab at Washington Univeristy in St. Louis. Pictured are the PicoQuant pulsed 638 nm laser (*left*), adjustable neutral density filter wheel (*middle-left*), secondary filter holder (*middle-right*), and Hamamatsu PMT (*right*). 171

B.2 High-gain amplitude response across varying levels of light for the Hamamatsu PMT. The straight, red lines are linear fits to the data points for high gain (and the same for low gain shown in Figure B.3). The black points are average amplitudes for one light level (or equivalently, one OD value), whereas the red points are computed by adopting one trace as a template, fitting each recorded trace for the given OD with a Gaussian, and time-shifting and amplitude-scaling to best match the template trace before averaging. The FADC maximum is shown as the dashed black line, and note that the red points extend beyond the FADC maximum since the truncated traces are all fit with Gaussian shapes. 173

B.3 Low-gain amplitude response across varying levels of light for the Hamamatsu PMT. The red points are computed in the same manner described above. The pulse amplitudes clearly do not follow a linear progression. . . . 174

B.4 Average high-gain pulse shape obtained from averaging all recorded traces. 174

B.5 Average low-gain pulse shape obtained from averaging all recorded traces in the low-gain linear regime. 175

B.6 An example of a low-gain trace in the nonlinear regime where significant pulse broadening can be seen. 175

SUMMARY

Pulsars are powerful cosmic particle accelerators known to emit radiation across the entire electromagnetic spectrum. Their gamma-ray emission has been intensely studied at energies up to $\sim$10 GeV, above which the predicted and observed fluxes rapidly decline due to characteristics of the radiation mechanism. The recent and unexpected detection of very high-energy (VHE, $E > 100$ GeV) gamma-ray emission from the Crab pulsar has posed a novel and exciting challenge for experimentalists and theoreticians alike. In the time since its detection above 100 GeV with the Imaging Atmospheric Cherenkov Telescope (IACT) array VERITAS, no other pulsar has been firmly detected in the same energy band despite ongoing observational efforts by multiple IACT collaborations. The origin of the pulsed VHE emission from the Crab is currently the subject of an ongoing debate in the literature with no complete solution, since model predictions do not adequately explain the observed features of the VHE radiation. To better understand the VHE gamma-ray production mechanism of pulsars, I have conducted a search for periodic emission above 100 GeV from a total of 16 pulsars with VERITAS comprising a set of data with an exposure in excess of 580 hours. The set of pulsars includes many of the youngest and brightest gamma-ray pulsars visible in the northern hemisphere. The data analysis presented in this thesis in every case resulted in non-detections of pulsed gamma rays above 100 GeV. Upper limits on a potential VHE flux for each pulsar are presented, and these limits place strong constraints on a possible flux component manifesting at VHEs as is seen for the Crab pulsar.

CHAPTER 1

INTRODUCTION

1.1 Very High-Energy Gamma-Ray Astronomy

Very high-energy gamma-ray astronomy is an ever-growing field that aims to better understand some of the most extreme particle accelerators in the universe such as active galactic nuclei, supernova remnants, and neutron stars. Following the detection of the Crab Nebula in 1989, the first confirmed VHE gamma-ray source [1], the VHE source catalog has seen a rapid increase in number with over 100 new members[1] joining in just the last decade. The types of physics questions that can be addressed are far-reaching as relativistic acceleration of particles appears now to be quite ubiquitous in the universe. A map of all of the current detected VHE gamma-ray sources is shown in Figure 1.1.

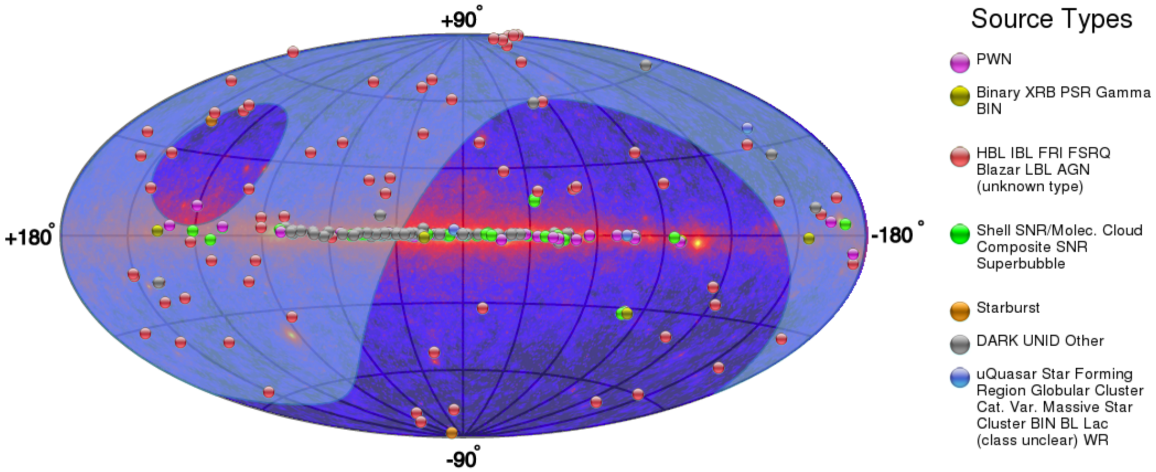

Figure 1.1: Map of all currently known very high-energy gamma-ray sources in galactic coordinates. The backdrop image is the high-energy gamma-ray sky seen by the *Fermi*-LAT. The fraction of the sky visible to VERITAS is indicated by the white shaded region. Figure from TeVCat [2] on September 25th, 2017.

The term “gamma ray” itself is fairly vague, given that it refers to any photon with an

---

[1] http://tevcat.uchicago.edu/

energy exceeding about $100\,\mathrm{keV}$. Gamma rays can be detected over many orders of magnitude in energy by different methods, thus it has become necessary to compartmentalize gamma ray energies into bins with different names. Relevant for this thesis are the high-energy (HE) and very high-energy (VHE) gamma-ray bands, which refer to photons with $30\,\mathrm{MeV} < E < 100\,\mathrm{GeV}$ and $100\,\mathrm{GeV} < E < 100\,\mathrm{TeV}$, respectively.

For each gamma-ray band, different detection techniques are employed. HE gamma rays are best detected with satellite-based pair-conversion instruments, such as the Large Area Telescope (LAT) aboard the *Fermi* satellite launched in 2008. When a gamma-ray falls into the telescope aperture, it interacts with the instrument via pair-production to $e^{+/-}$. The electron and positron are tracked through consecutive layers of silicon, eventually ending up in the calorimeter where their energy is measured. VHE gamma rays are detected on the ground by Imaging Atmospheric Cherenkov Telescopes (IACTs). A VHE gamma ray entering the atmosphere also interacts via pair-production, which causes a cascade of superluminal charged particles to form. These particles create a flash of Cherenkov light in a manner analogous to the formation of a sonic boom for supersonic motion. Some of the Cherenkov light is collected by IACTs, and the resulting images are used reconstruct the direction and energy of the VHE gamma ray that initiated the cascade.

There are currently three main IACTs in operation: H.E.S.S., located in the southern hemisphere in Namibia; MAGIC, located in the northern hemisphere in La Palma; and VERITAS, located in the northern hemisphere in southern Arizona. The data analyzed in this thesis were collected with VERITAS (the Very Energetic Radiation Imaging Telescope Array System), which completed construction in March 2007 and is still operational as of this writing. To date, VERITAS has detected nearly 60 sources of VHE gamma rays [2].

1.2 Gamma-Ray Astronomy and Pulsars

It was not until very recently that pulsars joined the VHE gamma-ray source class list with the paradigm-shifting detection of the Crab pulsar above $100\,\mathrm{GeV}$ by VERITAS [3]. The

Crab pulsar detection was later extened even further, up to 1.5 TeV by MAGIC [4]. As of this writing, the VHE detection of the Crab pulsar remains the only firm detection of a pulsar in the VHE band. The high-energy gamma-ray spectra that have been seen for pulsars in gamma rays are all well characterized by a broad curvature radiation component that originates from relativistic electrons and positrons that follow a curved trajectory as they are confined to the magnetic field lines. Curvature radiation can extend to GeV energies, where the gains from acceleration are balanced by energy losses [5]. The spectra in the GeV band detected by the *Fermi*-LAT can all be well described with an exponential cut-off as expected for curvature radiation [6], though statistics are sparse above $\sim$10 GeV due to the poor sensitivity of the LAT at these high energies. Based on the detection of the Crab pulsar above 100 GeV, it appears to be the case that curvature radiation is not adequate for a full explanation of the radiation from at least the Crab pulsar; the combined *Fermi*-LAT and VHE spectrum favors a power-law fit above ~ 10 GeV.

Several theories have been put forward in the past five years attempting to explain the observed radiation characteristics of the Crab pulsar at VHEs. However, as discussed later in Chapter 3, none are currently capable of offering a complete answer. It is therefore clear that in order to better understand the physics of gamma-ray radiation from pulsars, more research must be done in the VHE band. A detection of another pulsar at energies above 100 GeV would provide valuable new insight into the emission mechanisms, the geometry of the pulsar magnetosphere, and the dynamics of particle acceleration at work in these astrophysical particle accelerators. Even in the case of non-detections, upper limits on the VHE flux can be placed to constrain the predictions by models. To achieve this goal, I have conducted a total of 16 searches for new VHE-emitting pulsars with the most sensitive VHE instrument in the northern hemisphere for point-like targets, VERITAS.

1.3 Thesis Outline

This thesis is structured in the following way:

- Chapter 2 serves as an introduction to pulsars and the physics of their radiation. This chapter is intended to provide the basic framework for how pulsars work.

- Chapter 3 focuses solely on the very high-energy gamma-ray emission from pulsars. This chapter begins with an overview of most of the observational results that have been obtained to date. The impact these results have had on shaping the recent theoretical models attempting to explain the VHE emission is then summarized.

- Chapters 4, 5, and 6 focus primarily on the IACT technique and analysis employed by VERITAS. Chapter 4 provides an overview of air-shower physics, while Chapter 5 details the hardware of VERITAS. Chapter 6 gives an in-depth description of the gamma-ray reconstruction analysis chain used in the projects presented herein. Pulsar timing and *Fermi*-LAT analysis methods are also summarized in Chapter 6.

- Chapter 7 gives an overview of the statistical methods used in forming and interpreting the analysis results.

- Chapter 8 reports on a search for VHE pulsations from the Geminga pulsar with VERITAS. This chapter is an adapted reproduction of an article I have published in [7].

- Chapter 9 gives the details of a search for steady and pulsed VHE emission from the binary system PSR J1023+0038 with VERITAS. This chapter is an adapted reproduction of an article I have published in [8].

- Chapter 10 details a search for pulsed VHE gamma rays from 14 young gamma-ray pulsars appearing in archival VERITAS data. This project is the subject of an upcoming publication that will be submitted in late 2017 / early 2018.

- Chapter 11 provides some concluding remarks.

- Appendix A is a reproduction of a paper describing a search for enhanced VHE gamma rays during a Crab Nebula flare that occurred in March 2013. It has been placed in the appendix since the material covered is not directly related to the pulsar studies that form the bulk of this thesis.
- Appendix B summarizes a project involving quantification of idiosyncrasies in the VERITAS electronics chain for improving the simulations used in data analysis.

CHAPTER 2

THE PHYSICS OF PULSARS

In this chapter I give an overview of pulsar physics, starting with a short introduction to pulsars. Subsequently, I explain the canonical properties of pulsars and how they are deduced. The bulk of the chapter thereafter focuses on pulsar emission mechanisms and the standard models seen in the literature. Lastly, I summarize how the era of the *Fermi*-LAT and high-energy gamma-ray pulsars has impacted our understanding of these models. Very high-energy gamma-ray emission (observations and models) is the subject of Chapter 3.

2.1 Introduction to Pulsars

The first detection of a pulsar was made in radio[1] by J. Bell and A. Hewish in 1968 [10]. The regularly repeating pulses they observed were at the time attributed to possible oscillations of a white dwarf or a (then purely hypothetical) neutron star. Confirmation of the rotating neutron star model came not long afterwards in 1968 with the detection of the Crab pulsar in the Crab Nebula. The Nebula was already thought to house a neutron star—indeed, in the previous year, F. Pacini had argued that radiation from a rotating neutron star could be responsible for the observed expansion of the Crab Nebula [11]. The case for the neutron star nature of pulsars was further expanded independently by T. Gold in 1968 [12], and this explanation has remained universally accepted ever since.

Pulsars are the spinning neutron star remnants of supernovae involving main-sequence stars with a mass greater than $\sim 8M_{\odot}$. When a star has depleted all of its fuel for fusing elements into iron in the stellar core, the fusion stops, and gravitation is no longer countered by pressure from the hot core. At this point, electron degeneracy pressure prevents further

---

[1] The *true* first detection may have actually been in visible light a decade earlier by a keen-eyed pilot viewing the Crab Nebula through a telescope at the University of Chicago; see [9].

collapse. For stars with $M > 8M_\odot$, the collapse continues even further under gravity and electron capture occurs:

$$p + e^- \rightarrow n + \nu_e, \tag{2.1}$$

which creates an outward flux of neutrinos. The outer layers of the star above the core are blown apart, leaving the now degenerate stellar core behind. The remaining remnant of the core is a ball of hot neutrons ($T \sim 10^6$ K) of radius ~10 km supported from gravitational collapse by neutron degeneracy pressure. This object is called a neutron star. The resulting neutron star has a fast rotation period due to conserving most of the angular momentum of the parent star, and it is also very highly magnetized from possible conservation of the original magnetic flux (though the origin of the strong magnetic field is not yet clear [13]).

In the time since the first pulsar detection, over 2000 more have been detected across the entire electromagnetic spectrum [14]. Pulsars are divided into three categories depending on the energy source powering the observed radiation: *rotation-powered pulsars*, *accretion-powered pulsars*, and *magnetars*. In this thesis, only rotation-powered pulsars are discussed since these pulsars are known to emit in gamma rays. The emission from rotation-powered pulsars originates in the magnetosphere and is a result of particle acceleration in electric fields, and the mechanisms and locations of this emission are the focus of the remainder of this chapter starting with Section 2.3.

2.2 Properties of Pulsars

If the period P of a pulsar and its time derivative $\dot{P}$ have been deduced from observations, several properties of the pulsar can be approximated after making a few assumptions. The first assumption that is typically made is that the mass M is equal to the Chandrasekhar mass: $M = 1.4M_\odot$, which is a reasonable approximation since neutron stars cannot be more than about twice as massive without experiencing gravitational collapse [15]. The other assumption is that a pulsar is approximately a rotating, perfectly spherical, misaligned magnetic dipole.

The spin-down power $\dot{E}$ of a pulsar can be calculated by taking the time derivative of the rotational kinetic energy:

$$\begin{aligned} \dot{E} &= \frac{d}{dt}\left(\frac{1}{2}I\Omega^2\right) \\ &= -4\pi^2 I \frac{\dot{P}}{P^3}, \end{aligned} \tag{2.2}$$

where I is the moment of inertia of a solid sphere.

The surface magnetic field strength can be estimated by setting the spin-down power equal to the equation for power radiated by a rotating dipole, which is given by

$$P_{\text{dipole}} = \frac{2}{3}\frac{\ddot{m}_{\perp}^2}{c^3}, \tag{2.3}$$

where $m_{\perp}$ is the perpendicular component of the magnetic dipole with respect to the spin axis $\vec{\Omega}$. It can then be shown that the minimum surface magnetic field strength is given by

$$B > 3.2 \times 10^{19} \left(\frac{P\dot{P}}{1\text{s}}\right)^{1/2} \text{[Gauss]}, \tag{2.4}$$

where the assumed magnetic inclination angle $\alpha = 90^\circ$ corresponds to the minimum.

The so-called "characteristic age" τ of a pulsar can be approximated after noting that $P\dot{P}$ is constant assuming a constant magnetic field and additionally assuming that the original pulsar period P_0 is much less than the current period P. Thus we can integrate the same quantity under different limits as follows:

$$\begin{aligned} \int_{P_0}^{P} P dP &= \int_0^{\tau} (P\dot{P}) dt \\ \Rightarrow \frac{1}{2}(P^2 - P_0^2) &= P\dot{P}\tau \\ \Rightarrow \tau &\approx \frac{P}{2\dot{P}}. \end{aligned} \tag{2.5}$$

Pulsars can be dot plotted on a P-$\dot{P}$ diagram as shown in Figure 2.1 to reveal properties of the general population of known pulsars. There are clearly two distinct groupings of pulsars in the P-$\dot{P}$ diagram distinguished by characteristic age and surface magnetic field strength. These populations are referred to as the young pulsars (top-right) and millisecond pulsars (bottom-left). From Figure 2.1, it can be seen that the young pulsars detected in gamma rays by the *Fermi*-LAT typically have surface magnetic field strengths of at least 10^{11} G, $\dot{E} > 10^{33}\,\mathrm{erg\,s^{-1}}$, $P \lesssim 1$ s, and $\dot{P} > 10^{-16}$.

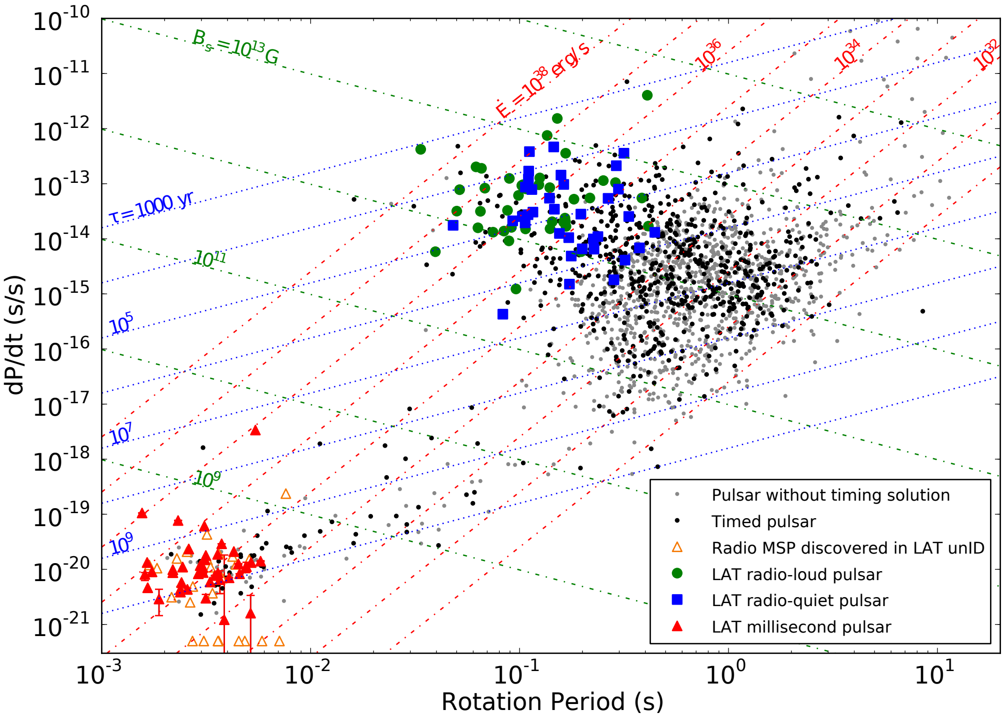

Figure 2.1: A P-$\dot{P}$ diagram from the 2PC. Lines of surface magnetic field strengths are shown in green, while characteristic ages are shown in blue, and spin-down powers are shown in red. Pulsars not detected by the *Fermi*-LAT are represented by the gray and black dots. Figure from [6]. © AAS. Reproduced with permission.

2.3 Mechanisms of Electromagnetic Radiation

In this section, an overview of the principal mechanisms for radiation from pulsar magnetospheres is given. The relevant processes are synchrotron radiation, curvature radiation, and inverse-Compton scattering. The expected multi-wavelength spectral manifestations of these three components are shown in Figure 2.2. The broad synchrotron component gives emission from radio waves through medium-energy gamma rays, while the broad curvature radiation component extends further to $\sim$10 GeV before petering off. A hypothetical inverse-Compton component could appear in VHE gamma rays, which is an idea treated in more detail in Chapter 3, though the basic mechanism is given in Section 2.3.3.

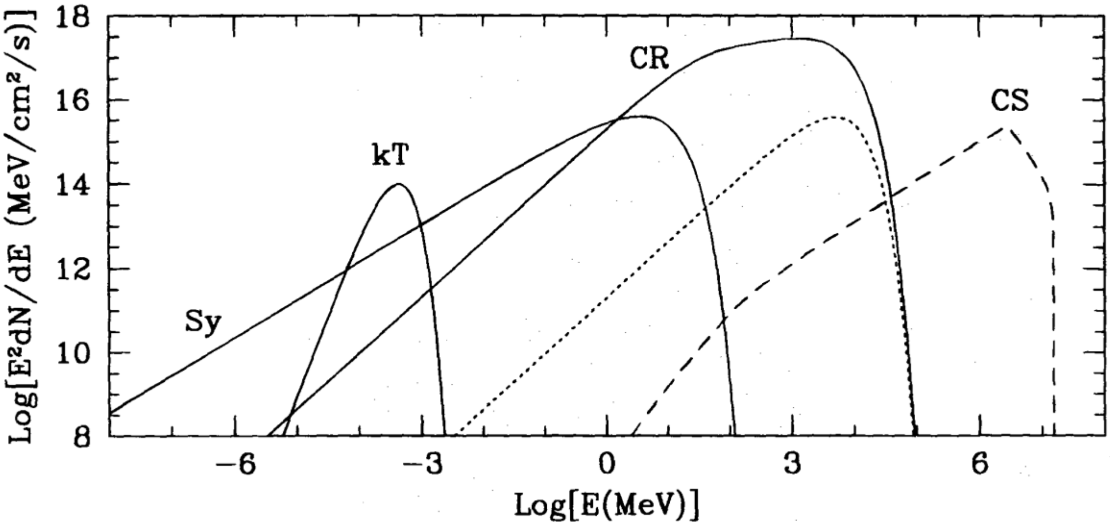

Figure 2.2: The standard pulsar spectrum from radio to very high-energy gamma rays. The different components are labeled as follows: Sy–synchrotron emission, kT–blackbody radiation, CR–curvature radiation, and CS–inverse-Compton scattering. The dotted line is the curvature spectrum due to a monoenergetic primary for comparison. Figure from [16]. © AAS. Reproduced with permission.

2.3.1 Synchrotron Radiation

Synchrotron radiation refers to radiation produced by a relativistic charged particle following a helical path along magnetic field lines. In the instantaneous plane of motion of a particle with Lorentz factor γ, as it swings around towards the observer, it emits electromagnetic radiation in a cone-shaped beam with an opening angle of γ^{-1}. A diagram of the emission mechanism is given in Figure 2.3. The emission contains many harmonics of the gyrofrequency, as opposed to the non-relativistic case (cyclotron radiation). The emission is inherently pulsed in that the emission beam only sweeps the line-of-sight of the observer once per gyration. However, in the case of real astrophysical sources of synchrotron radiation, the emission is produced by a population of particles with some variance in energy that do not move synchronously, thus the emission is detected as a continuous spectrum over a wide range of energies. The power spectrum in approximate form is given by

$$P(\nu) \approx 4 \times 10^{-22} B \left(\frac{\nu}{\nu_\mathrm{c}}\right)^{1/3} \exp\left(-\frac{\nu}{\nu_\mathrm{c}}\right) \mathrm{ergs}^{-1}\mathrm{Hz}^{-1}, \tag{2.6}$$

where B is the magnetic field strength in Gauss, and ν_c is the characteristic frequency

$$\nu_\mathrm{c} \sim \gamma^2 \nu_\mathrm{L}; \quad \nu_\mathrm{L} = \frac{eB}{2\pi mc}, \tag{2.7}$$

where ν_L is the Larmor frequency [17]. It can be seen from Equation 2.6 that the synchrotron radiation spectrum has two features: it follows a power law below ν_c, but it falls exponentially above ν_c. The typical synchrotron spectral shape for pulsar magnetospheric emission is shown in Figure 2.2 as the curve labeled "Sy."

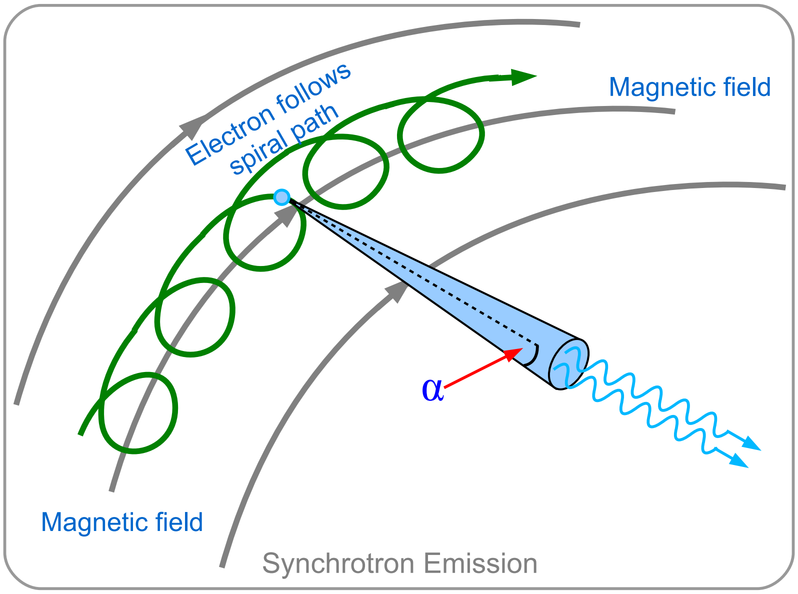

Figure 2.3: An emission schematic for synchrotron emission. The radiation is produced in a cone-shaped beam of angular width $\alpha = \gamma^{-1}$, as shown by the blue cone. The path of the electron is shown as the green helix. Figure from [18].

2.3.2 Curvature Radiation

Closely related to synchrotron radiation is curvature radiation, which describes emission due to a relativistic charged particle following a curved magnetic field line. For high magnetic field strengths, particles become tightly bound to field lines due to the $1/B$ dependence of the gyroradius. A particle trapped in a pulsar magnetosphere rapidly radiates energy via synchrotron radiation, quickly losing nearly all of its momentum perpendicular to the magnetic field. This process leaves the particle in the lowest Landau level[2]. Due to the curvature of the magnetospheric field lines, the particle will also emit a radiation beam tangential to the curved field line it follows in a manner analogous to synchrotron radiation. A schematic of the curvature radiation mechanism is shown in Figure 2.4. The typical curvature radiation spectrum is shown in Figure 2.2 labeled as "CR."

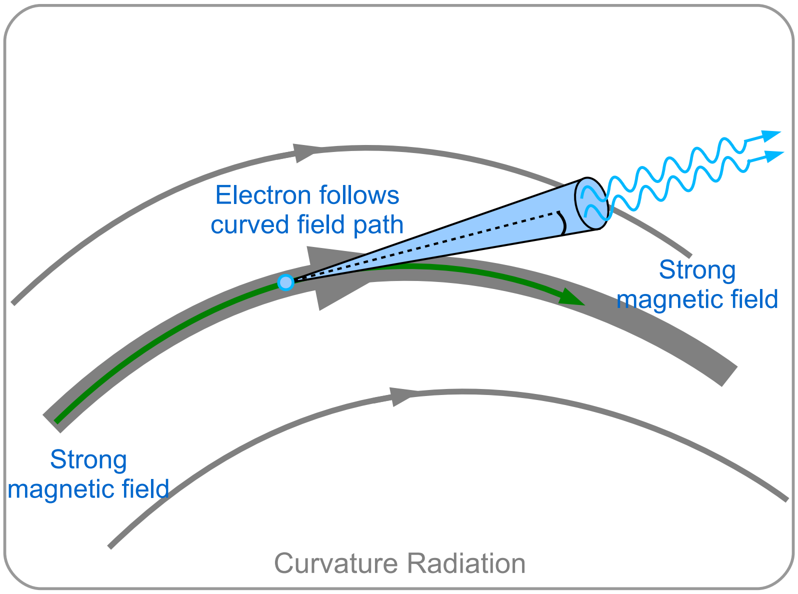

Figure 2.4: An emission schematic for curvature radiation. As a charged particle follows a magnetic field line to which it is bound, it emits photons in a cone due to the curved trajectory. Figure from [18].

As for synchrotron radiation, the power spectrum of curvature radiation displays a $\nu^{1/3}$ power-law dependence before the characteristic frequency ν_c and an exponential cut-off at

---

[2] Landau levels are quantized cyclotron orbits for charged particles moving in magnetic fields.

higher frequencies. The characteristic frequency for curvature radiation is given by

$$\nu_{\mathrm{c}} = \frac{3c}{4\pi\rho}\gamma^3, \tag{2.8}$$

where ρ is the curvature radius.

2.3.3 Inverse-Compton Scattering

Inverse-Compton scattering refers to the scattering of a photon off of a charged particle, taken here to be an electron (or positron), with the scattered photon receiving a boost in energy. Inverse-Compton scattering is the primary mechanism for producing VHE gamma rays in most known sources, and it may be responsible for the mysterious VHE emission seen from the Crab Pulsar as discussed in the next chapter. Diagrams for Compton and inverse-Compton scattering are given in Figure 2.5, and a hypothetical inverse-Compton spectral component for a pulsar is shown in Figure 2.2 as the dashed curve labeled "CS."

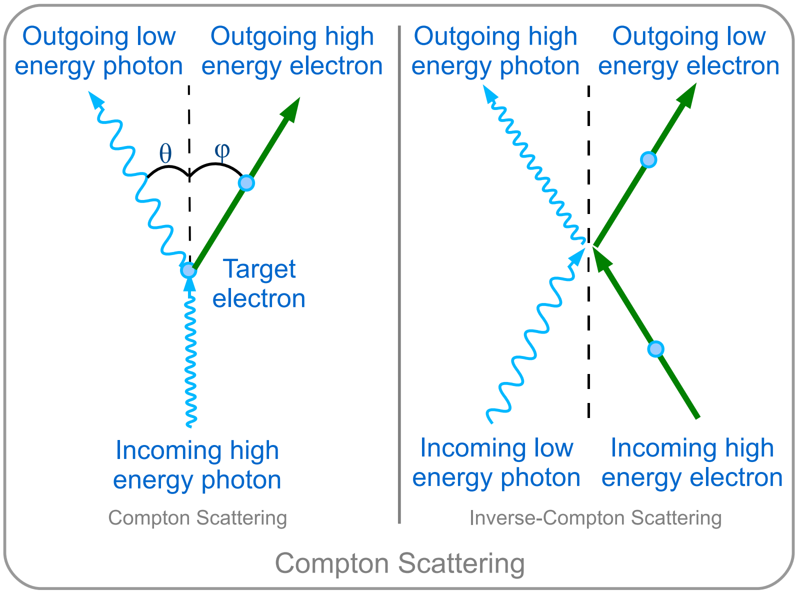

Figure 2.5: Two-panel diagram of Compton scattering. In the inverse-Compton scattering case (*right*), a high-energy charged particle collides with a lower-energy photon. The photon is "upscattered," receiving a large amount of energy from the charged particle in the interaction. Figure from [18].

The energy E'_{ph} of a Compton-scattered photon in the classical case by an electron at rest is given by

$$E'_{\text{ph}} = \frac{E_{\text{ph}}}{1 + \frac{E_{\text{ph}}}{m_e c^2}(1 - \cos\theta)}, \tag{2.9}$$

with the Thomson cross section

$$\sigma_T = \frac{8\pi}{3} r_0^2, \tag{2.10}$$

where r_0 is the electron radius. In the case that $E_{\text{ph}} \ll m_e c^2$, the energy of the scattered photon is essentially unchanged. However, in the regime where $E_{\text{ph}} > m_e c^2 = 511\,\text{keV}$, a quantum mechanical suppression effect called Klein-Nishina suppression manifests, due to the fact that the gamma-ray wavelength becomes less than the de Broglie wavelength of the electron. The smaller Klein-Nishina cross section is given by

$$\sigma_{\text{KN}} = \frac{3}{8}\sigma_{\text{T}} \left(\frac{m_e c^2}{E_{\text{ph}}}\right) \left[\ln\left(\frac{2E_{\text{ph}}}{m_e c^2}\right) + \frac{1}{2}\right], \quad E_{\text{ph}} > m_e c^2, \tag{2.11}$$

which is smaller than σ_T for all $E_{\text{ph}} > m_e c^2$. Therefore, Compton scattering occurs preferentially in the Thomson regime (i.e., for lower-energy photons).

If the charged particle is not taken to be at rest but rather has been accelerated to relativistic energies, the scattered photon can gain a large amount of energy. Assuming scattering in the Thomson regime in the rest frame of the electron, the photon energy does not change before and after scattering. The conversion of energy between laboratory and electron rest frames before scattering amounts to a Lorentz boost where $E'_{\text{ph}} = \gamma E_{\text{ph}}$. Conversion back to the laboratory frame picks up another factor of γ, so the resulting photon energy is $\gamma^2 E_{\text{ph}}$. Note that the scattering angles have been assumed to be $\sim \pi/2$, and that the scattered photon energy can never exceed $\gamma m_e c^2 + E_{\text{ph}}$.

2.4 Magnetospheric Emission Models

2.4.1 Overall Structure of the Magnetosphere

Goldreich and Julian [19] showed that a pulsar must have a plasma filling the surrounding magnetosphere. By assuming that the neutron star itself is a very good conductor, charges within the star will rearrange to screen electric fields induced by the pulsar rotation. Goldreich and Julian showed that by solving Laplace equation assuming a vacuum outside the star, one can show that $\vec{E} \cdot \vec{B} \neq 0$, indicating that some component of the electric field points along the magnetic field above the stellar surface. This electric field is sufficiently strong to overcome the force of gravity at the surface of the star and rip particles into the magnetosphere. Therefore, a pulsar is not surrounded by a vacuum (at least not for long)—a plasma fills the magnetosphere and can move about within the magnetosphere, confined to the field lines. It is not known whether the plasma composition is solely $e^{+/-}$ or if it contains some percentage of hadrons [20], though most models assume an $e^{+/-}$ plasma.

At a certain distance from the pulsar, a magnetic field line (and frozen-in plasma particles) should co-rotate at the speed of light, which is not possible in reality. This distance defines the so-called "light cylinder," which has a radius r_L given by

$$r_\mathrm{L} = \frac{c}{\Omega}, \tag{2.12}$$

where Ω is the angular frequency of the pulsar rotation. Typical light cylinder radii are on the order of 1000 km. Beyond a distance of r_L, the magnetic field lines can no longer close back to the neutron star surface, so instead they flow outwards in a spiral structure as shown in Figure 2.6. The field lines carry the $e^{+/-}$ plasma particles away from the pulsar in what is known as the "pulsar wind." This pulsar wind powers pulsar wind nebulae (PWNe; e.g., the Crab Nebula[3]) via shock acceleration.

---

[3] For more information about PWNe and particularly the Crab Nebula, see the study I have done in Appendix A.

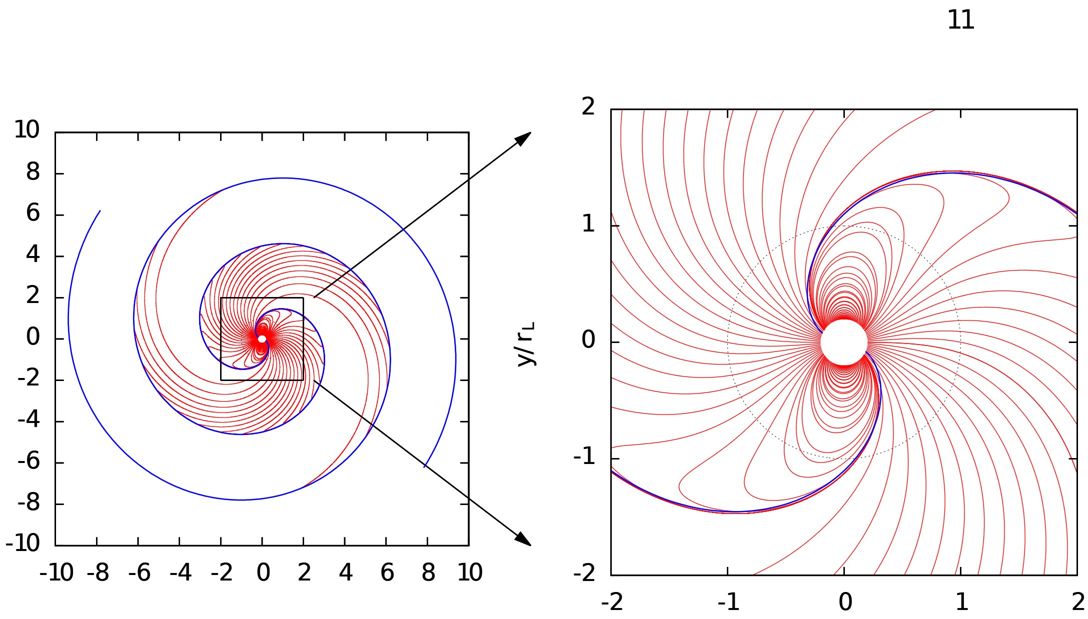

Figure 2.6: Magnetic field lines for a pulsar with a 90° misalignment between the spin and magnetic dipole axes. The right panel is a zoom of the left, and the gray circle indicates the light cylinder. The axis units are multiples of the light cylinder radius. The blue spirals are meant to show the wave structure of the magnetic field as it flows away from the pulsar. Figure from [20].

Broadly speaking, the general structure of the magnetosphere can be divided into three regions:

- The closed field, where the magnetic field lines close back to the neutron star surface. Here, charges are capable of rearranging freely, so no electric fields are possible.
- The open field, defined by magnetic field lines that intersect the light cylinder. In this region, magnetic field lines cannot close, so particles stream outwards. Electric fields can appear.
- Beyond the light cylinder, where the magnetic fields lines spiral outwards and shepherd the pulsar wind. Particle acceleration and pulsed emission may occur due to, e.g., magnetic reconnection. See Section 3.3 for further discussion.

There must exist electric fields present in the magnetospheres of pulsars, since particle acceleration is necessary to generate the non-thermal emission observed from many pulsars. Although the plasma that fills the pulsar magnetosphere shorts most of the electric fields generated due to the rotating magnetic field, it cannot do so everywhere in the open magnetic field. Regions of the magnetosphere where non-zero electric fields can manifest are known as the "gaps," and there are three main proposed gap locations:

1. *The Polar Cap*: The region near the neutron star surface around the magnetic poles (Section 2.4.2).
2. *The Slot Gap*: A thin region above the last closed magnetic field line towards the magnetic poles (Section 2.4.3).
3. *The Outer Gap*: A region formed by the last closed magnetic field line (tangential to the light cylinder) and the intersection of the null charge surface (Section 2.4.4).

These three regions are depicted visually in Figure 2.7. Note that in all three cases, the gaps involve magnetospheric locations where there exist open magnetic field lines. In the following sections of this chapter, details about these gap models and their importance in predicting the observed radiative characteristics of pulsars are given.

2.4.2 The Polar Cap

The polar cap model was introduced by Sturrock in 1971 [22], who argued that in the region above the magnetic poles of a rotating neutron star, a pair-creation cascade can form. Since the magnetic field lines do not close back to the neutron star in this region, electric fields will build up and accelerate electrons from the neutron star surface. These particles radiate photons via synchrotron and curvature radiation, with the photons then interacting in the strong magnetic field to pair-produce $e^{+/-}$. The synchroton radiation from the accelerated charges should be responsible for the observed optical and X-ray components, with the curvature radiation giving a gamma-ray component. Sturrock also argued that the features

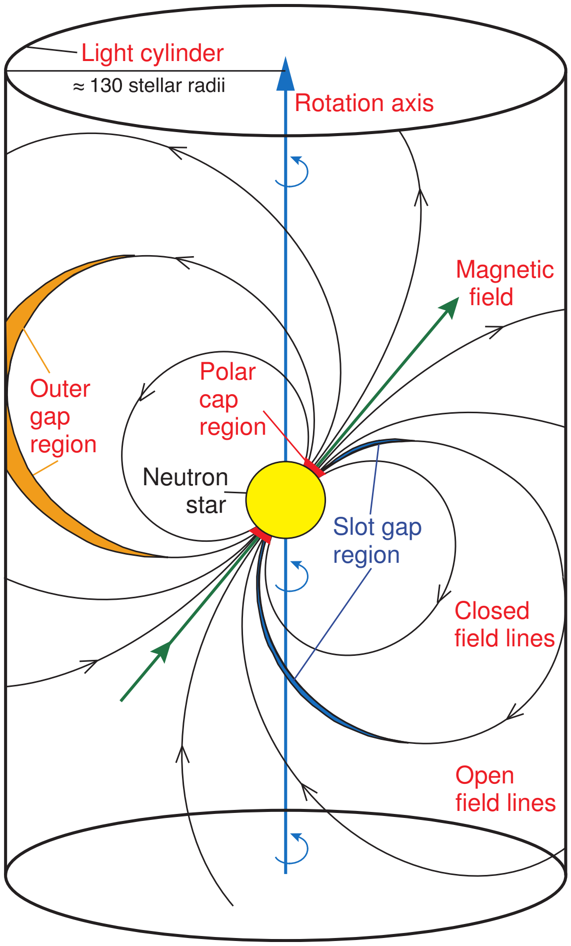

Figure 2.7: General structure of the pulsar mangetosphere and locations of the gap regions. The polar cap is just above the magnetic poles of the star and is shown in red. The slot gap is shown in blue, and the outer gap is shown in orange. The pulsar spin axis is indicated by the vertical light blue line, and the magnetic dipole axis is shown as a green line. Figure from [21].

of pulse profiles could be explained by the observer line-of-sight across the emitting region and gave some of the first examples of how this geometrical effect could manifest in a pulsar light curve.

A few years later in 1975, Ruderman and Sutherland [23] argued that the strong neutron star magnetic field causes an iron surface lattice to form, which prevents charges from being pulled from the stellar surface. Charges flow out of the magnetosphere along the open polar field lines, which results in a charge-depleted region and enables a static electric field to build up to about $\sim 10^{12}$ V. At this point, a perturbation by, e.g., a stray photon pair-producing in the strong electromagnetic field creates a $e^{+/-}$ pair, which then is accelerated. As before the particles generate a cascade via radiation of synchrotron and curvature photons, which cause further pair-production. The cascade quenches the electric field very quickly, and the cycle repeats itself with a timescale of a few microseconds. A diagram of a cascade in the polar cap region is shown in Figure 2.8.

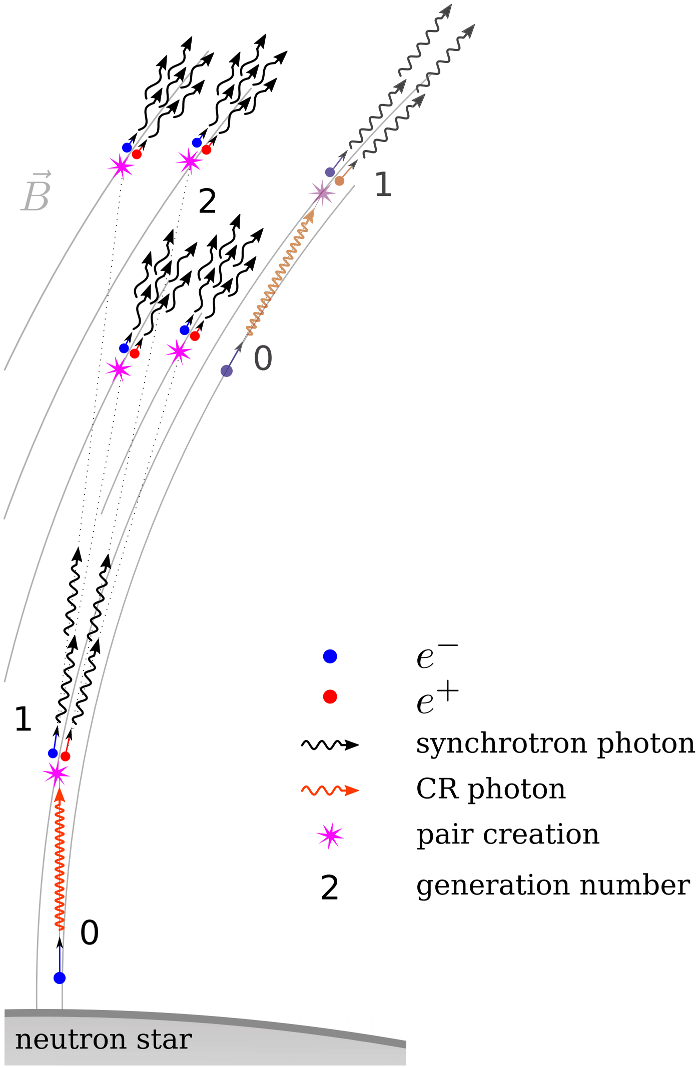

Figure 2.8: Diagram of particle cascades in the polar cap. Figure from [24]. © AAS. Reproduced with permission.

Another feature of polar cap models, predicted by [22] and [25] among others, is that the electrostatic potential difference that builds up in the gap depends on pulsar age. For the young pulsars, the accelerating potential difference is essentially independent of the age of the pulsar, while for older pulsars, age has a detrimental effect on the pair-production. Sturrock [22] suggests that this age effect could explain why only a relatively small subset of pulsars have been detected with spin periods less than $\sim$1 s, since slower-rotating pulsars tend to be older.

Polar cap models typically predict a spectral shape characterized by a “super-exponential” cut-off [26], which manifests as a steep decline in the energy spectrum at gamma-ray energies. Due to the strong surface magnetic field strength in the polar-cap region of the magnetosphere, gamma rays produced by curvature radiation are absorbed via single-photon pair-production. The predicted flux of these gamma rays is expected to fall super-exponentially above the escape energy, which is proportional to the inverse magnetic field strength.

2.4.3 The Slot Gap

Slot-gap models are essentially extensions of the polar-cap model in that they predict electromagnetic radiation from the magnetosphere near the polar cap, but at higher altitudes. The strength of the electric field near the magnetic poles should decrease to zero moving downward in latitude toward the last closed field line, where the magnetosphere is assumed to be a perfect conductor. Therefore, near the last closed field lines, the distance required for charges to be accelerated sufficiently to radiate photons capable of pair-production is much larger. A thin gap region thus forms, with a shape curved toward the last closed field line and approaching it asymptotically (see Figure 2.9) [27]. This gap is called the “slot gap” due to its shape. Emission from the slot gap is predicted to come from low to high altitudes ($r < 2R_{\text{NS}}$ up to $0.8r_{\text{L}}$) in various models (e.g., [28, 29, 30]).

2.4.4 The Outer Gap

First proposed by Cheng, Ho, and Ruderman in 1986 [31, 5], the outer gap refers to the region defined by the last closed field line and the null charge surface where $\vec{\Omega} \cdot \vec{B} = 0$. The null charge surface is a consequence of the Goldreich-Julian pulsar model [19], where

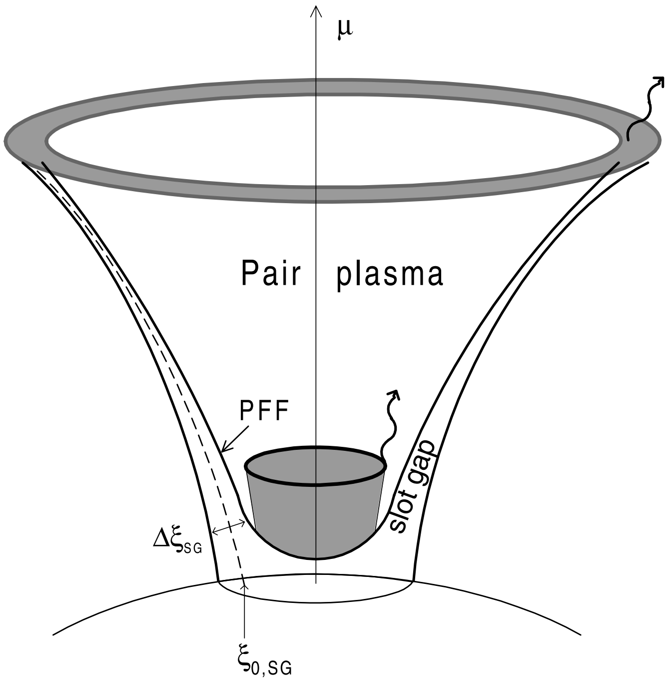

Figure 2.9: Diagram of the polar-cap and low-altitude slot-gap region in a pulsar magnetosphere. The curve labeled PFF refers to the pair-formation front—the propagation of the particle cascade in the polar cap. The gray hollow-cone beam shows the standard polar cap emission geometry. $\Delta\xi_{\mathrm{SG}}$ is the slot-gap thickness, and μ labels the magnetic dipole axis. Figure from [29]. © AAS. Reproduced with permission.

the predicted magnetospheric charge density is given by

$$\rho_{\mathrm{GJ}} = \frac{\nabla \cdot \vec{E}}{4\pi} = \frac{-\vec{\Omega} \cdot \vec{B}}{2\pi c} \frac{1}{[1 - (\Omega r/c)^2 \sin^2\theta]}, \tag{2.13}$$

and thus $\rho_{\mathrm{GJ}} = 0$ where $\vec{\Omega} \cdot \vec{B} = 0$. This expression for the charge is a result of taking the divergence of the Lorentz force equation with no net force and assuming axial symmetry. It can be seen from Equation 2.13 that the charge density switches signs across the null surface. Because charges flow out along the last closed field line and are unable to return, a charge-depleted region forms as depicted in Figure 2.10 and an electrostatic potential can begin to build.

In the outer gap, pair-production occurs (similar to the polar cap), which sustains the gap. Charges are accelerated due to an induced potential drop along the magnetic field

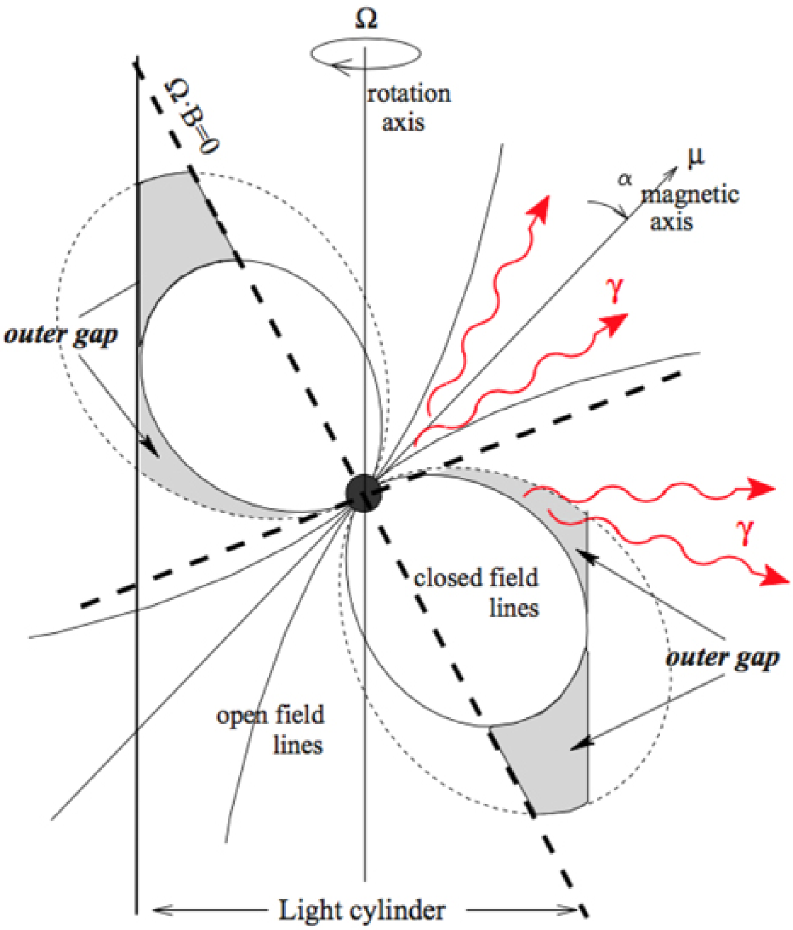

Figure 2.10: A pulsar magnetosphere diagram showing the outer gap (solid gray region). The null charge surface is indicated by the dashed line labelled $\Omega \cdot B = 0$. The magnetic dipole axis is labelled μ, and the rotation axis is labelled Ω. The angle between these two axes is given by α. The red squiggly lines depict gamma-ray emission from both the polar-cap and outer-gap regions. Figure from [32].

lines of up to $\sim 10^{15}$ V [31]. These charges radiate synchrotron and curvature photons, which then undergo two-photon pair production via interaction with softer photons. A cascade in the outer-gap region is thus formed [31]. It is not likely that a sustained outer gap is possible beyond a certain P-$\dot{P}$ death line [33] ($P \gtrsim 300\,\text{ms}$; $B \lesssim 10^{12}\,\text{G}$). In this case, the pair-production in the gap cannot be sustained for longer than about 10^7 yr, and emission from the gap stops.

The spectral cut-off shape predicted in the outer-gap accelerator for escaping high-energy gamma rays falls more slowly than in the polar-cap scenario. The magnetic field in the outer gap is weaker than in the polar-cap region due to its relative distance from the neutron star surface. Since single-photon pair production does not occur in the outer-gap cascade, the primary HE spectral cut-off feature is a result of the $e^{+/-}$ population being radiation-reaction limited. Therefore, different spectral cut-off features are predicted in the polar-cap and outer-gap models.

2.4.5 The *Fermi*-LAT and the Gaps

An overview of the three pulsar gap models has been given in the previous sections, and the natural question arises: given that gamma-ray emission is predicted from both the polar cap and outer gap, which model best explains the observations? The *Fermi*-LAT has now detected over 200 gamma-ray pulsars $>100\,\mathrm{MeV}$, and these observations have been studied in the context of the gap models to better understand the origin of the emission. The current consensus is that the majority of the gamma-ray emission seen from the LAT pulsars is likely produced in the outer gap.

The polar-cap model predicts a relatively thin emission beam centered around the magnetic poles of the neutron star. Due to the formation of the slot gap near the last closed field lines at the magnetic poles (as shown in Figure 2.9), this emission beam has its highest photon concentration in an annulus where photons from the slot gap escape. When the beam sweeps the observer line-of-sight, two peaks should emerge in the pulse profile, separated by a phase distance depending on the viewing angle ζ. One or zero peaks could also be seen given a different angle ζ.

The outer gap predicts a more broad emission beam, which is misaligned with respect to the polar-cap beam. The geometry of the outer-gap beam is more complicated due to its larger size and distance from the neutron star surface, where relativistic distortions should be taken into account. Outer-gap simulations are capable of predicting a wide variety of high-energy pulse profiles depending on ζ and the magnetic inclination angle α [34, 35]. The simulated gamma-ray light curves range from displaying two sharp peaks separated by a “bridge” of emission to single, broad peaks spanning almost all rotation phases. An example intensity pattern showing emission strength as a function of phase and ζ for a pulsar with $\alpha = 65°$ is shown in Figure 2.11.

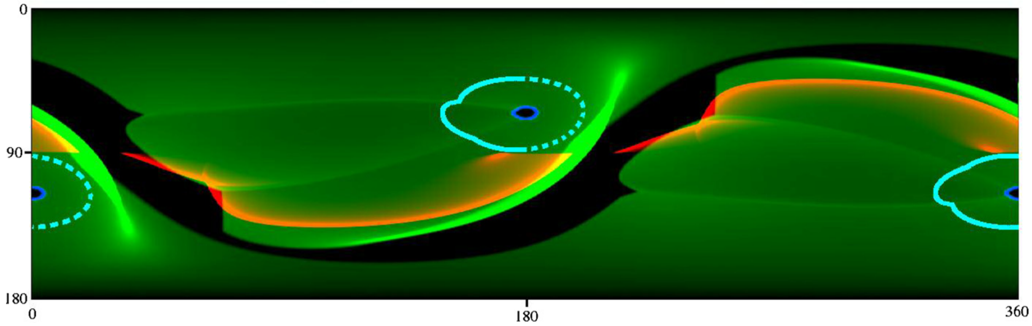

Figure 2.11: A simulated intensity pattern for a pulsar with $\alpha = 65°$. The rotation phase in degrees is given on the horizontal axis, while the vertical axis shows the viewing angle ζ. Emission from the three gap regions are shown with the polar cap in blue, slot gap in green, and the outer-gap component in orange. A horizontal slice through the pattern for a specific ζ would give a pulse profile. Figure from [34]. © AAS. Reproduced with permission.

The primary evidence for the outer-gap origin of the HE gamma-ray emission comes in the form of the observed pulsar light curves seen in the *Fermi*-LAT data (14 of which are shown in Figure 10.1). The observed HE light curves vary widely in peak morphology, which is difficult to explain in the polar-cap scenario. Furthermore, the location of the peaks in the light curves are not typically aligned from radio to gamma rays, which indicates that the gamma-ray emission originates in a different magnetospheric location. A subset of the detected HE gamma-ray pulsars are radio-quiet (e.g., Geminga), which is also difficult to explain if the radio and gamma-ray emission come from the same beam.

The high-energy gamma-ray spectra observed for *Fermi*-LAT-detected pulsars typically display a spectral cut-off at a few GeV, above which the flux falls exponentially [6]. For the brightest LAT pulsars, evidence has emerged that the HE flux falls sub-exponentially above the break energy (e.g., Vela [36]), which has been attributed to the summed contributions of multiple emission zones, each with different spectral index and break energy [37]. As previously stated for the polar-cap scenario, a super-exponential cut-off in the HE spectrum is expected due to single-photon pair-production, so once again it seems unlikely that most of the observed HE emission originates in the polar cap.

CHAPTER 3

REVIEW OF VERY HIGH-ENERGY PULSAR OBSERVATIONS AND MODELS

In this chapter, I present a short review of the major observational results that have been published to date regarding VHE pulsar studies. In the last section, I give an overview of a few of the theoretical models attempting to explain the observed VHE features (from principally the Crab pulsar). Portions of this text have been adapted from a conference proceeding I have written (to be published October 2017).

3.1 The Crab Pulsar

The Crab pulsar (PSR B0531+21) is the left over neutron-star remnant of a historic supernova that was observed in the year 1054 AD, and it is one of the most powerful known gamma-ray pulsars [38]. Located at a relatively nearby distance of 2.0 kpc with a spin period of ~33 ms, it is also the most energetic pulsar in the galaxy, with a spin-down luminosity of 4.6×10^{38} erg s^{-1}. Furthermore, the Crab Nebula surrounding the pulsar is one of the best-studied sources in VHE gamma rays.

3.1.1 Past Results

The first results searching for pulsed VHE gamma rays from the Crab pulsar in the current generation of IACTs came from the MAGIC Collaboration in 2007 with the announcement of a 2.9σ hint of pulsed emission above an energy threshold of 60 GeV in 16 hr of observations [39]. About one year later in November of 2008, the MAGIC Collaboration reported a firm detection above an energy of 25 GeV [21]. MAGIC observed the Crab between 2007 October and 2008 February, accumulating a total of 22.3 hr of data. The analysis of the data revealed a detection above 25 GeV at the 6.4σ level and a hint of emission above 60 GeV at the 3.4σ level. This detection implied an unusually high cut-off energy for the gamma-ray spectrum, indicating that the emission likely originates far from the pulsar in the magnetosphere and therefore excluding theoretical scenarios in which the emission is produced closer to the pulsar (e.g., polar-cap models). Furthermore, these observations revealed that the ratio P2/P1[1] increases with increasing energy and becomes >1 at around 60 GeV [21], thus indicating that the dominant peak at VHEs is P2.

A few years passed before the next major result concerning the gamma-ray emission from the Crab pulsar, and that was the detection of pulsed gamma rays above 100 GeV by VERITAS [3], first announced in August of 2011[2]. VERITAS observed the Crab between 2007 September and 2011 March, obtaining a total of 107 hr of data, which resulted in a detection at a level of 6σ[3]. The VERITAS data showed a narrowing of the pulse widths compared to what is seen at lower gamma-ray energies by the *Fermi*-LAT, and a proposed explanation was given of an acceleration region that becomes smaller following along the magnetic field confining the particles. The VHE spectrum measured extended to 400 GeV, and was well characterized by a power law with a spectral index of $3.8 \pm 0.5_{\text{stat}} \pm 0.2_{\text{sys}}$. Combining the VERITAS spectrum with that obtained from *Fermi*-LAT data >100 GeV, a power law with an exponential cut-off characterization of the spectrum was significantly excluded for the first time [3]. The combined spectrum is shown in Figure 3.1. Though the gamma-ray spectra seen for pulsars up to a few tens of GeV can be explained by a curvature radiation mechanism, the VERITAS detection posed the challenge that a new component is required for a complete explanation (at least for the Crab).

Updated results on the Crab pulsar from MAGIC came around the same time as the VERITAS announcement, with an addition of 34 hr more (59 hr total) of quality-selected data obtained in the winter of 2008/2009 [41]. In addition presenting phase-resolved spectral measurements in the energy range 25–100 GeV (which have since been superseded by the latest MAGIC results [4]), a variability study was performed by comparing the Crab

---

[1] Peaks seen in pulsar light curves are numbered, with P1 typically corresponding to the dominant peak seen in radio.

[2] Though published in October, the arXiv submission date is 2011 August 18.

[3] This significance was calculated using the *H*-Test [40].

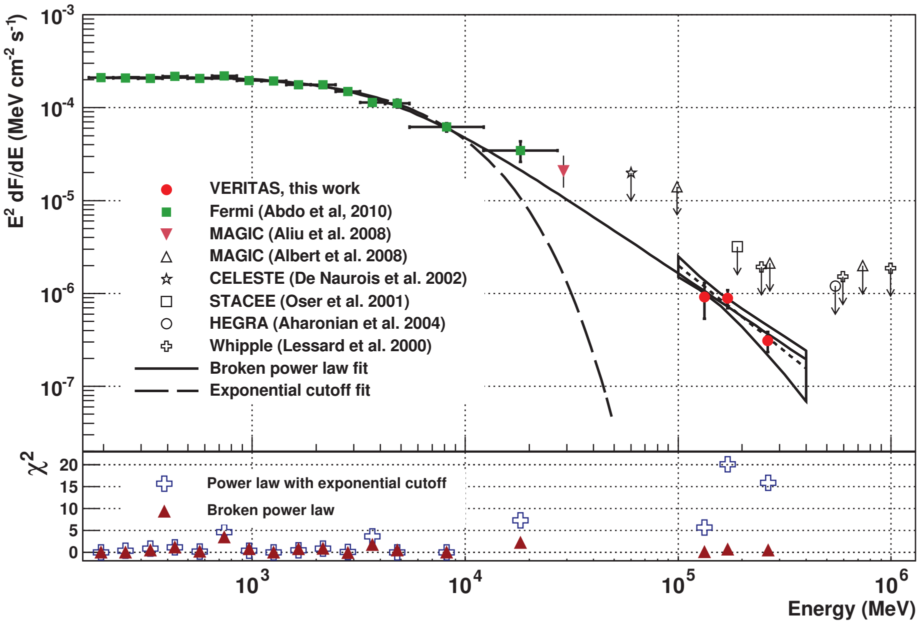

Figure 3.1: Crab pulsar spectral energy distribution for the energy range from 100 MeV to 400 GeV. Spectral measurements from the *Fermi*-LAT (green squares), MAGIC (upside-down maroon triangle), and VERITAS (red circles) are shown along with various flux upper limits from other VHE gamma-ray instruments. The exponential cut-off fit to the *Fermi*-LAT data is clearly a poor description for the tail of the spectrum. Figure from [3].

pulsar fluxes seen in the 2007/2008 season and the 2008/2009 season. No significant variability was found on the timescale of a year [41], though this does not preclude the possibility of variability on other timescales. Lastly, P1 and P2 were shown to be narrower in the MAGIC data compared to their appearance in the *Fermi*-LAT data, and the measured Crab pulsar flux significantly deviated from an exponential cut-off extrapolation of the *Fermi*-LAT data [41]. The MAGIC and VERITAS results in 2011 thus independently confirmed one another in these regards.

3.1.2 Recent Results

MAGIC has detected bridge emission above 50 GeV from the Crab pulsar after analyzing a data set comprising 135 hr of observations. The bridge region is defined as the phase range between P1 and P2, and an excess corresponding to 6.2σ is found after subtracting the background [42]. The detection of a bridge region above 50 GeV in the Crab pulsar light curve further complicates the task of modeling the gamma-ray emission—models need to be able to predict the spectral shape, the location and shape of the sharp peaks seen in the light curve, and now the bridge emission as well.

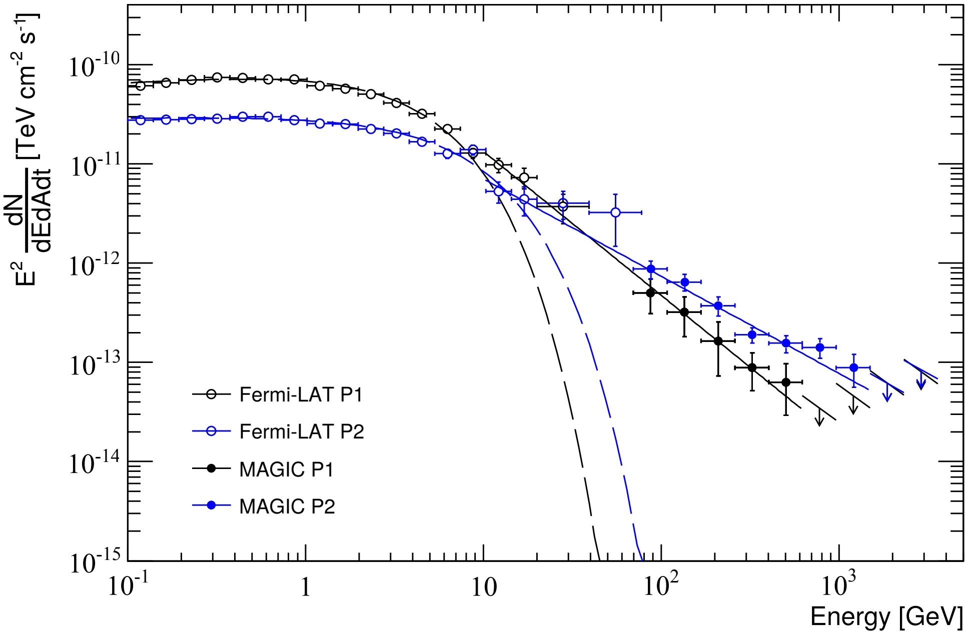

Figure 3.2: MAGIC and *Fermi*-LAT phase-resolved Crab pulsar spectra. The black and blue straight lines are power-law fits to the data above 10 GeV. The arrows represent 95% confidence level upper limits, with the slope of the line indicating the assumed spectral index for the upper limit calculation. The dashed lines are fits to the *Fermi*-LAT data of a power law with an exponential cut-off for P1 and P2. Figure from [4]

.

Most recently, the MAGIC collaboration reported the detection of pulsed emission from the Crab pulsar reaching up to 1.5 TeV in energy [4]. The Crab data set is 318 h of good quality data recorded between February 2007 and April 2014, and P2 (the dominant peak at these energies) shows significances of 6.0σ and 3.5σ for lower energy thresholds of 400 and 950 GeV, respectively. Phase-resolved spectra are derived for P1 and P2, and both are well described by simple power laws across the approximately one decade in energy probed in the data analysis. The spectral indices derived from power-law fits $>$150 GeV are $3.2 \pm 0.4_{\text{stat}} \pm 0.3_{\text{sys}}$ and $2.9 \pm 0.2_{\text{stat}} \pm 0.3_{\text{sys}}$ for P1 and P2, respectively [4]. The MAGIC and *Fermi*-LAT spectra for P1 and P2 are reproduced here in Figure 3.2.

3.2 Other Pulsars Observed by IACTs

Other pulsars (aside from the Crab) observed by IACTs include Geminga, Vela, and PSR J1023+0038. In this section, I briefly summarize the results obtained by MAGIC for the Geminga pulsar and by H.E.S.S. II for the Vela pulsar. The VERITAS observations, analysis, and results for the Geminga pulsar and PSR J1023+0038 are the subjects of Chapters 8 and 9, respectively.

3.2.1 The Geminga Pulsar

The Geminga pulsar (PSR J0633+1746) is located at the close distance of $\sim$250 pc [43, 44] and is the second-brightest steady gamma-ray emitter as seen by the *Fermi*-LAT, making it an obvious target for VHE observations. The Geminga pulsar has a period of $\sim$240 ms and a spin-down power of $3.2 \times 10^{34}\,\mathrm{erg\,s^{-1}}$ [43]. It is the first radio-quiet gamma-ray pulsar ever detected [45]. The gamma-ray pulse profile of Geminga shows two peaks separated by a bridge of emission, similar to what is seen for the Crab and Vela pulsars. Like for other gamma-ray pulsars, the Geminga pulsar spectrum $>$100 MeV can be described by a power law with an exponential cut-off [6]; however, [46] has claimed that the spectral tail may be better characterized by a simple power law. Please refer to Section 8.2 for more information about the Geminga pulsar.

MAGIC Observations and Analysis

The MAGIC campaign on the Geminga pulsar resulted in 63 hr of good quality data recorded between December 2012 and March 2013. Events were phase-folded with a *Fermi*-LAT timing solution. The P1 region was selected by fitting an asymmetric Gaussian to the *Fermi*-LAT light curve $>$5 GeV and $>$10 GeV for P2. No significant evidence for pulsed emission was found in any of the three energy ranges ($>$50 GeV, 50–100 GeV, 100–200 GeV) tested in the MAGIC gamma-ray data [47], so only upper limits on a possible flux were reported.

For full details of the MAGIC Geminga campaign (including the steady-source search), please see the MAGIC collaboration publication [47].

The MAGIC VHE flux upper limits do not constrain a simple power-law extrapolation of the *Fermi*-LAT data above 10 GeV. Observations with a future-generation instrument operating in the VHE band could help determine whether or not the Geminga pulsar spectrum extends to VHEs as a simple power law, as seen for the Crab pulsar.

3.2.2 The Vela Pulsar

As the brightest steady source seen by the *Fermi*-LAT [37], the Vela pulsar (PSR J0835–4510) makes a prime candidate for a VHE pulsar search. Though not a young pulsar, Vela is located nearby at a distance of ∼287 pc [48] and has a spin-down power of 6.3×10^{36} erg s^{-1} with a period of 89 ms. In the gamma-ray light curve, Vela shows two sharp peaks separated by a complex bridge region, with P2 seen as the dominant peak at gamma-ray energies above ∼300 MeV [49].

H.E.S.S. II Observations

The H.E.S.S. array of IACTs underwent an upgrade in 2012 with the addition of a new 28 m diameter telescope called CT5 [4]. Given the large light collection area of the telescope, it has enabled the detection of fainter gamma-ray showers initiated by gamma rays with energies below 100 GeV. This has helped bridge the H.E.S.S. sensitivity into an overlapping energy regime with satellite-based gamma-ray telescopes, namely the currently operational *Fermi*-LAT.

The H.E.S.S. collaboration obtained 40.3 hr of good quality data at zenith angles less than 40° during the CT5 commissioning period. After performing a likelihood ratio test for the presence of P2 (phase range: [0.5-0.6]) in the monoscopic data set, the Vela pulsar (P2 only) was detected at the 15.6σ level and at the 17.9σ level with the *H*-Test. As of this

---

[4] https://www.mpi-hd.mpg.de/hfm/HESS/pages/home/hess2inaug/

writing, this detection makes the Vela pulsar the second pulsar detected from the ground with the IACT technique. For a more complete account of the H.E.S.S. II detection of the Vela pulsar, please see [50].

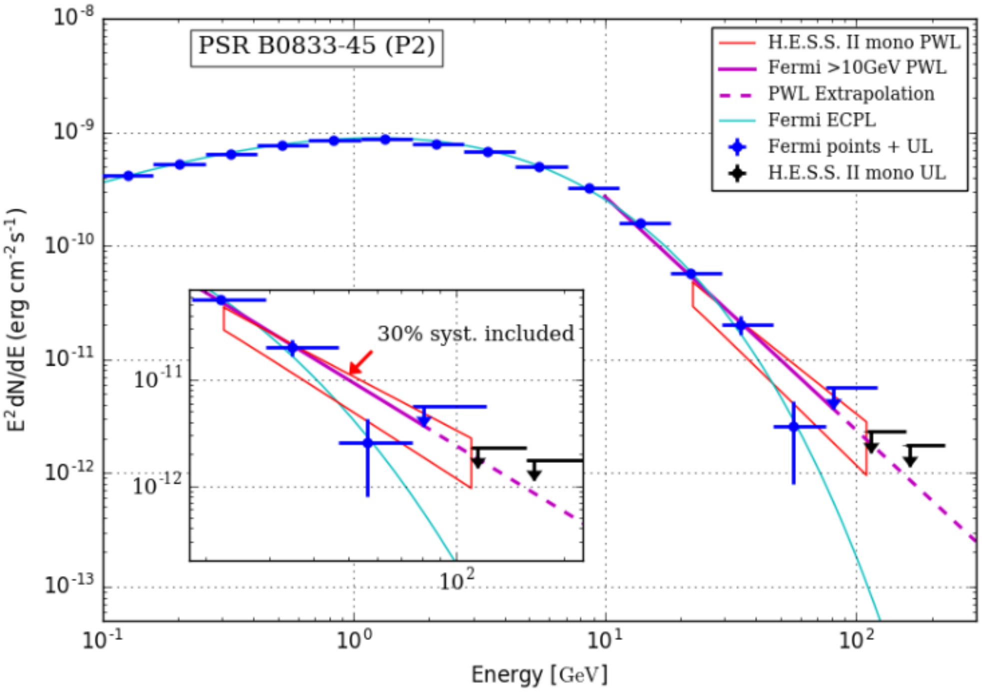

Figure 3.3: *Fermi*-LAT and H.E.S.S. II spectra for the dominant gamma-ray peak seen from the Vela pulsar, P2. The *Fermi*-LAT points are shown in blue; the H.E.S.S. detection bow tie is shown in red; a simple power-law fit to the LAT data is given by the purple solid and dashed lines; and the cyan line is a power-law-with-an-exponential-cut-off (denoted ECPL in the legend) fit to the LAT data above 100 MeV. Reproduced from [50], with the permission of AIP Publishing.

The H.E.S.S. II spectrum of the Vela pulsar was generated using a forward-folding maximum-likelihood method above a lower-energy threshold of 20 GeV and is shown in Figure 3.3. A simple power-law fit in the energy range 20–110 GeV revealed a spectral index of $4.1 \pm 0.2_{\text{stat}} \pm 0.2_{\text{sys}}$, consistent with a power-law fit index derived from a *Fermi*-LAT data sample. Fitting with a log-parabola in the same energy range to test for curvature did not show a significant improvement of the fit [50]. The *Fermi*-LAT data on its own indicates a very marginal preference for curvature when fit $>$10 GeV [50]. For now, the Vela P2 spectrum seen at the highest energies is consistent with both curvature and a power-law fits. Given that the Crab pulsar spectrum is seen to extend into VHEs as a simple power law, whether or not curvature is present at the highest energies in the Vela P2 spectrum is an important question that remains unanswered for the time being.

3.3 Status of Theory

It has long been postulated that particle acceleration occurs in pulsar magnetospheres in so-called "gap" regions—regions where particles are accelerated in electric fields induced by the rotating magnetic dipole. As discussed in Section 2.4, the three canonical gap regions are the polar cap, the slot gap, and the outer gap. High-energy gamma-ray production is most commonly thought to be a result of curvature radiation in one of the gap regions, where charged particles follow curved magnetic fields lines and thus radiate electromagnetically. Curvature radiation predicts an exponentially decaying flux above energies of a few GeV, and the sub-exponential cut-offs seen for (most) pulsars are thought to be a result of the superposition of curvature spectra from multiple particle populations with different break energies [36, 37]. Observations in the era of the *Fermi*-LAT have given favor to outer-gap-type models due to the ability of these models to reproduce the gamma-ray light curves [51] and the shape of the exponential cut-off in the spectra. Furthermore, the sheer number of gamma-ray pulsar detections is better explained in an outer-gap emission scenario due to the wider emission beam compared to that of the polar cap.

Since the detection of the Crab pulsar in the VHE gamma-ray band in 2011, much work has been done attempting to explain the VHE emission. In [46], it is argued that the observed VHE emission is a result of synchrotron self-Compton (SSC) scattering of UV–X-ray photons by secondary particles in the pair cascade. In this scenario, the UV–X-ray photon are a result of synchroton emission, and the same particle population emitting these photons is responsible for up-scattering to VHEs (hence "self" in SSC). The inverse-Compton scattering is argued to occur near the light cylinder in the Klein-Nishina regime due to the predicted Lorentz factor required for particles in the radiation-reaction limit for curvature radiation. The maximum energy of inverse-Compton scattered photons is estimated to be

$$E_{\mathrm{max}} \approx 150\,\mathrm{GeV}\,\left(\frac{\eta}{10^{-2}}\right)^{1/4}\sqrt{\xi}\left(\frac{\lambda}{10^{2}}\right)^{-1}, \tag{3.1}$$

where η is the ratio E/B, ξ is the ratio of the radius of curvature for curvature radiation to the light cylinder radius ($r_{\mathrm{c}}/r_{\mathrm{L}}$), and λ is the particle multiplicity. If the emitting region is taken to be close to the light cylinder, then $r_{\mathrm{c}}/r_{\mathrm{L}} \approx 1$, and η is roughly a few percent. The multiplicity λ is more uncertain, with values of $\sim 10^2$ [52] or $\sim 10^4$–10^6 [53] found in the literature for the outer gap accelerator. Equation 3.1 predicts inverse-Compton VHE gamma rays up to 150 GeV assuming the quantities are approximately unity, though gamma rays of higher energies could be produced for $\eta > 0.01$.

Another more recent synchrotron self-Compton model (Harding and Kalapotharakos [54]) uses numerical simulations of the particle cascades produced near the polar cap to predict the multi-wavelength spectra for young pulsars. These particles flow out to high altitudes in the magnetospheric slot gap near (and beyond) the light cylinder while radiating and scattering synchrotron photons. Detectable VHE emission from the Crab pulsar is predicted to appear as a result of SSC scattering by the particle pairs in the cascades. For other pulsars (including the brightest HE gamma-ray pulsar Vela), the simulated pair SSC component is orders of magnitude below the detection threshold for current instruments, even assuming a deep exposure, due to lower $\dot{E}$ and magnetic field strengths compared to the Crab.

It has also been argued that the pulsed VHE emission from the Crab originates outside the light cylinder due to the acceleration in the pulsar wind (e.g., [55], [56], [57]). In one such model [55], it is argued that the particle wind beyond the light cylinder is accelerated in a cylindrical region of radius between 20–50 r_{L} called the "wind acceleration zone." In this region, the incoming Poynting-flux-dominated wind is converted to a wind dominated by its kinetic energy, which involves acceleration of the wind particles to some Lorentz factor Γ_{w} via an unknown mechanism[5]. These accelerated particles preferentially up-scatter

---

[5] This is the so-called "sigma problem" of pulsar wind nebulae.

pulsed X-rays to VHEs via inverse-Compton scattering in the Klein-Nishina regime. The location of the X-ray / HE and VHE gamma-ray pulses in the observed light curves are predicted to be offset in phase due to geometrical effects involved in the inverse-Compton scattering that takes place far from the light cylinder. Predicted VHE spectra for the Crab pulsar for various Γ_w and wind-acceleration-zone widths are shown in Figure 3.4.

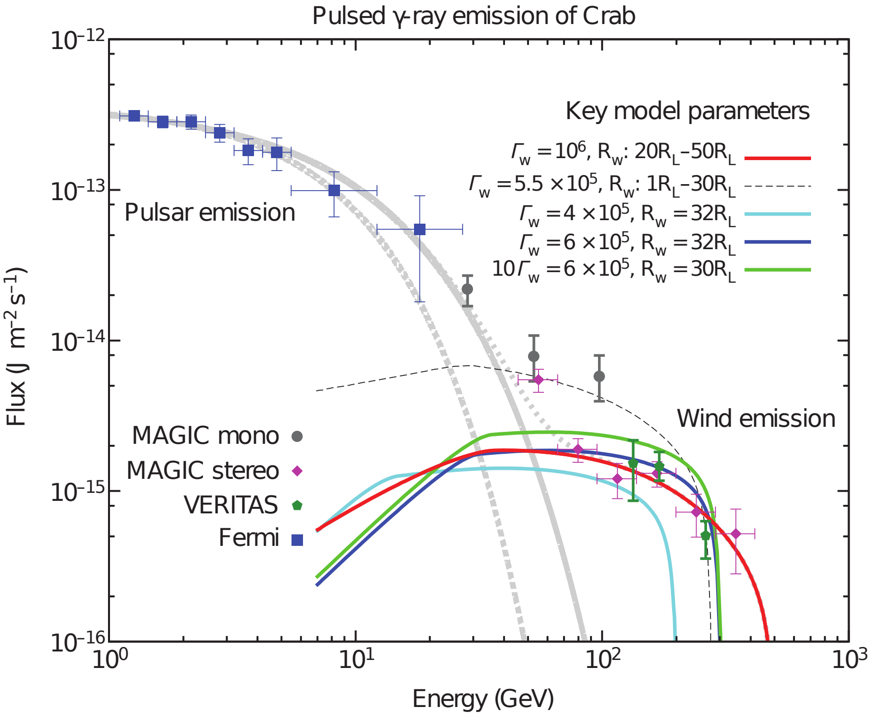

Figure 3.4: Crab pulsar spectrum between 1 GeV and 1 TeV with superposed model predictions from [55]. The *Fermi*-LAT data are shown as blue squares, while the VHE data are given as the gray circles and magenta diamonds (MAGIC) and the green hexagons (VERITAS). The gray dashed and solid lines are fits to the LAT data, while the dotted gray line is the sum of the red and gray solid lines. The colored lines give the predictions from the wind model as specified in the legend. The parameter Γ_w is the wind Lorentz factor, R_w is the distance from the neutron star to the center of the wind acceleration zone, and R_L is the light-cylinder radius ($\sim 10^6$ m). Figure from [55].

Another mechanism for explaining the pulsed VHE gamma-ray emission from the Crab pulsar is that of magnetic reconnection occurring in a “striped wind” beyond the light cylinder [57]. The magnetic field far from the neutron star has regions of reversing magnetic polarity (see Figure 2.6), and turbulent magnetic reconnection in the boundaries accelerates particles in the pulsar wind. These particles then radiate and up-scatter synchrotron photons, which gives rise to the gamma-ray spectrum of the pulsar including an SSC component at VHEs.

3.4 Conclusion

The recent extension of the Crab pulsar spectrum up to 1.5 TeV [4] in late 2015 has posed the new challenge that the models must be able to predict the power-law shape seen in the data up to 1.5 TeV, in addition to the VHE light curve. The emitting region must be far from the neutron star surface given the energies of the detected gamma rays, since VHE gamma rays generated at smaller radial distances should be absorbed in the strong magnetic field via pair-production. The VHE emission cannot be explained by curvature radiation, since the radius of curvature would need to be extremely large, larger than the light-cylinder radius [3]. Inverse-Compton scattering of lower-energy photons is most likely the fundamental mechanism, though the specifics regarding where and how it occurs are currently a subject of debate in the literature as discussed in the previous section.

For now, no model is capable of simultaneously predicting the Crab pulsar VHE light curve and the spectral shape [58]. The explanation for the VHE emission given in [46] can predict photons up to $\sim$150 GeV in energy (or slightly higher), but the power-law spectrum seen by MAGIC extends to 1.5 TeV. The SSC model from [54] predicts the multi-wavelength Crab pulsar emission fairly well up to VHEs, though it struggles above $\sim$100 GeV, and no light-curve predictions are made. The wind-acceleration-zone model presented in [55] predicts a spectral component that falls above $\sim$400 GeV (see Figure 3.4), and thus is also challenged by the MAGIC detection to TeV energies. The striped-wind model from [57] currently fares well in predicting the observed Crab pulsar spectrum, though predictions from this model for the gamma-ray light curves remain to be seen.

Predictions of VHE gamma-ray emission from pulsars other than the Crab have in general not been the main focus of models in the literature. In most models, predicted VHE emission (for the Crab or otherwise) typically depends strongly on parameters such as the pair multiplicity, magnetic field strength, and the spin-down power (e.g., [46] and [54]). The Crab pulsar is rather unique in this regard, possessing the highest spin-down power[6] of any known pulsar in our galaxy. The Crab also has a high surface magnetic field strength relative to most other young gamma-ray pulsars. Though detectable VHE emission is predicted from the Crab pulsar in the framework of recent models, similar predictions for other pulsars are unlikely given their more modest physical parameters. However, since the current state of the theory of VHE emission from the Crab pulsar is inconclusive, the potential for a surprising discovery could still be present, even if unlikely.

---

[6] Only PSR J0537–6910 is known to have a higher $\dot{E}$, though it resides in the Large Magellanic Cloud.

CHAPTER 4

THE PHYSICS OF AIR SHOWERS

4.1 Introduction

Central to the IACT technique is the detection of Cherenkov photons produced in gamma-ray- and cosmic-ray-initiated atmospheric air showers, which are described in this chapter. Firstly, the production of Cherenkov radiation and its properties are discussed, followed by summaries of electromagnetic and hadronic air showers. An illustration of the general atmospheric-shower-imaging problem is the subject of Figure 4.1.

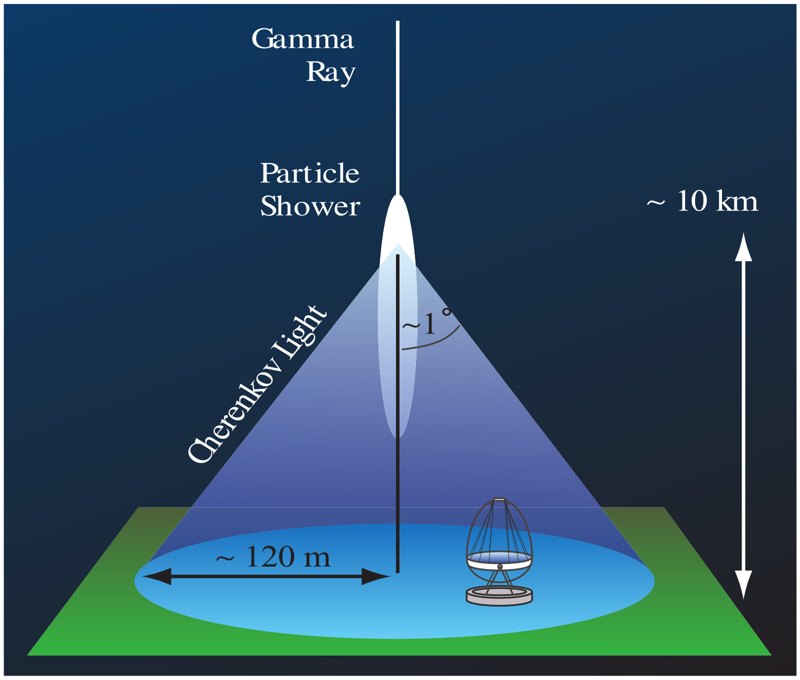

Figure 4.1: Cartoon depicting the creation of a Cherenkov light pool due to a gamma-ray induced air shower. An IACT located within the light pool collects some of the Cherenkov photons and images the air shower, which is then used to reconstruct properties of the primary gamma ray.

4.2 Cherenkov Radiation

Cherenkov radiation is the light emitted when a charged particle travels through an electrically polarizable medium at a speed greater than the speed of light in that medium. The speed of light in such a medium is c/n where n is the index of refraction, thus Cherenkov radiation is emitted if

$$v > \frac{c}{n} \quad \text{or} \quad \beta > \frac{1}{n}, \tag{4.1}$$

where v is the particle velocity. The process of emission is analogous to the creation of a sonic boom when an object exceeds the local speed of sound, wherein the emitted sound waves cannot propagate forward relative to the object resulting in the generation of a shock front behind the object. In the case of a superluminal charged particle, as it moves through a dielectric medium, it will polarize and reorient the nearby atoms (or molecules) in a way that results in a coherent photonic shock front created behind the particle as shown in Figures 4.2 and 4.3.

The angle of Cherenkov emission θ relative to the particle path can be found by considering the cone shape of the wake, perpendicular to which the Cherenkov photons are emitted. As shown in Figure 4.3, if in some elapsed time t the particle has traveled a distance $vt = \beta ct$, then an emitted Cherenkov photon will have traveled a distance $(c/n)t$. The Cherenkov angle is then:

$$\theta = \cos^{-1}\left(\frac{1}{\beta n}\right). \tag{4.2}$$

Assuming $\beta = 1$, for Cherenkov radiation in air with $n_{\text{air}} = 1.00029$, the emission angle is $\theta_{\text{air}} = 1.3°$. Assuming Cherenkov photon production at a height of $\sim$10 km, the photons will land on the ground in a circle of radius $\sim$100 m, which is commonly referred to as the light-pool radius. In reality, the index of refraction changes with the density of air, causing the Cherenkov angle to increase with decreasing altitude.

The minimum value for β is $1/n$, since Cherenkov radiation only occurs for $v > c/n$. That there is a minimum β implies a minimum particle energy for Cherenkov radiation for a

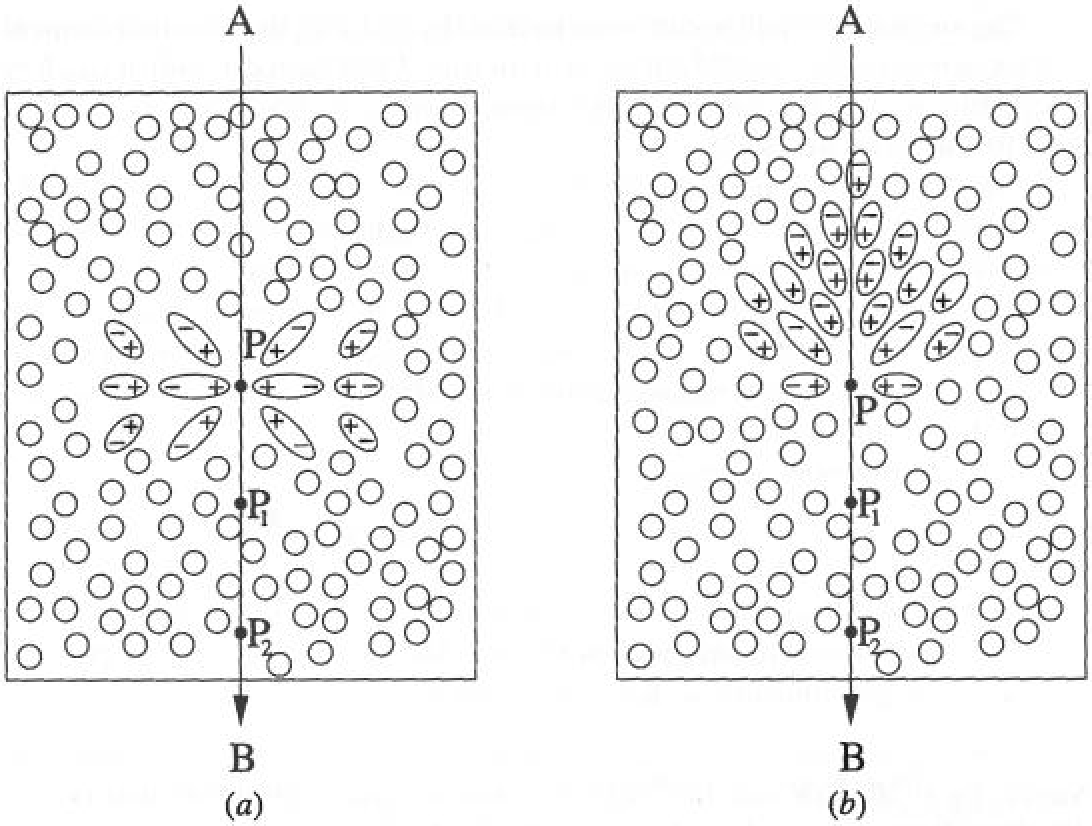

Figure 4.2: Illustrations showing the polarization induced in nearby atoms due to a passing charged particle. In *(a)*, a subluminal particle is shown polarizing atoms in a symmetric fashion, which will not produce coherent depolarization. In *(b)*, a superluminal particle is shown leaving a wake of polarized atoms, which will depolarize coherently, producing Cherenkov radidation. The particles take the trajectory from A to B, as indicated by the vertical arrow. Figure from [59].

given index of refraction. Taking $n_{\text{air}} = 1.00029$, the minimum β is then $\beta\text{min} = 0.99971$, which gives $\gamma_{\text{min}} = 41.53$. The minimum particle energy for Cherenkov radiation in air due to an electron or positron is then $E_{\text{min}} = \gamma m_e c^2 = 21.2\,\text{MeV}$.

It can be shown that [60] the spectrum of Cherenkov radiation per path length x per wavelength λ is given by:

$$\frac{d^2N}{dxd\lambda} = \frac{q^2 2\pi\alpha}{\lambda^2}\left(1 - \frac{1}{\beta^2 n^2(\lambda)}\right) \tag{4.3}$$

where q is the elementary charge of the particle and α is the fine-structure constant. It can

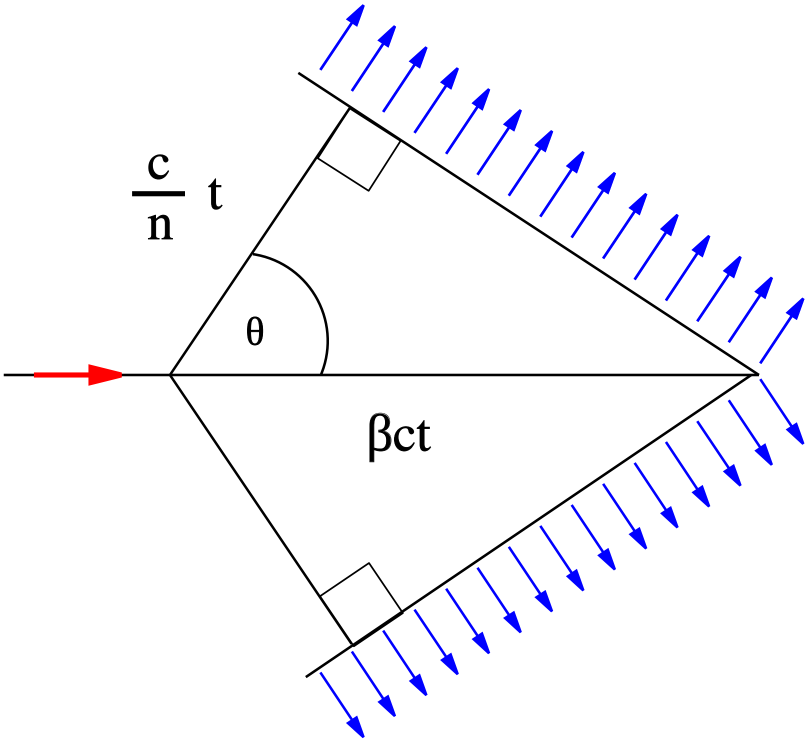

Figure 4.3: The geometry of Cherenkov light emission showing how to find the Cherenkov angle θ.

be seen from Equation 4.3 that the spectrum is inversely proportional to the emitted wavelength squared, meaning that more Cherenkov photons are radiated at lower wavelengths. To find the spectrum seen at the ground due to Cherenkov radiation in an atmospheric shower, convolution of the emission spectrum with the distribution of particle energies (since β differs for each particle) and spectral transmission of the atmosphere is required. Such a spectrum, along with the spectrum of the night-sky-background (NSB) light, is shown in Figure 4.4. The primary atmospheric effects on the spectrum are Rayleigh scattering of photons and absorption of higher-frequency photons by ozone, the latter of which is responsible for the drop in the spectrum below $\sim$350 nm.

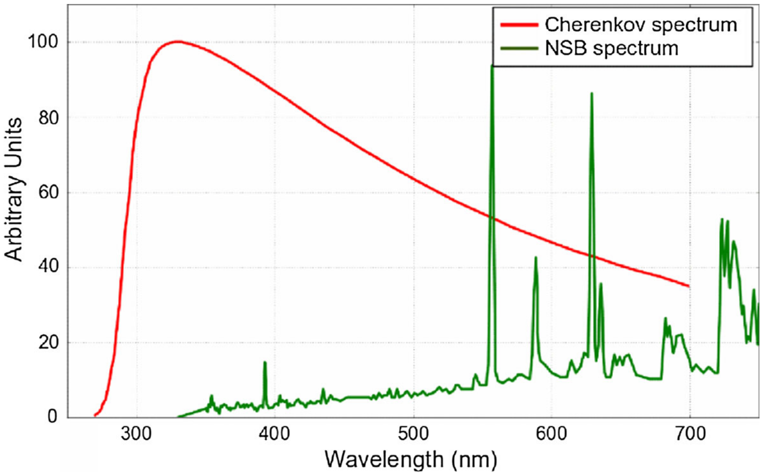

Figure 4.4: Spectrum of Cherenkov light (red) at $\sim$2 km above sea level in arbitrary units, shown along with the spectrum of night-sky-background light (green). Figure from [61].

4.3 Air Showers

4.3.1 Electromagnetic Showers

Electromagnetic air showers are those that are induced by an electromagnetically interacting particle, such as a photon or a charged lepton. The formation of an electromagnetic cascade in the atmosphere, assuming a single gamma ray starting point, occurs in two repeating steps:

1. After travelling one radiation length X_0, the gamma ray pair-produces off of a virtual photon in the strong magnetic field around a nucleus, creating an electron-positron pair via $\gamma + \gamma \longrightarrow e^+ + e^-$. Each particle produced has $\sim$1/2 the energy of the parent gamma ray.

2. The new electron and positron radiate one gamma ray each via the bremsstrahlung mechanism near an atomic nucleus, giving away $\sim$2/3 of their energy in the process. This interaction happens after an average length $(9/7)X_0$.

This cycle repeats at step 1, with the newly produced gamma rays pair producing to give a total of $2n$ $e^{+/-}$, where n is the number of interaction lengths traveled, each with $\sim$1/3^n the energy of initial gamma ray. There exist other interaction mechanisms for the gamma ray in addition to pair-production, though the interaction probabilities are a factor of $\sim 10^{-4}$ lower and thus not described here. A diagram of an electromagnetic cascade is shown in Figure 4.5.

The "shower maximum" occurs at the altitude where the number of Cherenkov-radiating particles is maximized, which is the point where energy losses due to bremsstrahlung and ionization are equal, and this corresponds to a particle energy of about 83 MeV in air. The shower maximum altitude for vertically incident gamma rays is in the neighborhood of $\sim$11–7 km, assuming initial gamma-ray energies between 0.1–10 TeV. Below the shower maximum, energy losses due to ionization begin to dominate, and the shower cascade dies out. A shower induced by a 1 TeV gamma ray results in roughly 150 photons per square meter. An illustration of the shower structure is shown in Figure 4.6, and a simulated electromagnetic cascade (with the resulting Cherenkov photon distributions) is shown in Figure 4.7, Figure 4.8, and Figure 4.9[1].

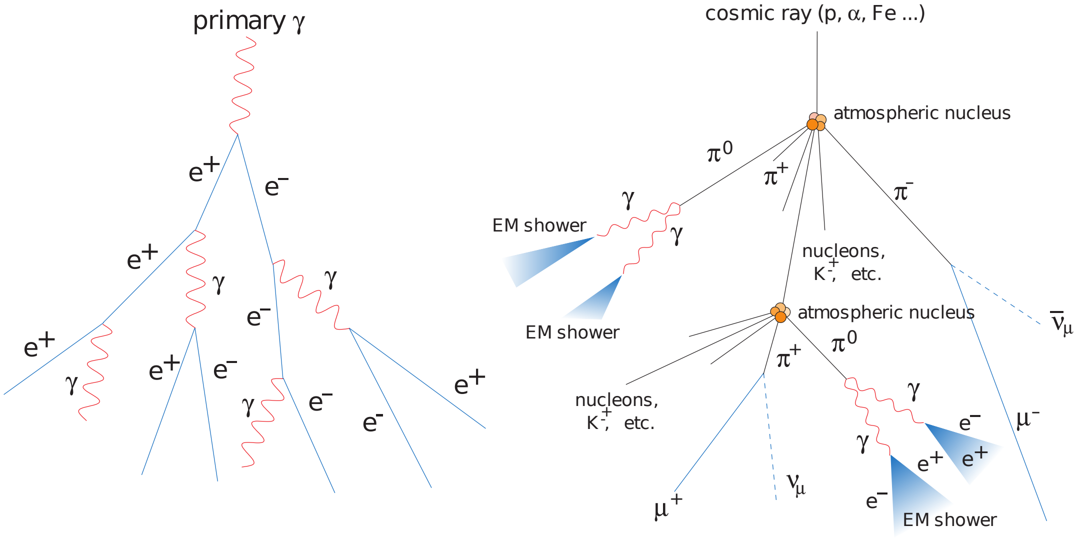

Figure 4.5: Air shower diagrams for an electromagnetic cascade (*left*) and a hadronic cascade (*right*). Figure from [62].

---

[1] The simulated shower figures in this thesis were generated and provided by Mary Kertzman (DePauw University). More figures are available at the website: http://www.depauw.edu/academics/departments-programs/physics-astronomy/department-research/high-energy-gamma-ray-astrophysics/the-kascade-air-shower-visualization-project/

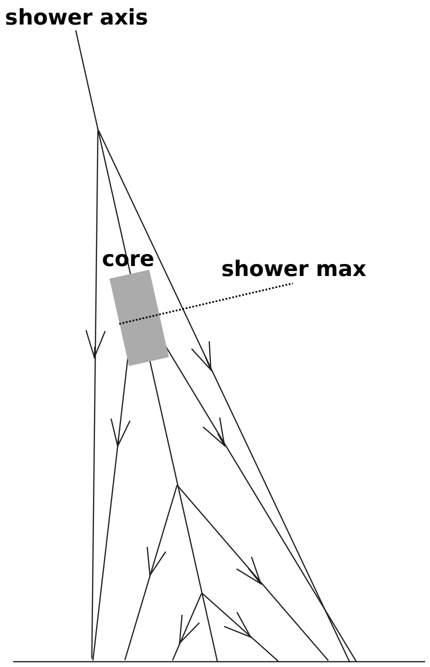

Figure 4.6: Structure of an electromagnetic cascade. The Cherenkov emission angle is seen to increase with decreasing altitude, which has the effect that the highest concentration of Cherenkov photons on the ground falls in an annulus of approximate radius 100 m. The locations of the shower maximum and shower core are also indicated. Figure adapted from [62].

4.3.2 Hadronic Showers

Hadronic air showers are created when a cosmic ray proton (or atomic nucleus) enters and interacts in the atmosphere. Generally, this interaction produces pions, which decay into gamma rays and muons, creating many sub-showers all producing Cherenkov light as the particles propagate toward the ground. The primary decay modes for pions are as follows:

$$\pi^0 \longrightarrow \gamma + \gamma \tag{4.4}$$

$$\pi^+ \longrightarrow \mu^+ + \nu_\mu \tag{4.5}$$

$$\pi^- \longrightarrow \mu^- + \bar{\nu}_\mu \tag{4.6}$$

The largest contributions to the total Cherenkov light in a hadronic shower are thus due to muon and electromagnetic sub-showers from pion decays. Of course, there are other

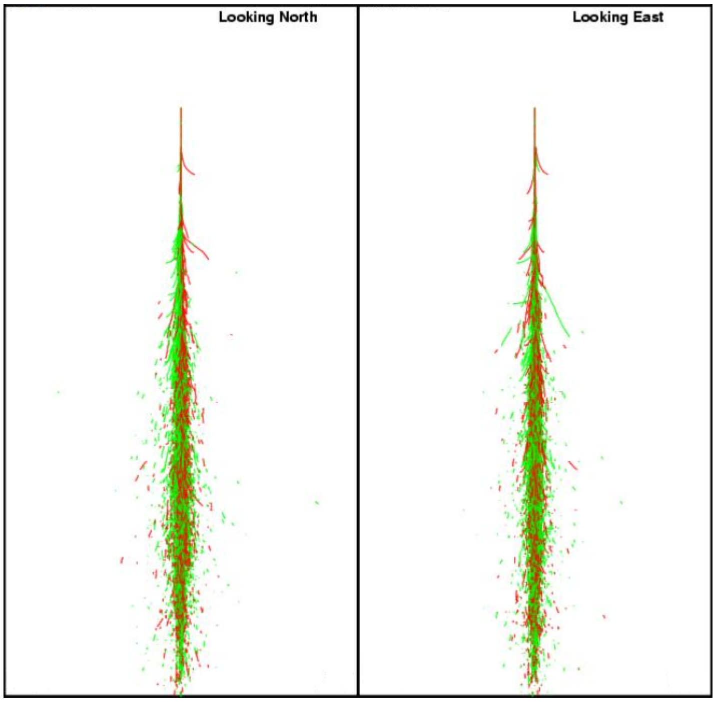

Figure 4.7: Simulated electron (green) and positron (red) tracks for an electromagnetic shower induced by a 700 GeV primary gamma ray. The vertical scale represents the altitude range from 20 km down to 1.3 km, and the horizontal scale spans a distance of 9.4 km. Figure courtesy of M. Kertzman.

contributions—the initial interaction of the proton with an atomic nucleus can produce a wide variety of particle products. A diagram of a hadronic air shower is given in Figure 4.5.

Particles produced in hadronic cascades typically receive more transverse momentum than those produced electromagnetically, which results in broader transverse particle motion and thus a larger total ground area illuminated by Cherenkov photons (see Figure 4.11). This broadness constitutes a feature that is used in data analysis to discriminate gamma-ray initiated showers from hadronic ones, as described in Section 6.3. A simulated hadronic cascade for a 900 GeV cosmic ray proton (with the resulting Cherenkov photon distributions) is shown in Figure 4.10, Figure 4.11, and Figure 4.12.

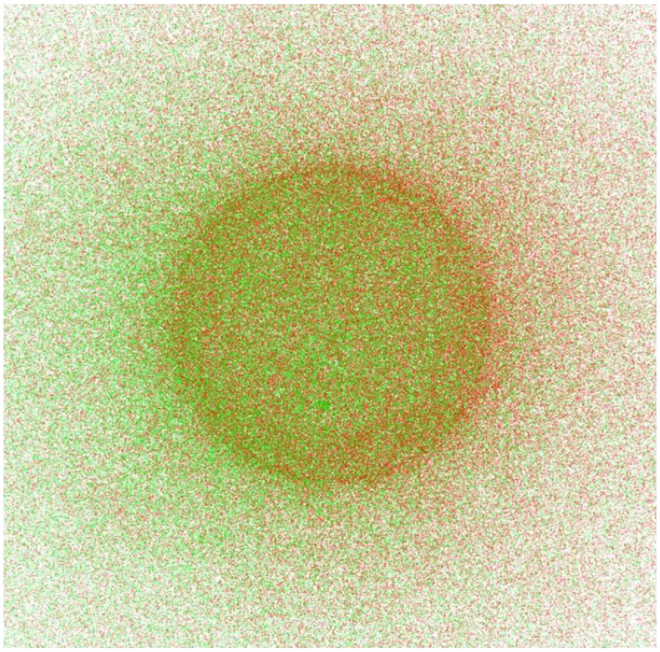

Figure 4.8: Bird's-eye view of the distribution of Cherenkov photons on the ground produced by shower electrons (green) and positrons (red) for a 700 GeV gamma-ray. The vertical and horizontal scales represent distances of about 600 m each. The top of the image corresponds to north. Figure courtesy of M. Kertzman.

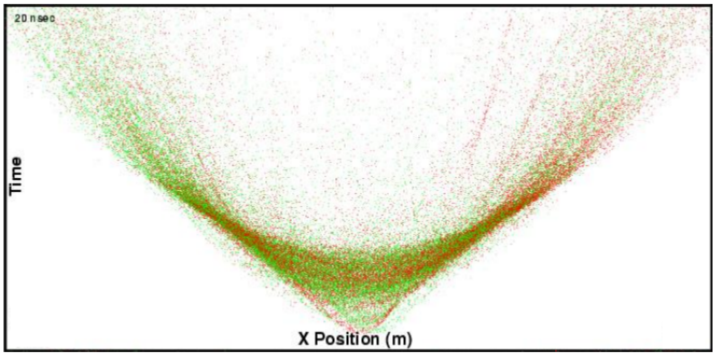

Figure 4.9: Side view of the photons in Figure 4.8 showing the time profile of the photons. The vertical scale is 20 ns, and the horizontal scale is 600 m. Figure courtesy of M. Kertzman.

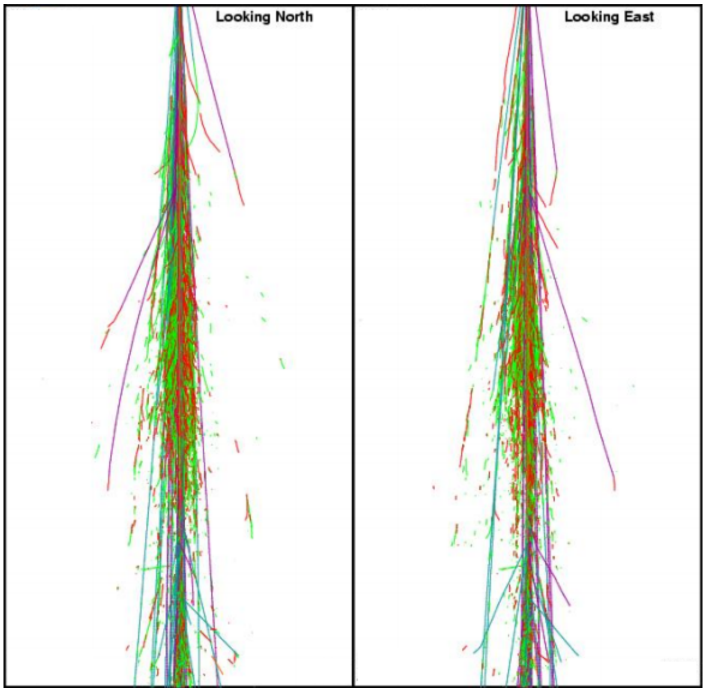

Figure 4.10: Simulated tracks for a hadronic shower induced by a 900 GeV primary proton. The color scheme is as follows: e^+–red, e^-–green, μ^+–purple, μ^-–cyan, π^0–yellow, π^+–maroon, π^-–teal, p^+–orange. Distance scales are the same as in Figure 4.7. Figure courtesy of M. Kertzman.

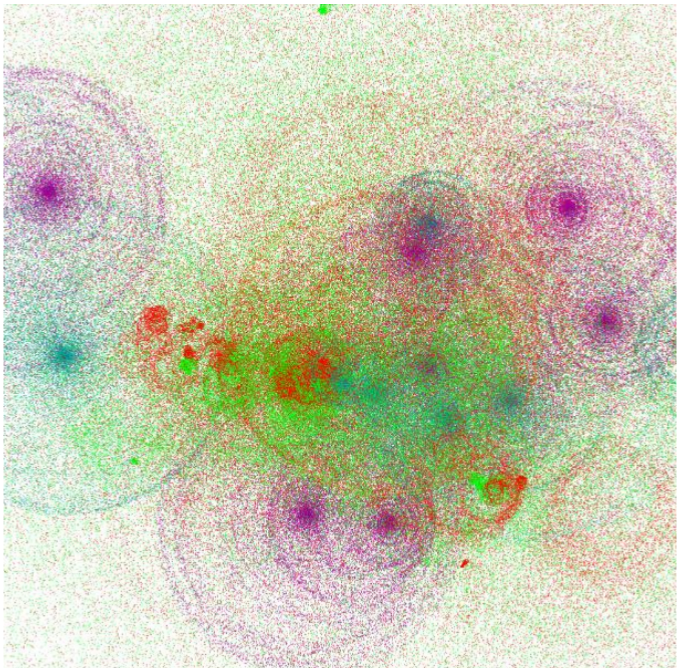

Figure 4.11: Bird's-eye view of the distribution of Cherenkov photons on the ground produced in a hadronic shower initiated by a 900 GeV proton. The color scale for the Cherenkov photons indicates the particle that produced the photon and is the same as in Figure 4.10. Distance scales are the same as in Figure 4.8. Figure courtesy of M. Kertzman.

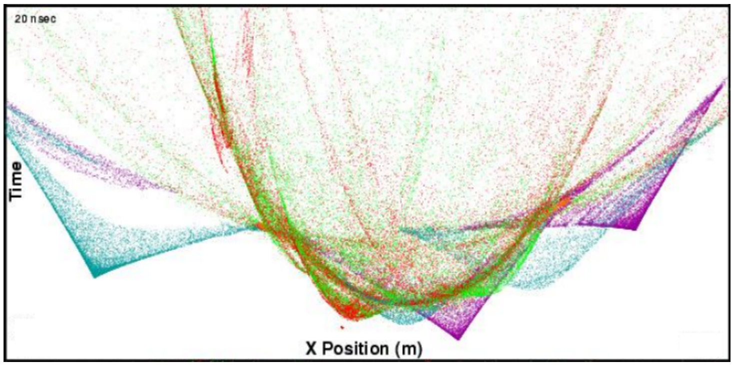

Figure 4.12: Side view of the photons in Figure 4.11 showing the time profiles. The vertical scale is 20 ns, and the horizontal scale is 600 m. Figure courtesy of M. Kertzman.

CHAPTER 5

THE VERITAS DETECTOR

Figure 5.1: The basecamp and VERITAS telescopes at the Fred Lawrence Whipple Observatory in Arizona.

5.1 Overview

The Very Energetic Radiation Imaging Telescope Array System (VERITAS) is an array of four 12 m diameter IACTs located in southern Arizona (31°40’30” N, 110°57’07” W; 1268 m above sea level) at the base of Mt. Hopkins at the Fred Lawrence Whipple Observatory (FLWO). Construction of the first telescope was completed in February 2005 [63], with full operations of all four telescopes beginning in March 2007 [64]. A photograph of the observatory site and VERITAS telescopes can been seen in Figure 5.1.

5.2 Structure and Optics

Each of the four VERITAS telescopes possess an altitude-over-azimuth positioner capable of reaching slew speeds of about one degree per second, a space-frame optical support structure, and a 499-pixel camera supported by a quadropod. The optical design of each telescope is that of the Davies-Cotton optical furnace [65], with a spherically curved, segmented-aperture reflector. Each reflector comprises 345 hexagonal mirror facets, and the reflector radius and focal length are both 12 m ($f = 1$ optics). The optical point spread function (PSF) is typically measured to be $\sim$0.08° at 68% containment over the elevation range under which observations are usually done (40–80°). An image of the reflector of telescope 1 (T1[1]) is shown in Figure 5.2.

5.3 Cameras

Each VERITAS camera is composed of 499 photomultiplier tube (PMT; often referred to as pixels since they are used in a camera) modules, each of which contains a PMT and pre-amplifier board. The pre-upgrade PMTs are Photonis model XP2970/02, and the PMTs deployed post-upgrade are Hamamatsu model R10560-100-20. The PMTs are pitched with angular distance 0.15° for a total camera field-of-view (FoV) diameter of 3.5°. The two types of PMTs used in the VERITAS cameras are shown in Figure 5.3. A plate of 499 hexagonal Winston cones, which are hollow, parabola-shaped, non-imaging light concentrators, sits in front of the PMTs. These cones have two purposes: to reduce contamination from stray light entering the cameras at angles larger than 26°, and to decrease the dead space between pixels, thus increasing the photon collection efficiency.

The PMTs are operated with gains of 250,000 electrons per photoelectron, which is achieved with average voltages of $\sim$800 / $\sim$1000 V for the Photonis / Hamamatsu PMTs, respectively. The HV values for individual pixels are adjusted to obtain uniform response across the camera. The pre-amplifier boards serve not only the purpose of amplifying the PMT signals, but also of allowing monitoring of the PMT anode currents and the injection of test pulses for calibration purposes into the signal chain. The typical pixel currents for moonless VERITAS operations are 5–10 μA. The output signal from the pre-amplifier is carried by a coaxial cable into a flash analog-to-digital converter (FADC) board housed

---

[1] The four VERITAS telescopes are numbered as follows: T1, T2, T3, T4.

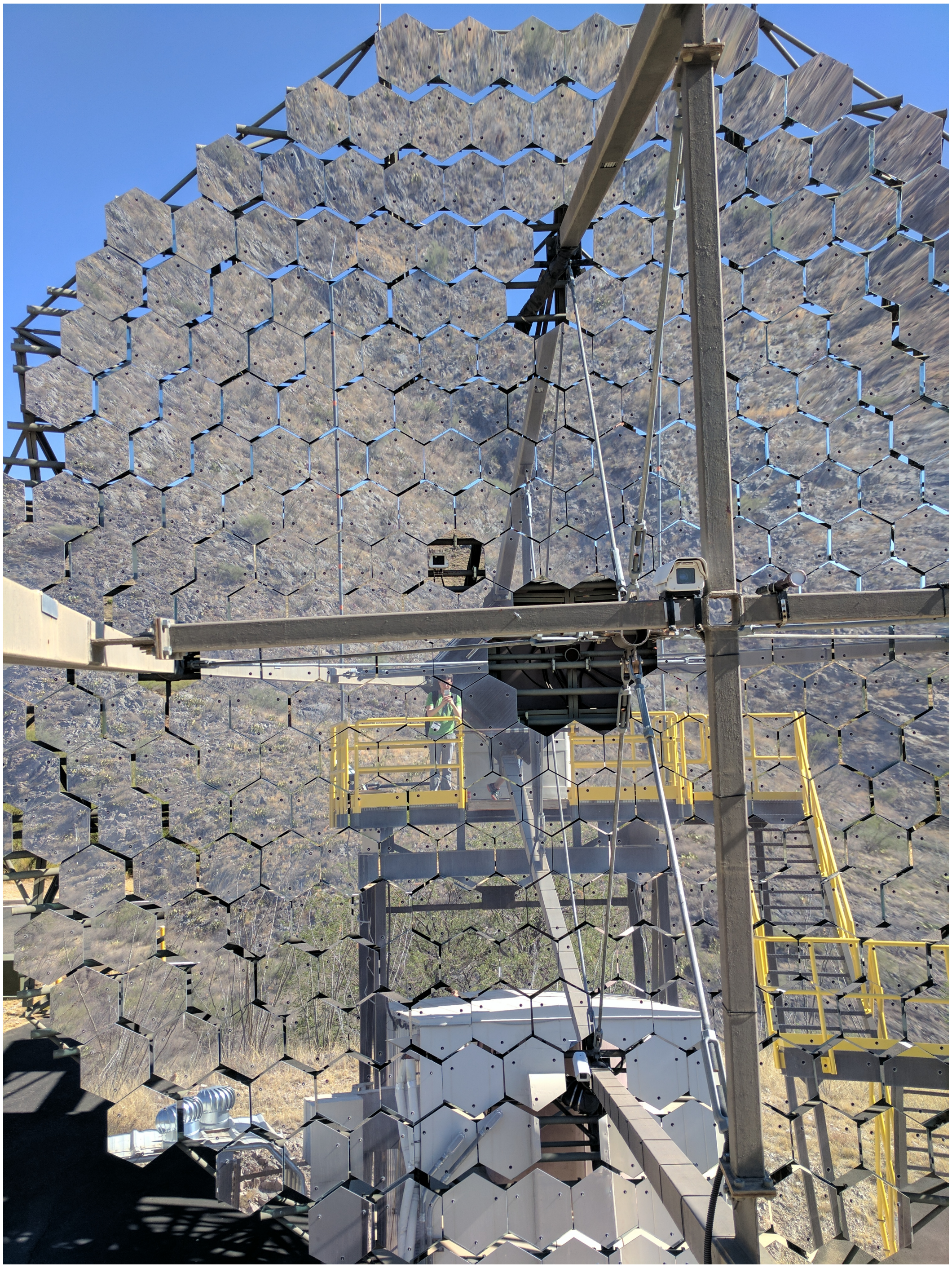

Figure 5.2: The reflector of T1 as imaged from the platform near the camera. Also pictured are the LED flasher and focal-plane camera, both mounted on the crossbeam, and the sky and reflectivity cameras, both situated in the reflector where there are missing facets. These components are discussed further in Section 5.7. A reflected image of the author in a green shirt can also be seen.

inside a climate-controlled trailer beneath the telescope.

Figure 5.3: The pre- and post-upgrade photomultiplier tubes used in the VERITAS cameras. The Hamamatsu R10560-100-20 is shown in the bottom-left and the Photonis XP2970/02 in the top-right.

5.4 Upgrades

The array has undergone two major upgrades since full operations began. In the original array layout, T1 was just 38 m from T4, which resulted in a substantial rise of the array threshold as T1 and T4 were triggered by muons close to the telescopes. To alleviate this problem, in the summer of 2009, T1 was relocated to a position east of its original location in order to increase the average distance between all telescopes to ∼114 m. The second major upgrade took place in the summer of 2012, and it involved switching out all 1996 Photonis photomultiplier tubes (PMTs) used in the telescope cameras with new, higher quantum-efficiency Hamamatsu PMTs. The primary aim of this upgrade was to reduce the energy threshold of VERITAS from ∼100 GeV down to ∼80 GeV [66]. The three epochs of the fully operational VERITAS and its data are referred to as V4 (original layout), V5 (after T1 move), and V6 (after camera upgrades)[2].

---

[2] V1, V2, and V3 refer to periods in which one, two, and three telescopes were functional.

5.5 Trigger System

The VERITAS trigger system is designed to discriminate air-shower signals from fluctuations in the night-sky background (NSB) light. The trigger system has three levels called L1, L2, and L3.

- **L1:** The level 1 trigger applies to each pixel individually. An L1 trigger occurs when the voltage threshold set in the constant fraction discriminator (CFD) is exceeded by a pulse in a single channel.

- **L2:** The level 2 trigger is specific to each telescope. If three adjacent pixels in one camera meet the L1 trigger requirement within ∼6 ns, the L2 trigger condition is met. Each of the three pixels must be adjacent in the camera with the other two; i.e., three pixels all in a row cannot satisfy the L2 trigger condition.

- **L3:** The level 3 trigger is an inter-telescope trigger. If any two (or more) telescopes give L2 triggers within 50 ns of one another, the L3 trigger condition is met and the digital contents of every channel in the array are written to disk. The L3 trigger is also called the array trigger.

The CFD thresholds are the same for all 1996 channels, and the CFD threshold is chosen to minimize the amount of triggers due to NSB photons, while maintaining triggers due to the signals produced by Cherenkov photons from air showers. A plot of the L1, L2, or L3 trigger rate versus CFD threshold is called a bias curve, and one such curve is shown in Figure 5.4. In the figure, there is a clear inflection point in the L3 rate for 3-fold adjacent pixel trigger topology beyond ∼45 mV, above which the triggers are no longer dominated by NSB photons. The CFD thresholds used in normal operations are selected based on this inflection point. The current CFD threshold used in VERITAS operations under moonless skies is 45 mV, and the typical L3 rate is ∼400 Hz.

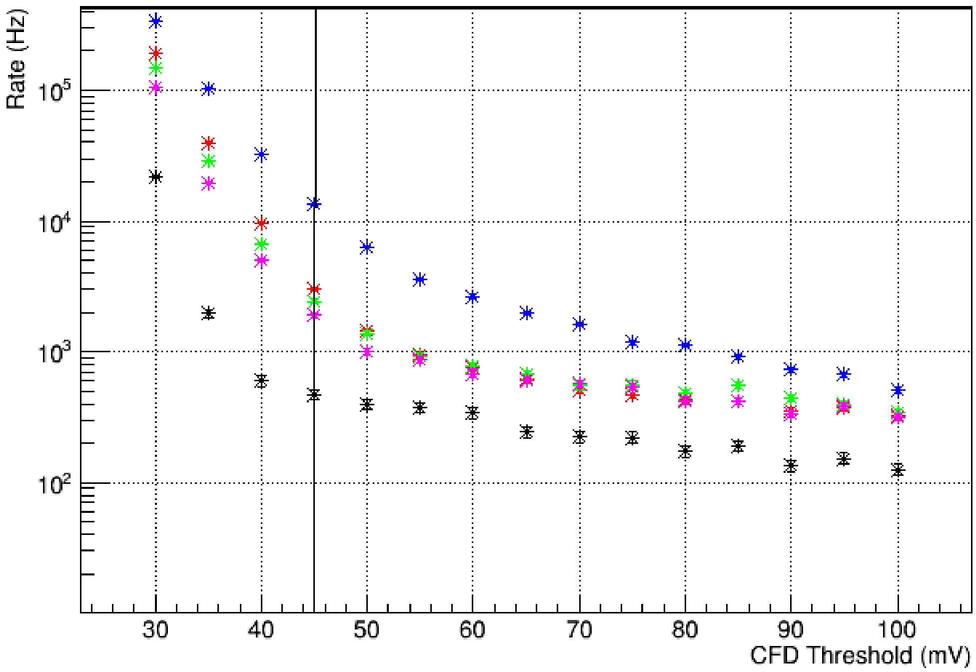

Figure 5.4: An example bias curve taken during the V6 era. The black points show the L3 rate, and the colored points are the L2 rate for a specific telescope as follows—T1: red, T2: green, T3: blue, T4: magenta. The vertical black line indicates the 45 mV CFD threshold that is currently used during observations.

5.6 Data Acquisition

The analog signal from each camera pixel connects into one of the custom-built FADC boards. These boards serve the primary purpose of digitizing the signal in each channel in increments of 2 ns and storing the digitized value a circular buffer with an 8-bit dynamic range and a 64 μs memory depth. At the input to the board, a DC bias voltage called the pedestal is applied. The Cherenkov flash intensity of high-energy showers saturates the dynamic range of the FADC at 255 digital counts. For that reason, the dynamic range of the digitization was extended by implementing an analog low-gain switch that sends the signal to a path in which it is attenuated and delayed relative to the high-gain signal. The high-low gain ratio is $\sim$6.

Only a portion of the 64 μs-deep buffer is written to disk when the L3 trigger signal is received, and this portion of the buffer that is read out is called the “readout window.” The window is adjustable in both the location in the buffer and the number of samples that are written to disk. It is set in such a way that when the low-gain switch has not been flipped (or flipped), the appropriate high-gain (or delayed low-gain) signal trace is selected in the window. The typical sample width of the readout window for current VERITAS operations is 16 (32 ns).

Each telescope has a data acquisition computer that records information about a telescope event after an L3 trigger occurs, such as the signal in each FADC channel, a GPS timestamp, and L1 and high/low-gain switch flags for each channel. A central computer called the “harvester” packages all of the information from each telescope’s event builder into a single data file per run. The data acquisition system takes 139 μs to write the contents of all channels to disk, which gives the array an average deadtime of about 10% at typical L3 trigger rates. The data files are transferred to an off-site archive from where they can be downloaded by members of the VERITAS Collaboration for analysis. As of fall 2012 (V6), typical data runs are 30 minutes long yielding a typical file size of $\sim$9.5 GB.

5.7 Calibration

Various calibration tasks are performed on a regular basis to monitor the stability of the instrument and the quality of the data, the most important of which are described in this section. As calibration group leader of the VERITAS Collaboration, I am responsible for scheduling and overseeing these various calibrations tasks, and as such, I have included a brief overview in this section of the thesis.

The absolute gain of each channel is monitored by keeping track of single photoelectron signals. Since the gain directly impacts the energy reconstruction (see Section 6.3.3), monitoring is necessary know when readjustment is needed, thus keeping the systematic uncertainty to a minimum. To compute the absolute gain for one telescope, all events

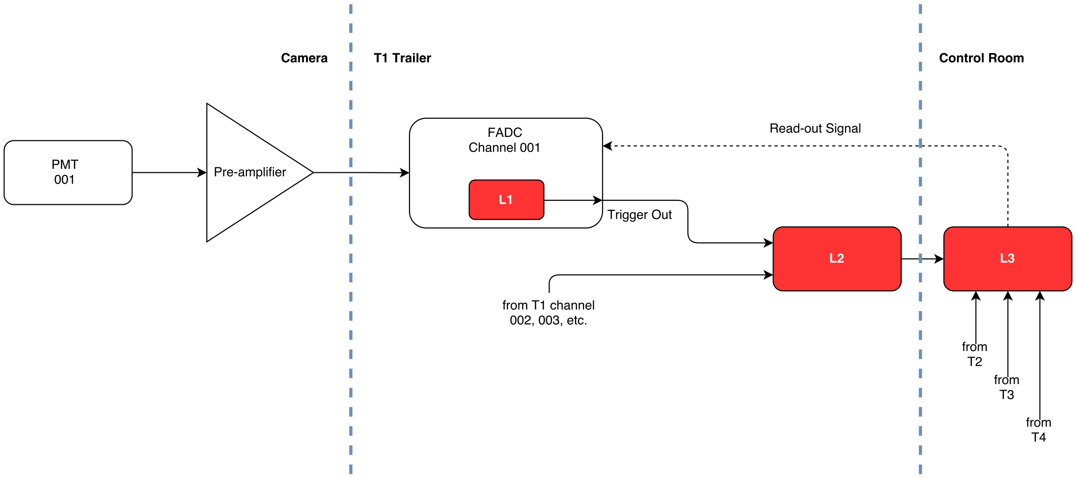

Figure 5.5: Block diagram of the VERITAS signal chain for a single-pixel signal. The dashed blue lines indicate transitions between the telescope camera, telescope trailer, and control room. The other 498 PMTs and channels that comprise the T1 electronics are not pictured, though all channels connect to the L2 board as indicated in the diagram. After an L3 trigger, a read-out signal (dashed black line) is sent to all channels in the array.

recorded at the lowest-level flasher[3] illumination are extracted, and the integral charge in each channel is computed for each event. Then for each channel a charge histogram can be constructed, which shows several overlapping peaks corresponding to pedestal, single photo-electron signals, double photo-electron signals, etc. The distribution is fit with a sum of Gaussian shapes, and the absolute gain for the channel is given as the mean of the single photo-electron Gaussian minus the mean of the pedestal Gaussian. The absolute gain for the telescope as a whole is reported as the mean of the individual gains for the channels.

If the absolute gain distribution for a telescope has become too wide, or if the gain has dropped by more than 5%, a procedure called “flat-fielding” is done to make the gain distribution more uniform by readjusting the HV values for each channel. The current method for flat-fielding involves scaling the HV for all PMTs and taking three (or more) flasher runs. The mean values of integrated charge histograms for each channel are computed,

---

[3] Each telescope is equipped with an LED-based flasher that illuminates the camera with various levels of light.

followed by plotting charge versus HV for each channel. A fit to the HV-dependent charge enables selection of a new HV value for the channel given a desired integrated charge value.

The VERITAS telescopes do not point precisely where they are told to point in azimuth / elevation due to imperfections in the positioners and deformation in the telescope structure. For that reason, the offset of the *actual* pointing position is regularly compared to the *set* pointing position, so that the offset can be corrected in the data analysis. This is done using the VERITAS pointing monitor (VPM) system, which allows comparison of the *actual* pointing of the telescope with the pointing reported by the positioner, giving the pointing offset for the telescope in question. If the pointing offset RMS is seen to exceed the acceptable threshold for any telescope, new pointing corrections are calculated using a method called T-Point. The optical PSF of the telescope can be extracted and monitored using the VPM system. Due to imperfections in the hexagonal mirrors and their pointing, a star appears smeared out in the focal plane. Monitoring the PSF for each telescope thus reveals the overall health of the alignment of the mirrors.

The whole-dish reflectivity of each telescope reflector is monitored by comparison of the intensity of the direct light from a star and from its reflection. A reflective target is mounted to the telescope cameras at the focal plane, and a wide-FoV camera mounted on the reflector captures an image of a star and its reflection on the reflective target in the same image. The whole-dish reflectivity is then quoted as a ratio of the intensities of the recorded starlight and its reflection. A filter wheel inside the camera housing allows measurement of wavelength dependence. This method is further described in [67].

CHAPTER 6

DATA ANALYSIS

This chapter covers the general data analysis techniques that are used in the projects described in this thesis. Section 6.1 gives an overview of the procedure for timing a pulsar. Sections 6.2 and 6.3 describe the *Fermi*-LAT and VERITAS data analysis techniques, with a special emphasis on the VERITAS analysis. Analysis details specific to one particular project are relegated to a section in a subsequent chapter for the project in question.

6.1 Pulsar Timing

An integral component of all the pulsar studies presented in this thesis is the timing of the pulsar, i.e., the conversion of photon arrival times into rotational phases of the pulsar when those photons were emitted. Applying a statistical test to the calculated phase data may reveal a periodic signal, in which case the pulsar is detected, or may reveal nothing, in which case a flux upper limit can be quoted. Either way, the conversion from arrival times to phases is necessary, which requires what is called a pulsar *timing solution*. A timing solution is a file that contains the necessary information to convert from arrival time to phase, such as the pulsar rotation frequency, time derivatives of the frequency, location in the sky, proper motion, glitch information, etc. If an analyzer has no timing solution for the pulsar in question, they must create their own. Blindly creating a timing solution requires a (typically large) set of data capable of being searched for periodicity with a wide variety of periods, period derivatives, and so on. Given that the VHE gamma-ray fluxes of pulsars are expected to be quite low (indeed, only one has been firmly detected above 100 GeV), blind searches for periodicity are extremely unlikely to be fruitful. For that reason, we borrow timing solutions from other energy bands in which pulsars are more easily detected, namely from radio and HE gamma rays. In this section, I give a general overview of the problem of converting photon arrival times into pulsar phases, assuming that a valid timing solution is available.

6.1.1 Barycentering

The term *barycentering* refers to the process of converting photon times of arrival (TOAs) at a telescope to would-be arrival times had they arrived instead at the center-of-mass of the solar system, called the barycenter. Assuming that the solar-system barycenter is a fixed location, the process of barycentering then removes the effects on the TOAs caused by Earth's motion and other solar-system-specific phenomena. These effects for gamma rays are listed below.

- Rotation of Earth, or, in the case that the telescope is aboard a satellite, the orbit of the satellite
- *The Römer correction*, which refers to Earth's orbit about the Sun; additionally, the ellipticity must be taken into account
- The gravitational potential at Earth, which varies throughout the year because Earth's orbit is elliptical
- *Shapiro delay*, which refers to the time lag introduced to a photon as it passes near a massive object (such as the Sun or Jupiter) as predicted by general relativity

Taking the above points into account, the barycentric time of arrival can be written as

$$t_{\mathrm{b}} \approx t - (\Delta_{\mathrm{R}} + \Delta_{\mathrm{E}} + \Delta_{\mathrm{S}}) \tag{6.1}$$

where t_{b} is the barycentric time, t is the TOA, Δ_{R} is the the Römer correction, Δ_{E} is the gravitational redshift correction, and Δ_{S} is the Shapiro delay. The equation is approximate since we disregard dispersion during photon propagation due to free electrons, which is an important effect for radio photons but is negligible for gamma rays. For details on the calculation of Δ_{R}, Δ_{E}, and Δ_{S}, please see, e.g., Chapter 5 in [17].

In practice, barycentering is a complicated procedure that is typically done using a publicly available software package called TEMPO2 [68], which is capable of achieving an accuracy down to $\sim$1 ns for the effects listed in the above bullet points. With TEMPO2, users specify their solar system ephemeris of choice, where for all analyses presented in this thesis DE405 [69] is used, and must be careful to add leap seconds when introduced by the International Earth Rotation and Reference Systems Service.

6.1.2 Phase Folding

The minimum ingredients needed to convert a series of barycentric times t_i^{b} to phases ϕ_i for a specific pulsar are: f, the pulsar frequency (which also gives the angular frequency ω), $\dot{f}$, the first time derivative, and t_0, a barycentric reference time where $\phi_0 = 0$. A timing solution provides these values, and converting barycentric times to phases is a matter of extrapolation from t_0 to each t_i^{b} using f and $\dot{f}$ and taking the remainder as the desired phase. Here it is assumed that each t_i^{b} falls within the window of validity of the timing solution. The i^{th} phase can then be written

$$\phi_i = \phi(t_i^{\mathrm{b}}) = \left(\int_{t_0}^{t_i^{\mathrm{b}}} \omega(t) dt \right) \mod 2\pi \tag{6.2}$$

which for one derivative on P and hence ω implies $\omega(t) = \omega_0 + \dot{\omega} t$ and gives

$$\phi(t_i^{\mathrm{b}}) = \left(\int_{t_0}^{t_i^{\mathrm{b}}} \omega_0 dt + \int_{t_0}^{t_i^{\mathrm{b}}} \dot{\omega} t dt \right) \mod 2\pi. \tag{6.3}$$

After integration and rewriting ω in terms of f, the i^{th} phase is found to be

$$\phi_i = \left(f_0(t_i^{\mathrm{b}} - t_0) + \frac{1}{2}\dot{f}((t_i^{\mathrm{b}})^2 - t_0^2) \right) \mod 1. \tag{6.4}$$

A few notes:

Table 6.1: Table of all relevant differences between the *Fermi*-LAT data analysis of the Geminga pulsar and the 15 archival pulsars. All differences are due solely to the fact that the LAT team refines the instrument IRFs, analysis software, and periodically reprocesses the data over time to improve the analysis.

	Geminga Analysis	Archival Pulsars Analysis
Science tools version	v9r27p1	v10r0p5
IRFs	Pass 7 reprocessed	Pass 8
Catalog version	2FGL	3FGL
Galactic diffuse version	gll_iem_v05_rev1	gll_iem_v06
Isotropic diffuse version	iso_source_v05	iso_P8R2_SOURCE_V6_v06
Data used per pulsar	5.2 yr	7.6 yr

- If N derivatives to the pulsar frequency beyond the first have been measured, the above procedure for calculating the phases can be revised by Taylor expansion of $\omega(t)$ as

  $$\omega(t) = \sum_{n=0}^{N} \frac{\omega^{(n)}(t)}{n!} t^n. \tag{6.5}$$

  and substituting into equation 6.2.

- In practice, the one-rotation phase range 0–2π *radians* is typically redefined as 0–1 *rotations*, so the phases ϕ_i take values between 0 and 1. All pulse profiles shown in this thesis use the phase range 0–1 (or -1 to 1 where the profile is shown twice).

- Likewise with the barycentering, all phase folding for the projects presented in this thesis has been done with TEMPO2.

6.2 *Fermi*-LAT Data Analysis

The *Fermi* large area telescope (LAT) is an electron-positron pair-conversion telescope sensitive to gamma-ray photons with energies between ~20 MeV and 300 GeV. It has a FoV of ~2.5 sr and attains full-sky coverage approximately every three hours. For a complete description of the instrument, see [70, 71].

To generate *Fermi*-LAT spectra for all pulsars treated in this thesis, the *Fermi*-LAT Science Tools are used with the standard quality cuts described in [72]. Events of "source"-

class with energies between 100 MeV and 300 GeV collected within 20° region-of-interest (ROI) of the 2PC location of each pulsar are processed with the maximum likelihood fitting routine. Details of the *Fermi*-LAT analysis specific to individual projects presented in this thesis are summarized in Table 6.1.

The spectral analysis presented here follows the same steps outlined in the second *Fermi*-LAT pulsar catalog (2PC) [6]. To generate spectral energy distributions of the *Fermi*-LAT data for each pulsar, a binned maximum likelihood analysis is done in each of 12 logarithmically spaced energy bins spanning the range 100 MeV to 300 GeV. Spectral models for all sources in the 3FGL catalog [73] in the ROI in addition to the galactic and isotropic diffuse backgrounds (gal_2yearp7v6_v0.fits, iso_p7v6source_rep.txt) are included in the likelihood fitting. Sources within a circle of 4° in radius have their spectral parameters left free in the fitting routine, while all others are fixed except for the normalization on the galactic and isotropic diffuse background models. In each bin, the pulsar is modeled as a point source with a simple power-law spectral shape:

$$\frac{dN}{dE} = N_0\left(\frac{E}{E_0}\right)^{\gamma}, \tag{6.6}$$

where N_0 is the flux normalization, E_0 is fixed to 300 GeV, and γ is the spectral index. The normalization and spectral index of each pulsar are left as free parameters in the fit.

6.3 VERITAS Data Analysis

6.3.1 Introduction

Analysis of data taken by VERITAS generally follows the following steps:

1. Data selection: Data runs deemed “good” are selected for analysis. Good runs are those that appear unaffected by weather and hardware problems based on data quality monitoring (DQM) plots that are automatically generated for each run. Examples of important information monitored in the DQM are the L3 rate, pointing offsets, and

median currents for each channel, and these plots have been vetted for every data run used in each analysis.

2. Calibration of Data (Section 6.3.2)
3. Event reconstruction and parametrization (Section 6.3.3)
4. Background estimation (Section 6.3.5)

All analyses presented in this thesis have been done using the *VERITAS Gamma-ray Analysis Software (VEGAS)* package, and they have additionally been cross-checked by another VERITAS collaboration member using a different software package called *Event Display*. This independent cross-check is done to ensure validity of the results by attempting to avoid systematic effects potentially introduced by the data analyzer or the analysis code of a particular software package.

6.3.2 Calibration of Data

The first step in the VERITAS analysis chain is the calibration and cleaning of the raw data, which is accomplished in five steps:

1. Division of the data run into three-minute time slices
2. Summation of pedestal events for each channel
3. Summation of all FADC traces
4. Subtraction of the mean pedestal value from summed traces
5. Cleaning of images.

First, a data run selected for analysis is divided into three-minute time slices in order to track changing noise conditions throughout the run. The pedestal events[1] are then ex-

---

[1] Pedestal events are injected into VERITAS data during runs at a rate of 3 Hz.

tracted and summed[2], and the means and standard deviations of the summed pedestals for each time slice are calculated. Subsequently, the traces in each channel for each L3-triggered event are summed using a *double pass* method. In the first pass, the signals are integrated to calculate the *charge* and the *t-zero* (the time in the window corresponding to the point at which the signal has risen to half its maximum value). The t-zero values form a gradient across the camera of a telescope due to the shape of the Cherenkov light front (see Figure 4.9), which has the effect that the signal positions differ slightly in time between channels. During the second pass, the start positions for each channel are set based on the time gradient found in the last pass, and the window used is smaller than in the first pass in order to optimize the signal-to-noise ratio. The first and second pass windows used for all analysis presented herein are 7 and 5 samples, respectively (14 and 10 ns, respectively). After the double-pass summation, the mean pedestal value is subtracted from all of the traces.

Once the pedestal and trace information for each channel have been calculated, image cleaning is performed. This step involves removal of channels that fail to meet the following criteria in an effort to preserve only channels that detected Cherenkov photons for further analysis. The general criteria are:

- **a)** Each channel must have a pedestal variance no more than four standard deviations above the mean of the distribution for that channel.
- **b)** "Bright" pixels are kept, where a bright pixel is defined as one in which the integrated signal is above five standard deviations of the pedestal-distribution mean for the given time slice.
- **c)** If a pixel neighboring a bright one fails to satisfy b), it is still kept if the integrated signal is 2.5σ above the pedestal-distribution mean.

Pixels not satisfying any of the above criteria have their integrated charge set to zero.

---

[2] Summation / integration in this context refers to simply adding up the digital counts of each sample in a given time window.

6.3.3 Event Parametrization and Reconstruction

After calibration and cleaning, image parameters are calculated on an event-by-event basis with the goal of subsequently applying an event selection on the data to reduce background due to cosmic-ray image contamination. The first of such parameters are *size*[3] and *ntubes*. The *size* parameter is the summed charge over all channels forming an image, and the cut value is the lower bound below which all images are discarded. The *ntubes* parameter is the minimum number of participatory channels required for keeping an image, which is set to five.

Parameters pertaining to the location and shape of an image in the camera come in the form of the so-called Hillas parameters [74]. Figure 6.1 shows a drawing of an ellipse along with several parameters used to describe the image. The first step in calculating these parameters is finding the principal components of the image based on the digital counts in each image channel. For example, assuming x-y coordinates, the first-order moments and second-order-moment variances are given by:

$$\langle x \rangle = \frac{\sum n_i x_i}{\sum n_i}; \quad \langle y \rangle = \frac{\sum n_i y_i}{\sum n_i} \tag{6.7}$$

$$\sigma_{x^2} = \langle x^2 \rangle - \langle x \rangle^2; \quad \sigma_{y^2} = \langle y^2 \rangle - \langle y \rangle^2 \tag{6.8}$$

where the sum index i runs over all of the channels forming the image, x and y are the x-y coordinates of the i^{th} pixel, and n is the number of digital counts. The Hillas parameter *distance* is then:

$$\sqrt{\langle x \rangle^2 + \langle y \rangle^2}, \tag{6.9}$$

which gives the distance from the camera center to the image centroid. The *distance* parameter cut is set to $distance < 1.43°$ to reject images that fall off the edge of the camera,

---

[3] All cut parameters will appear italicized for clarity.

and are not fully contained. The parameters *length* and *width* are given by:

$$length = \sqrt{\frac{\sigma_{x^2} + \sigma_{y^2} + s}{2}}; \quad width = \sqrt{\frac{\sigma_{x^2} + \sigma_{y^2} - s}{2}} \tag{6.10}$$

where $s = \sqrt{(\sigma_{y^2} - \sigma_{x^2})^2 + (2\sigma_{xy})^2}$ [75].

This moment analysis can be used to determine the major axis of the elliptical image. The intersection of the major axes of the recorded images for one event in the image plane gives the gamma-ray arrival direction. Given that generally the major axes will not perfectly intersect for $N_{\mathrm{tel}} > 2$, a weighting method is used in order to achieve a more accurate reconstruction. The weight used for each axis is the $\log_{10}$ of the corresponding *size* of the image, and the direction is found by minimization of the perpendicular distances from each weighted image axis. See Figure 6.2 for an illustration of the direction reconstruction.

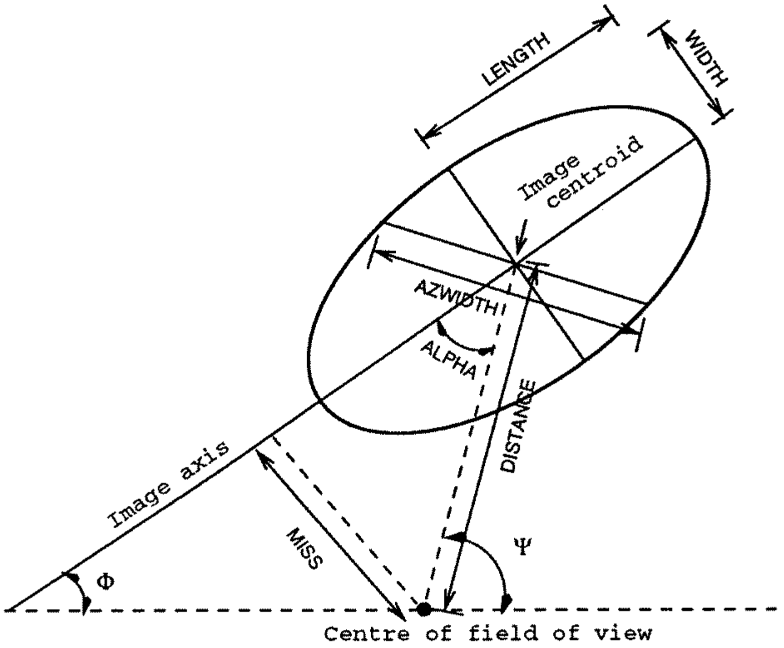

Figure 6.1: Illustration of commonly used parameters for a Cherenkov shower imaged by an IACT. Figure from [75]

In addition to reconstructing the arrival direction in the image plane, it is also useful to find the *impact distance* of the event seen by each telescope by determining the *shower*

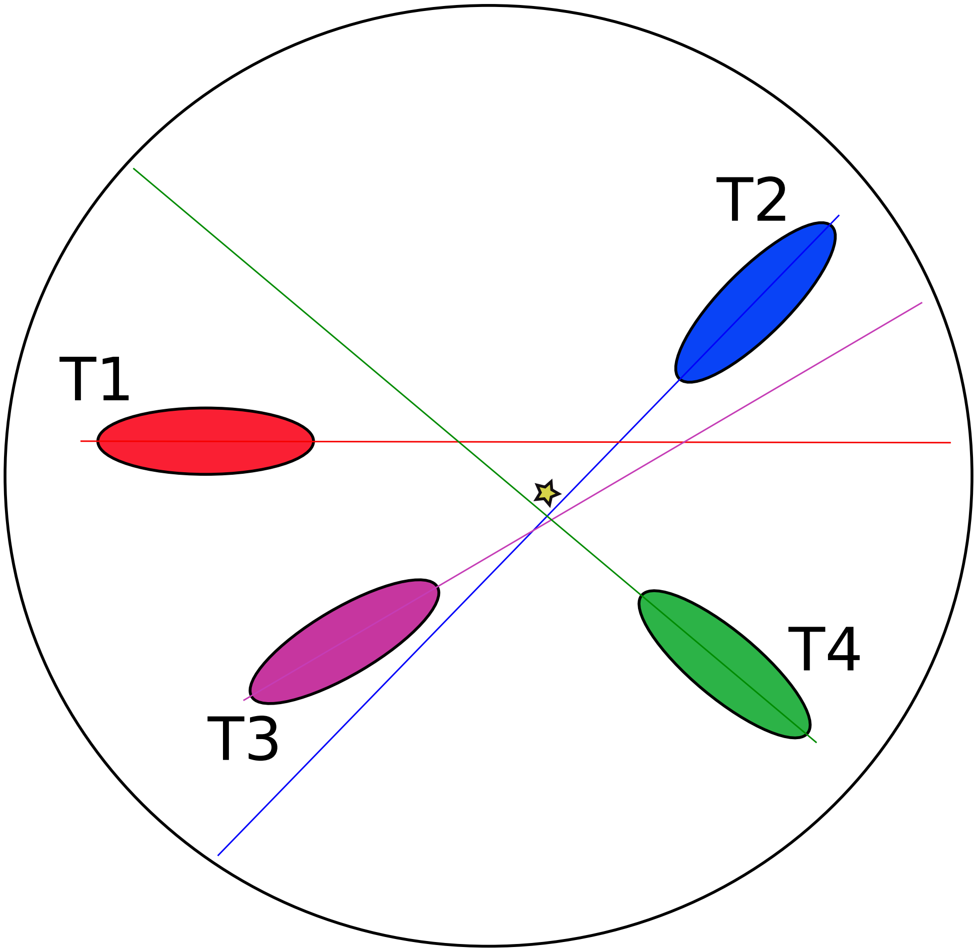

Figure 6.2: Illustration of the camera plane showing the direction reconstruction method. The intersection of the major axis of each ellipse gives the arrival direction. Note that in the general case and as pictured here, the major axes will not exactly intersect for $N_{\text{tel}} > 2$, so a weighting method is used to determine the arrival direction (shown as a gold star).

core location, which refers to the location on the ground where the gamma ray would have landed, had it not been absorbed in the atmosphere via e^+e^--production. The core location is found in a similar fashion to the arrival direction in camera coordinates, again by a weighting method involving intersection of the major axes of the ellipses, but this time the images and axes are projected onto the ground plane. The impact distance is then the distances from a telescope to the shower core location on the ground. An image illustrating this method is shown in Figure 6.3. Armed with the four impact distances, the *shower maximum* of the event can now be determined from trigonometry. The shower maximum is the point in the air shower where the number of Cherenkov-light-producing particles

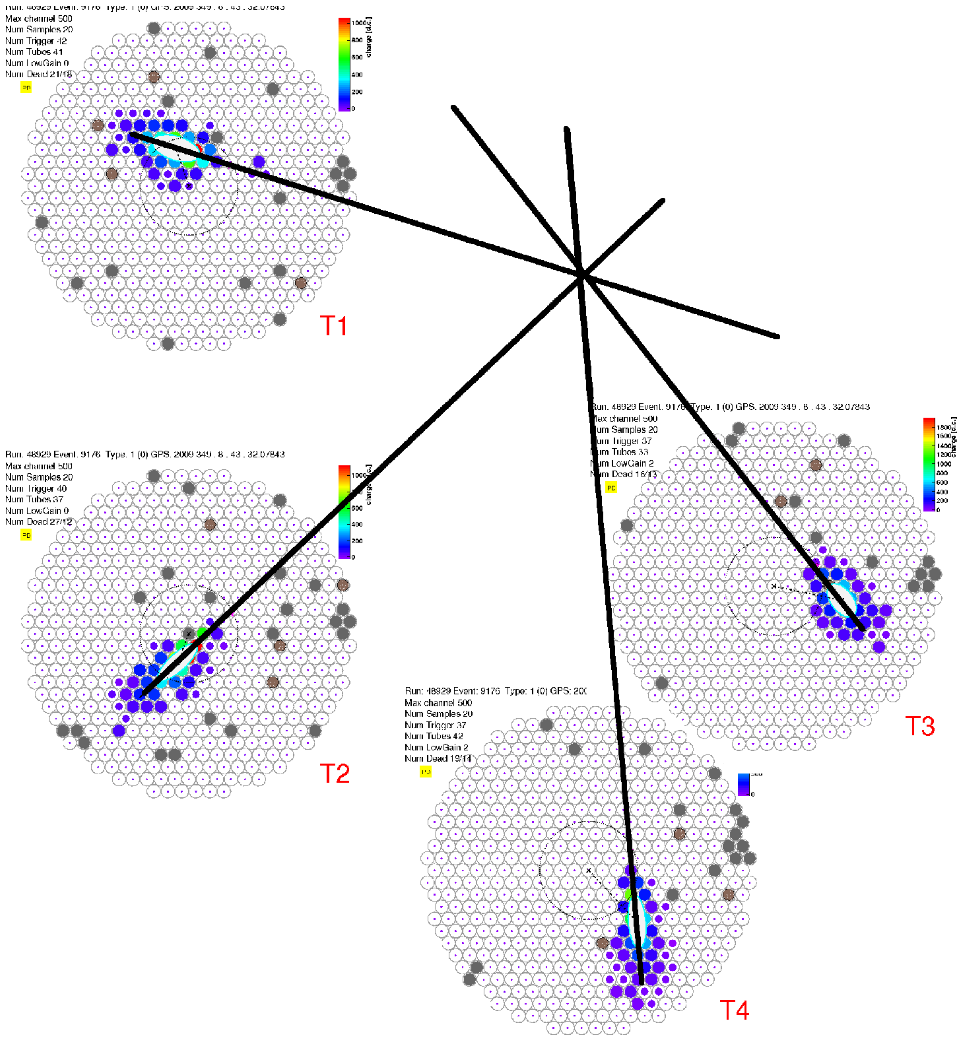

Figure 6.3: Image showing the impact distance and core location of a gamma-ray shower based on the intersection of the image major axes.

is at its maximum. It is a useful cut parameter in the analysis, since cosmic-ray showers penetrate farther into the atmosphere compared to gamma-ray showers. Let ϕ_i be the angle between the image centroid and the reconstructed arrival direction, and let r_i be the impact distance for telescope i, respectively. Then the *shower maximum* h can be calculated:

$$\tan(\phi_i) = \frac{r_i}{h_i}. \tag{6.11}$$

The four h values calculated for one event should all be equal, however they will differ in reality due to uncertainties. They are combined into one value assigned to the event by taking the mean.

Determining the energy of the shower-initiating gamma ray is a procedure that involves Monte-Carlo simulation of many gamma-ray air showers. The simulated Cherenkov light then enters a simulation of the telescope optics and electronics to arrive at an estimate for the *size* parameter seen for a gamma-ray event with known energy and direction. These simulations are used to fill multi-dimensional lookup tables (LTs) with the *size*-to-energy conversion information for various parameters specific to the event, which include the observing azimuth and zenith angles, impact distance, and noise level due to NSB light. The basic procedure in the analysis is to "look up" the energy estimate for an observed *size*, impact distance, and noise level (plus azimuth / zenith angle) for each telescope. The standard deviation of the energy for a lookup-table bin is also estimated from these simulations, and it is used as a weight when averaging over the individual events seen by each telescope to get the energy of the event as a whole.

6.3.4 Cosmic-Ray Rejection and Cut Selection

The next step in the analysis is to suppress the background due to cosmic-ray-initiated air showers as much as possible. The background-rejection method used in this thesis is a relatively simple one that involves making cuts on the data based on image parameters, the *shower maximum*, and the distance from the source. The cuts values are selected in an optimization procedure that involves analysis of known VHE sources via scanning the cut parameter space in order to find the values that maximize the detection significance. The same procedure can also be done on simulated data. The optimal cut values have been determined for three spectral indices ranging from softer to harder, henceforth referred to as *soft*, *moderate*, and *hard* cuts. Additionally, the three different physical configuration of VERITAS (V4, V5, and V6) undergo the optimization separately, resulting in a total of nine sets of cuts.

Two more parameters must be introduced: the *mean-scaled length (MSL)*, *mean-scaled width (MSW)*, which relate the *length* and *width* of the image as shown in Figure 6.1 and defined above. They are defined as follows:

$$MSW \equiv \frac{1}{N_{\text{tel}}} \sum_{i=1}^{N_{\text{tel}}} \frac{w_i}{w_{\text{sim}}(\theta, size_i, r_i)} \tag{6.12}$$

$$MSL \equiv \frac{1}{N_{\text{tel}}} \sum_{i=1}^{N_{\text{tel}}} \frac{l_i}{l_{\text{sim}}(\theta, size_i, r_i)} \tag{6.13}$$

where in the above two equations, w_i and l_i are the *width* and *length* parameters for the image in telescope i, and w_{sim} and l_{sim} are simulated average widths and lengths for a given a zenith angle θ, image *size*, and impact distance r_i [76]. The simulations discussed in Section 6.3.3 produce simulated camera images, which can be parametrized in the same manner as the real data. The *widths* and *lengths* of these simulated images are indices of the LTs, and the appropriate values are pulled from the LT during analysis given a zenith angle, *size*, and impact distance.

Now that the data parametrization is complete, the next step in the analysis chain is to perform an event selection based on the cut parameters. Determining the best selection of cuts depending on the expected source spectrum requires an optimization scheme. This optimization was conducted by scanning the cut-parameter space as follows:

1. Process a large set of data of a known source through the point of applying the *size* cut. Increment *size* by 100 and repeat.
2. For each *size* cut, finish processing by scanning over *MSL*, *MSW* in increments of 0.05, and *shower maximum* in increments of 1 km.
3. Take the set of cuts that maximizes the significance of the source detection as the one to be used for analysis.
4. Repeat steps 1–3 for a known soft-, moderate-, and hard-spectrum source.

Table 6.2: Definition of all cut values used in the analyses described in this thesis.

Epoch	Cut Type	Size	MSW Lower	MSW Upper	MSL Lower	MSL Upper	Shower Max	θ^2	Notes
V4	Soft	200	0.05	1.1	0.05	1.3	7	0.03	no T1T4
	Moderate	400	0.05	1.1	0.05	1.3	7	0.01	no T1T4
	Hard	1000	0.05	1.1	0.05	1.4	0	0.01	no T1T4
V5	Soft	200	0.05	1.1	0.05	1.3	7	0.03	-
	Moderate	400	0.05	1.1	0.05	1.3	7	0.01	-
	Hard	1000	0.05	1.1	0.05	1.4	0	0.01	-
V6	Soft	400	0.05	1.1	0.05	1.3	7	0.03	-
	Moderate	700	0.05	1.1	0.05	1.3	7	0.01	-
	Hard	1200	0.05	1.1	0.05	1.4	0	0.01	-

5. Repeat steps 1–4 for data taken during VERITAS epochs V4, V5, and V6.

All of the cut values derived from the above procedure and used in the projects described in this thesis are given in Table 6.2, including the θ^2 cut which will be explained in Section 6.3.5. Note as indicated in the table that for V4 data, the T1+T4 trigger topology at L3 is rejected for reasons discussed in Section 5.4.

6.3.5 Background Estimation

After applying cuts to the data for the gamma-hadron separation, the next analysis steps are background estimation followed by the excess / significance calculation. Calculation of the excess counts requires counting the total number of events falling into the expected signal region (call it the *ON* region) and into the background region (call it *OFF*). The ratio of the sizes of the ON and OFF regions is a parameter called α. Once the total counts in each region and α are known, the *excess* is given by

$$N_{\text{excess}} = N_{\text{on}} - \alpha N_{\text{off}}, \tag{6.14}$$

and the significance can be calculated as described in Section 7.2. In the rest of this section, two methods for defining the ON and OFF regions are described, followed by a description of the θ^2 parameter which determines the angular size of the regions.

Background Estimation for a Standard Search

There are a few established ways to estimate the background, with the most commonly used being the reflected-region method paired with a wobble-mode observing strategy [77]. Wobble-mode observations involve displacing the center of the telescope cameras from the expected source location by some amount (typically for VERITAS by $0.5°$), and alternating this offset between data runs in each of the four cardinal directions. This strategy provides the advantage that background and data can be accumulated simultaneously, and systematic effects in the background estimation cancel out [78]. The reflected-region background estimation method involves defining OFF regions for background events reflected about the center of the FoV relative to the ON region (where the source is expected), thus ensuring that all ON and OFF regions are the same radial distance from the center of the camera. This is desirable since the telescope acceptance is radially symmetric. An illustration of this technique can bee seen in Figure 6.4.

Background Estimation for a Pulsar Search

For pulsar searches, a more sensitive approach to estimating the background is employed in the phase (i.e. time) domain, rather than the spatial domain described previously. While a pulsar could be detected using a reflected-region method, assuming it is sufficiently bright, it is favorable to increase the search sensitivity by a priori definition of ON and OFF counting regions based on the pulse profile characteristics seen at other wavelengths. For example, if a pulsar has been seen by the *Fermi*-LAT, one can use the phase-folded LAT data to create a pulse profile and then define the ON regions in phase where the peaks are seen. The background is then defined as the region where there is no emission from the pulsar. This procedure is often referred to as “phase gating” and the ON / OFF regions as “phase gates.” The α parameter is still easily calculated as the ratio of the ON and OFF region sizes in phase. This method makes the assumption that the locations and shapes of the peaks in the pulsar light curve are the same as those seen in the other wavelength band where the pulsar

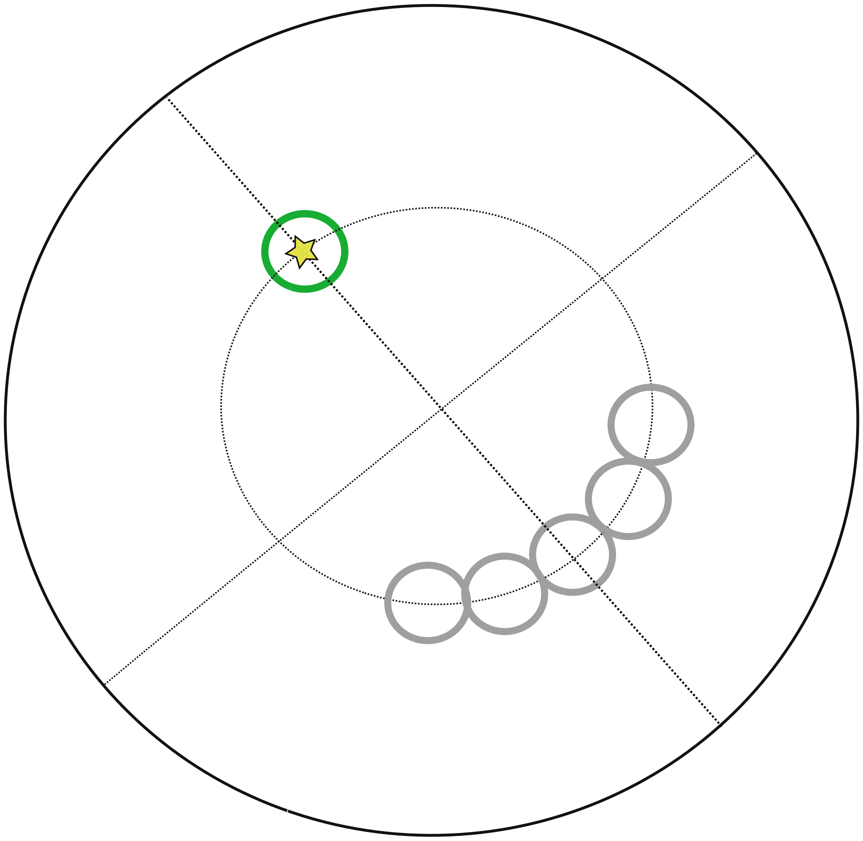

Figure 6.4: A drawing of the reflected region method. The largest circle represents the FoV of a telescope, with the two intersecting dashed lines showing the center. The expected source location is represented by the yellow star. The ON region is shown encircling the expected source location in green, and the "reflected" OFF regions are given by the gray circles, which are all the same distance from the center as the ON region.

is detected. A different statistical test that avoids this (potentially incorrect) assumption is also used in the searches described in this thesis. It is called the *H*-test (see Section 7.3.1).

The θ^2 Parameter

In either case of searching for steady or pulsed emission, the question of exactly how large a region on the sky select for analysis still remains. For each event, the squared angular distance from the expected source location, called θ^2, is calculated and used as a cut parameter. Given that a potential signal will be spatially confined (whereas the background is approximately isotropic), the optimal θ^2 cut is chosen based on the expected angular size of the signal. For a point source, this size is dictated by the instrument angular resolution.

The angular resolution of VERITAS is worse at lower energies, hence the θ^2 cut used for the soft-cuts analysis is looser than that used for moderate- or hard-cuts analysis. The θ^2 cut definitions used in all of the analyses described in this thesis are given in Table 6.2.

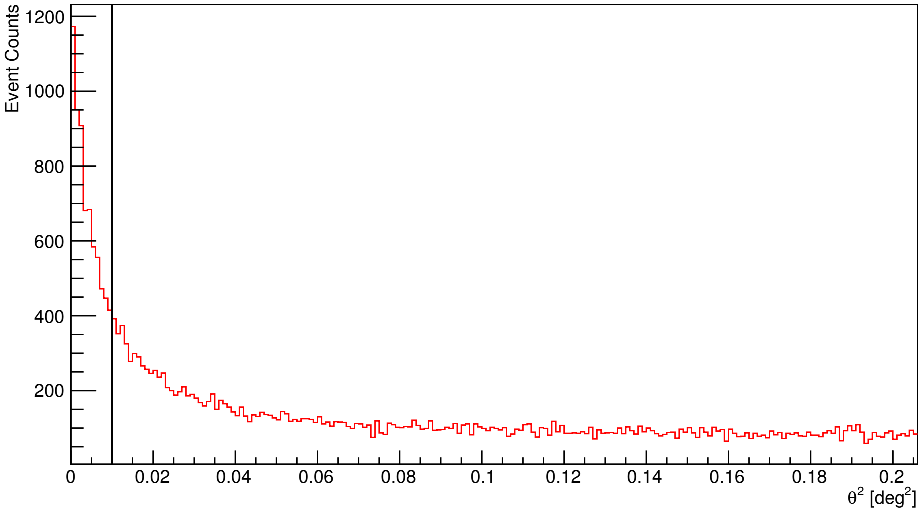

Figure 6.5: An example θ^2 distribution derived from Crab Nebula data. The vertical black line indicates a θ^2 cut of 0.01. The event counts fall rapidly, leaving only background moving away from the source, though not instantaneously due to the nonzero gamma-ray PSF.

6.3.6 Calculating Flux from Excess Counts

Calculation of a flux value from the computed excess requires knowledge of the effective area of the detector. Because a Cherenkov shower can be imaged no matter where it lands on the ground so long as at least two telescopes are within the light pool, the size of the light pool itself is the best approximation for the effective area of the IACT array. However, the actual effective area depends on many parameters, including the cuts used, the zenith angle of the observation, the NSB noise level, and the telescope electronic response. In general, if some aspect of the experiment affects the excess found (i.e., affects the efficiency of collecting gamma-ray events), then it will affect the effective area. Effective areas for use in analysis are created in a Monte-Carlo simulation where many simulated gamma ray events over a large impact area are pushed through the detector simulation. An example of an effective area created in this way is shown in Figure 6.6.

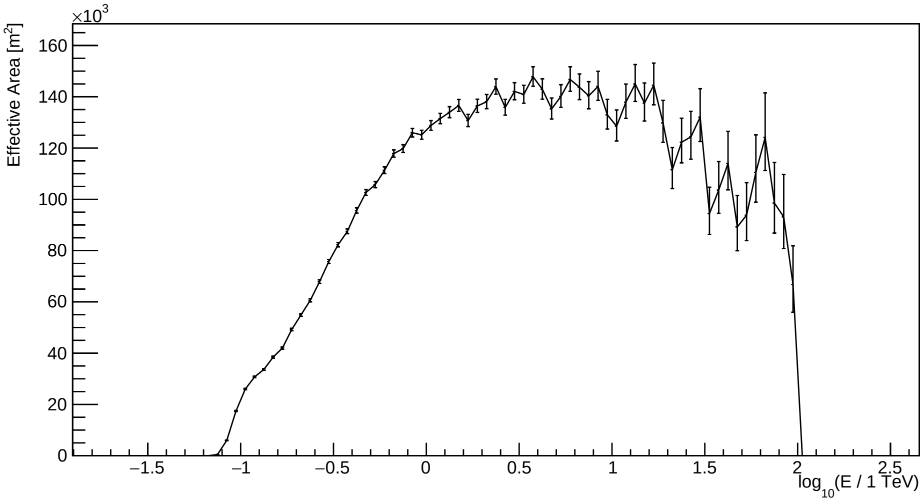

Figure 6.6: An example simulated effective area of the V6 configuration of VERITAS for 0° zenith and 0° azimuth with cuts $MSW = 1.1$, $MSL = 1.3$, and $\theta^2 = 0.03$.

Using a set of effective areas simulated for the optimized set of cuts used in the analysis, the excess can be converted into a meaningful flux or limit on the flux. Flux is a measure of the rate of flow of a quantity (e.g., counts or energy) per unit area. The number flux[4] N of some discrete counting quantity can be calculated simply as

$$N = \frac{N_{\text{excess}}}{AT} \tag{6.15}$$

where A is the effective area, and T is the exposure time. The dependence on the reconstructed photon energy can be included to compute a differential energy spectrum:

$$\frac{dN}{dE} = \frac{d}{dE}\frac{N_{\text{excess}}(E)}{A(E)T}. \tag{6.16}$$

Over the course of one observation period, different effective areas will need to be used as the observing conditions change (e.g. zenith angle, NSB level), so in practice N_{excess} is

---

[4] The units for this flux typically are: counts m^{-2} s^{-1}.

subdivided, and the appropriate effective area is selected for each division[5]. The integral flux N_{int} above some lower energy threshold E_{min} can be found by summing over all events above that energy:

$$N_{\text{int}} = \frac{1}{T}\left(\sum_{i}^{N_{\text{on}}}\frac{1}{A_i} - \alpha\sum_{k}^{N_{\text{off}}}\frac{1}{A_k}\right) \tag{6.17}$$

where the index i runs over all ON events, index k over all OFF events, and the term in parentheses is N_{excess}/A but rewritten to include the appropriate effective areas A_i or A_k for ON event i or OFF event k.

In the case that no signal is seen, an upper limit on the excess $N_{\text{excess}}^{\text{UL}}$ can be found and converted into a meaningful limit on the integral flux. Computing an upper limit on the excess at a given confidence level is a procedure involving assumption of parent distributions for N_{on} and N_{off} (typically Gaussian or Poissonian) and using the method of, e.g., Rolke [79] or Helene [80] to find $N_{\text{excess}}^{\text{UL}}$ at a predetermined confidence level. $N_{\text{excess}}^{\text{UL}}$ is then converted into an integral flux limit $N_{\text{int}}^{\text{UL}}$ by computing:

$$N_{\text{int}}^{\text{UL}} = \frac{N_{\text{excess}}^{\text{UL}}}{T}\frac{\int E^{-\Gamma}dE}{\int \bar{A}E^{-\Gamma}dE} \tag{6.18}$$

where $\bar{A}$ is an averaged effective area. The above integrals are over the entire energy range starting at E_{min}, and an assumed spectral shape given by $E^{-\Gamma}$ is invoked a priori with spectral index Γ. In VEGAS, the integrals in Equation 6.18 are done in a discrete fashion by summing over 400 energy bins per decade. The lower-energy threshold E_{min} above which the aforementioned calculations are done is selected by multiplying the assumed spectrum $E^{-\Gamma}$ by the average effective area and taking E_{min} as the energy corresponding to the maximum value.

---

[5] In VEGAS, this is done on an event-by-event basis.

CHAPTER 7

STATISTICAL METHODS

7.1 Introduction

Application of the appropriate statistical methods is an important requirement for obtaining or interpreting the results of an analysis. Details of the most important methods used in this thesis are the subject of this chapter. The chapter begins by first introducing and motivating the equation used for calculation of the significance of an observation where ON / OFF counting has been done, which is used in all projects presented in this thesis. Subsequently, a brief summary of testing for periodicity with the *H* test is given in the final two sections.

7.2 Significance from ON / OFF Counting

When counting “ON” events from an a-priori-defined expected region of signal and “OFF” events from a background region, the standard and most commonly used equation gamma-ray astronomy for computing the significance of the search is Li and Ma [81] Equation 17:

$$S = \sqrt{2}\left\{N_{\text{on}}\ln\left[\frac{1+\alpha}{\alpha}\left(\frac{N_{\text{on}}}{N_{\text{on}}+N_{\text{off}}}\right)\right] + N_{\text{off}}\ln\left[(1+\alpha)\left(\frac{N_{\text{off}}}{N_{\text{on}}+N_{\text{off}}}\right)\right]\right\}^{1/2} \tag{7.1}$$

where S is the significance, N_{on} is the number of events falling in the expected signal region, N_{off} is the number of events falling in the background region, and α is the ON exposure divided by the OFF exposure. Equation 7.1 is the equation used to compute significances for all of the gamma-ray-emission searches treated in this thesis.

A simpler calculation of the significance proceeds as follows. The excess counts are given by

$$N_{\text{excess}} = N_{\text{on}} - \alpha N_{\text{off}}. \tag{7.2}$$

Then the standard deviation of the excess is

$$\begin{aligned}
\Delta N_{\text{excess}} &= \sqrt{\left(\frac{\partial N_{\text{excess}}}{\partial N_{\text{on}}}\Delta N_{\text{on}}\right)^2 + \left(\frac{\partial N_{\text{excess}}}{\partial N_{\text{off}}}\Delta N_{\text{off}}\right)^2} \\
&= \sqrt{\Delta N_{\text{on}}^2 + \alpha^2 \Delta N_{\text{off}}^2} \\
&= \sqrt{N_{\text{on}} + \alpha^2 N_{\text{off}}}
\end{aligned} \tag{7.3}$$

where we have invoked the assumptions that N_{on} and N_{off} are independent and Poisson-distributed variables, thus their standard deviations are simply equal to the square roots of the number of events. The significance is then defined as

$$S = \frac{N_{\text{excess}}}{\Delta N_{\text{excess}}} = \frac{N_{\text{on}} - \alpha N_{\text{off}}}{\sqrt{N_{\text{on}} + \alpha^2 N_{\text{off}}}}. \tag{7.4}$$

Significances calculated this way have the problem that they tend to deviate substantially from the expected normal distribution when $\alpha \neq 1$. Li and Ma [81] have shown that using a likelihood ratio hypothesis test for estimating the expected number of source and background counts and computing the significance results in Equation 7.1, which fares far better than Equation 7.4 in giving normally distributed significances for a wider range of α values. It is for that reason that Equation 7.1 is the standard in the field for significance calculation.

7.3 Periodicity Tests

Testing for periodicity amounts to rejecting the hypothesis that no periodic signal is present, i.e., that the data are well described by a constant. One could test for periodicity quite simply using a χ^2 test by creating a histogram of the data and minimizing the χ^2 statistic with a constant as the one degree of freedom. If the resulting χ^2 statistic is too large, the null hypothesis can be rejected and a periodic signal claimed. However, the χ^2 test suffers from the fact that the somewhat arbitrary choice of histogram binning will affect the fit results, and there is no clear way to define the optimal binning a priori. Fortunately, there exist *bin-free* methods that require no prior knowledge of an expected region of signal. The method employed in analyses described in this thesis is the *H*-test [40], which is built upon the Z_m^2-test statistic [82].

7.3.1 The *H*-Test

Most tests for periodicity that were proposed before the introduction of the *H*-test are only suitable for detecting certain light curve shapes when statistics are sparse (i.e., the sensitivity of these tests is strongly profile-shape-dependent). The *H*-test offers an improvement upon these other tests by achieving the highest flux sensitivity for a larger range of pulsar light curves. In particular, the *H*-test improves upon the previously mentioned Z_m^2 test primarily by allowing the harmonic number m to be set to any integer value between 1 and 20, rather than a fixed choice typically of $m = 2$. Given the wide variety of such light curves now seen (especially in the gamma-ray band), the *H*-test is therefore the test of choice for bin-free periodicity searches.

Assume we have as input data a series of phases θ_i, each of which has some value between 0 and 2π. We want to test for a periodic signal in the data, which amounts to a test of uniformity on the circle, where $f(\theta)$ is the unknown real light-curve shape, and the null hypothesis can be stated:

$$f(\theta) = 1/2\pi. \tag{7.5}$$

The "distance" between the real light curve shape $f(\theta)$ from the uniform distribution given in Equation 7.5 can be written:

$$\psi(f) = \int_0^{2\pi} (f(\theta) - 1/2\pi)^2 d\theta. \tag{7.6}$$

We can use $\psi(f)$ as a test statistic for uniformity, but since $\psi(f)$ is unknown, we must estimate it. One reasonable choice of estimator is the Fourier Series Estimator (FSE) [83] $\hat{f}_m$ with m harmonics:

$$\hat{f}_m(\theta) = \frac{1}{2\pi}\left(1 + 2\sum_{k=1}^{m}(\alpha_k \text{cos}(k\theta) + \beta_k \text{sin}(k\theta))\right), \tag{7.7}$$

where α_k and β_k are the trigonometric moments

$$\alpha_k = \frac{1}{n}\sum_{i=1}^{n}\cos(k\theta_i) \;\text{ and }\; \beta_k = \frac{1}{n}\sum_{i=1}^{n}\sin(k\theta_i), \tag{7.8}$$

and n is the total number of observed phases. Using the FSE amounts to conducting a Fourier decomposition of the data in constructing our test statistic in Equation 7.6. Substituting $\hat{f}_m(\theta)$ from Equation 7.7 into Equation 7.6, one can show that $\psi(f)$ reduces within constants to the Z_m^2 statistic [82], which is given by

$$Z_m^2 = 2n\sum_{k=1}^{m}(\alpha_k^2 + \beta_k^2). \tag{7.9}$$

The Z_m^2 statistic has the problem that the number of harmonics m used in the decomposition is fixed (typically $m = 2$), which cripples its detection power for more sharply peaked pulse profiles [40].

The H-test improves upon the Z_m^2 statistic by allowing the number of harmonics to assume any value, specifically one that minimizes an estimator of the mean-integrated-squared error [83]. This leads to the definition of the *H* statistic:[1]

$$H \equiv \max_{1\leq m\leq 20}(Z_m^2 - 4m + 4), \tag{7.10}$$

where m is truncated at 20 for practical reasons following the suggestion of De Jager et al.

---

[1] *Minimizing* the mean-integrated-squared error turns to finding a *maximum* in Equation 7.10 due to an arbitrary sign flip done in [83].

in [40].

A probability distribution for the *H* test derived based on Monte Carlo simulations for *H* is best fit with an exponential function:

$$\text{Prob}(H > h) = ae^{-bh} \tag{7.11}$$

with parameters $a = 1.000$ and $b = 0.398$. In simple terms, Equation 7.11 gives the probability of observing a higher *H* statistic, call it *H*, than the one calculated from your data, h. These probabilities can be converted into a significance by calculating the value such that a normal distribution integrated from said value to ∞ equals the probability (this must be solved numerically or looked up in a table).

7.4 Upper Limits from the H-Test Statistic

In Section 7.3.1, the properties of the *H* test and the corresponding test statistic were presented. For a given value of the test statistic H, an upper limit on N_{excess} can be calculated as shown by [84] at a desired confidence level. Call the excess counts upper limit x. In [84], it is shown that for a pulse profile with a single peak:

$$x_{2\sigma} = \sqrt{N}(1.3 + 8.7\delta)(0.174H)^{0.24+0.13\delta}\text{exp}[(0.03 + 0.13\delta)(\log_{10}(0.174H))^2] \tag{7.12}$$

and

$$x_{3\sigma} = \sqrt{N}(1.5 + 10.7\delta)(0.174H)^{0.17+0.14\delta}\text{exp}[(0.08 + 0.15\delta)(\log_{10}(0.174H))^2] \tag{7.13}$$

where N is the total number of events, and δ is the “duty cycle,” i.e., the FWHM of the assumed Gaussian shape of the peak in the pulse profile. These equations are parametrizations of curves obtained from a Monte-Carlo simulation, which gives x as a function of H for the assumed 2σ and 3σ confidence level. The simulations were repeated for $\delta = 0.1$, 0.3, and 0.5. The above equations are only valid for $H > 0.3$; if $H \leq 0.3$, then H is set to 0.3 and the upper limit calculation proceeds as normal[2]. Converting the excess counts upper limit x to a flux upper limit is then just a matter of dividing by the exposure time and effective area of the observation, as previously discussed in Section 6.3.6.

---

[2] For a justification of this, see the Appendix in [84].

CHAPTER 8
THE GEMINGA PULSAR

This chapter is an adapted reproduction of a paper I have co-authored as a corresponding author with former colleague A. McCann (Universtiy of Chicago, McGill University) published in [7]. I provided the secondary analysis, where A. McCann acted as lead analyzer and author. The paper text was drafted by A. McCann, and I provided revision input as the coauthor at every step. Information already given in another section in this thesis has been removed for sake of avoiding redundancy.

8.1 Abstract

We present the results of 71.6 hours of observations of the Geminga pulsar (PSR J0633+1746) with the VERITAS very high-energy gamma-ray telescope array. Data taken with VERITAS between November 2007 and February 2013 were phase-folded using a Geminga pulsar timing solution derived from data recorded by the XMM-Newton and *Fermi*-LAT space telescopes. No significant pulsed emission above 100 GeV is observed, and we report upper limits at the 95% confidence level on the integral flux above 135 GeV (spectral analysis threshold) of $4.0 \times 10^{-13}\,\mathrm{s}^{-1}\,\mathrm{cm}^{-2}$ and $1.7 \times 10^{-13}\,\mathrm{s}^{-1}\mathrm{cm}^{-2}$ for the two principal peaks in the emission profile. These upper limits, placed in context with phase-resolved spectral energy distributions determined from five years of data from the Fermi-LAT, constrain possible hardening of the Geminga pulsar emission spectra above 50 GeV.

8.2 Introduction

Following the completion of the Compton Gamma Ray Observatory (CGRO) mission in 2000, seven gamma-ray pulsars were known to exist. A combined total of 37 photons with energies exceeding 10 GeV were observed from five of these pulsars by the EGRET instrument on-board CGRO [85]. The *Fermi* Large Area Telescope (LAT) has now detected over 160 gamma-ray pulsars[1] (see [86] for a review) and pulsar studies presented in the *Fermi*-LAT catalog of sources above 10 GeV (1FHL) have shown that 20 of these pulsars have *Fermi*-LAT detections above 10 GeV, with 12 also seen at energies above 25 GeV [87, 88]. One common feature exhibited by all known gamma-ray pulsars is the shape of the spectral energy distribution (SED), which can be described by a power law followed by a spectral break occurring between 1 and 10 GeV [6]. The 12 pulsars observed above 25 GeV are largely drawn from the brightest of the *Fermi* pulsars ($\mathrm{F}_{>100\ \mathrm{MeV}} > 1.6 \times 10^{-7}\mathrm{s}^{-1}\mathrm{cm}^{-2}$) and thus are sufficiently bright to be detected by *Fermi* at these energies even as their spectrum falls rapidly above the break. The most favored general description of gamma-ray emission from pulsars in the *Fermi* era postulates that electrons are accelerated in the outer magnetosphere. This acceleration is limited by the radiation of synchrotron and curvature photons, leading to spectral cut-offs. Outer-magnetospheric models (outer-gap or slot-gap models) that implement this emission framework can, in general, reproduce the pulsar light curves and SEDs measured by the *Fermi*-LAT.

Recently the Vela pulsar—the brightest known gamma-ray pulsar—has been detected at energies above 30 GeV by H.E.S.S. (refer to Section 3.2.2 for more information) and above 50 GeV in the *Fermi*-LAT data [36]. The Crab pulsar, however, remains the only pulsar known to emit above 100 GeV. The power-law extension of the Crab pulsar SED measured above the GeV break by VERITAS [3] and MAGIC [41, 89] cannot be easily explained by curvature emission from the outer magnetosphere [3, 46] unless the radius of curvature of the magnetic field line is larger than the radius of the light cylinder [90]. Some recent models attribute the pulsed very-high-energy (VHE; E >100 GeV) emission from the Crab pulsar to inverse-Compton (IC) scattering originating in the outer magnetosphere [46, 91, 92] or to IC scattering from beyond the light cylinder [55, 93]. The question of

---

[1] `https://confluence.slac.stanford.edu/display/GLAMCOG/Public+List+of+LAT-Detected+Gamma-Ray+Pulsars`

whether Crab-pulsar-like non-exponentially-suppressed VHE spectra are common in other gamma-ray pulsars, such as Geminga, has meaningful implications for our understanding of the physics of particle acceleration and emission from pulsars.

Located at a distance of $\sim$200 pc [94, 44], the Geminga pulsar is the second-brightest steady GeV source in the gamma-ray sky and is the original "radio-quiet" pulsar. It has a period of 237 ms, a spin-down age of 3×10^5 yr and a spin-down luminosity of 3.26×10^{34} erg s^{-1} [95]. Originally detected as an unidentified source of $\sim$100 MeV gamma-ray emission by the SAS-2 and COS-B instruments [96, 97], its nature as a pulsar was established following the detection of pulsed X-ray emission in data recorded by the ROSAT satellite [98]. Reanalysis of the COS-B and SAS-2 data, using the pulsar timing solution determined from the ROSAT data, confirmed the MeV source to be a gamma-ray pulsar [99, 100]. Analysis of the available EGRET data further confirmed the identification [45]. The pulsed X-ray source is composed of thermal radiation from hot-spots on the surface of the neutron star and non-thermal magnetospheric emission [101]. Detailed gamma-ray observations of the Geminga pulsar have been made with the EGRET, *AGILE* and *Fermi* space telescopes [102, 103, 104, 105]. Repeated radio searches have failed to find a radio-pulsar counterpart [106, 107] while optical and UV pulsations have been reported at the 3.5σ and 5σ level, respectively [108, 109].

The Geminga pulsar has been a target for ground-based very high-energy gamma-ray detectors for over two decades. Limits on the pulsed gamma-ray flux in the TeV regime at the $\sim$10% Crab Nebula level have been reported by the Whipple, HEGRA and PACT collaborations [110, 111, 112], while the Ootacamund, Durham and Crimean groups have reported weak evidence ($\sim 3\sigma$ level) for pulsed emission at the $\sim$50-100% Crab Nebula level [113, 114, 115]. Given the far higher sensitivity of current ground-based gamma-ray arrays, it seems likely that these reported excesses are due to statistical fluctuations. At multi-TeV energies, an unpulsed and spatially extended source attributed to the Geminga pulsar wind nebula [116] has been detected at the $\sim$20% Crab Nebula level by the Milagro water-Cherenkov telescope [117, 118]. Weak evidence (2.2σ) for this unpulsed source has also been reported at TeV energies by the Tibet air-shower array [119].

The phase-averaged differential photon flux of the Geminga pulsar, as measured by the *Fermi*-LAT in the range 0.1-50 GeV, is well described by a power law with an index of 1.3 ± 0.01 at low energies, followed by a spectral break at $\sim$2.5 GeV [105]. Above the break energy, a sub-exponential cut-off in the spectrum is favored over a pure exponential or super-exponential shape, as is commonly seen in the bright *Fermi* pulsars [6]. [92] argues that above the spectral break, the spectrum can be described by a power law, a behavior similar to what has been measured by VERITAS and MAGIC in the Crab pulsar above the spectral break. Geminga is one of the 12 pulsars detected above 25 GeV in the 1FHL with the highest-energy photon attributed to the Geminga pulsar with a 95% confidence level having an energy of 33 GeV [88].

8.3 Observations

The VERITAS observations of Geminga presented here were made under clear, moonless skies between November 2007 and February 2013. After data-quality selection, the resulting observations span a total of 71.6 hours performed at an average elevation of 72°. The data set spans three different configurations of the VERITAS array: March 2007 to July 2009, the original array layout; August 2009 to July 2012, the layout following the relocation of one telescope; and August 2012 to present, following the upgrade of the VERITAS cameras and trigger system (see [66] for further details). The data were acquired in a mixture of *ON* and *wobble* (also known as *false source*) observation modes [77].

8.4 Data Analysis

8.4.1 Fermi-LAT Analysis

Fermi-LAT photon event times are folded using a timing model for Geminga derived from *Fermi*-LAT data provided by Matthew Kerr[2] [120]. The resulting pulsar light curve, which is dominated by two emission peaks, labeled P1 and P2, connected by a "bridge" of enhanced emission, is plotted in Figure 8.1. The P1 and P2 peaks are fitted with asymmetric Gaussian functions above 5 GeV and 10 GeV, respectively. These energy cuts enable us to measure the width of the emission peaks at high energies while maintaining good statistics in each phase region. The $\pm 1\sigma$ regions around each peak (phases [0.072 - 0.125] for P1 and phases [0.575 - 0.617] for P2) are then used as gates for phase-resolved *Fermi*-LAT spectra and as signal regions for pulsed searches in the VERITAS data. To generate the LAT spectra, binned maximum-likelihood analyses are performed in 12 logarithmically spaced energy bands between 100 MeV and 100 GeV. In each energy band, a source model derived from the LAT 2-year point-source catalog [72] is fitted to binned counts maps in a $14^\circ \times 14^\circ$ region centered at the location of the Geminga pulsar. The normalization of the galactic diffuse model and the normalization of all sources within 4° of Geminga are allowed to float, while all other parameters are fixed to the 2-year point-source catalog values. In each energy band, Geminga is modeled as a point source with a power-law spectrum, floating normalization, and a differential photon flux index fixed to the value 2. In addition, binned likelihood analyses are performed across the entire 100 MeV to 100 GeV energy range with the same prescription as above, with the differential photon flux of Geminga modeled as a power law multiplied by an exponential cut-off:

$$\frac{dF}{dE} = A\left(\frac{E}{E_0}\right)^{-\Gamma} e^{-\left(\frac{E}{E_{\mathrm{brk}}}\right)} \tag{8.1}$$

---

[2] `www.slac.stanford.edu/~kerrm/fermi_pulsar_timing/`

where the normalization (A), index (Γ) and break energy ($E_{\rm brk}$) values allowed to float. The E_0 parameter is fixed to the value 615.7 MeV, which is the decorrelation energy value for Geminga reported in the LAT 2-year point-source catalog [72]. Finally, and in order to probe a possible power-law shape of the emission above the break, binned likelihood analyses are performed between 10 and 100 GeV, modeling the Geminga spectrum as a power law with floating normalization and index. The SEDs for P1 and P2 derived from these likelihood analyses, where the relevant cut on phase is applied to all events prior to performing the likelihood fits, are plotted alongside the phase-averaged SED (where no phase cut is applied) in Figure 8.2. For each likelihood fit, residual maps are generated between the measured counts map and corresponding best-fit model map, and are found to show good agreement between the data and model.

8.4.2 VERITAS Analysis

For details on the VERITAS analysis chain, please refer to Section 6.3.

After event selection, the event GPS times are converted to barycentric dynamical time and phase-folded using `Tempo2`. VERITAS events recorded prior to the launch of *Fermi* are folded using a timing solution derived from XMM-*Newton* observations of the Geminga pulsar (provided by E. Gotthelf; private communication). VERITAS events recorded after the launch of *Fermi* are folded using the *Fermi*-LAT timing solution described in Section 3.1. The value of the timing parameter `TZRMJD` in the XMM-*Newton* model is adjusted to ensure the definition of phase zero is consistent between the two timing solutions.

VERITAS events that fall within the P1 and P2 phase gates are counted as signal-plus-background events, with background-only events selected from the phase region [0.7 - 1.0][3]. In addition, an *H*-Test for periodicity [40] is also performed on the VERITAS events.

---

[3] We note that, in this framework, VERITAS is not sensitive to the absolute flux level of the Geminga pulsar but to the difference in the flux level between the peak phase regions and the chosen background phase region. In contrast, the likelihood fitting employed in the *Fermi*-LAT analysis is sensitive to constant emission components. The Geminga pulsar flux above 100 MeV in the 0.7 to 1.0 phase range is $\lesssim$10% of the flux level measured during the peak phases [105], thus any constant emission component is constrained to be at or below this level. Therefore any mismatch between the *Fermi*-LAT and VERITAS flux scales arising

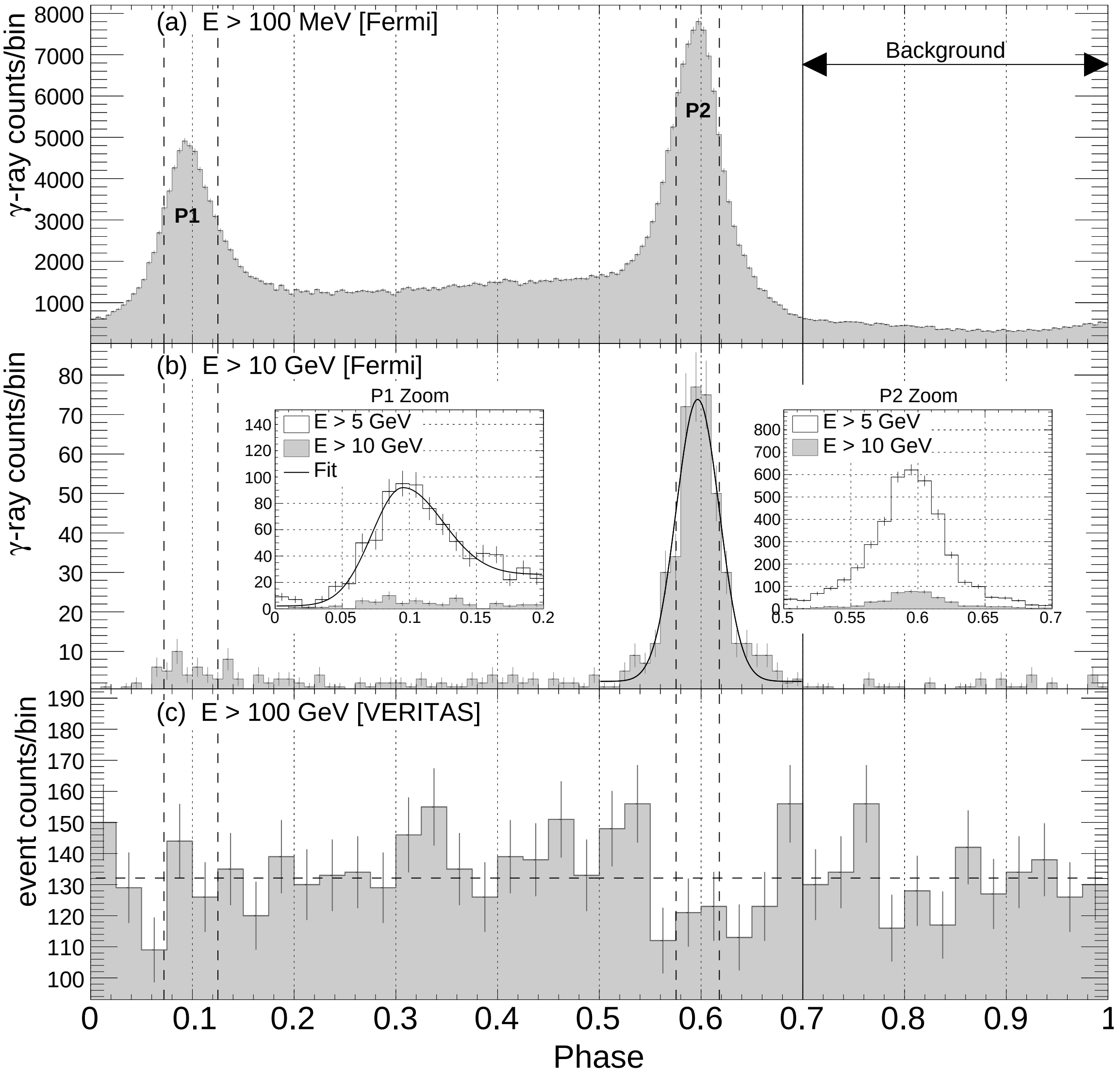

Figure 8.1: The phase-folded light curve of the Geminga pulsar as measured by the *Fermi*-LAT. The *Fermi* light curve contains all events that fell within a 2° radius centered on the position of the Geminga pulsar. The energy-dependent evolution of the light curve is in clear agreement with the light curves presented in [87] and [88]. The P1 and P2 emission peaks were fitted with asymmetric Gaussian functions above 5 GeV and 10 GeV, respectively. These fits, which are plotted as smooth black curves in panel (b), were used to define the signal regions for the P1 and P2 spectral analyses. These phase regions, [0.072 - 0.125] for P1 and [0.575 - 0.617] for P2, are indicated as vertical dashed lines. The background-event sample for the VERITAS analysis was selected from the phase range [0.7 - 1.0]. There is no evidence of pulsed emission above 100 GeV at any phase in the VERITAS data plotted in panel (c).

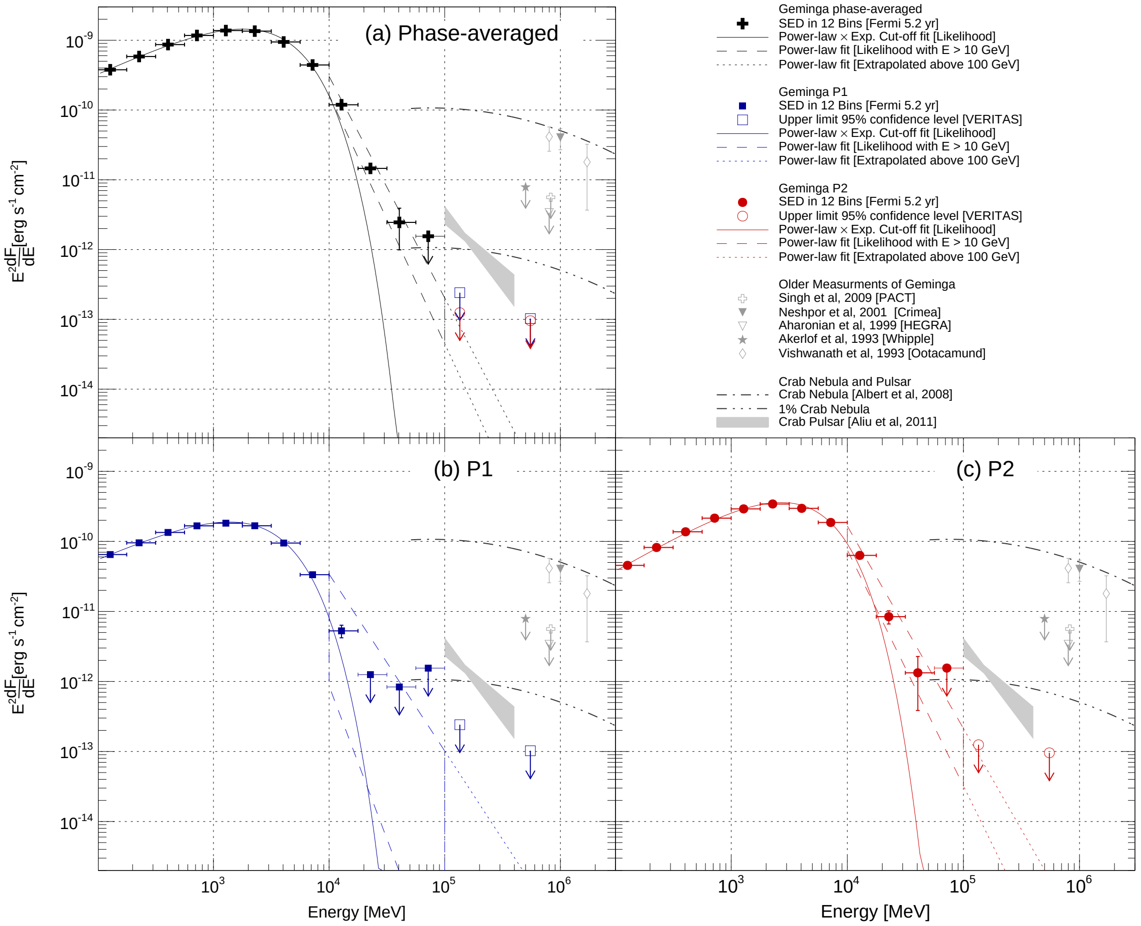

Figure 8.2: Measured SEDs and flux upper limits for the Geminga pulsar. Measurements of the Crab Nebula and pulsar are plotted for comparison. The Geminga limits and fluxes shown for PACT, Crimea, HEGRA, Whipple and Ootacamund were derived from the integral values reported by those experiments, assuming a power law with index 2.5 in each case.

All steps in the VERITAS analysis chain are cross checked and verified with an independent analysis pipeline[4]. Due to the method of background estimation, the VERITAS analysis presented here is not sensitive to unpulsed gamma-ray emission that might originate from the pulsar magnetosphere or the pulsar wind nebula. An analysis tuned for this type of unpulsed and possibly spatially extended emission is ongoing and will be presented in a future publication.

8.5 Results

8.5.1 Light curve

Our results from the analysis of 5.2 years of *Fermi*-LAT data (see Figure 8.1) are consistent with those previously reported by [105], [87], and [88]. The light curve clearly evolves with energy, with the P2 peak remaining visible at energies above 10 GeV, while the P1 peak and the "bridge" are diminished. Above 100 GeV, there is no evidence for pulsed emission. The VERITAS phase data plotted in Figure 8.1c have an *H*-Test value of 1.8, which has a probability of randomly occurring equal to 0.49. A χ^2-fit of the binned phase data for constant counts has a χ^2/n.d.f value of 45.95/39 and a fit probability of 0.2, indicating that the phase distribution is entirely consistent with a random distribution.

8.5.2 Spectrum

The spectral analysis of 5.2 years of *Fermi*-LAT data (see Figure 8.2) are consistent with those previously reported by the *Fermi*-LAT team [105, 6]. The phase-averaged SED, and the SEDs for P1 and P2, are all well described by power laws with spectral breaks occurring between 1.8 and 2.8 GeV (see Table 8.1 for the best-fit values returned from the maximum-likelihood analysis). Above the break, the SED data points lie above the best-fit exponential cut-off function derived from the likelihood analysis and appear more

---

from the difference in background-estimation methods is within the systematic uncertainty on the absolute flux scale of both instruments.

[4] Both analysis pipelines were used for the Crab pulsar data analysis presented in [3].

Table 8.1: Results from maximum-likelihood fits to the *Fermi*-LAT data. Between 100 MeV and 100 GeV the differential photon flux of Geminga was modeled as a power law multiplied by an exponential cut-off as defined in Equation 1. Between 10 GeV and 100 GeV, the differential photon flux of Geminga was modeled as a pure power law with the normalizing E_0 parameter fixed to 5 GeV. The quoted uncertainties are statistical only. The systematic uncertainty on the estimation of pulsar spectral values was studied by the *Fermi*-LAT collaboration in [6] and found to be, on average, 14% for Γ and 4% for E_{brk}.

Peak	100 MeV$< E <$100 GeV			10 GeV$< E <$100 GeV	
	A [$\times10^{-10}$cm^{-2} s^{-1}MeV^{-1}]	Γ	E_{brk} [GeV]	A [$\times10^{-11}$cm^{-2} s^{-1}MeV^{-1}]	Γ
P1	3.60±0.04	1.27±0.01	1.87±0.03	0.27±0.22	5.44±0.92
P2	3.72±0.02	1.03±0.10	2.78±0.04	2.51±0.56	5.13±0.24
Phase-averaged	22.60±0.07	1.23±0.01	2.33±0.02	5.83±1.02	5.37±0.19

compatible with a pure power-law function, as was previously noted by [92] (see the dashed lines in Figure 8.2). The last bin in the P1 SED with a significant detection (likelihood test statistic $>$12) is between 10 GeV and 17 GeV, while the P2 and phase-averaged SEDs have significant flux detected up to 56 GeV. We report upper limits on the Geminga flux at the $\sim$1% Crab Nebula level from the *Fermi*-LAT data in the 50–100 GeV energy range.

In the VERITAS data above $\sim$100 GeV, the number of events falling in the P1 and P2 signal regions is fully consistent with background only (see Table 8.2). Using the method of [121], the upper limit on the number of excess counts at the 95% confidence level is calculated. This upper limit divided by the duration of the observation and effective area of VERITAS yields the upper limit on the integral flux from the Geminga pulsar. For the integral flux upper limit calculation, a power law with a spectral index of 3.8 is assumed, which is the same index value measured by VERITAS in the Crab pulsar above 100 GeV [3]. The resulting 95% confidence level upper limits are 4.0×10^{-13} s^{-1} cm^{-2} and 1.7×10^{-13} s^{-1} cm^{-2} on the integrated flux above 135 GeV[5] for P1 and P2, respectively. Above 550 GeV, the 95% confidence level upper limits are 5.1×10^{-14} s^{-1} cm^{-2} and 3.9×10^{-14} s^{-1} cm^{-2} for P1 and P2, respectively. The corresponding energy fluxes,

---

[5] While this VERITAS analysis is sensitive to photons above $\sim$100 GeV in a search for pulsations, the threshold for spectral analysis is 135 GeV, and therefore upper limits are quoted above this energy.

Table 8.2: VERITAS event counts in the signal and background phase ranges. α is the ratio of the size of the signal phase gate to the background phase gate. The significance values were calculated using Equation 17 from [81].

Peak	#Signal	#Background	α	#Scaled Background	#Excess	Significance
P1	284	1578	0.176	278.9	5.0	0.28σ
P2	211	1578	0.141	223.7	-12.7	-0.80σ
P1+P2	495	1578	0.318	502.6	-7.6	-0.29σ

expressed in erg s^{-1} cm^{-2}, are plotted in Figure 8.2.

8.6 Discussion and Conclusion

Following a 71.6 hour exposure, we observe no significant pulsed emission from the Geminga pulsar above 100 GeV. The VERITAS 95% confidence level integral flux limits on the emission from the P1 and P2 phase ranges limit any putative hard emission component above 135 GeV to be at or below the $\sim$0.25% Crab Nebula level. The spectral data points derived from the analysis of 5.2 years of *Fermi*-LAT observations are compatible with a power law up to the break energy, but fall more slowly than what would be expected from a simple exponential cut-off. It can be shown that the rounder, sub-exponential shape, seen above the break in the phase-averaged SED, can be reproduced by a superposition of several exponential cut-off functions with different break energy [37, 36]. Such a shape is expected in multizone curvature-radiation models, when multiple acceleration regions with different break energies combine to produce the observed emission. Only at energies sufficiently above the maximum break energy will the emission clearly fall exponentially.

Non-exponentially-suppressed emission above the GeV break energy, expected in inverse-Compton emission pulsar models, has yet to be conclusively observed with high significance in any pulsar other than the Crab pulsar. In Geminga above 10 GeV, we see that pure power laws with indices between 5.1 and 5.5 are compatible with the differential photon flux points and predict a level of emission below the VERITAS limits (see Table 8.1 and Figure 8.2 for more details). Similar results were found by [92]. A cursory inspection of the Vela SED in [36] suggests that a power law with an index of ∼2.4 (∼4.4 for the differential photon flux spectrum) is compatible with the data points between 10 and 100 GeV, though the authors show the SED is well fit by a multizone curvature emission model. Given this is the case for the two brightest gamma-ray pulsars, and given the low fluxes from most pulsars above a few tens of GeV[6], we conclude that power-law-type emission cannot be distinguished from the rounded exponential cut-off shape expected in multizone curvature-emission models with the available spectral data.

In the case of the Crab pulsar, and in several other cases where the GeV break energy requires an acceleration efficiency close to or exceeding unity [46], canonical curvature-radiation scenarios at the light cylinder are stressed. In the case of Geminga, applying Formula 1 from [92] and using the Geminga parameters from the ATNF Pulsar Catalog [14], we find that the maximal break energy for curvature radiation from the outer magnetosphere is ϵ_{br} = 2.53 GeV. The phase-averaged break-energy value reported here, 2.33±0.02 GeV, is consistent with this ϵ_{br}. The P2 break energy, 2.78±0.04 GeV, does exceed the maximal curvature break energy within the adopted outer-magnetospheric emission framework. We note, however, that ϵ_{br} is a function of the assumed neutron-star radius and surface B-field strength to the powers of $9/4$ and $3/4$, respectively. Changes in either of these parameters at the 5-10% level bring the derived ϵ_{br} into agreement with our measured value. However, the measured break energies in Geminga do require the acceleration efficiency to approach unity at the light cylinder in this radiation-reaction-limited curvature-emission framework. This, in addition to the compatibility of the power-law shape with the high-energy data, positions Geminga as a viable candidate for inverse-Compton emission. Assuming the Cherenkov Telescope Array (CTA) performs as expected [122], future observations with CTA should be able to firmly detect the steep power law extrapolated from the *Fermi*-LAT data at energies above 100 GeV in roughly one hundred hours.

---

[6] Only 4 of the 117 pulsars described in the second *Fermi*-LAT catalog of gamma-ray pulsars [6] have a measured flux point above 30 GeV with an average flux in the 30–50 GeV range of 7.6×10^{-11} s^{-1} cm^{-2}. For the remaining pulsars undetected in this energy range, the average 95% confidence level flux upper limit is 4.9×10^{-11} s^{-1} cm^{-2}.

CHAPTER 9

THE SEARCH FOR VHE EMISSION FROM THE MISSING LINK BINARY PULSAR J1023+0038

This chapter is an adapted reproduction of a paper I have published [8], along with other corresponding authors E. Aliu, M. Chernyakova, and M. S. E. Roberts. My responsibilities on this project comprised the following:

- Conducted all of the analysis presented herein
- Drafted and revised text throughout the paper
- Acted as lead author and led the paper through collaboration review to publication.

M. Chernyakova and M. S. E. Roberts were responsible for drafting the text in the Introduction and providing the theoretical interpretation given in Section 9.5. Much work was also done by E. Aliu before leaving the VERITAS collaboration, at which point I took over the paper.

The paper details both steady- and pulsed-flux searches for VHE gamma rays from the binary system containing the pulsar J1023+0038. Information already given in another section in this thesis has been removed for sake of avoiding redundancy.

9.1 Abstract

The binary millisecond radio pulsar PSR J1023+0038 exhibits many characteristics similar to the gamma-ray binary system PSR B1259–63/LS 2883, making it an ideal candidate for the study of high-energy non-thermal emission. It has been the subject of multi-wavelength campaigns following the disappearance of the pulsed radio emission in June 2013, which revealed the appearance of an accretion disk around the neutron star. We present the results

of very high-energy gamma-ray observations carried out by VERITAS before and after this change of state. Searches for steady and pulsed emission of both data sets yield no significant gamma-ray signal above 100 GeV, and upper limits are given for both a steady and pulsed gamma-ray flux. These upper limits are used to constrain the magnetic field strength in the shock region of the PSR J1023+0038 system. Assuming that very high-energy gamma rays are produced via an inverse-Compton mechanism in the shock region, we constrain the shock magnetic field to be greater than $\sim$2 G before the disappearance of the radio pulsar and greater than $\sim$10 G afterwards.

9.2 Introduction

Radio millisecond pulsars (MSPs) are old neutron stars that have been spun up to millisecond periods via accretion of material from a companion star in a low-mass X-ray binary (LMXB) [123]. In the past few years, new MSP discoveries have taken place at a greatly elevated rate due to searches for radio pulsars in unassociated *Fermi*-LAT-detected gamma-ray sources [124]. This new population of MSPs has enriched the known diversity of binary MSP companions. This is especially true for eclipsing systems, which were rarely seen outside of globular clusters: the "black widows" with very low-mass ($M \ll 0.1M_{\odot}$) companions and "redback" systems with more massive ($M_c \gtrsim 0.1M_{\odot}$), non-degenerate companions [125]. Some of these redbacks have been observed to transition between LMXB and MSP states, providing the first direct observational evidence to support the theory of the MSP formation mechanism. There are now three systems where transitions have been observed: PSR J1023+0038 [126] and XSS 12270–4859 [127, 128] in the Galactic plane, and PSR J1824–2452I [129], located in the globular cluster M28. Additionally, it has recently been suggested that the galactic binary 1RXS J154439.4–112820 may also be a transitional system [130].

Very high-energy gamma-ray emission from binaries containing MSPs has been predicted to occur through diverse mechanisms. [131] propose that leptons accelerated above the polar cap can produce inverse-Compton or curvature radiation emission that could potentially be identified as gamma-ray pulsations at energies up to and above 100 GeV, similar to what has been observed from the young Crab pulsar [21, 3]. Additionally, leptons could be accelerated at the shock that appears as a result of the interaction between the pulsar wind and material ablated off of the companion. These leptons could then radiate VHE gamma rays via inverse-Compton scattering, which could be modulated with the binary orbital period. This emission scenario is thought to occur in the VHE-detected binary system PSR B1259–63/LS 2883, a radio pulsar in a $\sim$3.4 yr orbit around a massive, luminous Be star [132].

The theory of VHE gamma-ray emission from PSR B1259–63 [133] was first explored in the context of the original Black Widow Pulsar system [134], which is a binary comprising the 1.6 ms pulsar PSR B1957+20 in a 9.2 hr orbit around a $\sim$0.02 $M_{\odot}$ companion. However, no VHE emission has been detected from the Black Widow [62]. Searches for VHE emission from several globular clusters have been undertaken, since they are known to contain many of these eclipsing binary systems. Recently, H.E.S.S. has detected VHE emission from the direction of the cluster Terzan 5 [135], which is especially rich in eclipsing binary systems among globular clusters [136]. This emission is thought to originate in a bow shock region where interaction between leptons from MSP winds and the galactic medium occur [137]. However, searches for VHE emission from the globular clusters 47 Tuc [138], M5, M15 [139], and M13 [140, 141] have revealed no such emission. The aforementioned eclipsing binary systems in globular clusters can be seen as smaller-scale versions of PSR B1259–63, because their more massive, nearly Roche-lobe-filling companions provide much larger targets and more copious seed photons for inverse-Compton scattering than companions of black widows. With the discovery of nearby redbacks in the Galactic field, it is thought that a single, energetic Galactic-field redback could be brighter at VHE energies than the combined emission from many eclipsing systems in a distant cluster [125].

PSR J1023+0038 is a redback system containing a 1.69 ms MSP in a 4.8 hr orbit around a G star with a mass of $\sim$0.2M$_\odot$ [126]. PSR J1023+0038 was selected as a promising candidate for VHE observations with VERITAS based on three parameters thought to be responsible for the VHE emission from PSR B1259–63: the high spin-down luminosity of the pulsar, the presence of an intense target photon field for inverse-Compton scattering provided by the companion, and the relatively small distance from Earth. Although the optical luminosity of the companion in PSR J1023+0038 is a factor of $\sim$10^4 less than that for the companion of PSR B1259–63, this discrepancy is possibly compensated by the much smaller distance separating the pulsar and its companion in PSR J1023+0038, potentially making the energy density of seed photons at the shock comparable for the two systems. However, the PSR B1259–63 system has a circumstellar disk that the pulsar passes through at periastron [142], though PSR J1023+0038 shows no evidence of such a disk.

While the actual VHE emission will depend on the details of the flow and the magnetic field at the shock, the inverse-Compton emission should roughly scale as $F_{\rm IC} \propto f(\dot{E}/d^2)u_{\rm ph}$ where d is the distance to the binary, $u_{\rm ph} \sim (R_c/R_s)^2\sigma T_c^4/c$ is the photon energy density at the shock, R_c is the radius of the companion, R_s is the radius of the shock measured from the companion, and f is a geometrical factor representing the fraction of the pulsar wind involved in the shock. If the shock region of PSR J1023+0038 (and by extension other redbacks and black widows) is very near the surface of the companion, as proposed by [143], then $R_c/R_s \sim 1$, and f is related to the angle subtended by the companion in the pulsar sky. In the extreme case of a shock only near the surface of the companion, f is approximately 0.01 if the pulsar wind is isotropic, and f is approximately 0.07 if the wind is confined to the equatorial plane. Based on this simple estimation, the expected TeV flux from PSR J1023+0038 would be on the order of $\sim 0.1f$ that of PSR B1259–63 near periastron, where it has an observed flux $F(E > 1{\rm TeV}) \sim 10^{-11}{\rm cm}^{-2}\,{\rm s}^{-1}$ [144]. We note that PSR J1023+0038 was selected for observations before the publication of the revised estimates for the distance and spin-down power given in [145], in which case the estimated TeV flux would have been closer to $1f$ that of PSR B1259–63.

Orbitally modulated X-ray emission has been observed from PSR J1023+0038, suggesting that the system contains shocked material [146], and the observed radio eclipses suggest that the shock region may be quite large. [147] found strong evidence of gamma-ray emission from the direction of PSR J1023+0038 in the high-energy (HE; $100\,\mathrm{MeV} \lesssim E \leq 100\,\mathrm{GeV}$) gamma-ray band using *Fermi*-LAT data. Given the observed steep spectrum of this emission ($\Gamma \sim 3$), the authors suggest that the gamma rays likely originate from the pulsar magnetosphere rather than the intrabinary shock. Indeed, [148] have reported a hint of pulsed HE gamma-ray emission from the pulsar magnetosphere with a statistical significance of 3.7σ.

A sudden change of state in PSR J1023+0038 was reported to have occurred in June 2013 after the pulsed radio emission from the MSP was no longer detected [149], and optical evidence for an accretion disk in the system was found for the first time since December 2001 [150, 151]. The X-ray emission increased only moderately [152, 153], implying that accretion may still be inhibited due to the influence of the pulsar magnetosphere, although low-level X-ray pulsations, thought to be powered by accretion, have been detected [154]. All of this new behavior coincided with a five-fold increase in the HE gamma-ray flux from PSR J1023+0038 [155].

The similarities between PSR J1023+0038 and PSR B1259–63/LS 2883 motivated the first VERITAS observations of the PSR J1023+0038 in 2010. Follow-up observations took place after the system was reported to have transitioned to an accretion/LMXB state in 2013, prompted by the substantial increase in flux in the HE gamma-ray band observed with the *Fermi*-LAT. Here we report the results of these observations of PSR J1023+0038, the first ever made in the VHE band, covering the two different states of this exceptional transitional object.

Table 9.1: VERITAS analysis results for the location of PSR J1023+0038 for each of the two different binary states. The parameter α indicates the ratio of the ON- to OFF-source region exposure, and the LiMa significance is calculated using equation 17 in [81] (same as Equation 7.1 given in Section 7.2.).

Binary State	On Events	Off Events	α	Excess Events	LiMa Significance	95% CL flux UL ($cm^{-2}s^{-1}$)	95% CL flux UL (flux units) (erg $cm^{-2}s^{-1}$)
Radio MSP	287	1815	0.17	-15.5	-0.8	8.1×10^{-13}	5.8×10^{-13}
Accretion/LMXB	72	422	0.17	1.7	0.2	9.6×10^{-13}	6.9×10^{-13}

9.3 VHE Gamma-Ray Observations

For details of the VERITAS array, please see Chapter 5.

The first observations of PSR J1023+0038 were made by VERITAS between 2010 December 8 and 2011 February 25 when the system was in the radio MSP state, resulting in 20 hr of live time available for analysis after data quality selection. Further observations took place in December 2013 for a total 10 hr of live time coinciding with the newly reported accretion/LMXB state of the system. The two sets of data were recorded in two different configurations of the VERITAS array: August 2009 to July 2012, with the original cameras and electronics; and August 2012 to present, following an upgrade to the telescope cameras and the trigger system (for details, see [66]). Data were taken on clear and moonless nights in *wobble* observation mode in which the telescope pointing is offset by $0^\circ.5$ from the position of PSR J1023+0038, alternating between the four cardinal directions to allow simultaneous accumulation of data and background [77]. The data span the zenith angle range of 31° to 39°.

9.4 VERITAS Analysis and Results

9.4.1 Analysis

The data were analyzed using the standard analysis pipeline described in Section 6.3.

Table 9.2: *H* statistic and integral pulsed VHE flux upper limit computed with the VERITAS data for the radio MSP state of PSR J1023+0038. Due to the unavailability of a valid pulsar timing solution for the accretion/LMXB state, no *H* statistic or flux upper limit is given for VERITAS data collected during this state.

PSR J1023+0038 State	*H* statistic	95% CL pulsed VHE flux UL ($\mathrm{cm^{-2}\ s^{-1}}$)	95% CL pulsed VHE flux UL (flux units; erg $\mathrm{cm^{-2}\ s^{-1}}$)
Radio MSP	0.50	1.5×10^{-12}	2.0×10^{-12}
Accretion/LMXB	-	-	-

9.4.2 Search for a Steady Signal

A search for a VHE gamma-ray excess signal from the direction of PSR J1023+0038 is carried out independently for the two states of the system observed with VERITAS. None of these searches yield a significant excess over the estimated background from the location of PSR J1023+0038. Upper limits (ULs) on the integral flux above 300 GeV from PSR J1023+0038 for each state are set. The approach of [156] is used to determine these ULs at the 95% confidence level (CL) assuming a power-law source spectrum with a photon index of $\Gamma = 2.5$. The 95% CL ULs are 8.1×10^{-13} and $9.6 \times 10^{-13}\,\mathrm{cm^{-2}\,s^{-1}}$, respectively. For more information, refer to Table 9.1.

Given that PSR J1023+0038 shows orbital modulation in the X-ray band, a search for VHE gamma-ray emission at different orbital phases is also performed. The data are divided into ten phase bins and undergo the same standard analysis as described in Section 9.4.1. For both the radio MSP state and the accretion/LMXB state, no significant excess is found in any of the orbital bins.

9.4.3 Search for Pulsations

A search for pulsed gamma-ray emission in the VHE band from the position of PSR J1023+0038 is performed in two parts using data recorded by VERITAS during time periods in which the radio MSP was active and after the disappearance of the MSP and reemergence of an accretion disk (accretion/LMXB state). After applying the background-rejection and data quality cuts outlined in Section 9.4.1, photon arrival times are barycentered and phase folded to the pulsar period in the `Tempo2` software package [68] using a PSR J1023+0038 Jodrell Bank timing solution derived from radio data spanning MJD 55540 to 55644 (2010 December 10 to 2011 March 24). Details on the creation of the Jodrell Bank radio timing solution can be found in Section 3 of [148]. Since the pulsar timing solution used is no longer valid during the accretion/LMXB phase, only results from the radio MSP state are shown. The phase-folded light curve of PSR J1023+0038 is shown in Figure 9.1. De Jager's *H* test is employed to compute *H* statistics that reflect the likelihood of the presence of a periodic signal in the light curve [40]. Application of the *H* test does not yield any evidence of periodicity in the VHE gamma-ray data. Subsequently, integral flux limits above an energy threshold of 166 GeV are computed with the method of [84] assuming a pulsar duty cycle of 10%, a Gaussian pulse shape, and a spectral index of 3.8 (the same index measured by VERITAS for the Crab pulsar in [3]). *H* statistics and integral VHE flux limits are given in Table 9.2.

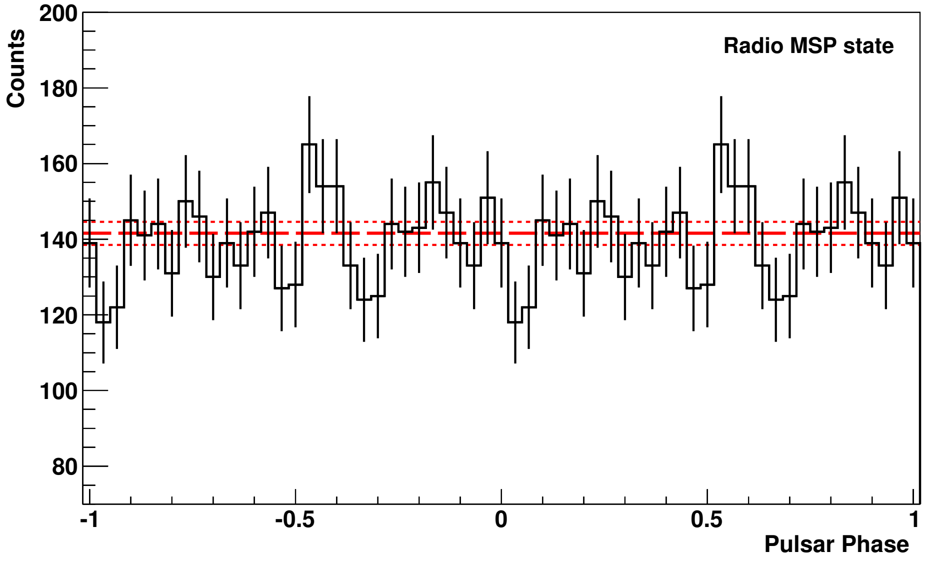

Figure 9.1: Light curve of events phase folded with the Jodrell Bank radio timing solution for the radio MSP state . The light curve shows two pulsar periods and contains 30 bins per period. The dashed and dotted red lines represent the average number of counts and error on the average, respectively.

9.5 Discussion and Conclusion

During the last decade, PSR J1023+0038 has been intensively investigated in different energy bands. In this paper we have reported two sets of VERITAS observations, taken during the radio MSP state and the accretion/LMXB state, that have both yielded upper limits on a VHE gamma-ray flux. While the beginning of the accretion phase was marked by a sharp rise of the luminosity both in X-rays and HE gamma rays as observed by *Swift* and the *Fermi*-LAT [149, 157], the source was not detected by VERITAS. In the following, we discuss the constraints that can be placed on the physical properties of PSR J1023+0038 with the VERITAS upper limits. First we will discuss the system when PSR J1023+0038 exhibited detectable radio pulses, and then will investigate what changed after the reappearence of the accretion disk.

9.5.1 Millisecond Pulsar Phase

During the millisecond pulsar phase, radio emission from PSR J1023+0038 was characterized by highly frequency-dependent eclipses at superior conjunction accompanied by short, irregular eclipses at all orbital phases [126]. Assuming a pulsar mass $M = 1.4M_{\odot}$ and an orbital inclination $i \sim 46^{\circ}$, it has been shown that the line of sight between the pulsar and the Earth does not intersect the Roche lobe of the companion at any point of the orbit [126]. Therefore, the eclipses must be caused by material driven off the surface of the companion by the impinging pulsar wind.

The V magnitude of the system is orbitally modulated, reaching a minimum during the inferior conjunction of the companion star [158]. Such behavior is consistent with a Roche-lobe-filling companion near $T_{\text{eff}} = 5650\,\text{K}$ being illuminated by a pulsar with an isotropic luminosity of $\sim 2L_{\odot}$.

Orbitally modulated X-ray emission from PSR J1023+0038 was observed by the *XMM*-Newton and *Chandra* X-ray observatories in 2004, 2008, and 2010 [159, 146, 143]. In

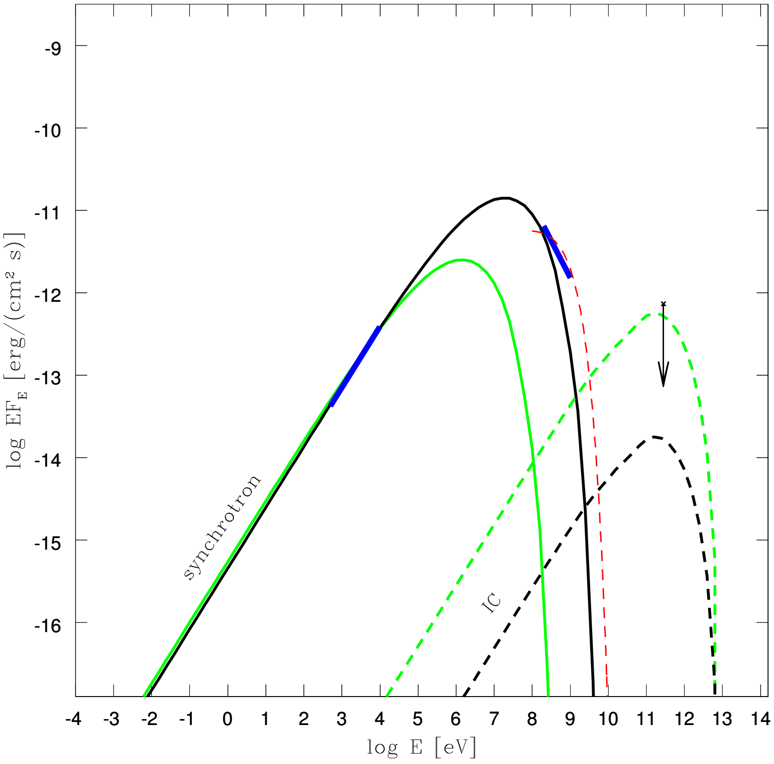

Figure 9.2: Broadband spectrum of PSR J1023+0038 during the millisecond pulsar phase. Thick blue bars show the detection of the X-ray emission by *XMM*-Newton in 2008 [146] and the *Fermi*-LAT GeV detection [147]. The black solid line represents synchrotron emission in a 40 G magnetic field, and the black dashed line represents the component due to inverse-Compton scattering of optical photons. The solid and dashed green lines represent those same components in the case of a 2 G magnetic field. The red dashed line represents a typical power-law model with an exponential cut-off spectrum of a GeV millisecond pulsar. The arrow represents the VERITAS flux upper limit reported in this work.

[146], it is shown that in the energy range 0.25–2.5 keV, the X-ray emission is also modulated at the 1.6 ms rotational period of the MSP with a mean-squared pulsed fraction of 0.11(2). X-ray emission observed with the *Swift*-XRT in the 0.3–8 keV energy range suggests a dominant non-thermal synchrotron component originating at the intrabinary shock. In the case of a magnetically dominated wind (with a ratio of magnetic energy to kinetic energy $\sigma \gg 1$), the shock should occur in a relatively strong magnetic field ($B \sim 40\,$G) due to the small separation between the pulsar and the companion [143]. In [143] it is shown that the depth and duration of the X-ray eclipses imply that the intrabinary shock is localized close to the L1 Lagrangian point and has a size of about $R \sim 5 \times 10^{10}$ cm. *NuSTAR*

has detected a power law throughout the 3–79 keV band with an estimated luminosity of $7.4 \times 10^{32}\,\mathrm{erg\,s^{-1}}$ [160]. If the estimate of the shock size by [143] is correct, then a very large fraction of the energy in the shocked portion of the wind must be converted to X-ray emission, which supports the high σ scenario. In [146] it is also noted that emission from the pulsar magnetosphere can contribute to the non-thermal X-ray emission, but the orbital modulation indicates that this component is not dominant.

In addition to the aforementioned non-thermal emission, there also is a faint thermal component possibly originating from the hot polar caps of the pulsar and optically thin thermal plasma responsible for the radio eclipses. There is no evidence in X-ray data for a wind nebula associated with the pulsar. The observed X-ray luminosity in the 0.5 – 10 keV energy range of $L_{\mathrm{X}} \sim 10^{32}\,\mathrm{erg\,s^{-1}}$ (assuming a distance of 1.4 kpc [161]) is much less than the spin-down luminosity: $L_{\mathrm{sd}} \simeq 3.2 \times 10^{34}\,\mathrm{erg\,s^{-1}}$ [148].

The broadband spectrum of PSR J1023+0038 from X-rays to VHE gamma rays is shown in Figure 9.2. While the X-ray data can be described by synchrotron emission from relativistic electrons exhibiting a power law with an exponential cut-off spectral shape, $dN/dE \propto E^{-2.52}\mathrm{exp}(-E/E_{\mathrm{cut}})$, the GeV data are not readily fitted with the same component. However, since the X-ray and GeV gamma-ray data are not strictly contemporaneous, spectral variability cannot be ruled out. The situation is similar if the observed GeV emission is produced in the pulsar magnetosphere. The typical spectral shape of the GeV millisecond pulsars is a power law with an exponential cut-off, e.g. [162]; see the red dashed line in Figure 9.2 for a best fit to the *Fermi*-LAT data [147]. This spectral shape is thought to be a result of curvature acceleration in a gap region in the magnetosphere [131]. More data are needed to distinguish between a synchrotron or curvature radiation origin of the GeV emission, although neither predicts emission above 10 GeV.

Synchrotron photons can inverse-Compton scatter on relativistic electrons and become VHE photons. The ratio of the total power radiated by the synchrotron radiation and by inverse-Compton scattering by the same distribution of electrons is equal to $\eta = \frac{(dE/dt)_{\mathrm{sync.}}}{(dE_e/dt)_{\mathrm{IC}}}$.

The value for η reaches a maximum in the Thomson limit in which $\eta_{\mathrm{T}} = \frac{B^2/8\pi}{U_{\mathrm{rad}}}$, where U_{rad} is the energy density of the synchrotron photons. It turns out that for PSR J1023+0038, the total energy of scattered photons is much smaller than the total energy of the synchrotron photons even in the Thomson limit where

$$\eta_{\mathrm{T}} \sim 600 \frac{(B/40\mathrm{G})^2 (R/5 \times 10^{10}\mathrm{cm})^2}{L/10^{32}\mathrm{erg/s}}. \tag{9.1}$$

An additional potential source of VHE emission is external inverse-Compton scattering of soft photons from the optically bright companion with an effective temperature of $T = 5650\,K$ [158]. This inverse-Compton component is shown in Figure 9.2 as a black dashed line. Given the assumed value of the magnetic field, $B = 40\,\mathrm{G}$, the component lies well below the VHE flux upper limit. However, for a lower magnetic field strength, the difference between the peak flux values of the synchrotron and inverse-Compton components will become smaller, allowing VERITAS observations to set a lower limit on the magnetic field strength. As shown by the green lines in Figure 9.2, the case of a 2 G magnetic field gives close to the peak inverse-Compton flux allowed by the upper limit derived from the VERITAS data.

Note that for a 2 G magnetic field, η_{T} defined by Equation 9.1 is close to unity. However, X-ray photons will be up-scattered in the Klein-Nishina regime, and in this case the total energy of scattered photons is much smaller than in the Thomson regime:

$$\eta_{\mathrm{KN}} = \frac{B^2/8\pi}{\frac{9}{32}U_{\mathrm{rad}}} \frac{\ln(\frac{\hbar\omega_0\gamma}{m_e c^2})}{\gamma^2\hbar^2\omega_0^2/(m_e c^2)^2} \sim \eta_{\mathrm{T}}/2000 \tag{9.2}$$

for 1 keV photons scattered into the VHE band by electrons with $\gamma = 10^4$ [163]. Although lower-energy photons are scattered in the transition regime between the Thomson and Klein-Nishina regimes, their energy density is much lower than that of the X-ray photons, and so the self-scattering process is not important in this case either.

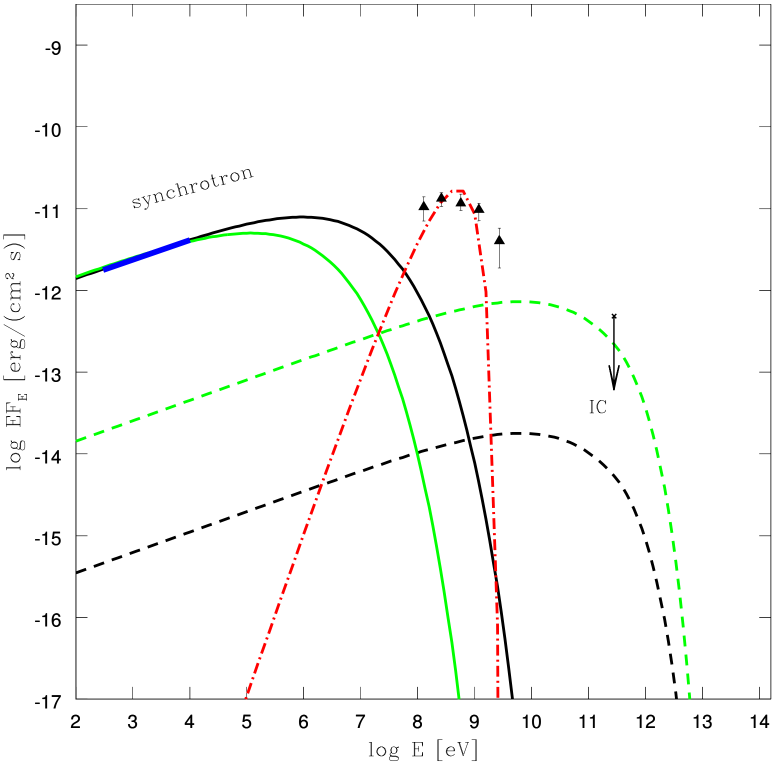

Figure 9.3: Broadband spectrum of PSR J1023+0038 after the reappearance of the accretion disk. The thick blue bar shows the X-ray emission detected by *Swift* in November 2013 [157]. Black triangles represent the *Fermi*-LAT HE gamma-ray detection in 2013 [157]. The arrow shows the VERITAS upper limit for the accretion/LMXB state, as reported in this work. Solid and dashed lines correspond to the synchrotron and inverse-Compton emission coming from the shock for the case of a 10 G (green lines) and 80 G (black lines) magnetic field. The spectral signature of inverse-Compton scattering of photons emitted by the accretion disk on the unshocked electrons is shown with a red dash-dotted line.

9.5.2 Accretion Phase

The reappearance of the accretion disk in June 2013 was accompanied by the disappearance of radio pulsations and an increase of the X-ray and HE gamma-ray luminosities. Accreting binary systems are not typically bright in the GeV domain. The only two binaries detected by the *Fermi*-LAT in which the presence of an accretion disk is certain are Cyg X-3 and Cyg X-1 [164, 165], and in both cases the HE emission is not believed to come from the disk, but rather to be generated in the relativistic jet. The formation of a jet in PSR J1023+0038 has not been observed in VLBI imaging, although variable point-source emission has been seen [145]. Further, it appears that the X-ray pulsations, indicating accretion onto the neutron star surface, are intermittent [154]. Therefore it could be the case that, as discussed by [157, 166, 167, 168], the rotation-powered MSP is still at least partially active in PSR J1023+0038, and the complete disappearance of the pulsations is due to absorption by matter evaporating from the accretion disk. In this case, the principal differences from the radio MSP state discussed in the previous section would be a) the presence of additional soft photons emitted by the accretion disk and b) the shift of the shock closer to the pulsar due to the inward pressure of the disk.

The presence of additional photons from the accretion disk leads to an increase of the HE luminosity as a result of scattering of those photons on the unshocked electrons of the pulsar wind [157]. The result of the scattering of the UV photons with temperature $T = 10\,\mathrm{eV}$ on the cold relativistic electrons with Lorentz factor $\gamma = 10^4$ is shown in Figure 9.3 with a red dash-dotted line. The shift of the shock closer to the pulsar up to a distance $r = 5 \times 10^{10}\,\mathrm{cm}$ [157] will lead to the increase of the magnetic field by a factor of two in comparison to the field strength discussed in the previous section if the magnetic field is dominated by that in the pulsar wind. The resulting synchrotron and inverse-Compton emission from the shocked electrons generated in the region with $B = 80\,\mathrm{G}$ is shown in Figure 9.3 with black solid and dashed lines, respectively. The VERITAS upper limit clearly shows that the field in the region cannot be much smaller than $10\,\mathrm{G}$ (green lines in Figure 9.3). Thus the VERITAS observations before and after the source state change put limits on the minimum value of the magnetic field in a compact, synchrotron-emitting region, regardless of the precise mechanism of the charge acceleration or the source of the magnetic field.

We note that [168] have proposed pulsar magnetic field threading of the accretion disk down to the corotation radius of PSR J1023+0038 ($\sim 24\,\mathrm{km}$) as a field source for the synchrotron emission. Were this the case, the strength of the magnetic field could be much larger.

The VERITAS limits support the conclusion of the magnetically-dominated pulsar wind discussed in [143]. However, in both the MSP and accretion/LMXB states, there are alternative sources of magnetic fields that should be considered, namely that of the companion in both cases and that of the accretion disk itself in the second case. Assuming that the companion is tidally locked, observations of rapidly-rotating, low-mass stars suggest a surface magnetic field strength on the order of 1 kG [169]. The observed orbital variations may also indicate a strong, subsurface magnetic field in the companion [148].

CHAPTER 10

THE FOURTEEN PULSARS APPEARING IN ARCHIVAL VERITAS DATA

This chapter details a search for very high-energy pulsed emission from 14 pulsars incidentally appearing in archival VERITAS data. This chapter forms the basis of a VERITAS publication draft to be submitted late 2017 / early 2018. I will lead the paper and be the primary corresponding author. The analysis presented here was done in collaboration with J. Tyler (McGill University).

10.1 Introduction

Of the total population of all known pulsars, the so-called "young" pulsars are a distinct subset defined by having characteristic age $\tau < 10^9$ yr and spin period $P > 30\,\mathrm{ms}$ as seen on the P-$\dot{P}$ diagram (see Figure 2.1). The young pulsar population includes the highest spin-down-power ($\dot{E}$) pulsars and those with the highest surface magnetic field strengths. All of the young pulsars known to emit gamma-rays are rotation powered [6]; i.e., almost all of the observed radiation is a consequence of rotation[1]. Of the ~200 currently known gamma-ray pulsars[2], a little over half are classified as young.

Since the unexpected detection of the Crab pulsar in VHE gamma rays by VERITAS [3] and MAGIC [21, 4], one of the principal unanswered questions in VHE astrophysics has been whether or not the Crab pulsar is the sole VHE-emitting pulsar. The VHE spectrum of the Crab pulsar was recently measured to be consistent with a pure power law up to 1.5 TeV [4] by MAGIC, which has allowed stringent constraints to be made on the mechanism and location of the particle acceleration responsible for the emission (see Chapter 3).

---

[1] By contrast, the accretion-powered pulsars and the magnetars, which display radiation due to accretion and magnetic field decay respectively, and are not treated in this thesis.

[2] https://confluence.slac.stanford.edu/display/GLAMCOG/Public+List+of+LAT-Detected+Gamma-Ray+Pulsars

In the time since the detection of the Crab pulsar, the Vela pulsar has been recently detected at energies up to $\sim$100 GeV by H.E.S.S. II [50] with a 10–100 GeV spectrum compatible with a pure power law, though the presence of curvature cannot be ruled out. Both the Crab and Vela pulsars are members of the young gamma-ray pulsar population, and both are very highly ranked in $\dot{E}/d^2$[3], taking the number one and two spots of all known gamma-ray pulsars. Given that the Crab and Vela are the only pulsars known to emit at these high energies, a natural starting point for a search for more pulsars in the VHE band is to sort observable pulsars according to $\dot{E}/d^2$.

One of the dominant source classes detected at VHEs by IACT arrays are the pulsar wind nebulae (PWNe), which are powered by pulsars. Through PWN searches, the major IACT observatories have all accumulated a large amount of PWN data that can be probed for pulsed emission from the pulsar housed within, whether the nebula was detected or not. The majority of known gamma-ray pulsars of the highest ranks in $\dot{E}/d^2$ are located in known PWNe detected in gamma-rays or other wavelengths, meaning that many of the top $\dot{E}/d^2$ pulsars have already been incidentally observed in VHE data.

Pulsars treated in this project that VERITAS has observed while primarily targeting a PWN or supernova remnant (or other object with a pulsar in the same instrument FoV) are listed in Table 10.1, along with some properties of the pulsars. There are 14 total pulsars, which are hereafter referred to as the *archival pulsars*. This list contains eight of the top twelve pulsars located in the northern-hemisphere sky visible to VERITAS when ranked in $\dot{E}/d^2$. Two of the top twelve are the Crab and Geminga pulsars, which have already been observed by VERITAS [3, 7].

A brief synopsis of a few of the pulsars studied here is given in the following.

- PSR J0007+7303 is a radio-quiet pulsar [180] associated with the supernova remnant CTA 1, which is detected in VHE gamma rays above 500 GeV [181]. It is bright at

---

[3] I.e., pulsars can be ranked by weighting their total power output ($\dot{E}$) with distance assuming the flux falls as $1/d^2$.

Table 10.1: Table of the pulsar properties. The right ascension and declination (J2000) values given in columns 2 and 3 used in analysis are taken from the timing solutions. Columns 4 and 5 give the pulsar period P and time derivative of the period $\dot{P}$. The spin-down powers ($\dot{E}$) are given in column 6, and the pulsar distances or distance limits are given in column 7. Column 8 lists the ranking in $\dot{E}/d^2$ for the northern hemisphere, and the final column gives the VERITAS exposure time for the pulsar. Values for P, $\dot{P}$, and $\dot{E}$ have been taken from the 2PC [6], unless otherwise noted. Where a distance upper limit is quoted, the limit is the distance to the Galaxy's edge as calculated in [6].

Pulsar	R.A. (°)	Dec. (°)	P (s)	$\dot{P}$ (10^{-15})	$\dot{E}$ (10^{34} erg s^{-1})	Distance (kpc)	$\dot{E}/d^2$ Rank	VERITAS Exposure (hr)
J0007+7303	1.7565	73.0522	315.9	357.	44.8	1.4 ± 0.3 [170]	9	32.4
J0205+6449	31.4080	64.8286	65.7	190.	2644.	1.95 ± 0.04 [171]	3	22.2
J0248+6021	42.0776	60.3597	217.1	55.0	21.2	2.0 ± 0.2 [172]	11	45.9
J0357+3205	59.4680	32.0891	444.1	13.1	0.6	$0.5^{+0.4}_{-0.2}$ [173]	14	7.92
J0631+1036	97.8657	10.6165	287.8	104.	17.3	1.0 ± 0.2 [174]	10	2.79
J0633+0632	98.4339	6.5418	297.4	79.6	11.9	< 8.7	-	108
J1907+0602	286.9782	6.0374	106.6	86.7	282.	3.2 ± 0.3 [175]	8	39.1
J1954+2836	298.5798	28.6013	92.7	21.2	105.	< 18.6	-	5.18
J1958+2846	299.6667	28.7653	290.4	212.	34.2	< 18.5	-	13.9
J2021+3651	305.2726	36.8513	103.7	95.6	338.	$1.8^{+1.7}_{-1.4}$ [176]	4	58.2
J2021+4026	305.3781	40.4461	265.3	54.2	11.4	1.5 ± 0.4 [177]	12	20.6
J2032+4127	308.0548	41.4568	143.2	20.4	27.3	3.7 ± 0.6 [178]	15	47.9
J2229+6114	337.2720	61.2359	51.6	77.9	2231.	$0.80^{+0.15}_{-0.20}$ [179]	2	47.2
J2238+5903	339.6173	59.0624	162.7	97.0	88.8	< 12.4	-	32.5

GeV energies and has the second-highest spectral cut-off energy among all gamma-ray pulsars in the 2PC [6].

- PSR J0205+6449 is associated with the PWN 3C 58, which is detected at VHEs above 400 GeV [182]. It has the third-highest $\dot{E}$ of any gamma-ray pulsar in the 2PC [6].

- PSR J0357+3205 is the slowest-rotating pulsar in the 2PC [6] (though now the second-slowest currently known[4]) and also one of the nearest known pulsars at a distance of ~0.5 kpc [173]. It is notable for having a very long X-ray emission tail that extends $9'$ behind the pulsar [183]. Its estimated runaway velocity of 1900 km s^{-1} makes it one of the highest-velocity pulsars known [14].

- PSR J2021+4026 is a radio-quiet gamma-ray pulsar [184] located within the radio shell of supernova remnant G78.2+2.1 [185]. The remnant has also been detected as an extended source at VHEs by VERITAS [186]. The flux above 100 MeV from the pulsar was seen to abruptly decrease by ~20% within less than one week, which coincided with a decrease in the pulsar period time derivative, $\dot{P}$. This is currently the only such observation of intermittent behavior (also called mode switching) seen for a pulsar at gamma-ray energies [187]. The sudden change in HE flux and $\dot{P}$ are possibly due to change in the emission beaming from a shift in the magnetic field structure [187].

- PSR J2032+4127 is a pulsar that was thought to be isolated but was recently found to be in a long-period ($P =$ 45–50 yr [188]) binary system [189], orbiting a 15 $M_\odot$ Be star [190] companion. The pulsar is spatially coincident with the extended VHE gamma-ray source TeV J2032+4130, which would generally be interpreted as a PWN powered by the pulsar [191]. However, the binary nature of the system lends more

---

[4] https://confluence.slac.stanford.edu/display/GLAMCOG/Public+List+of+LAT-Detected+Gamma-Ray+Pulsars

evidence that the system may be a gamma-ray binary, though this is still yet to be firmly confirmed. PSR J2032+4127 will start its periastron approach in November 2017 [188], with coordinated multi-wavelength coverage planned across the electromagnetic spectrum.

Searches have been conducted for pulsed emission from all 14 of the pulsars appearing in archival VERITAS data, which are the first such VHE searches for each pulsar ever done before. The remainder of this chapter is structured in the following way: in Section 10.2, details of the data selection are given; in Section 10.3, the *Fermi*-LAT and VERITAS analysis methods are summarized; Section 10.4 gives the results of the searches for VHE pulsed emission; and finally in Section 10.5 we discuss these results and offer short conclusion.

10.2 Data Selection

Given that the analysis for each pulsar is done on archival VERITAS data, the total set of available VERITAS data for each pulsar varies considerably. Locations of each pulsar were taken to be those provided in the corresponding timing solution, and these coordinates are given in Table 10.1. The data selected for analysis satisfy two criteria: a) an archival pulsar is within 1.5° of the center of the instrument FoV, and b) the date the data were taken falls within the window of validity of the corresponding *Fermi*-LAT pulsar timing solution. The total set of data spans all three epochs of the VERITAS array (as described in Section 5.4). The data then underwent a quality-selection process, with the sum of all VERITAS data analyzed here constituting a total exposure time of 483.8 hr. The exposure times for each individual pulsar are given in column 2 of Table 10.3.

A total of 7.6 yr of *Fermi*-LAT data for each pulsar were analyzed. Details of the *Fermi*-LAT data selection are given in Section 6.2.

10.3 Data Analysis

The data analysis methodology specific to the archival pulsar search project is the subject of this section. Where information that has already been provided in other sections in this thesis would be repeated, reference to the appropriate section is given instead.

High-energy gamma-ray spectra are derived from the *Fermi*-LAT data for each pulsar following the procedure outlined in the 2PC [120]. Further details of the *Fermi*-LAT spectral analysis are already covered in Section 6.2 and thus omitted here.

10.3.1 Pulsar Timing and Phase Gating for the VERITAS Analysis

The regions in the pulsar light curves where signal and background counting are done, also referred to as "phase gates," were defined a priori using a method developed by colleague J. Tyler (McGill University). In short, the method utilizes pulsar light curves seen in the *Fermi*-LAT data to define the phase gates for the VERITAS search. The method attempts to define the gates in such a way that would maximize the detection significance of the VERITAS search, though there are two assumptions implicit in the method that should be stated:

- Assumption 1 – The potential VHE light curve will have the same features of the HE light curve seen in the LAT data (e.g. location and shape of the pulse peaks).
- Assumption 2 – The VHE flux of the pulsar in question is $\sim$1% of the Crab pulsar flux.

If the first assumption is not true, then the search for pulsed emission will be less sensitive[5]. However, any method for defining the phase gates for a discovery search comes down to what is essentially a guess, since only the Crab pulsar has been firmly detected at VHEs.

---

[5] Or possibly not sensitive at all. For that reason, we also use the *H* test to search for pulsed emission in case the phase gates are incorrectly defined. See Section 7.3.1.

The method for defining the phase gates for the search for pulsations from the archival pulsars comprises the following steps:

1. Determine signal and background event rates for the Crab Nebula using cuts optimized for a 1% Crab Nebula source.
2. Multiply by source exposure time to get N_{on} and αN_{off}, then find $N_{\text{excess}} = N_{\text{on}} - \alpha N_{\text{off}}$.
3. Scale the Crab Nebula excess by 0.01 to mimic a 1% Crab Nebula source.
4. Obtain the pulse profile from the 2PC for the pulsar in question and subtract the lowest bin in the profile from all bins to remove the background.
5. Normalize the pulse profile from the previous step and multiply each bin by the scaled excess found in step 3.
6. Add the estimated background expected in a VERITAS observation to the profile by adding $\alpha N_{\text{off}}/N_{\text{bins}}$ to each bin, where N_{bins} is the total number of bins.
7. Calculate the significance (using Equation 7.1) corresponding to all non-overlapping phase gate combinations (including a background gate). The phase gates selected for the VERITAS analysis are those where this significance is maximized.

The results of the above procedure are shown visually in Figure 10.1, and phase-gate definitions are given in numerical form in Table 10.2.

Where possible, the latest publicly available timing solutions are used in the VERITAS analysis, which are more up-to-date than the ones in the 2PC. The use of different timing solutions to fold the data for a pulsar in most cases introduces a phase offset, which must be accounted for. To determine the phase offsets for the 14 archival pulsars, a *Fermi*-LAT data set for each pulsar is phase-folded using both the 2PC and the latest timing solutions. The resulting light curves are then cross-correlated, and the point where the correlation

Table 10.2: Table of the phase gate and phase offset definitions. Columns 2 and 3 give the gate definitions for the peak locations P1 and P2, respectively. Column 4 gives the background phase-gate definitions. Column 5 lists the phase offsets between the used timing solutions and those appearing in the 2PC, which were used to calculate the phase gates.

Pulsar	P1	P2	Background	Phase Offset
J0007+7303	0.05–0.36	None	0.41–0.01	0.9275
J0205+6449	0.04–0.11	0.51–0.59	0.60–0.04	0.8545
J0248+6021	0.28–0.50	None	0.54–0.24	0.033
J0357+3205	0.02–0.24	None	0.33–0.96	0.003
J0631+1036	0.36–0.54	None	0.64–0.24	0.023
J0633+0632	0.56–0.60	0.09–0.16	0.63–0.06	0.0145
J1907+0602	0.52–0.62	0.19–0.27	0.64–0.15	0.002
J1954+2836	0.52–0.58	0.08–0.16	0.64–0.02	0.0125
J1958+2846	0.46–0.58	0.10–0.12	0.62–0.08	0.0135
J2021+3651	0.58–0.62	0.11–0.15	0.66–0.07	0.0355
J2021+4026	0.00–0.16	0.50–0.66	0.20–0.48	0.9505
J2032+4127	0.60–0.62	0.09–0.13	0.64–0.04	0.1585
J2229+6114	0.38–0.53	None	0.59–0.15	0.9365
J2238+5903	0.59–0.62	0.09–0.13	0.64–0.06	0.4355

coefficient is maximized is taken to be the offset in phase. The resulting offset for each pulsar is given in Table 10.2. A phase offset of 0 in Table 10.2 indicates that the 2PC timing solution is the latest (and thus the one used in the VERITAS analysis), meaning computation of an offset was not required.

10.3.2 VERITAS Data Analysis

The steps of the general VERITAS data analysis chain are the subject of Section 6.3. After the VERITAS data are processed through the standard analysis pipeline, the data are phase folded with the appropriate timing solution. Pulsar timing and phase folding are described in more detail in Section 6.1. Details specific to the archival pulsar project are given in this section.

A total of six tests (trials factor of six) are applied to the data for each pulsar. Three sets of cuts are used for each individual analysis, with each set tuned to optimize sensitivity for different spectral shapes varying from softer to harder. The set of cuts applied to the

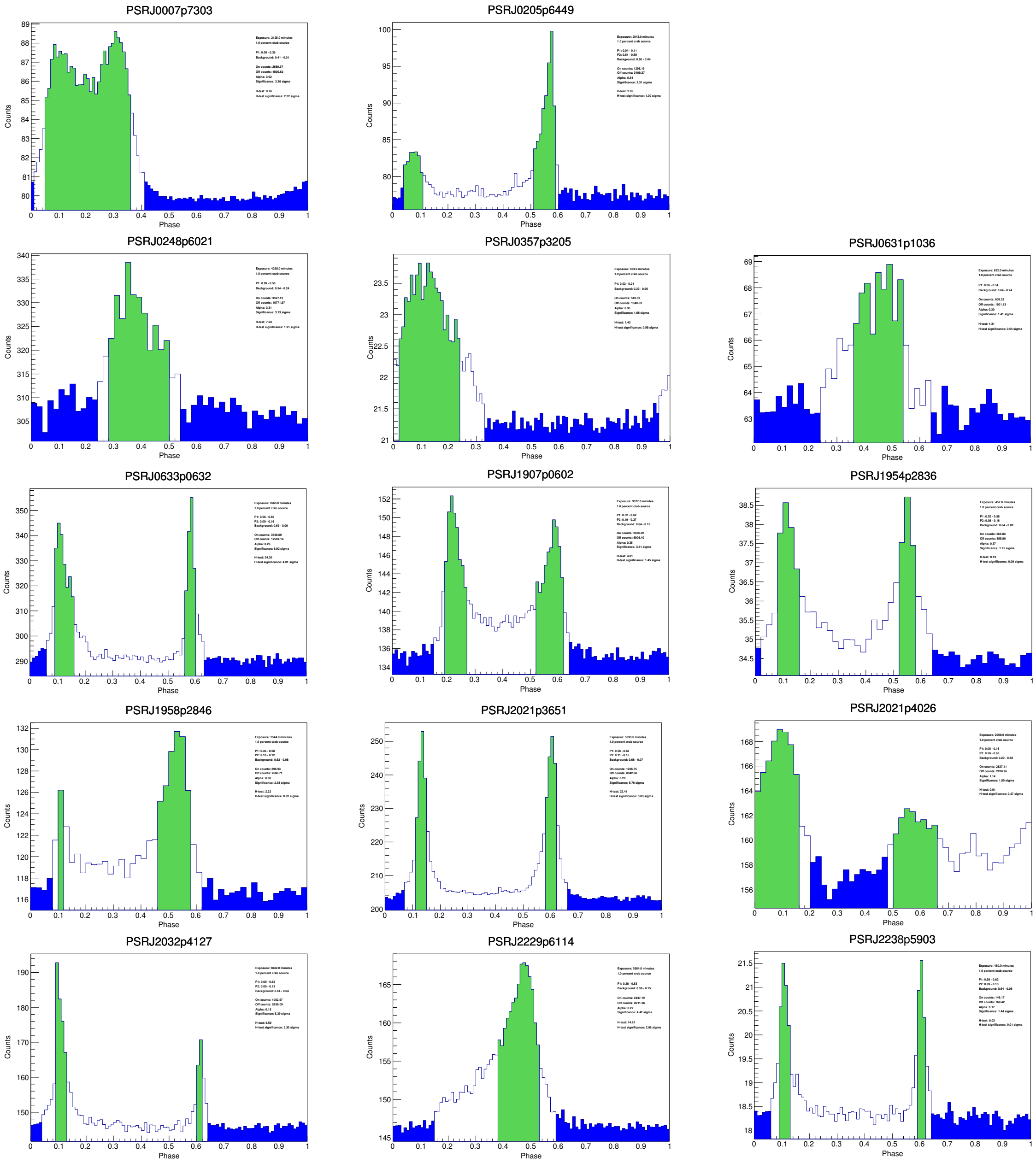

Figure 10.1: Phase-gate definitions for all 14 pulsars appearing in archival VERITAS data. The ON-counting regions, corresponding to the locations of P1 and P2, are shown in green, and the OFF-counting background region is shown in blue. Figure created by J. Tyler (McGill University).

data are referred to as *soft*, *moderate*, and *hard* and are given in Table 6.2. Details of the of the procedure that yields these cut values are given in Section 6.3.4. For each set of cuts, two independent tests for a pulsed signal in the phase-folded VERITAS data are applied.

The first test uses the a-priori-defined expected signal and background regions (henceforth referred to as the "phase-gate test") described in Section 10.3.1. The significance is calculated by counting N_{on} and N_{off} in the gated phase regions and using equation 7.1. For the second test, the H test to the un-binned phase data, which has the advantage that no a-priori knowledge of expected peaks in the light curves are needed (see Section 7.3.1). The total number of tests (and thus trials) is, therefore, six per pulsar search (three sets of cuts with two tests for signal each for a total of six tests).

10.4 Results

The six tests did not result in the detection of VHE pulsations from any of the 14 archival pulsars. The distribution of significances from equation 7.1 in the phase-gate test has minimum and maximum values of -1.93σ and $+1.86\sigma$, respectively. From the *H* test, the maximum *H* statistic is 4.29, which corresponds to a chance probability of 0.18. All tests applied to the data therefore failed to reveal any evidence for pulsed emission in the VERITAS data. Significances and *H* statistics for each pulsar are given in Table 10.3, and significance distributions from the phase-gate test are shown in Figure 10.2.

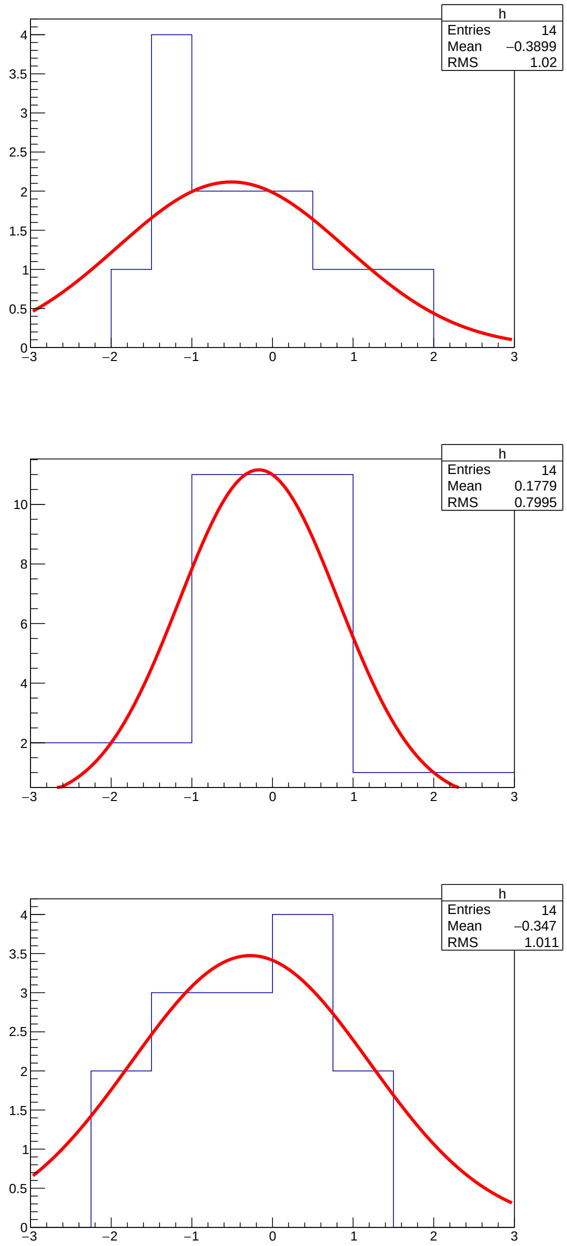

Figure 10.2: Significance distributions between $\pm 3\sigma$ from the phase-gate test for soft (*top*), moderate (*middle*), and hard (*bottom*) cuts. Each distribution is fitted with a Gaussian (red curve), and all are consistent with being normally distributed.

For each of the six searches for pulsed emission, integral VHE flux upper limits from the VERITAS data are computed at the 95% confidence level. For the phase-gate test results for each set of cuts, the method of Rolke [79] is used to set an upper limit on the excess counts, which is converted into an integral flux UL by dividing by the exposure. For the results from the *H* test, an integral flux UL is set using the method summarized in section 7.4. A spectral index of 3.8 is assumed for all upper limit calculations, which is the same index as seen for the Crab pulsar in [3]. Six 95% CL flux ULs per pulsar are therefore calculated, which are given in Table 10.3.

The *Fermi*-LAT pulsar spectra derived from 7.6 yr of data, along with VHE energy flux ULs, are shown in Figures 10.17–10.30. The Crab pulsar bowtie from [3] and the Crab Nebula spectral shape from [192] scaled by 1% are also shown to help indicate the relative strength of the limits. The *Fermi*-LAT spectra are all consistent with those reported in the 2PC [6]. For both PSR J0007+7303 and PSR J2021+4026, sufficient spectral points are reconstructed to enable fitting a power law above an energy threshold of 10 GeV. This power-law fit is intended to help indicate whether or not a power-law extension of the spectrum from HEs to VHEs is possible, as has been seen for the Crab and possibly Vela pulsars. Only the flux UL for PSR J2021+4026 (hard cuts; Rolke method) constrains the possible power-law extension fitted for these two pulsars.

10.4.1 The PSR J2238+5903 Observation Campaign

In addition to the archival VERITAS data used in the search for pulsations from PSR J2238+5903, additional data was taken due to a minor hint of a signal in the preliminary analysis results. In the results of the analysis of $\sim$10 hr of quality-selected archival PSR J2238+5903 data taken in the 2013/2014 observing season, a 2.4σ hint of pulsed emission was seen in the moderate-cuts analysis. This prompted follow-up observations in the fall of 2015, which resulted in the accumulation of a further 8.3 hr exposure and an increase in the medium-cuts significance to 2.8σ. Based on the signal increase after roughly doubling the data set, a request for director's discretionary time was approved for an additional observations, which were completed in fall 2015. In the final analysis of 32.5 hr of observations, the moderate-cuts significance fell to 1.9σ. The observational campaign was then discontinued. Throughout the fall of 2015, updated timing solutions were required to phase-fold the new data, since it was collected after the period of validity of the publicly available *Fermi*-LAT-derived solution. Updated timing solutions were computed by M. Kerr (ATNF) of the *Fermi*-LAT collaboration using LAT data contemporaneous with the newly obtained VERITAS data. The method used for generating updated timing solutions derived from the LAT data is given in [120].

Table 10.3: Results for the 14 pulsars appearing in archival VERITAS data. Each pulsar has three sets of results, one for each set of cuts applied to the data. Column 2 lists the exposure time for each pulsar, copied here from Table 10.1 for convenience. Column 3 specifies the set of cuts used in the analysis. Column 4 gives the lower energy threshold for the analysis in GeV. Columns 5 and 6 give the phase-gate test significance and *H* statistic, respectively. Integral flux upper limits at the 95% CL from the *H* test and the Rolke method are given in columns 7 and 8, respectively.

Pulsar	Exposure Time (hr)	Cut Type	Energy Threshold (GeV)	Significance	*H* Statistic	*H*-Test Flux UL ($10^{-9}\,\mathrm{m}^{-2}\,\mathrm{s}^{-1}$)	Rolke Flux UL ($10^{-9}\,\mathrm{m}^{-2}\,\mathrm{s}^{-1}$)
J0007+7303	32.4	soft	316	–1.74	4.32	16.7	1.24
		moderate	457	–0.95	2.37	6.20	2.48
		hard	1050	–0.51	3.15	1.38	0.767
J0205+6449	22.2	soft	240	–1.29	1.28	13.7	2.77
		moderate	347	–1.11	3.29	7.63	1.63
		hard	501	–1.40	3.94	4.12	0.575
J0248+6021	45.9	soft	219	0.00	3.26	19.4	11.0
		moderate	288	0.85	3.69	10.7	8.65
		hard	603	0.44	1.34	1.9	1.72
J0357+3205	7.92	soft	138	–0.47	0.74	33.6	20.9
		moderate	200	–0.17	0.32	10.7	10.1
		hard	380	0.12	2.36	5.26	4.01
J0631+1036	2.79	soft	151	–1.27	3.61	79.4	13.9
		moderate	219	0.81	0.56	18.2	22.2
		hard	457	–1.07	1.44	7.44	2.44
J0633+0632	108	soft	182	–1.37	3.66	8.92	1.00
		moderate	263	0.41	0.32	1.95	1.59
		hard	501	0.70	4.80	1.01	0.523
J1907+0602	39.1	soft	182	–1.49	1.60	11.7	1.72
		moderate	263	0.36	10.4	7.72	3.72
		hard	550	–0.15	2.60	1.73	0.953
J1954+2836	5.18	soft	126	1.07	7.01	68.4	40.3
		moderate	200	0.58	2.46	19.3	14.0
		hard	288	–1.50	0.60	8.24	1.48
J1958+2846	13.9	soft	126	–0.70	1.62	24.9	8.62
		moderate	182	–1.24	0.82	9.49	2.24
		hard	263	–1.54	3.00	6.81	0.658
J2021+3651	58.2	soft	151	–0.56	9.46	25.4	4.53
		moderate	219	0.25	2.28	7.23	2.96
		hard	417	0.95	6.46	2.48	1.06
J2021+4026	20.6	soft	166	0.18	0.73	24.1	32.1
		moderate	240	0.15	3.28	15.0	13.8
		hard	457	–1.93	2.42	4.68	0.0615
J2032+4127	47.9	soft	166	–0.37	0.34	10.9	4.07
		moderate	219	0.58	4.29	10.4	3.56
		hard	457	0.42	2.00	2.22	0.974
J2229+6114	47.2	soft	240	0.72	0.30	8.75	9.41
		moderate	316	0.19	0.58	5.28	4.07
		hard	661	–0.75	2.35	1.97	0.648
J2238+5903	32.5	soft	182	1.86	1.93	12.1	8.48
		moderate	288	1.79	0.42	3.27	3.32
		hard	417	1.37	1.10	2.13	1.66

10.4.2 Pulse Profiles from the VERITAS Data

The pulsar light curves obtained by phase folding the VERITAS data for each of the 14 archival pulsars are shown in this section beginning on the next page. Each figure shows the P1 and P2 phase gates from Table 10.2 in green, with the background gate shown in gray. The inset text box gives N_{on}, αN_{off}, N_{excess}, and the significance from Equation 7.1 in that order from top to bottom.

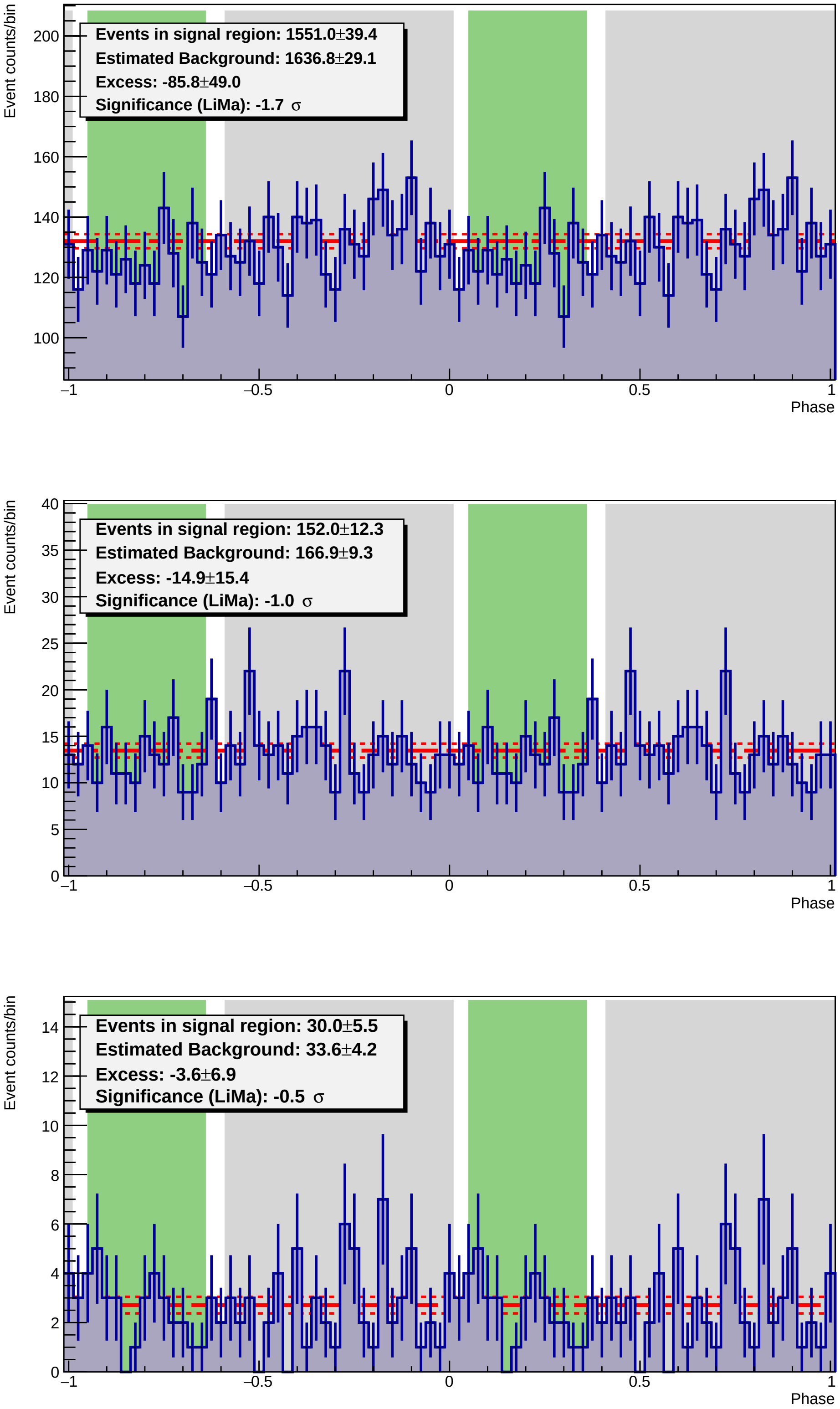

Figure 10.3: Pulse profiles of **PSR J0007+7303** from VERITAS data for soft cuts (top panel), moderate cuts (middle panel), and hard cuts (bottom panel).

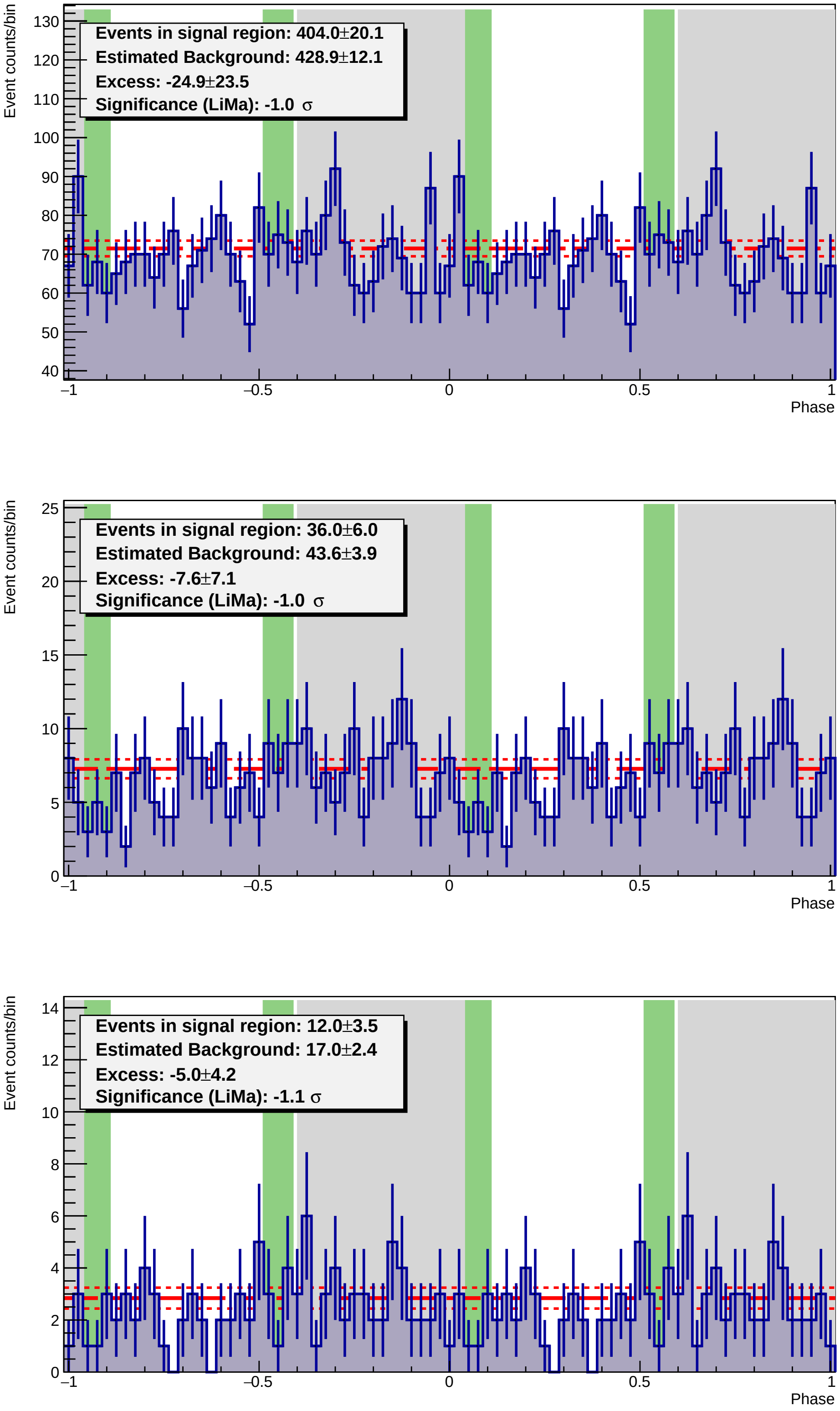

Figure 10.4: Pulse profiles of **PSR J0205+6449** from VERITAS data for soft cuts (top panel), moderate cuts (middle panel), and hard cuts (bottom panel).

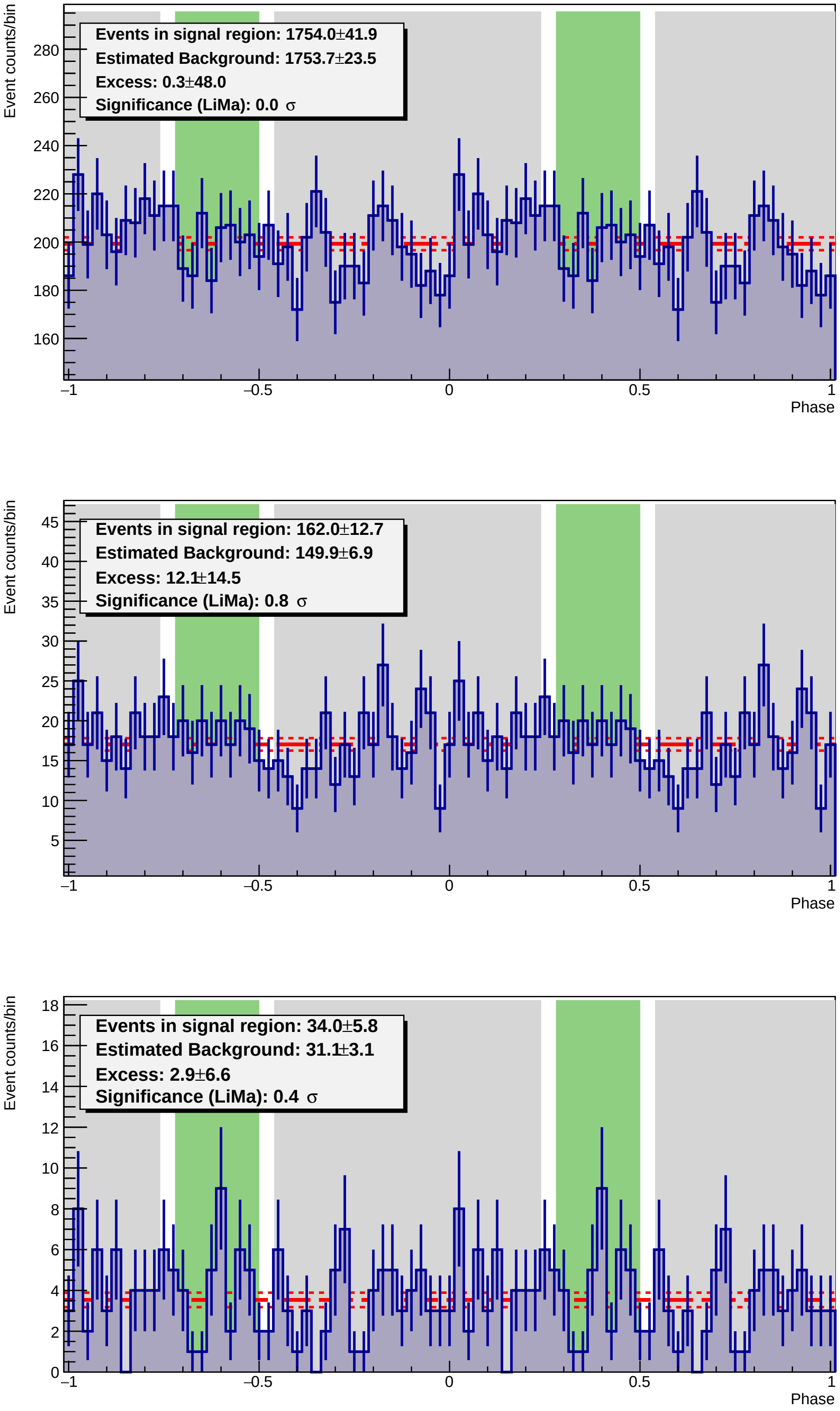

Figure 10.5: Pulse profiles of **PSR J0248+6021** from VERITAS data for soft cuts (top panel), moderate cuts (middle panel), and hard cuts (bottom panel).

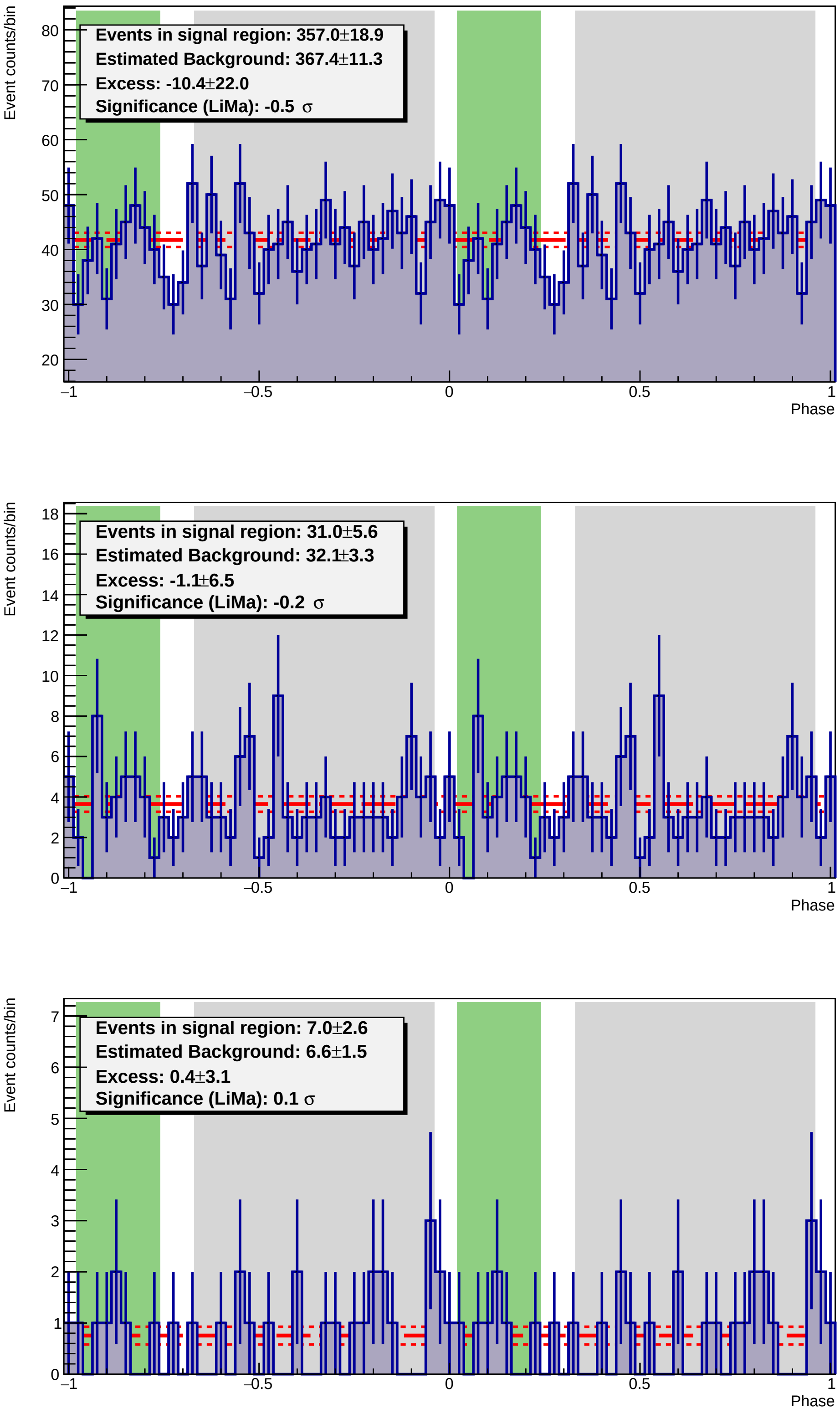

Figure 10.6: Pulse profiles of **PSR J0357+3205** from VERITAS data for soft cuts (top panel), moderate cuts (middle panel), and hard cuts (bottom panel).

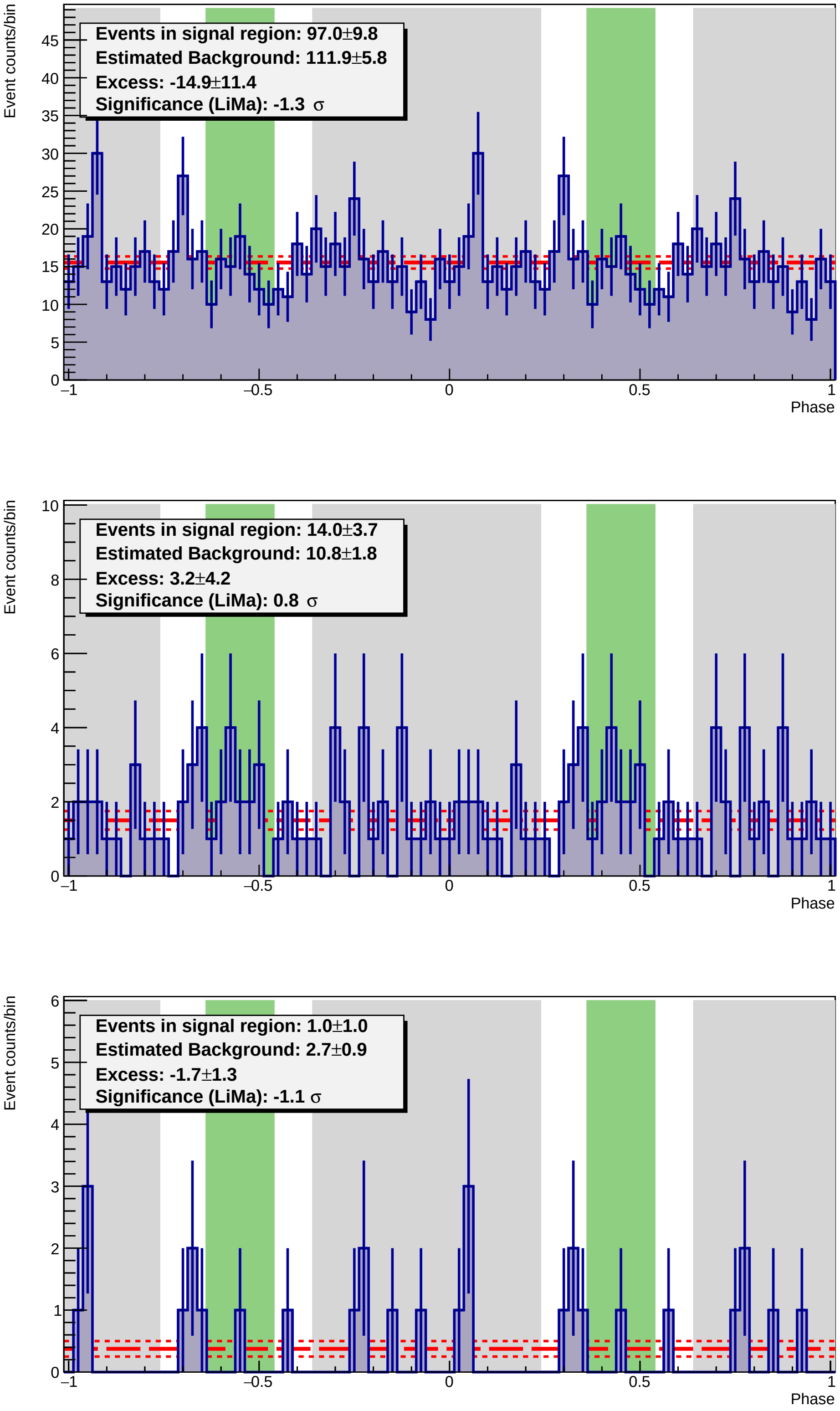

Figure 10.7: Pulse profiles of **PSR J0631+1036** from VERITAS data for soft cuts (top panel), moderate cuts (middle panel), and hard cuts (bottom panel).

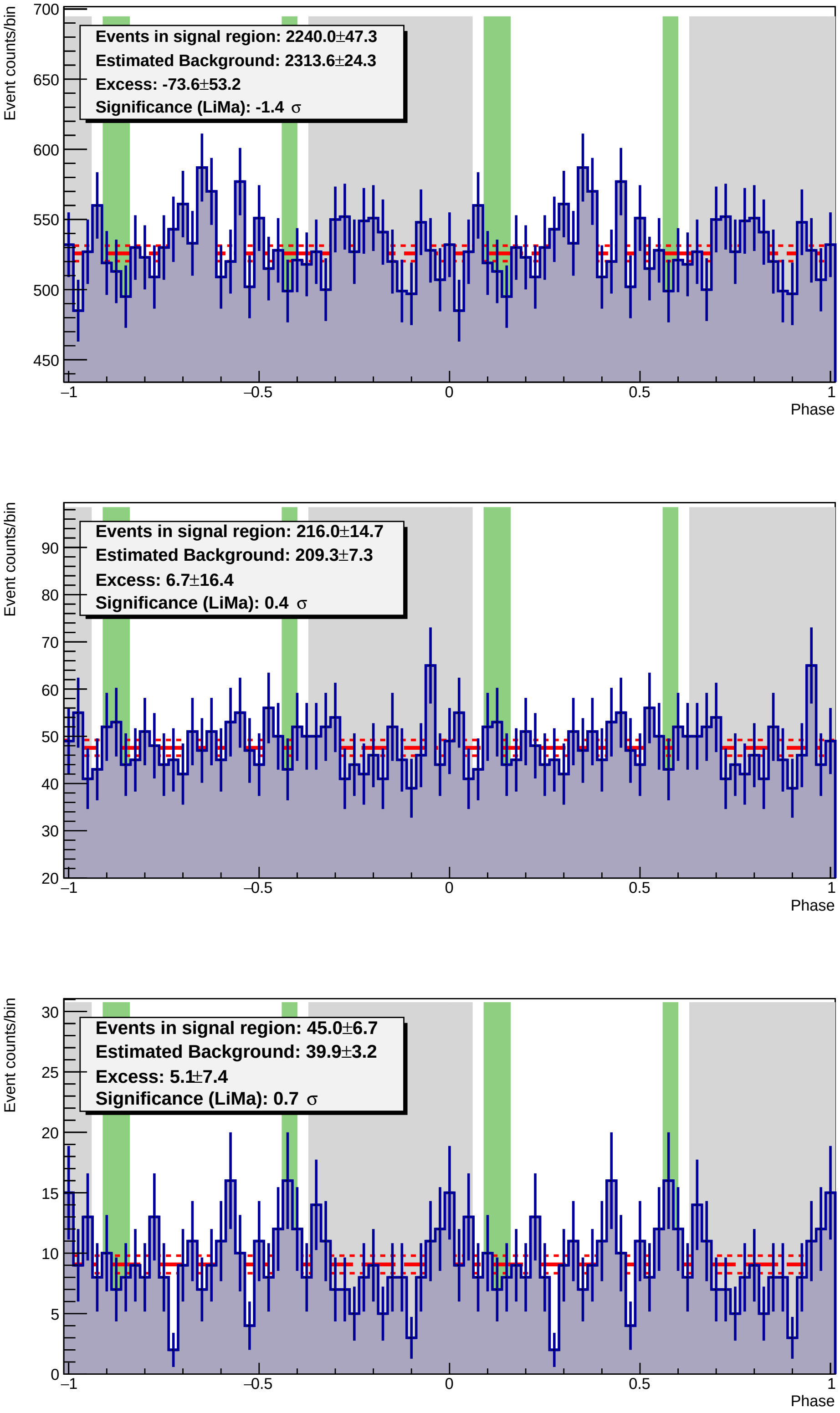

Figure 10.8: Pulse profiles of **PSR J0633+0632** from VERITAS data for soft cuts (top panel), moderate cuts (middle panel), and hard cuts (bottom panel).

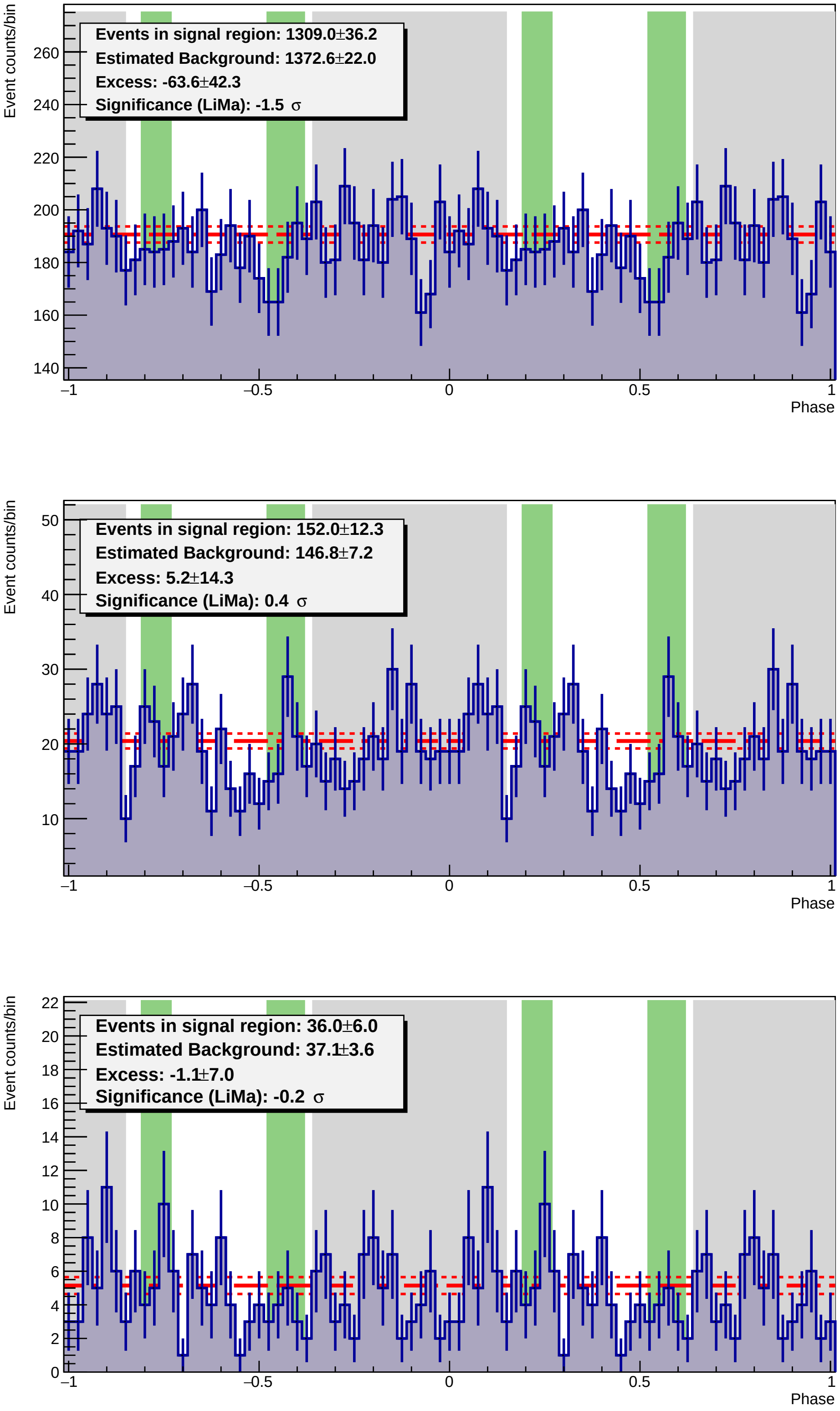

Figure 10.9: Pulse profiles of **PSR J1907+0602** from VERITAS data for soft cuts (top panel), moderate cuts (middle panel), and hard cuts (bottom panel).

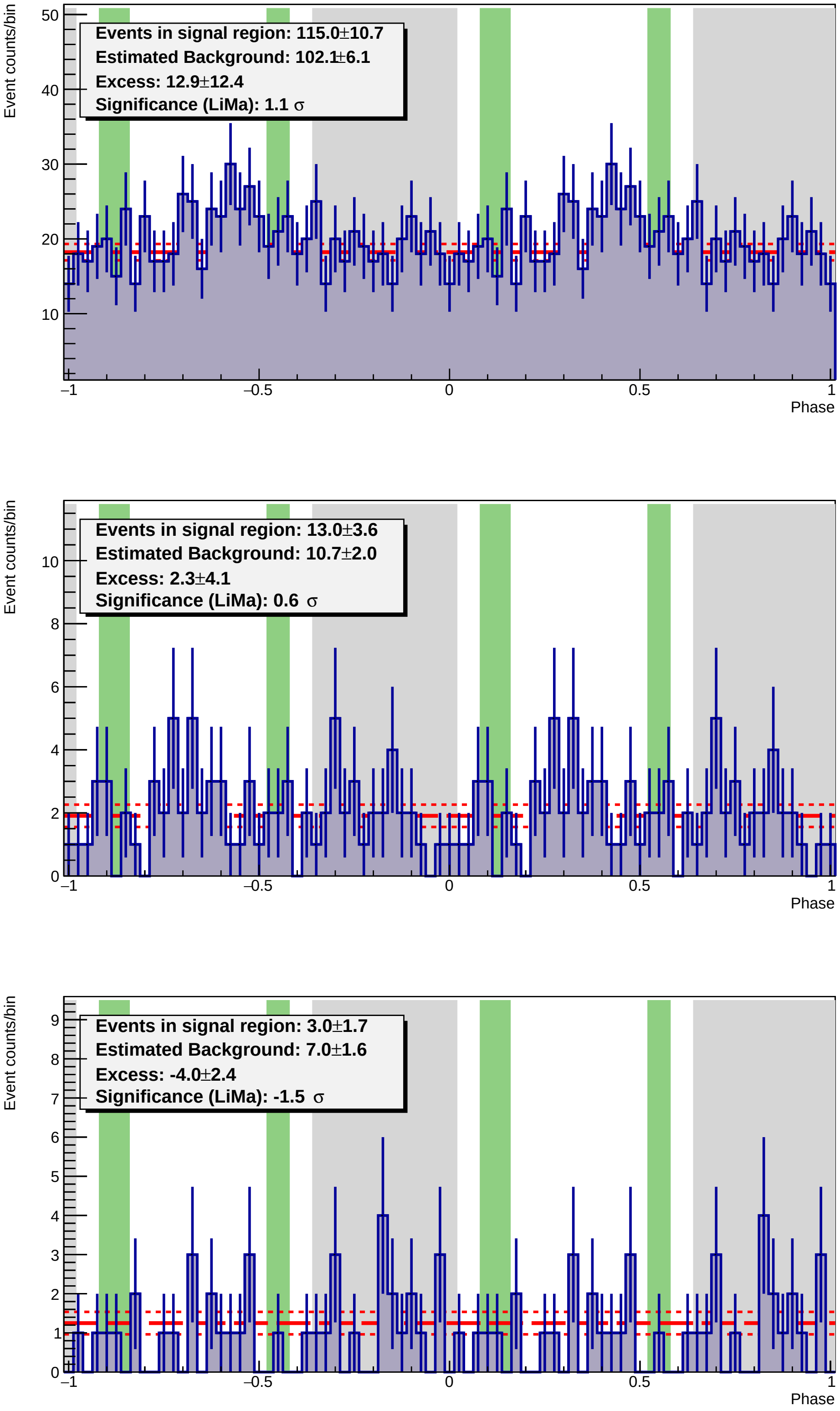

Figure 10.10: Pulse profiles of **PSR J1954+2836** from VERITAS data for soft cuts (top panel), moderate cuts (middle panel), and hard cuts (bottom panel).

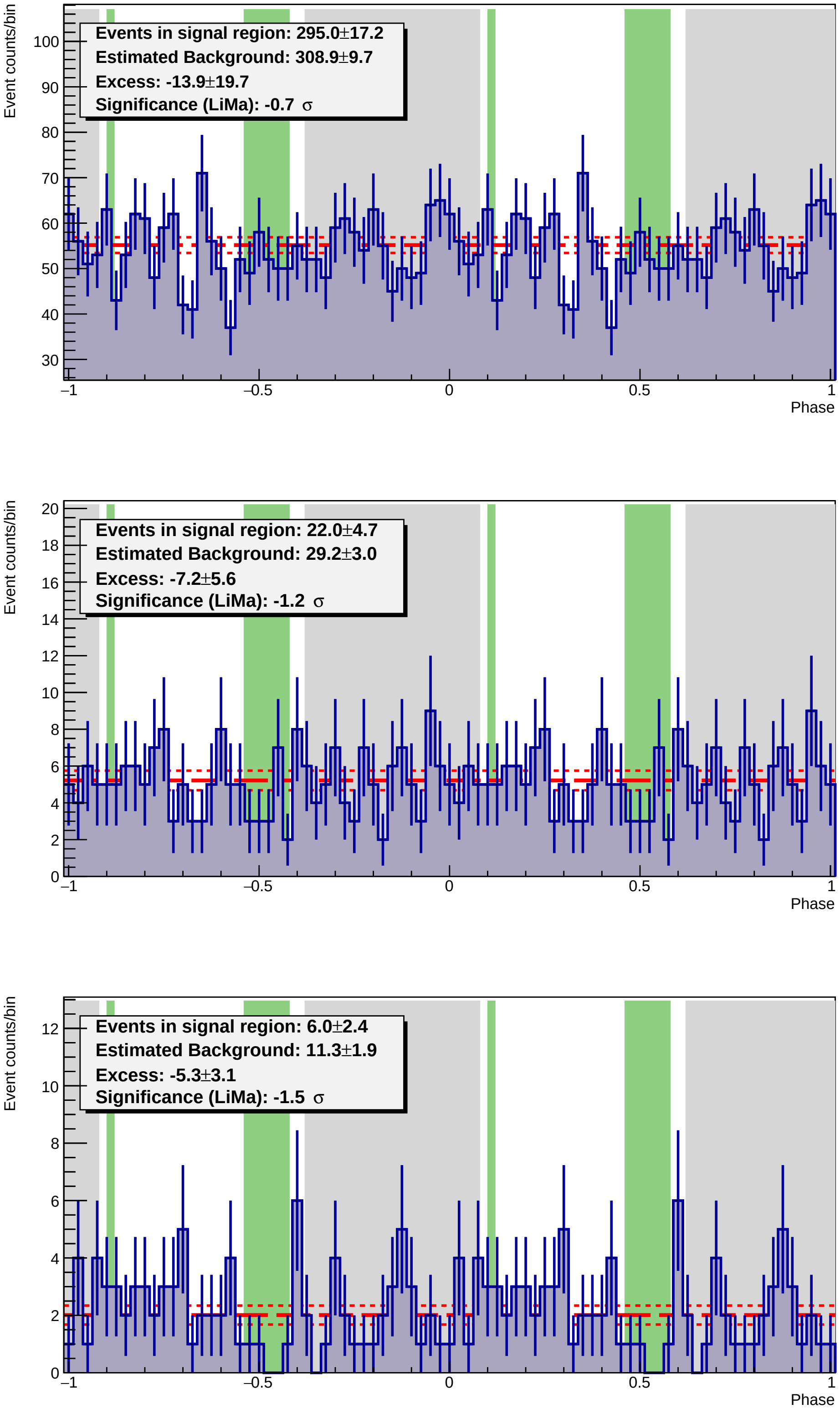

Figure 10.11: Pulse profiles of **PSR J1958+2846** from VERITAS data for soft cuts (top panel), moderate cuts (middle panel), and hard cuts (bottom panel).

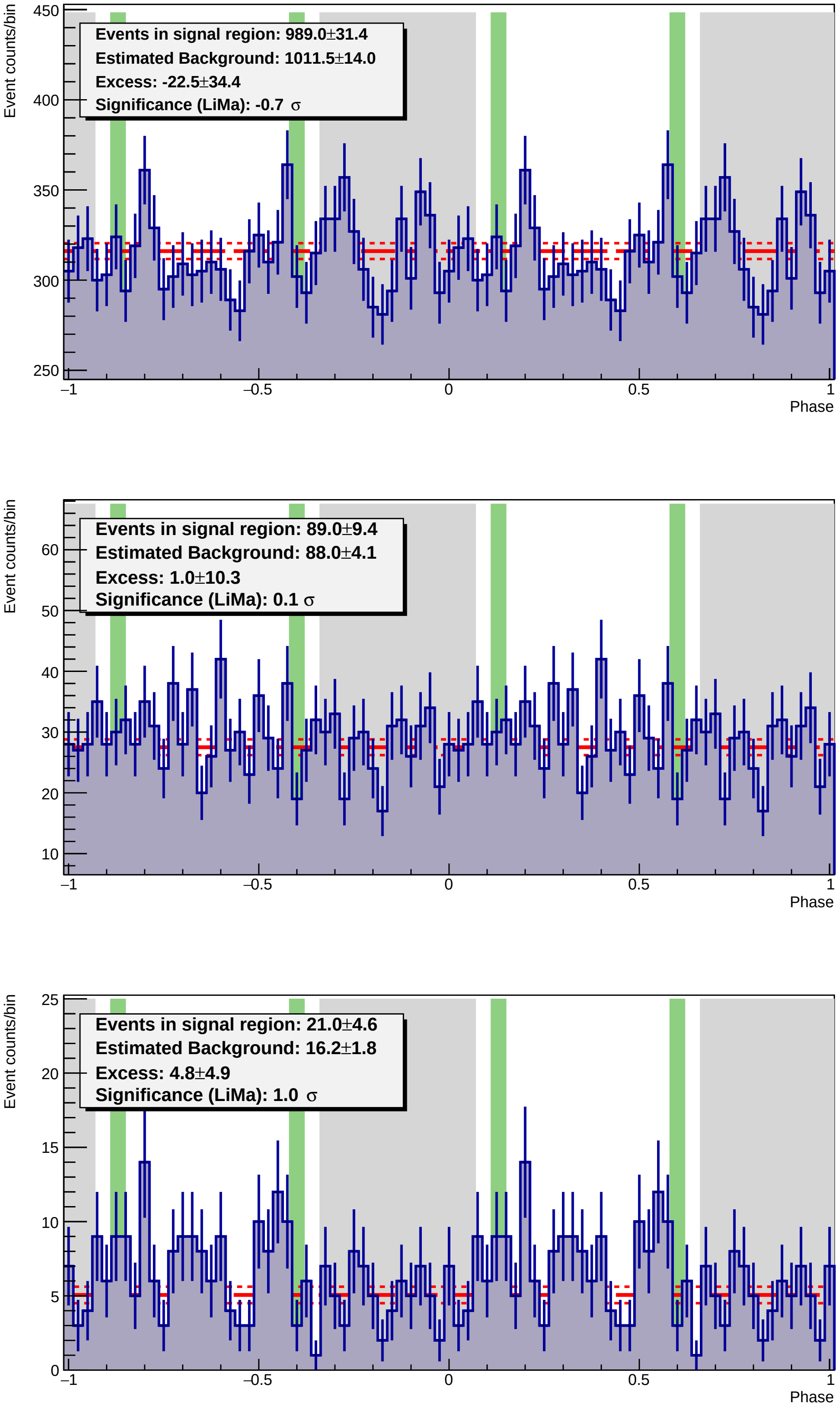

Figure 10.12: Pulse profiles of **PSR J2021+3651** from VERITAS data for soft cuts (top panel), moderate cuts (middle panel), and hard cuts (bottom panel).

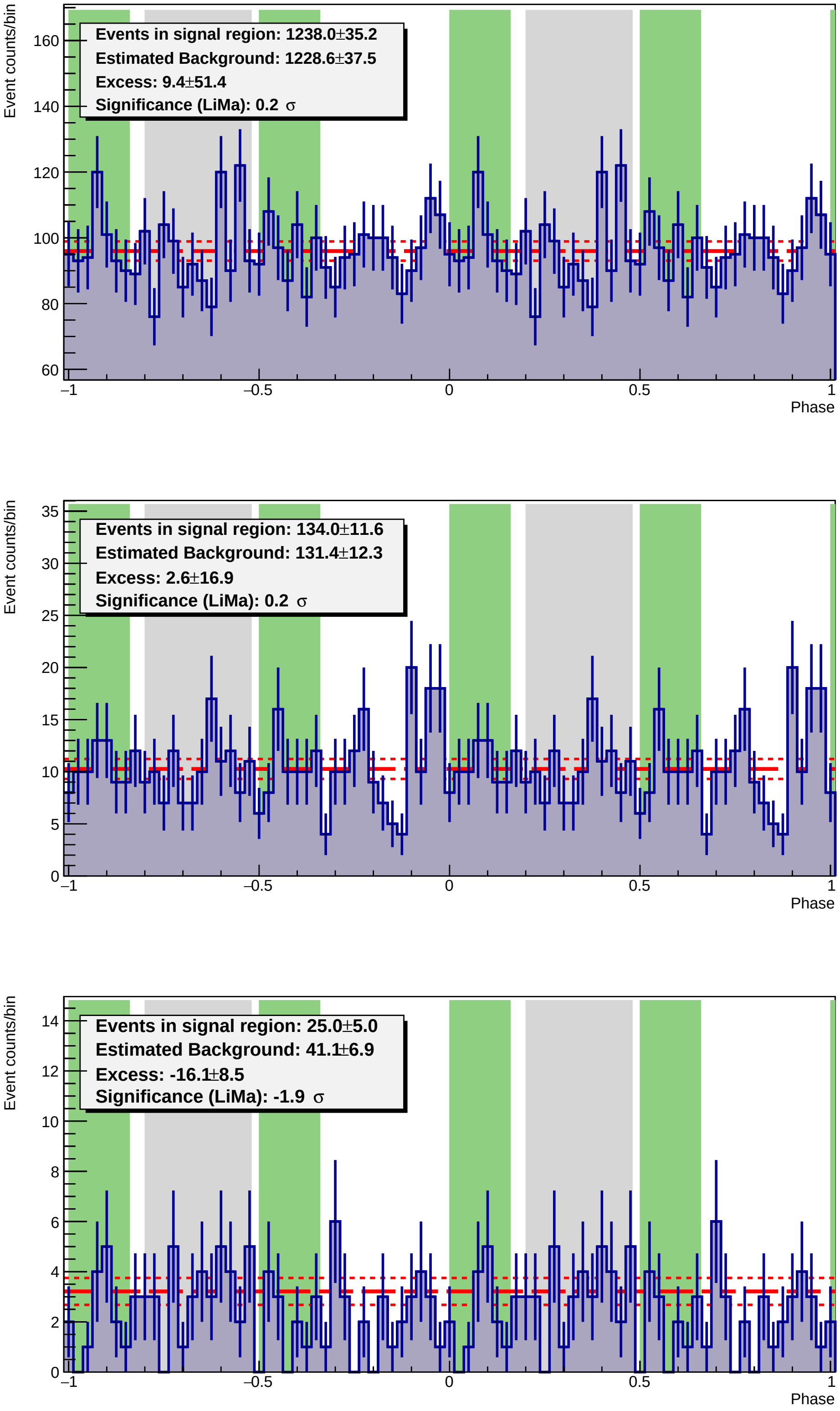

Figure 10.13: Pulse profiles of **PSR J2021+4026** from VERITAS data for soft cuts (top panel), moderate cuts (middle panel), and hard cuts (bottom panel).

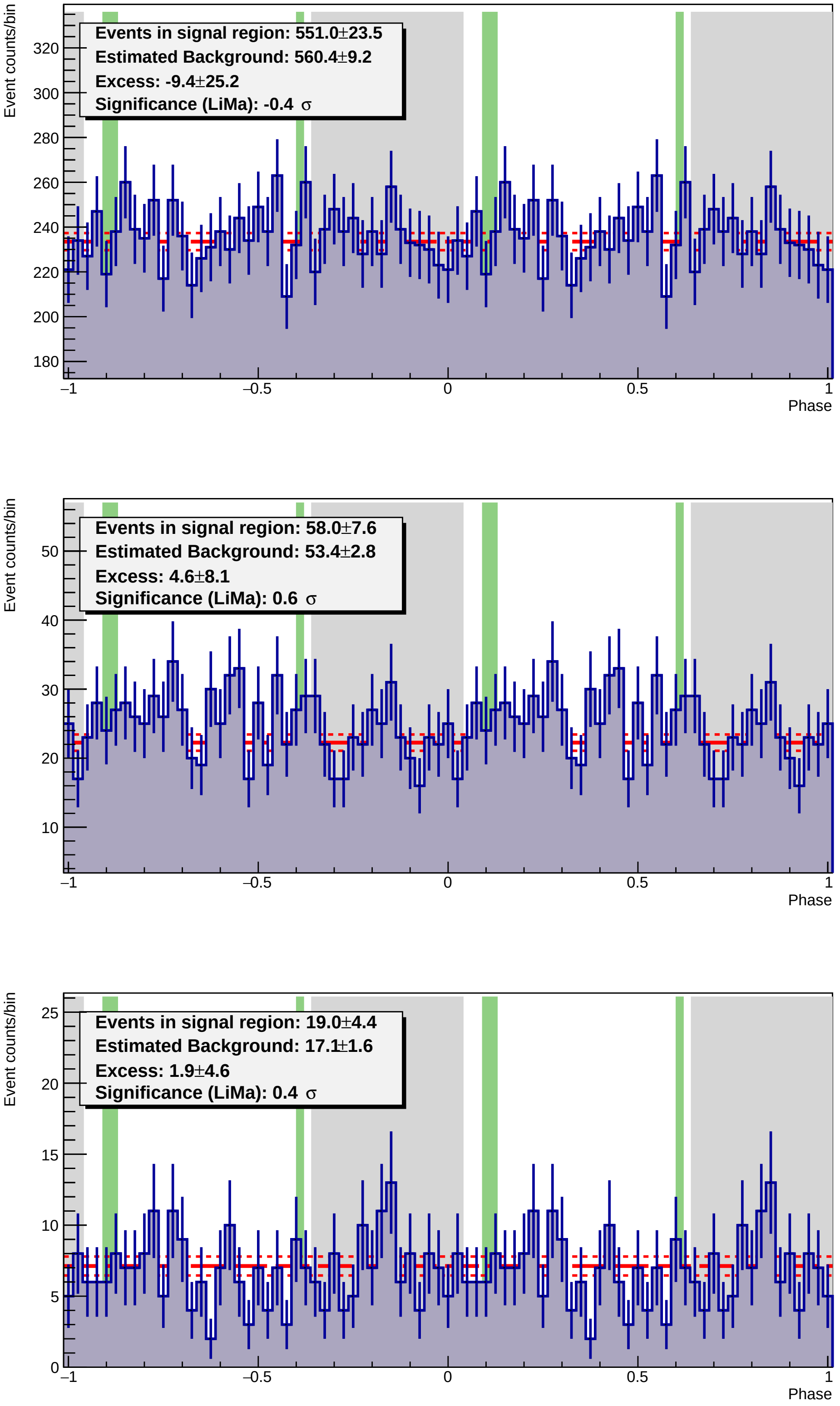

Figure 10.14: Pulse profiles of **PSR J2032+4127** from VERITAS data for soft cuts (top panel), moderate cuts (middle panel), and hard cuts (bottom panel).

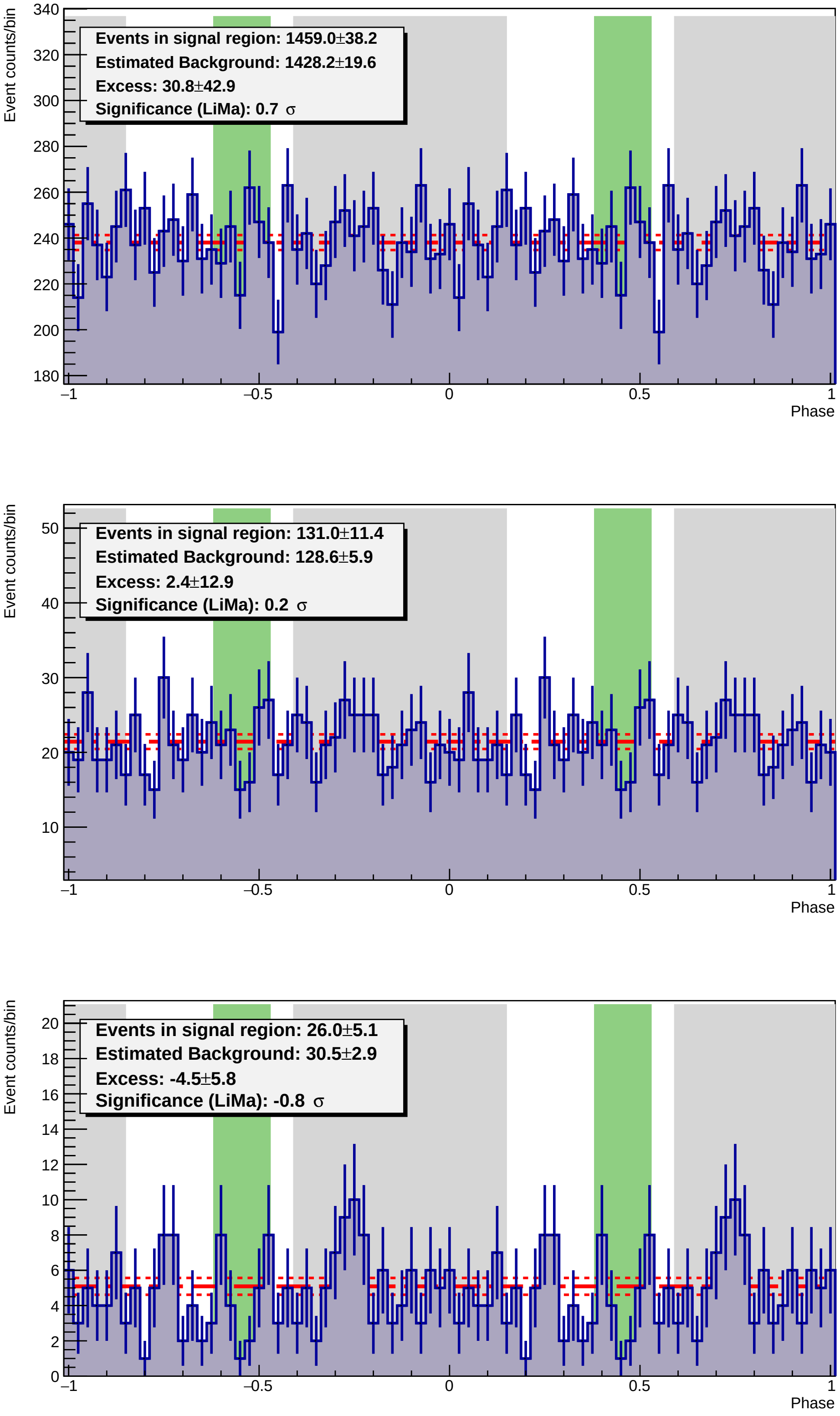

Figure 10.15: Pulse profiles of **PSR J2229+6114** from VERITAS data for soft cuts (top panel), moderate cuts (middle panel), and hard cuts (bottom panel).

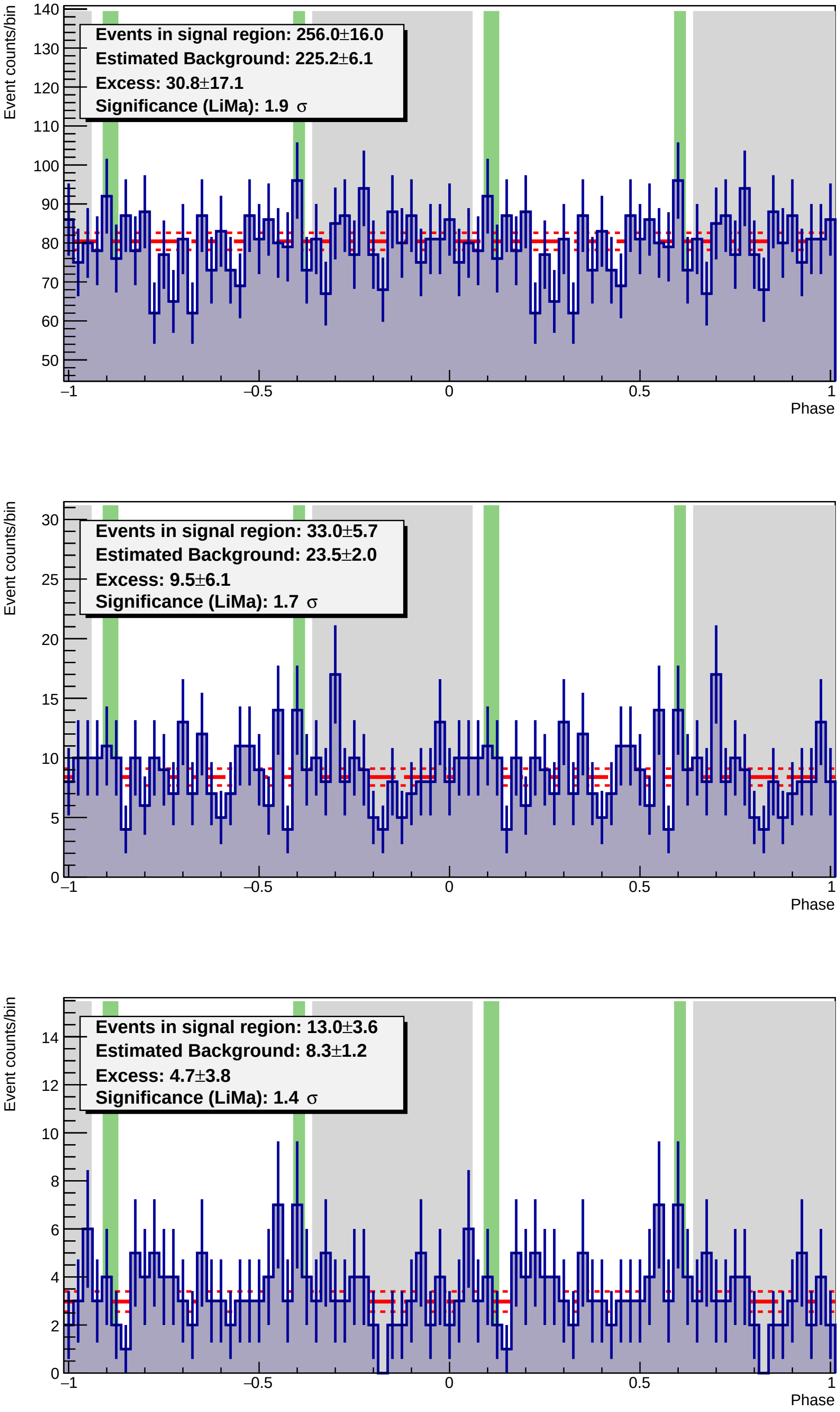

Figure 10.16: Pulse profiles of **PSR J2238+5903** from VERITAS data for soft cuts (top panel), moderate cuts (middle panel), and hard cuts (bottom panel).

10.4.3 *Fermi*-LAT Spectra with VERITAS Limits

The *Fermi*-LAT spectra derived for each pulsar, along with the VERITAS VHE flux upper limits, are presented in this section. The *Fermi* spectral points are shown in black; the VERITAS 95% CL flux ULs from the *H* test are indicated by the red arrows; while those from the method of Rolke from the phase-gate test are given by the blue arrows. For reference, the Crab pulsar spectral bowtie from [3] is also shown (gray shaded region), in addition to the Crab Nebula spectral shape from [192] scaled to 1% (black curved line). For the two pulsars J0007+7303 and J2021+4026, a power-law fit above 10 GeV is given by the black dashed line.

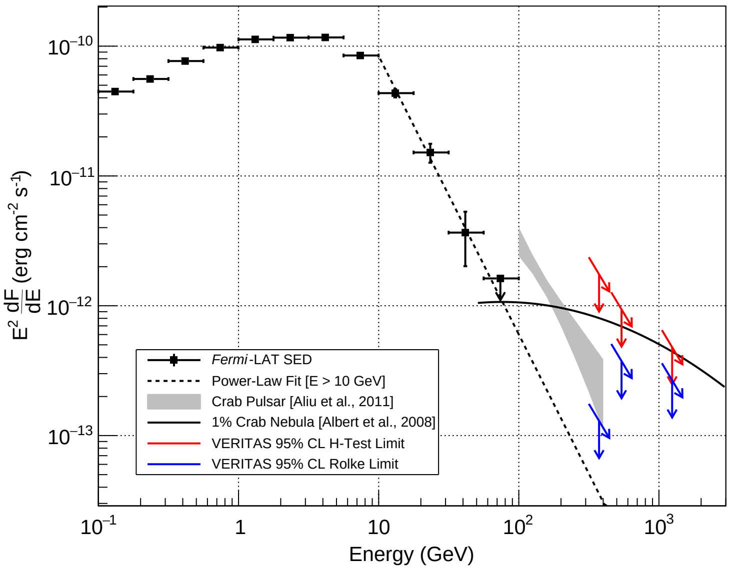

Figure 10.17: **PSR J0007+7303** *Fermi*-LAT spectrum (black squares) with VERITAS flux upper limits (red and blue arrows). A power-law fit to the *Fermi* data above 10 GeV is given by the black dashed line.

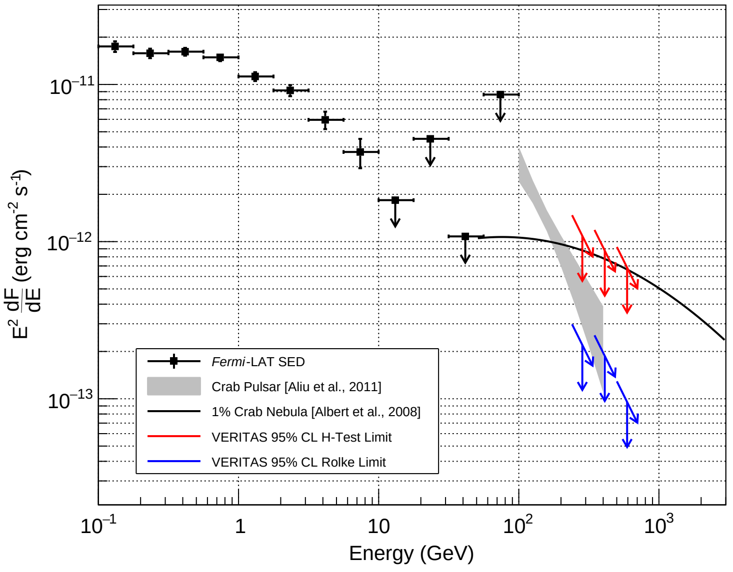

Figure 10.18: **PSR J0205+6449** *Fermi*-LAT spectrum (black squares) with VERITAS flux upper limits (red and blue arrows).

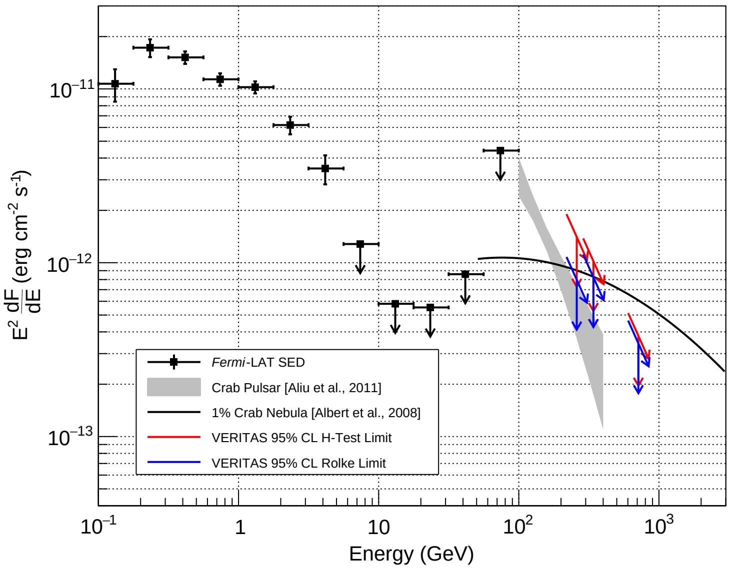

Figure 10.19: **PSR J0248+6021** *Fermi*-LAT spectrum (black squares) with VERITAS flux upper limits (red and blue arrows).

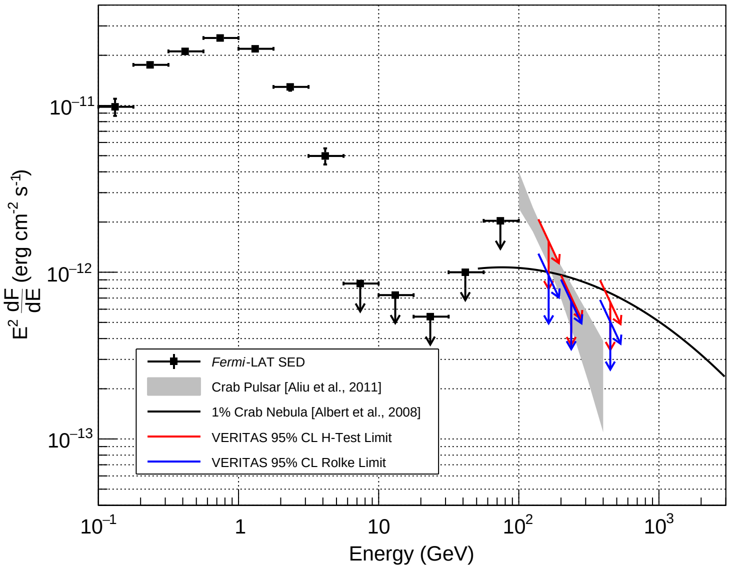

Figure 10.20: **PSR J0357+3205** *Fermi*-LAT spectrum (black squares) with VERITAS flux upper limits (red and blue arrows).

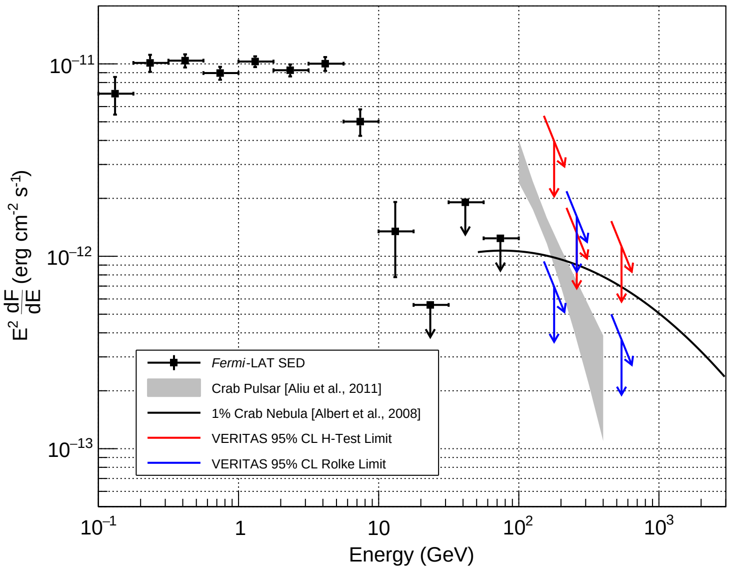

Figure 10.21: **PSR J0631+1036** *Fermi*-LAT spectrum (black squares) with VERITAS flux upper limits (red and blue arrows).

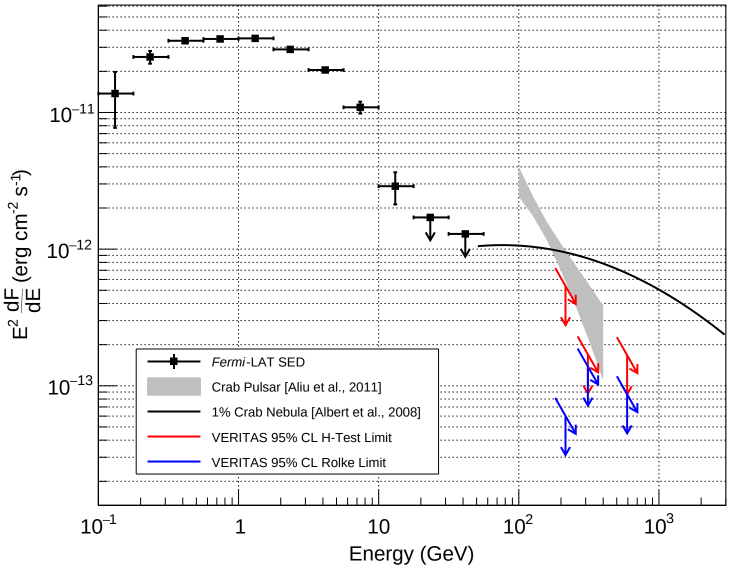

Figure 10.22: **PSR J0633+0632** *Fermi*-LAT spectrum (black squares) with VERITAS flux upper limits (red and blue arrows).

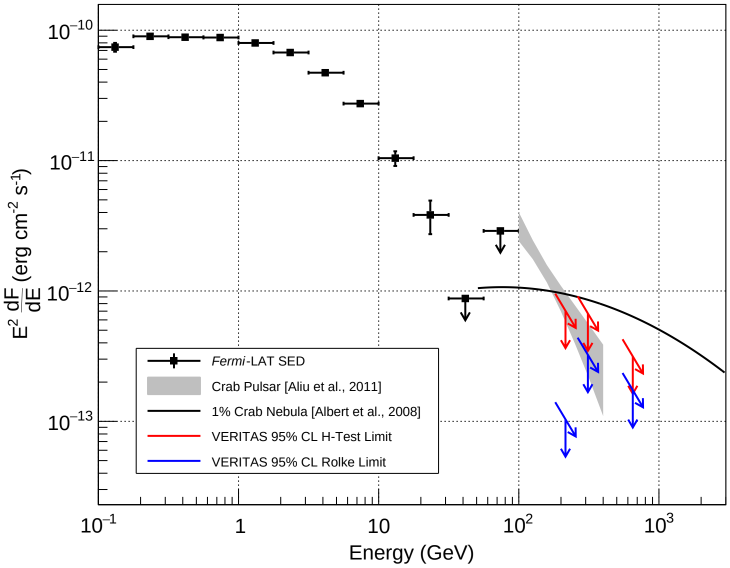

Figure 10.23: **PSR J1907+0602** *Fermi*-LAT spectrum (black squares) with VERITAS flux upper limits (red and blue arrows).

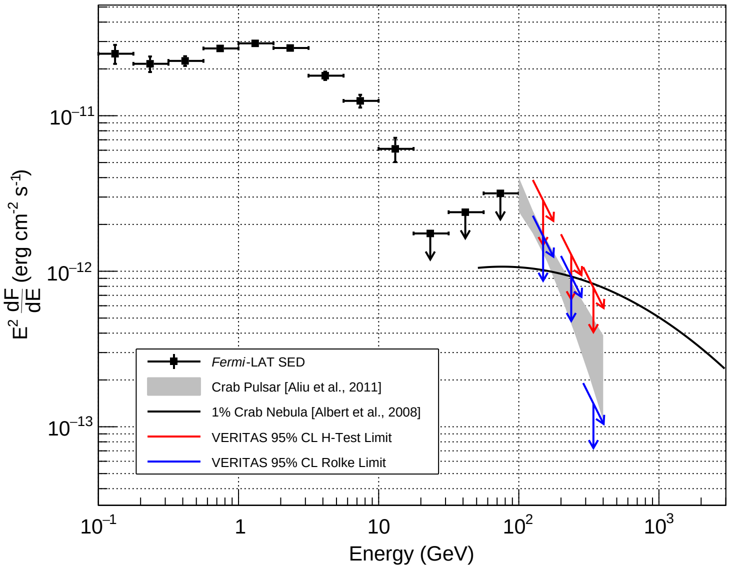

Figure 10.24: **PSR J1954+2836** *Fermi*-LAT spectrum (black squares) with VERITAS flux upper limits (red and blue arrows).

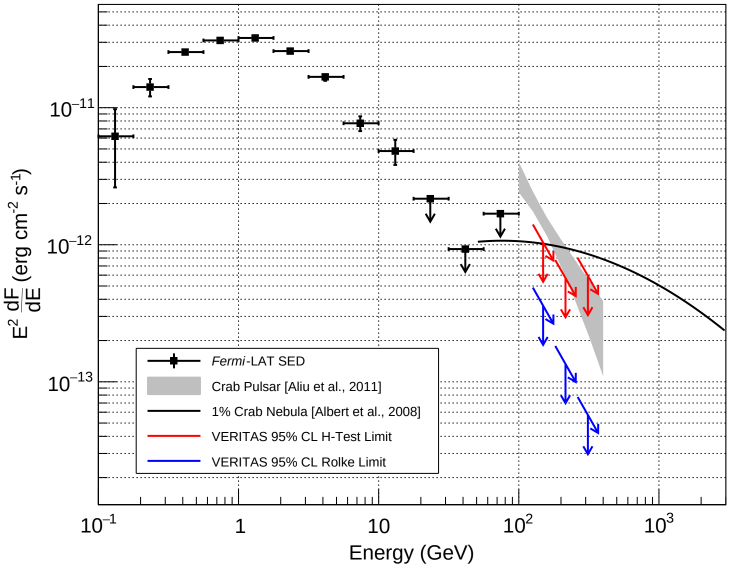

Figure 10.25: **PSR J1958+2846** *Fermi*-LAT spectrum (black squares) with VERITAS flux upper limits (red and blue arrows).

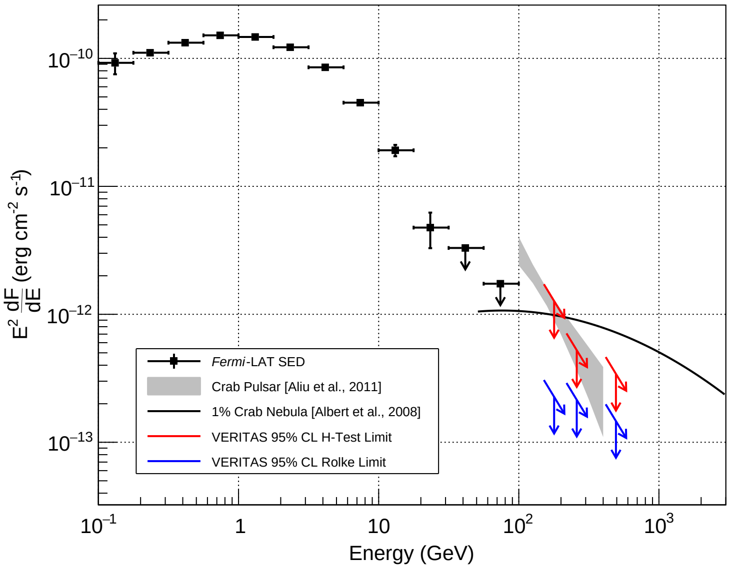

Figure 10.26: **PSR J2021+3651** *Fermi*-LAT spectrum (black squares) with VERITAS flux upper limits (red and blue arrows).

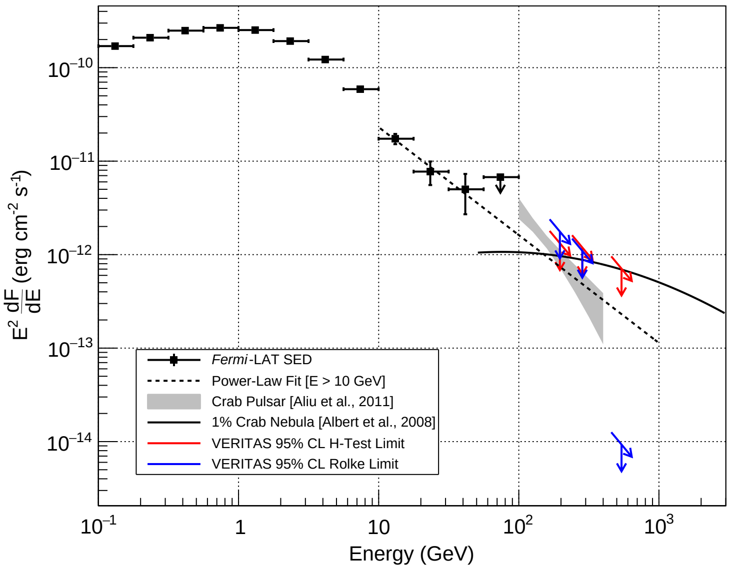

Figure 10.27: **PSR J2021+4026** *Fermi*-LAT spectrum (black squares) with VERITAS flux upper limits (red and blue arrows). A power-law fit to the *Fermi* data above 10 GeV is given by the black dashed line.

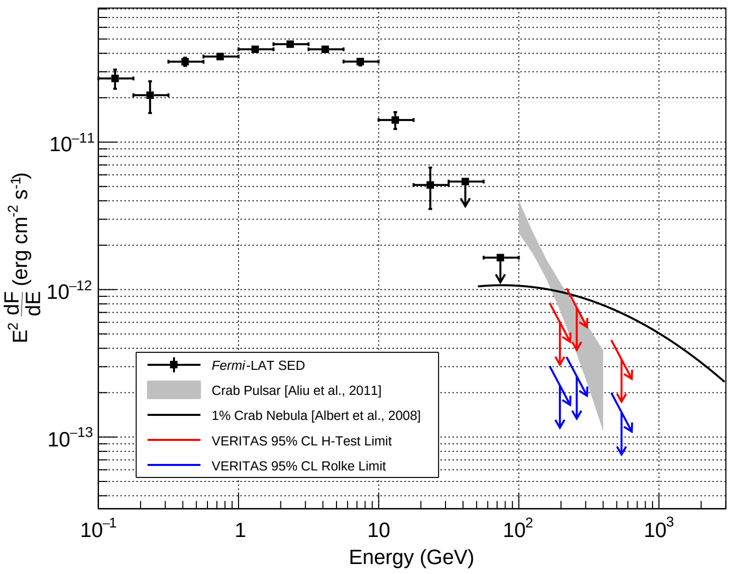

Figure 10.28: **PSR J2032+4127** *Fermi*-LAT spectrum (black squares) with VERITAS flux upper limits (red and blue arrows).

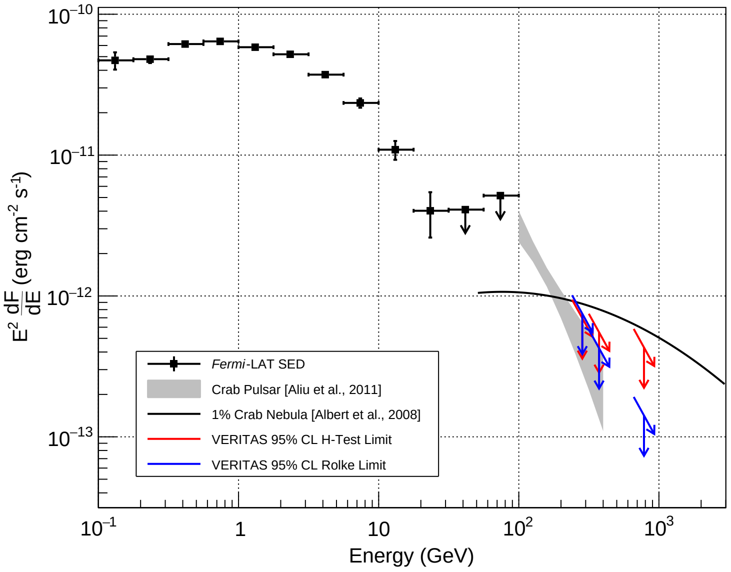

Figure 10.29: **PSR J2229+6114** *Fermi*-LAT spectrum (black squares) with VERITAS flux upper limits (red and blue arrows).

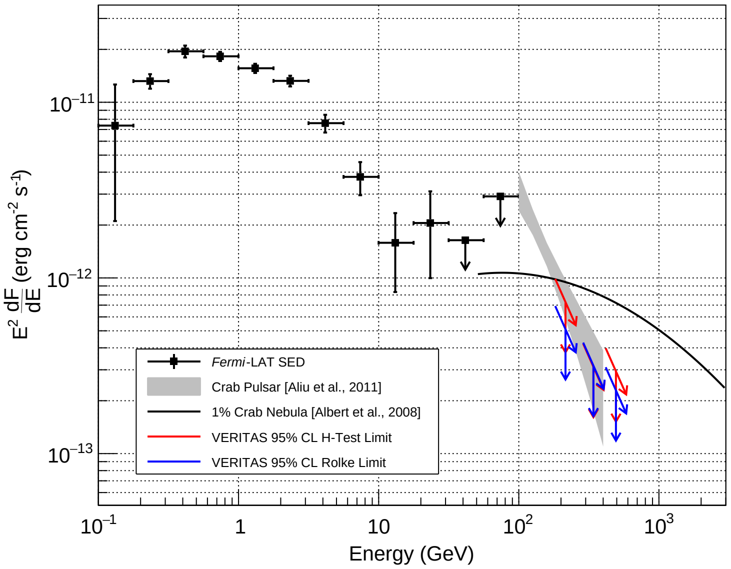

Figure 10.30: **PSR J2238+5903** *Fermi*-LAT spectrum (black squares) with VERITAS flux upper limits (red and blue arrows).

10.5 Discussion and Conclusion

Six searches for VHE pulsed emission from each of 14 pulsars appearing in archival VERITAS data have been performed. No search reveals any evidence of VHE pulsed emission. To the best of our knowledge, these searches for VHE pulsed emission from the set of 14 archival pulsars are the first ever done in the VHE band and represent the first comprehensive northern-hemisphere survey of its kind. We note that the upper limits constrain a flux that is in many cases below the flux level of the Crab pulsar, so the broad statement can be made that potential VHE pulsed emission from each pulsar must be more faint than the VHE flux from the Crab pulsar ($\sim$1% Crab Nebula level). The *Fermi*-LAT spectral reconstruction that has also been done for each pulsar did not result in sufficient photon statistics to enable making any claim about the shapes of the spectra above 10 GeV. Two of the LAT spectra were fitted with a power law above 10 GeV, and one flux UL calculated for PSR J2021+4026 constrains a possible power-law continuation to VHEs (see Figure 10.27).

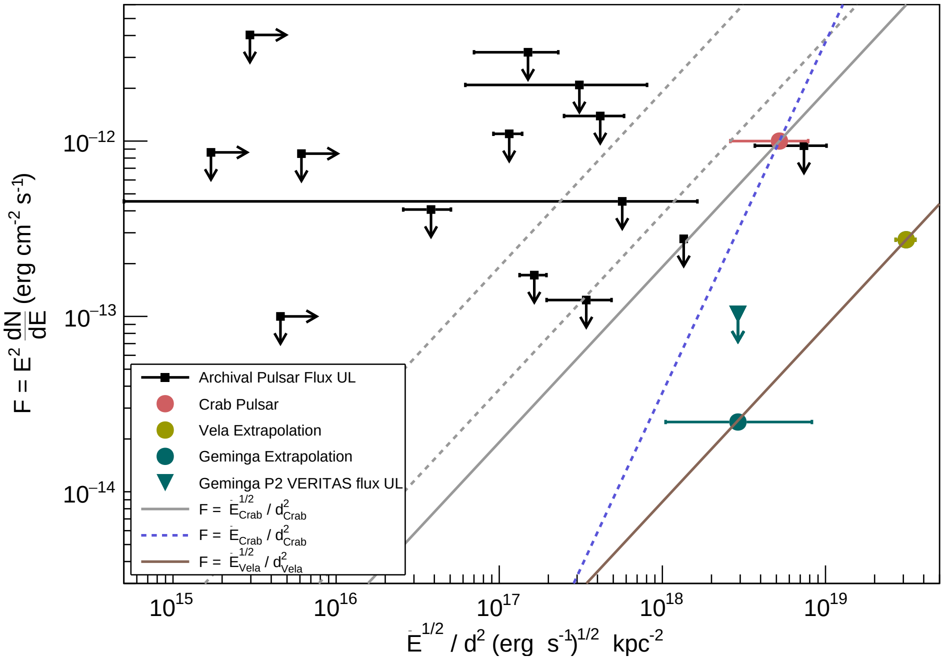

Figure 10.31: Flux upper limits from the phase-gate test versus $\sqrt{\dot{E}}/d^2$ for soft cuts. The VHE flux limits are shown by the black squares, and the right-pointing arrows indicate an upper limit on $\sqrt{\dot{E}}/d^2$ for pulsars where only a distance limit is available. Error bars come from propagation of the uncertainty on the distance as given in Table 10.1. The flux and $\sqrt{\dot{E}}/d^2$ for the Crab pulsar are represented by the red dot. Extrapolated fluxes (see text) for the Geminga and Vela pulsars are shown as a teal and olive circles, respectively. The teal triangle and arrow is a Geminga VHE flux upper limit from VERITAS at 135 GeV from [7]. The Crab pulsar flux shown here is calculated according to the method given in the text. The solid gray line corresponds to $F \propto \sqrt{\dot{E}}/d^2$, where the line has been drawn to intersect the Crab pulsar flux point. The gray dashed lines have the same proportionality but indicate a flux level of two and ten times the Crab pulsar flux. The blue dashed line corresponds to $F \propto \dot{E}/d^2$, which is equivalent to the prediction $L_\gamma \propto \dot{E}$ that has been made for the gamma-ray luminosity in some models (e.g., [46]). The brown solid line is the same as the solid gray line but instead drawn to intersect the Vela flux point.

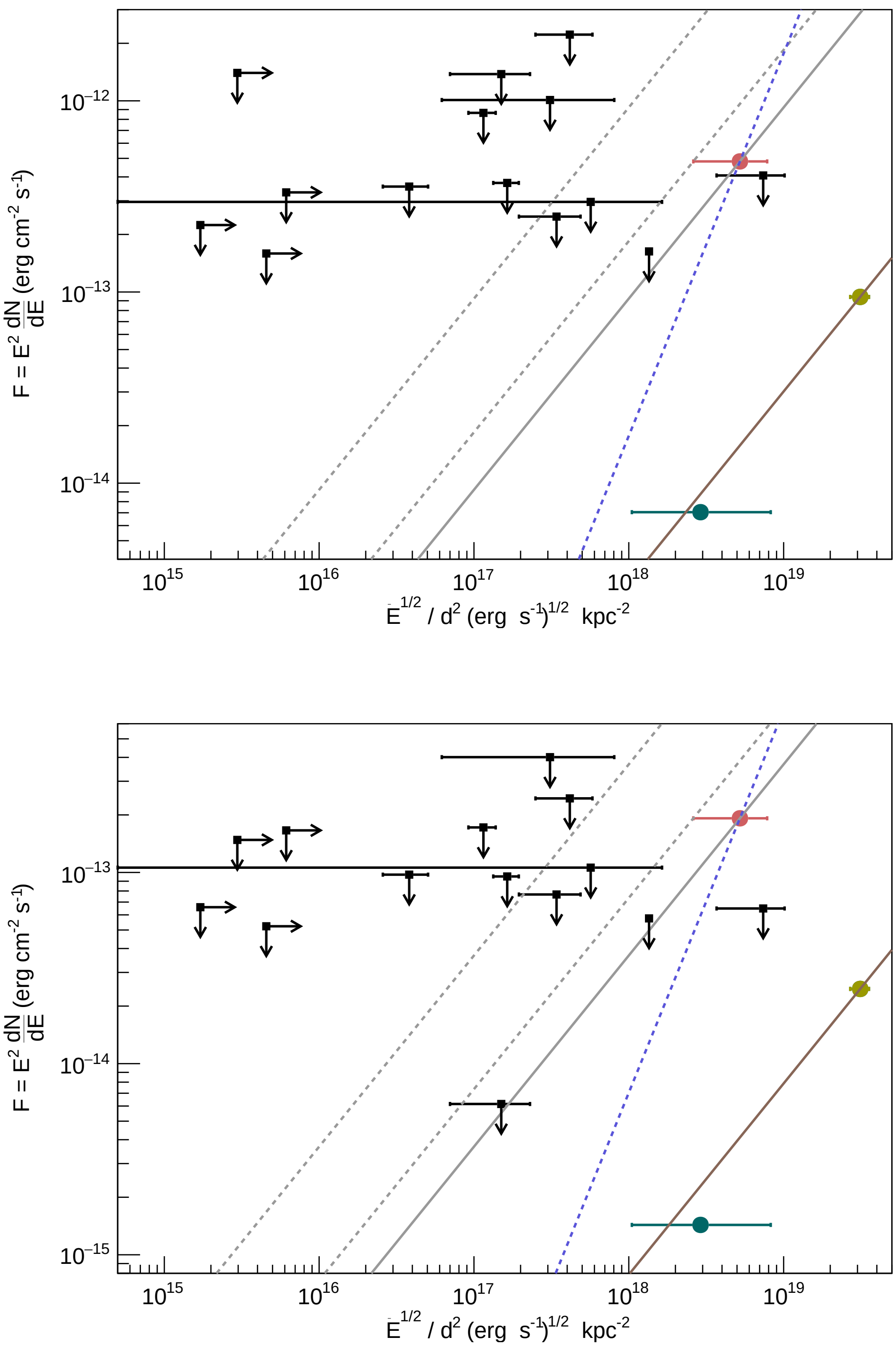

Figure 10.32: Continuation of Figure 10.31 for moderate cuts (*top*) and hard cuts (*bottom*).

A population study was conducted using the flux upper limits derived from the VERITAS data. The VHE limits from the phase-gate tests for the three sets of cuts are shown as a function of $\sqrt{\dot{E}}/d^2$ in Figures 10.31 and 10.32. The Crab pulsar flux that is shown for soft cuts is chosen to be $1 \times 10^{-12}\,\mathrm{erg\,cm^{-1}\,s^{-1}}$, which is the differential flux measured at 200 GeV by VERITAS [3]. For moderate and hard cuts, the Crab flux is extrapolated to 300 and 500 GeV, respectively, according to a power law with $\Gamma = 3.8$ (the same spectral index for the Crab pulsar measured in [3]). These energies are chosen to approximately match the average energy thresholds given in Table 10.3.

An assumption that the flux F displays proportionality to $\sqrt{\dot{E}}/d^2$ (gray and brown lines in Figures 10.31 and 10.32) is essentially a restatement of the equivalent assumption $L_\gamma \propto \sqrt{\dot{E}}$, where L_γ is the gamma-ray luminosity, since $F \propto L_\gamma/d^2$. Such a prediction for L_γ has been made in models that assume a constant voltage drop across the acceleration gap [34]. The 2PC *Fermi*-LAT gamma-ray pulsar population plotted as L_γ against $\dot{E}$ roughly follow a power-law trend [6], though there is likely too much scatter in the data to make a firm empirical claim about the the proportionality of L_γ on $\sqrt{\dot{E}}$ in HE gamma rays.

Invoking the assumption that young gamma-ray pulsars should all have the same $\sqrt{\dot{E}}/d^2$ as that for the Crab pulsar would result in *detected* VHE pulsars trending around the solid gray line in Figures 10.31 and 10.32. Almost all of the VERITAS flux ULs lie well above the gray line, so a prediction that VHE pulsars follow $\sqrt{\dot{E}}/d^2$ for the Crab remains unconstrained in most cases. However, the three flux limits for one pulsar (PSR J2229+6114) all fall below the gray line. The error on $\sqrt{\dot{E}}/d^2$ due to the uncertainty on the distance measurement places the PSR J2229+6114 limits in each case within 1 or 2σ of the gray line, so no firm claim regarding the validity of the $\sqrt{\dot{E}}/d^2$ trend can be made with the UL for this pulsar. Furthermore, systematic errors on distance measurements are typically quite large. Flux points derived from extrapolation for both the Vela and Geminga pulsars are also shown, and both lie well below the $\sqrt{\dot{E}}/d^2$ expectation from the Crab. The VHE Geminga and Vela fluxes are derived from their *Fermi*-LAT spectra above 10 GeV[6], which are fitted with a power-law shape and extrapolated to 200, 300, and 500 GeV. Measures of

---

[6] The spectral reconstruction mentioned here for Geminga and Vela was done by me using 7.2 yr of *Fermi*-LAT data and the analysis methods given in Section 6.2.

$\dot{E}$ and the distances for Geminga and Vela are taken from the 2PC [6] (references therein for the distances are [193] and [48], respectively). That these flux extrapolations lie well below the $F \propto \sqrt{\dot{E}}/d^2$ prediction from the Crab pulsar challenges the assumption that at VHEs pulsars may trend along the gray line in Figures 10.31 and 10.32. If the assumption is made that $F \propto \sqrt{\dot{E}}/d^2$ for the *Vela* pulsar extrapolation instead of the Crab, detected VHE pulsars should trend around the brown lines in the figures. We note that for all three sets of cuts, the brown line intersects the extrapolated Geminga flux point error. Further, for the extrapolated Vela and Geminga fluxes shown in Figure 10.31, the brown line defined solely by the parameters of the Vela pulsar assuming $F \propto \sqrt{\dot{E}}/d^2$ exactly intersects the Geminga point. It could be the case that VHE pulsars follow the assumed $\sqrt{\dot{E}}$ trend, though with a much lower constant of proportionality compared to that defined by the Crab pulsar.

The upper limits presented here constrain potential spectral hardening or a new spectral component to be at or below the level of the limits, though pulsar models generally predict VHE emission several orders of magnitude below the flux levels probed in this search (e.g., Harding and Kalapotharakos [54]). The upcoming IACT called the Cherenkov Telescope Array (CTA) aims to achieve a ten-times-improved sensitivity at VHEs compared to current-generation instruments. Observations with CTA will, therefore, be able to lower pulsar flux ULs by a factor of ten given the same exposure time. The limits presented in this project can help guide future observations with CTA via providing an estimate for the observational time cost versus potential benefit if an important constraint can be made. Of course, the firm *detection* of another pulsar above 100 GeV will have a very high scientific impact, but for now the nature of the VHE emission from pulsars mostly remains unresolved.

CHAPTER 11

CONCLUSION

In the presented analyses, I have performed searches for pulsed very high-energy gamma rays from a total of 16 unique pulsars with VERITAS. The total amount of data processed in obtaining the results presented in this thesis is roughly 580 hours. The analyses fall into three separate projects:

- A search for pulsed VHE emission from the Geminga pulsar (Chapter 8)
- A search for steady and pulsed VHE emission from the binary system PSR J1023+0038 (Chapter 9)
- A search for pulsed VHE emission from the 14 pulsars appearing in archival VERITAS data (Chapter 10).

In every case, these searches resulted in non-detections, and these non-detections are used to place important flux upper limits to constrain a potential VHE spectral component. For both PSR J1023+0038 and the Geminga pulsar, the calculated VHE upper limits were the first to appear in the literature in their respective publications. In the time since publication, the MAGIC Collaboration has published pulsed-flux limits at about the same level of the VERITAS limits and with a lower energy threshold [47]. The VHE upper limits for the 14 pulsars appearing in archival VERITAS data are the first such limits for each pulsar, and they are the subject of an upcoming publication currently in preparation.

Theoretical model predictions of a pulsed very high-energy gamma-ray emission component currently remain the subject of much debate in the literature. Before the VHE detections of the Crab pulsar by VERITAS [3] and MAGIC [42, 4], an inverse-Compton VHE component had been considered by some (e.g., [16]), though was not a principal focus of attention from modellers. In the six years that have elapsed since the Crab pulsar detection, several new models have appeared attempting to explain the pulsed VHE emission seen from the Crab (see Chapter 3). At least one such model has also been used to make explicit predictions for a few other pulsars (the model of Harding and Kalapotharakos in [54]). Currently, no model for the Crab pulsar is capable of simultaneously explaining the observed VHE spectrum up to 1.5 TeV and the gamma-ray pulse profile [58]. Given the inconclusiveness surrounding the theory of VHE emission from the Crab, which remains the only firmly detected VHE pulsar, predictions in this area for other pulsars are likewise highly uncertain.

Though resulting in non-detections, the projects presented in this thesis offer insight regarding the question of VHE gamma-ray emission from young pulsars. It could be the case that spectral hardening or an altogether new spectral component manifests at VHEs for many pulsars. That no such flux component was observed is a result in itself since any spectral hardening at VHEs is now constrained to be at or below the VERITAS limits for each pulsar discussed in this thesis. These upper limits can thus serve as a guide for modellers who attempt to predict the features of VHE emission from the general population of young gamma-ray pulsars.

The non-detection of the Geminga pulsar with VERITAS enabled placing the first upper limits on a potential pulsed VHE flux. The VERITAS observational campaign on Geminga resulted in 71.6 hr of data that was used to probe for pulsed emission. An analysis of 5.2 yr of *Fermi*-LAT data was also conducted, and the high-energy gamma-ray spectrum was reconstructed. The HE spectrum was observed to fall more slowly than a simple exponential function, which is expected for multi-zone curvature radiation where the observed spectrum is a superposition of spectra with different break energies [36, 37]. Above 10 GeV, it is not possible to distinguish an exponential cut-off from a power law due to sparse photon statistics in the LAT data. The VERITAS flux upper limits lie above the flux level predicted from a simple power-law extrapolation of the HE Geminga spectrum above 10 GeV. While the power-law spectral extension remains unconstrained, a significant hardening of the spectral shape can be excluded in light of the VERITAS flux limits. If the spectrum extends as a simple power law as seen for the Crab pulsar, a deeper exposure will be necessary to detect the VHE emission, which could be the subject of a study with a future-generation instrument.

A search for pulsed VHE gamma-ray emission from the millisecond pulsar in the binary system PSR J1023+0038 also resulted in a non-detection. The 20 hr observation during the active phase of the pulsar is the deepest such exposure published to date involving a search for pulsed VHE gamma rays from an MSP. Although no emission was detected, the importance of this search lies in the fact that the rapid rotation rates of MSPs can give rise to contrasting magnetospheric conditions compared to the younger pulsar population. Therefore, a search for VHE gamma rays from MSPs naturally probes a different set of physical parameters, and the VERITAS flux limits can be of some use to modellers who attempt to predict features of gamma-ray radiation from this class of pulsar.

Following the aforementioned non-detections of the Geminga pulsar and PSR J1023+0038, a search for pulsed VHE emission from 14 young pulsars appearing in archival VERITAS data was conducted. The total VERITAS exposure across all pulsars was 483.8 hr, and no pulsed VHE emission was detected from any of the 14 pulsars in the analysis. A *Fermi*-LAT spectral analysis was also performed for each pulsar, though the HE gamma-ray statistics were too sparse to enable any claim regarding the shape of the spectra above 10 GeV. VHE flux upper limits were computed at three energy thresholds for each pulsar, which constrain potential spectral hardening and the emergence of a new spectral component at the level of the limits. A population study was conducted involving contextualization of the flux limits with respect to the spin-down powers and distances of the pulsars. Assuming that the VHE fluxes F from all young gamma-ray pulsars follow $F \propto \sqrt{\dot{E}}/d^2$, the constant of proportionality can be fixed given the detection of the Crab pulsar at VHEs. This revealed that all of the calculated VERITAS flux limits fall above (or within errors of) the proportionality line for the Crab pulsar. That no VHE emission was detected is therefore entirely consistent with an expectation that the gamma-ray luminosity roughly scales with $\sqrt{\dot{E}}/d^2$.

The collection of VHE gamma-ray flux upper limits derived from VERITAS data presented in this thesis can be used to guide future pulsar observations by the next-generation IACT, the Cherenkov Telescope Array (CTA). CTA aims to achieve a factor-of-ten improvement in sensitivity compared to currently operational IACTs, which will enable greatly enhanced studies of all source classes at VHEs. The limits for the pulsars presented in this thesis are in some cases reasonably close to constraining a prediction (or potentially making a discovery of VHE emission). With a similar exposure as obtained by VERITAS for the Geminga pulsar, a power-law extension above 10 GeV into VHEs could be definitively ruled out for a non-detection. From the archival pulsar project, for example, the limit for VHE emission from PSR J2229+6114 has an error bar that overlaps the $\sqrt{\dot{E}}/d^2$ proportionality line for the Crab pulsar. A similar exposure with CTA ($\sim$50 hr) would improve the limit by an order of magnitude and therefore rule out the idea that in general $F \propto \sqrt{\dot{E}_{\text{Crab}}}/d^2_{\text{Crab}}$ (assuming a non-detection). In any case, for now the nature of the VHE gamma-ray emission from pulsars remains largely unresolved. With any luck, future observations at VHEs will help shed more light on the fundamental features of these cosmic accelerators.

Appendices

APPENDIX A

A SEARCH FOR ELEVATED VERY HIGH-ENERGY GAMMA-RAY FLUX DURING A CRAB NEBULA FLARE WITH VERITAS

This appendix is a reproduction of a paper I have published in [194]. It has been left unedited. All figures are provided after the text.

A.1 Abstract

In March 2013, a flaring episode from the Crab Nebula lasting $\sim$2 weeks was detected by the *Fermi*-LAT (Large Area Telescope on board the *Fermi* Gamma-ray Space Telescope). VERITAS provides simultaneous observations throughout this period. During the flare, the *Fermi*-LAT detected a 20-fold increase in flux above the average synchrotron flux $> 100\,\mathrm{MeV}$ seen from the Crab Nebula. Simultaneous measurements with VERITAS are consistent with the non-variable long-term average Crab Nebula flux at TeV energies. Assuming a linear correlation between the very-high-energy flux change $> 1\,\mathrm{TeV}$ and the flux change seen in the *Fermi*-LAT band $> 100\,\mathrm{MeV}$ during the period of simultaneous observations, the linear correlation factor can be constrained to be at most 8.6×10^{-3} with 95% confidence.

A.2 Introduction

The Crab Nebula is one of the best-studied cosmic particle accelerators. Its distance of $\sim$2 kpc and absolute luminosity of 5×10^{38} erg s^{-1} allow the study of the nebula in great detail across the entire electromagnetic spectrum. From radio to GeV energies, the emission is consistent with synchrotron emission of relativistic electrons [195]. However, at higher energies, the dominant emission mechanism is thought to be inverse-Compton up-scattering of low-energy photons by the same population of electrons [196, 197, 198, 199].

The energy source powering the nebula is believed to be the Crab pulsar located at its center [200]. With the pulsar as the central engine, a self-consistent magnetohydrodynamic model can be developed that explains the main features of the nebula [201, 202]. The discovery of flaring episodes by the AGILE [203] and *Fermi*-LAT [204] teams was unexpected in this framework. The Crab Nebula flux was seen to increase by more than a factor of ten in less than a day between 100 MeV and 1 GeV in the most extreme of these flares.

Determining the cause of these flares is a major experimental and theoretical challenge. The observed flaring timescales of 12 hours [205] and 8 hours [206] imply that the emission region is less than 3×10^{-4} pc in diameter. This size constraint coupled with the observation that the emitted isotropic power peaks at about 1% of the pulsar spin-down power argues in favor of an emission region that moves mildly relativistically [206, 207, 208, 209]. As no enhancement of the pulsed emission has been observed during flares, it has been concluded that the emission region likely resides outside the corotating magnetosphere [206, 205].

The investigation of the origin of the flares is complicated because no correlated enhancements have been observed at other wavelengths to date [205, 210, 211, 206]. Multiwavelength campaigns have been executed every time a flare has been observed since the detection of the September 2010 flare [203]. Extensive simultaneous coverage over the entire synchrotron emission from radio to X-rays did not reveal correlated activity [212, 213] that could have shed light on the location of the flares due to better angular resolution at these energies.

The non-detection of correlated activity favors a monoenergetic population of relativistic electrons as the origin of the observed flares. While multiwavelength coverage has been excellent in radio, optical, and X-rays, it has been rather sparse at energies above 100 GeV, i.e., in the inverse-Compton component. No enhancement of the TeV emission was reported by MAGIC or VERITAS during the September 2010 flare [214, 215]. The ARGO-YBJ Collaboration have reported enhanced signals with a median energy of 1 TeV from the direction of the Crab Nebula contemporaneous to GeV-band flares, although these enhancements did not reach the 5σ level [216, 217, 218].

The electrons responsible for the flares should also upscatter soft photons in the nebula to produce TeV photons, which enables constraining the dynamics of the electrons. In this paper we present the most sensitive observations at TeV energies performed during a flare of the Crab Nebula to date. These observations with VERITAS are discussed in the context of observations with the *Fermi*-LAT.

A.3 Observations and Analysis

A.3.1 VERITAS

The Very Energetic Radiation Imaging Telescope Array System (VERITAS) is an array of four 12 m diameter imaging atmospheric Cherenkov telescopes (IACTs) located at the base of Mt. Hopkins in southern Arizona, USA that observes very-high-energy (VHE; $E > 100\,\mathrm{GeV}$) gamma rays. Each telescope in the array has a reflector that is composed of 345 hexagonal mirror facets that focus light onto a 499-pixel photomultiplier tube (PMT) camera at the focal plane with a field of view (FoV) of $\sim 3.^{\circ}5$. The array operates in the energy range $\sim 0.1 - 30\,\mathrm{TeV}$ with an energy resolution of $\sim 15\%$ at energies above 1 TeV and an angular resolution of $0.^{\circ}15$ [64].

VERITAS observations of the Crab Nebula in its flaring state were triggered by an automated *Fermi*-LAT analysis pipeline at Barnard College-Columbia University [219] on 2013 March 02, two days prior to the ATel from the *Fermi*-LAT collaboration announcing the gamma-ray flare [220]. The VERITAS data during the flare are composed of ten nights of observations in the period MJD 56353 to 56366 (2013 March 02 to 2013 March 15, henceforth referred to as the flare time window, FTW). Observations of the Crab Nebula as part of the standard observing schedule from 2012 October 13 to 2013 April 02 excluding the FTW comprise a data set on the source in its non-flaring state, which is used as a baseline with which to compare the flare data.

All VERITAS Crab observations were taken in *wobble mode* with an offset of $0\overset{\circ}{.}5$ from the source position alternately in each of the four cardinal directions, so that the background can be estimated from simultaneously gathered data, and systematic effects in the background estimation cancel out [221, 78]. Observations were conducted using the full four-telescope array in a range of zenith angles $12^\circ - 55^\circ$, giving a total of 10.3 hours of live time on the source during the FTW and 17.4 hours during the rest of the season. Two nights of flare observations (MJD 56353 and 56358) were conducted at large zenith angles, which has the effect of increasing the effective energy threshold of the array. Due to this dependence of the energy threshold, the low-energy threshold for the spectral analysis is set to a common value of 1 TeV.

The recorded images are first flat-fielded using information from nightly calibration runs taken with a pulsed UV LED [222]. The images are cleaned using a form of the picture/boundary method [76] and parameterized [74] to suppress the cosmic ray background. The shower direction is reconstructed from the data in each telescope, and a set of selection criteria is applied to reject background events [223, 76].

Energy spectra are calculated $> 1\,\mathrm{TeV}$ both for the FTW and the baseline observations and are shown in Figure A.1. The spectra are parametrized as power laws of the form

$$\frac{dN}{dE} = N_0 \left(\frac{E}{1\,\mathrm{TeV}} \right)^{\gamma} . \tag{A.1}$$

The baseline spectral fit gives a normalization of $N_0^{\text{baseline}} = (3.48 \pm 0.14_{\text{stat.}} \pm 1.08_{\text{sys.}}) \times 10^{-7}$ TeV^{-1} m^{-2} s^{-1} and $\gamma^{\text{baseline}} = -2.65 \pm 0.04_{\text{stat.}} \pm 0.3_{\text{sys.}}$, with a χ^2 value of 16.6 with 12 degrees of freedom (dof). The FTW spectral fit gives a normalization of $N_0^{\text{flare}} = (3.53 \pm 0.15_{\text{stat.}} \pm 1.12_{\text{sys.}}) \times 10^{-7}$ TeV^{-1} m^{-2} s^{-1} and a spectral index $\gamma^{\text{flare}} = -2.72 \pm 0.05_{\text{sys.}} \pm 0.3_{\text{sys.}}$, with a χ^2 value of 10.1 with 12 dof. The fit probabilities are 16% and 61%, respectively. These spectral parameters are mutually consistent, implying no change of the TeV flux during the FTW. The systematic uncertainties on the flux normalization and spectral index are expected to vary slowly with time, and a paper containing a proper treatment of these uncertainties is currently in preparation.

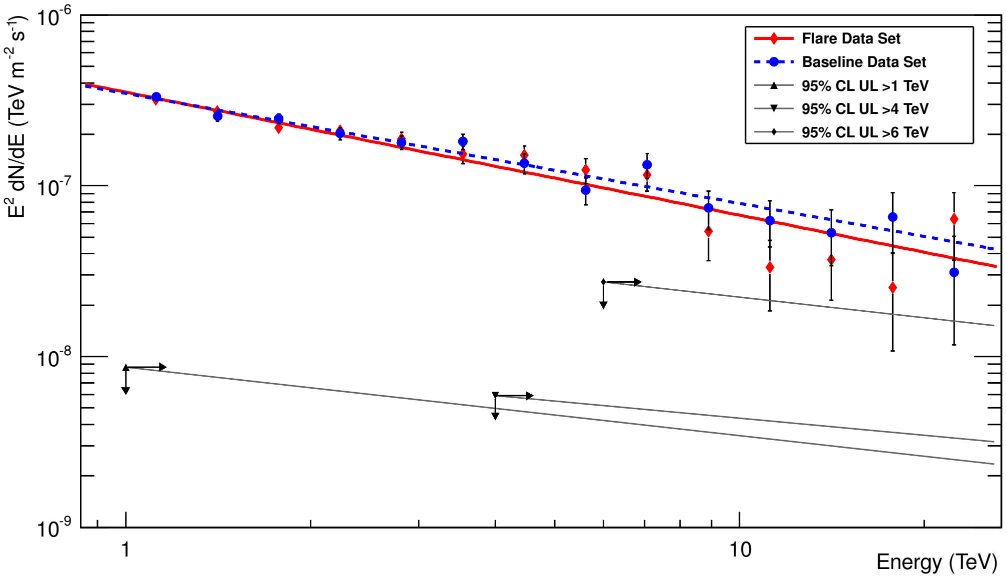

Figure A.1: VHE Crab Nebula spectral energy distributions for the flare and non-flare data sets. The SEDs are fit with power-law functions (§ A.3.1). From the limits on the relative flux change above 1 TeV, 4 TeV, and 6 TeV (§ A.4), upper limits on an extra flux component in the flare are computed assuming a spectral index of -2.4.

A.3.2 *Fermi*-LAT

The *Fermi*-LAT is a pair-conversion telescope sensitive to gamma-ray photons with energies between 20 MeV and 300 GeV. It has a wide FoV of ∼2.5 sr and surveys the entire sky every three hours. For a complete description of the instrument, see [70, 71].

In order to extract spectral parameters of the Crab, the *Fermi*-LAT `Science Tools v9r27p1` with `P7V6` instrument response functions (IRFs) and the standard quality cuts described in [72] are used. Two years of "source"-class events with energies between 100 MeV and 300 GeV collected between MJD 54832 and 55562 within 20° of the Crab are processed with the maximum likelihood fitting routine. A model of the background is obtained in a binned likelihood analysis by fitting spectral models for all sources in the 2FGL catalog within 20° of the Crab in addition to the galactic and isotropic diffuse backgrounds (`gal_2yearp7v6_v0.fits`, `iso_p7v6source.txt`). Photon arrival times are barycentered with `Tempo2` [68] using a publicly-available Jodrell Bank radio ephemeris for the Crab pulsar [224] to allow a selection of the off-pulse phase region $0.48-0.88$. Under the assumption that emission from the pulsar is negligible in the off-pulse region, spectral parameters for the synchrotron and inverse-Compton components of the Crab Nebula are calculated. These parameters are fixed in the model to allow fitting of the pulsar spectral component after undoing the selection on pulsar phase.

The Crab Nebula synchrotron differential spectrum is parameterized as a power law (PowerLaw2 in the *Fermi*-LAT `Science Tools`) of the form

$$\frac{dN}{dE} = \frac{F_0(\gamma+1)E^{\gamma}}{(300\,\mathrm{GeV})^{\gamma+1} - (0.1\,\mathrm{GeV})^{\gamma+1}}. \tag{A.2}$$

The fit of the quiescent state yields a synchrotron integral flux above $100\,\mathrm{MeV}$ of $F_0 = (6.40 \pm 0.11) \times 10^{-7}\,\mathrm{cm}^{-2}\,\mathrm{s}^{-1}$ and photon index of $\gamma = -3.69 \pm 0.11$, which are consistent with previously published results [e.g., 206].

A similar analysis is done for the FTW. Since the *Fermi*-LAT carried out a targeted observation of the Crab during the flare, the recommended `P7V6MC` IRFs and pointed mode data selection criteria are used in this analysis[1]. The synchrotron integral flux above $100\,\mathrm{MeV}$ for the FTW is found to be $(5.30 \pm 0.13) \times 10^{-6}\,\mathrm{cm}^{-2}\,\mathrm{s}^{-1}$ with a harder photon index of -3.10 ± 0.05. A combined spectral energy distribution (SED) showing the *Fermi*-LAT and VERITAS spectra is given in Figure A.2.

A.4 Results

A test for variability in the VERITAS FTW light curve (shown in Figure A.3) is performed by fitting the light curve with a constant flux. This fit gives a flux $> 1\,\mathrm{TeV}$ of $(2.05 \pm$

---

[1] http://fermi.gsfc.nasa.gov/ssc/data/analysis/documentation/Cicerone/Cicerone_Likelihood/Exposure.html

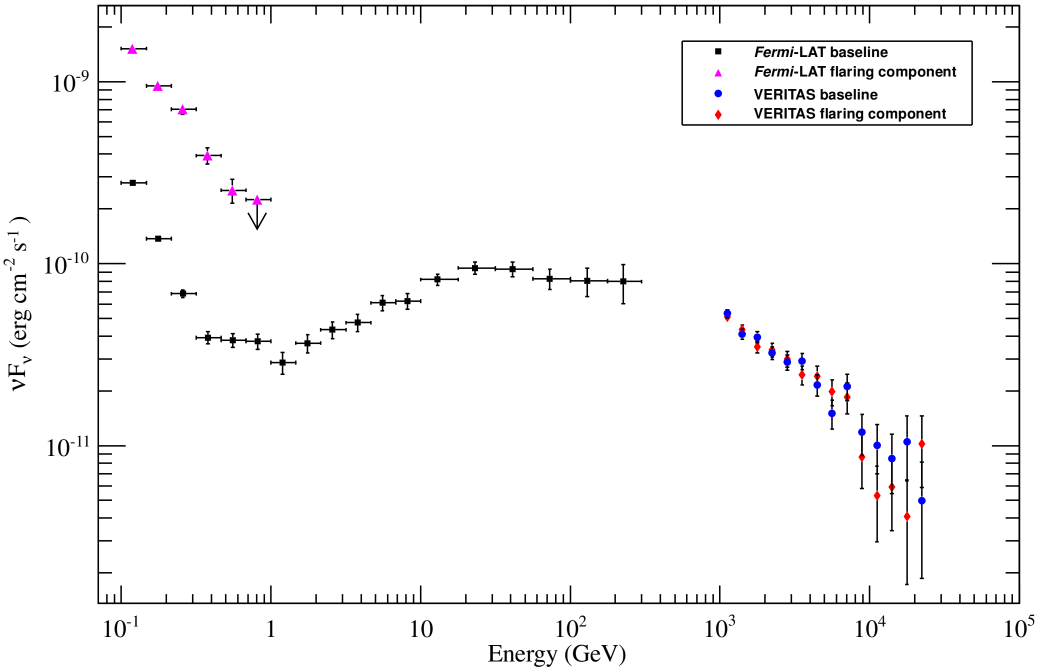

Figure A.2: Combined SED of the Crab Nebula. The baseline *Fermi*-LAT spectrum (black squares) is averaged over ~5 years of observations, while the baseline VHE spectrum (blue circles) includes all good data taken outside of the FTW in the $2012 - 2013$ VERITAS observing season. The FTW VHE spectrum (red diamonds) shows no significant deviation from the baseline, while the synchrotron spectrum during this period (magenta triangles) exhibits spectral hardening. All spectral parameters given in § A.3.1, A.3.2.

$0.07) \times 10^{-7}$ m^{-2} s^{-1} with a χ^2 value of 19.1 with 9 dof (probability ~2.4%). By fitting a light curve of data taken outside of the FTW, the Crab Nebula is detected with a baseline VHE flux > 1 TeV of $(2.10 \pm 0.06) \times 10^{-7}$ m^{-2} s^{-1} with a χ^2 value of 21.7 with 22 dof (probability ~47.8%). The FTW flux is thus consistent with the baseline flux and with no statistically significant variability during the flare. An analysis of a subset of the data with energies extending down to ~150 GeV was also conducted (shown in Figure A.3), however no variability is revealed at these energies.

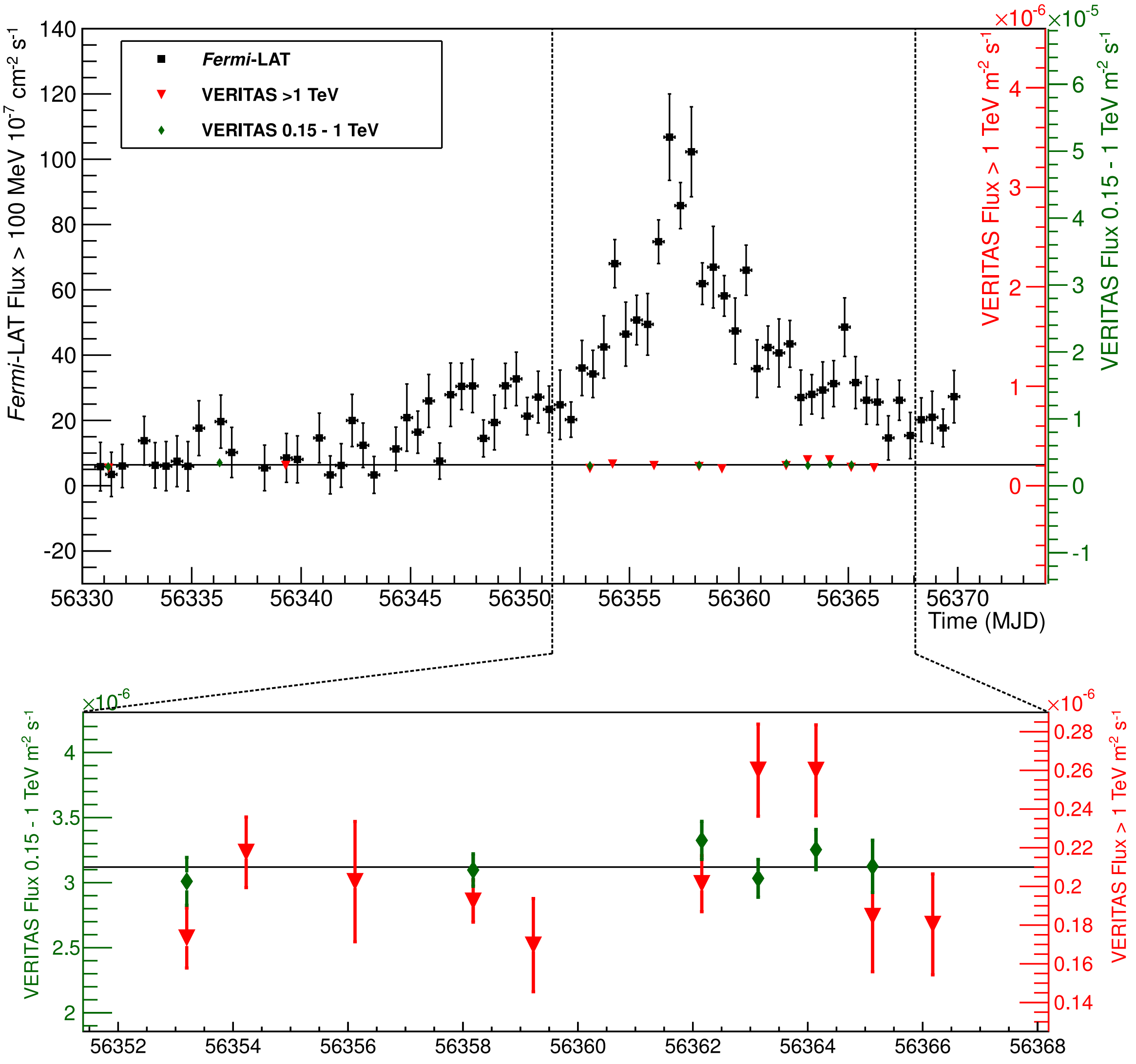

Figure A.3: *Fermi*-LAT and VERITAS light curves for the March 2013 Crab Nebula flare. The 12-hour binned *Fermi*-LAT light curve (square markers) spans MJD $56330 - 56370$. The VERITAS light curves (triangle and diamond markers) span ten nights during the FTW where weather permitted observations. The baseline Crab Nebula synchrotron flux above 100 MeV and average VHE flux above 0.15 TeV and 1 TeV are aligned and are indicated by the solid black line. The vertical scales of the three light curves have been adjusted such that the zero points and baseline fluxes are coincident.

In order to test for correlated *Fermi*-LAT and VERITAS ($> 1\,\mathrm{TeV}$) flux variability in the light curves shown in Figure A.3, a publicly available implementation of the z-transformed discrete correlation function (ZDCF) is employed [225, 226]. The ZDCF method requires a minimum of 12 observations in each light curve for a statistically valid analysis, so two nights of pre-flare VERITAS Crab Nebula observations taken on MJD 56331 and 56339 (February 8 and 16, respectively) are added before the cross-correlation is performed. The zero time-lag bin reported a ZDCF correlation coefficient of

$$\mathrm{DCF} = -0.07 \pm 0.31 \tag{A.3}$$

which is consistent with no correlation at zero lag. Results for all other time-lag bins are also consistent with no statistically significant correlation.

Relative flux changes during the FTW are calculated for VERITAS and *Fermi*-LAT. The i^{th} relative flux change $\Delta F^i_{\text{rel.}}$ for both VERITAS and *Fermi*-LAT observations on the i^{th} night is computed as

$$\Delta F^i_{\text{rel.}} = \frac{F^i - \overline{F}}{\overline{F}}. \tag{A.4}$$

For VERITAS, F^i is the average flux for one night. For *Fermi*-LAT, F^i is the average flux in one 12-hour time bin centered on midnight Arizona time (MST, 0700 UTC). $\overline{F}$ is the average non-flare flux from the nebula. The VERITAS and *Fermi*-LAT relative flux changes for simultaneous observations are shown in Figure A.4. Averaged over the simultaneous observations in the FTW, the relative flux changes are

$$\overline{\Delta F^{\text{VTS}}_{\text{rel.}}} = -0.026 \pm 0.035 \qquad (\text{VERITAS} > 1\,\text{TeV}) \tag{A.5}$$

$$\overline{\Delta F^{\text{Fermi}}_{\text{rel.}}} = 6.14 \pm 0.38 \qquad (\textit{Fermi}\text{-LAT} > 100\,\text{MeV}) \tag{A.6}$$

From $\overline{\Delta F^{\text{VTS}}_{\text{rel.}}}$, a 95% confidence level upper limit (UL) is computed for an elevated VHE flux. Given the assumption of a positive and non-zero correlation of *Fermi*-LAT and

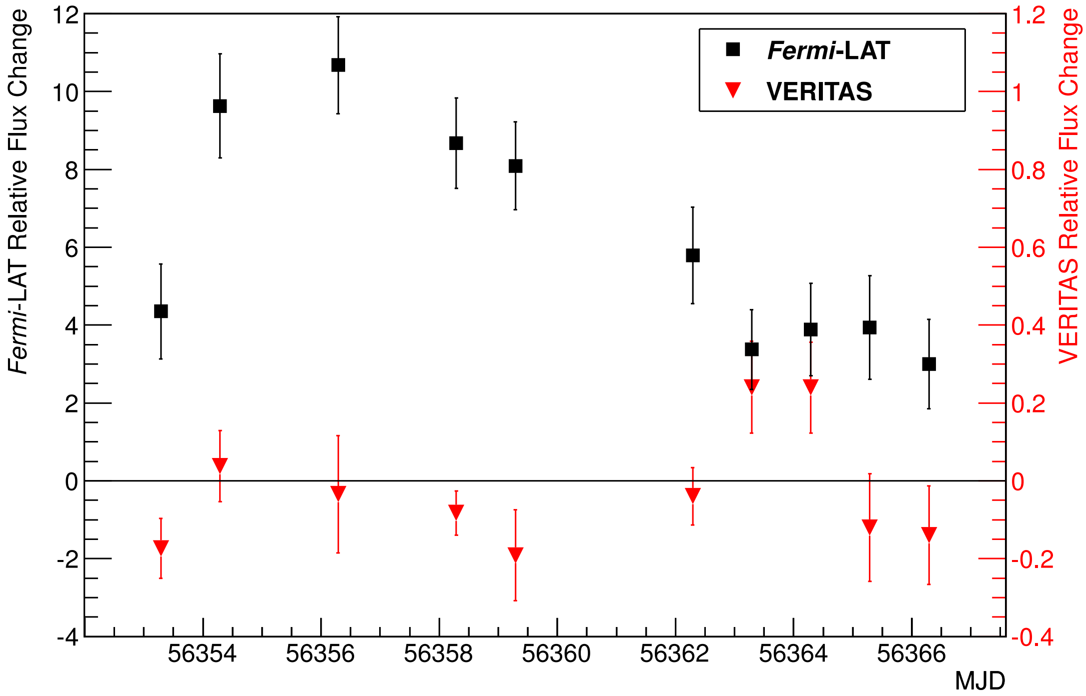

Figure A.4: Relative flux changes for simultaneous *Fermi*-LAT (square markers) and VERITAS (triangle markers) observations during the FTW. The zero line corresponds to an observed flux equal to the average. Note that the vertical scale for the VERITAS points is a factor of ten smaller than the vertical scale for the *Fermi*-LAT points.

VERITAS flux changes, a Bayesian prior is introduced in the limit calculation that is zero for negative relative flux changes and one elsewhere. This prior is equivalent to invoking the physical constraint that all of the VHE flux changes are at least zero. The upper limit is calculated over the Bayesian interval $[0, x^{\mathrm{up}}]$ such that

$$\frac{\int\limits_0^{x^{\mathrm{up}}} \exp\left(-\frac{(\overline{\Delta F_{\mathrm{rel}}^{\mathrm{VTS}}}-x)^2}{2\sigma^2}\right) dx}{\int\limits_0^{\infty} \exp\left(-\frac{(\overline{\Delta F_{\mathrm{rel}}^{\mathrm{VTS}}}-x')^2}{2\sigma^2}\right) dx'} = 0.95 \;\; (x^{\mathrm{up}} > 0) \tag{A.7}$$

where σ is the error on $\overline{\Delta F_{\mathrm{rel.}}^{\mathrm{VTS}}}$, and the 95% CL upper limit is given by x^{up}, which is obtained by solving the equation numerically. Limits are calculated for three different energy thresholds shown in Table A.1.

Table A.1: 95% CL Bayesian upper limits on the VHE relative flux increase during the flare period for three energy thresholds.

Energy band (TeV)	$\overline{\Delta F^{\text{VTS}}_{\text{rel.}}}$ 95% CL UL	95% CL integral UL at threshold (TeV m^{-2} s^{-1})
> 1	5.3%	8.7×10^{-9}
> 4	6.8%	5.9×10^{-9}
> 6	37.4%	2.7×10^{-8}

By adopting the assumption that the relative flux change seen by VERITAS is linearly related to that seen by the *Fermi*-LAT during the flare:

$$\overline{\Delta F^{\text{VTS}}_{\text{rel.}}} = \alpha \overline{\Delta F^{\textit{Fermi}}_{\text{rel.}}}, \tag{A.8}$$

a constraint on the linear correlation factor α can be calculated, which can be used to test model predictions. Taking the ratio of the > 1 TeV upper limit and the average *Fermi*-LAT relative flux change, we find that $\alpha < 8.6 \times 10^{-3}$ (95% CL) for the average of the ten nights of simultaneous observations. The constraint on α is also computed night-by-night, though only MJD 56358 gives the slightly better constraint of $\alpha < 8.1 \times 10^{-3}$ (95% CL).

A.5 Discussion

In this paper we present observations of the Crab Nebula with VERITAS and the *Fermi*-LAT during the March 2013 flare. The light curve and reconstructed energy spectrum between 1 TeV and 10 TeV do not indicate any flux enhancement at TeV energies, while the flux above 100 MeV was six times elevated during our observations.

Earlier flares had very hard spectra with peak energy reaching up to $\epsilon_{\text{flare}} \approx 500$ MeV [206], though in the present flare, a peak could not be resolved in the MeV–GeV spectrum leaving the electron spectrum unconstrained at lower energies. The synchrotron spectrum above 100 MeV is slightly harder than for the quiescent Crab, which may reflect a separate electron population and/or an increase in the magnetic-field strength in the emission zone that shifts a harder section of a curved synchrotron spectrum into the frequency band accessible with the *Fermi*-LAT. Neglecting the weak modifications arising from the possibility of mildly relativistic bulk motion, we suggest that some excess electron acceleration took place.

From classical electrodynamics, the Lorentz factor of electrons that would emit 200 MeV synchrotron radiation is

$$\gamma_{\rm sy} = 3 \times 10^9 \left(\frac{B}{\rm mG}\right)^{-0.5} , \tag{A.9}$$

and their energy-loss rate and life time are

$$\dot{E}_{\rm sy} = (8 \times 10^{-3}\,{\rm erg/s}) \left(\frac{B}{\rm mG}\right), \qquad \tau_{\rm sy} = (3 \times 10^5\,{\rm s}) \left(\frac{B}{\rm mG}\right)^{-1.5} . \tag{A.10}$$

Assuming a magnetic field of 1 mG in the emission region, similar to that deduced in [209], the flare duration $\tau_{\rm sy}$ is on the order of a few days, which is consistent with observed flares at a few hundred MeV. If the magnetic field were significantly stronger than 1 mG, the synchrotron lifetime would become very short compared to the flare duration, and so the electron population would need to be continuously replenished to sustain the flare. Thus, the main cause of the synchrotron flare was likely the injection of a large number of excess electrons at PeV energies.

[209] consider a model in which electrons are injected into the magnetic field of the pulsar wind zone and produce synchrotron gamma rays through acceleration in reconnection regions of the magnetic field. Assuming the electrons reach an equilibrium spectrum described by a differential power law with index between $3.0-3.6$ and with a characteristic cut-off at $\gamma = 3 \times 10^9$ for flares, they suggest variability above $\sim 1\,\mathrm{TeV}$ of roughly 10% with more substantial changes above $\sim 10\,\mathrm{TeV}$ as a result of inverse-Compton scattering. However, inverse-Compton scattering of soft photons by electrons with Lorentz factors $\sim 10^9$ is heavily Klein-Nishina suppressed and would provide gamma rays in the PeV

band, beyond the reach of VERITAS. Excess electrons with Lorentz factors of $\gamma_{\rm IC} \simeq 10^7$ may produce a flux enhancement at TeV energies, but the non-detection with VERITAS poses challenges for this model and thus constrains the number of electrons with Lorentz factors of $\gamma_{\rm IC}$.

The number of electrons with Lorentz factors of $\sim 3 \times 10^9$ can be estimated as

$$N_{\rm e,sy} = \frac{L_{\rm sy}}{\dot{E}_{\rm sy}} \simeq 6 \times 10^{37} \left(\frac{B}{\rm mG}\right)^{-1} , \tag{A.11}$$

where $L_{\rm sy}$ is the synchrotron luminosity at 200 MeV. To calculate the number of electrons that may inverse-Compton scatter soft (infrared, IR) photons into the TeV band, we need to know the density of low-frequency radiation in the nebula. To this end we use $L_{\rm soft} \sim 10^{37}$ erg s^{-1} [227] as the pulsar wind nebula (PWN) luminosity in IR photons, $\epsilon_{\rm soft} \sim 0.1\,\rm eV$ as the photon energy, and $d_{\rm PWN} \simeq 1\,\rm pc$ as the characteristic size of the Crab Nebula. The density of IR photons is then

$$n_{\rm soft} \simeq \frac{L_{\rm soft}}{4\pi\, d_{\rm PWN}^2\, c\epsilon_{\rm soft}} \simeq 20~{\rm cm}^{-3}. \tag{A.12}$$

Using the upper limit on an extra flux component $> 1\,\rm TeV$ given in Table A.1, we find that the inverse-Compton luminosity $L_{\rm IC} \lesssim 4 \times 10^{32}$ erg s^{-1}. The number of electrons that upscatter photons to TeV energies is given by

$$N_{\rm e,IC} = \frac{L_{\rm IC}}{\sigma_{\rm T} n_{\rm soft} c \times \gamma m_e c^2}, \tag{A.13}$$

where $\sigma_{\rm T}$ is the Thomson cross-section. Ignoring the moderate Klein-Nishina suppression (the kinematic parameter $4\,\epsilon_{\rm soft}\epsilon_\gamma/(m_e^2\, c^4) \simeq 10$), the upper limit derived on excess TeV gamma rays corresponds to at most

$$N_{\rm e,IC}\left(\gamma \approx 10^7\right) \lesssim 10^{44} . \tag{A.14}$$

Assuming for ease of exposition that the spectrum of excess electrons follows a power law, $N_e(\gamma) \propto \gamma^{-s}$, the corresponding constraint on the spectral index is

$$s \lesssim \frac{6.2 + \log\left(\frac{B}{\mathrm{mG}}\right)}{2.5 - \frac{1}{2}\log\left(\frac{B}{\mathrm{mG}}\right)}\ , \tag{A.15}$$

which permits $s \simeq 2.5$ for the fiducial magnetic-field strength of 1 mG. This index is harder than that assumed by [209] and constrains the number of electrons that may be responsible for the Crab flare. Future observations with VERITAS or next-generation telescope arrays will likely provide more stringent constraints.

APPENDIX B

MEASURING THE SHAPES OF PULSES IN THE VERITAS ELECTRONICS

The goal of this project was to determine and quantify idiosyncrasies (e.g., nonlinear effects) in the electronics chain used on site at VERITAS. This chain comprises the photomultiplier tube (PMT) and the FADC used to digitize the pulses from the PMT. Such effects must be taken into account in simulations of the electronics chain of VERITAS for an accurate energy reconstruction to be possible.

B.1 Experimental Setup

A PicoQuant 638 nm pulsed laser (model LDH 8-1-469) was triggered at 200 Hz by a Stanford delay/pulse generator (model DG535). The laser fired picosecond pulses of red light through a series of up to three Edmund Optics non-reflective visible neutral density filters (model 64-352; contained optical densities 0.5, 0.6, 0.9, 1.0, 1.3, 1.5, 2.0, 2.5, 3.0) into a spare VERITAS PMT (both Hamamatsu and Photonis tubes were tested). The optical density (OD) of a neutral density filter tells the percent transmission T by

$$T = 10^{-\mathrm{OD}} \times 100. \tag{B.1}$$

All of the aforementioned components were secured to a black base using optical mounts. The PMT pre-amplifier was biased at ±5 V, and the high-voltage was set to 800 V for the Hamamatsu PMT and 1000 V for the Photonis. The charge-injection line was terminated at 50 Ω to avoid signal pickup. The coaxial signal cable was connected to a spare 75 Ω VERITAS cable procured from D. Kieda (University of Utah), which connected to the FADC or oscilloscope with 75 Ω terminator. A flat-black metal casing was placed over the components on optical mounts to ensure darkness in the enclosure. Lastly, a black cloth was placed over the enclosure to further reduce contamination by stray light. A picture of the experimental setup is given in Figure B.1.

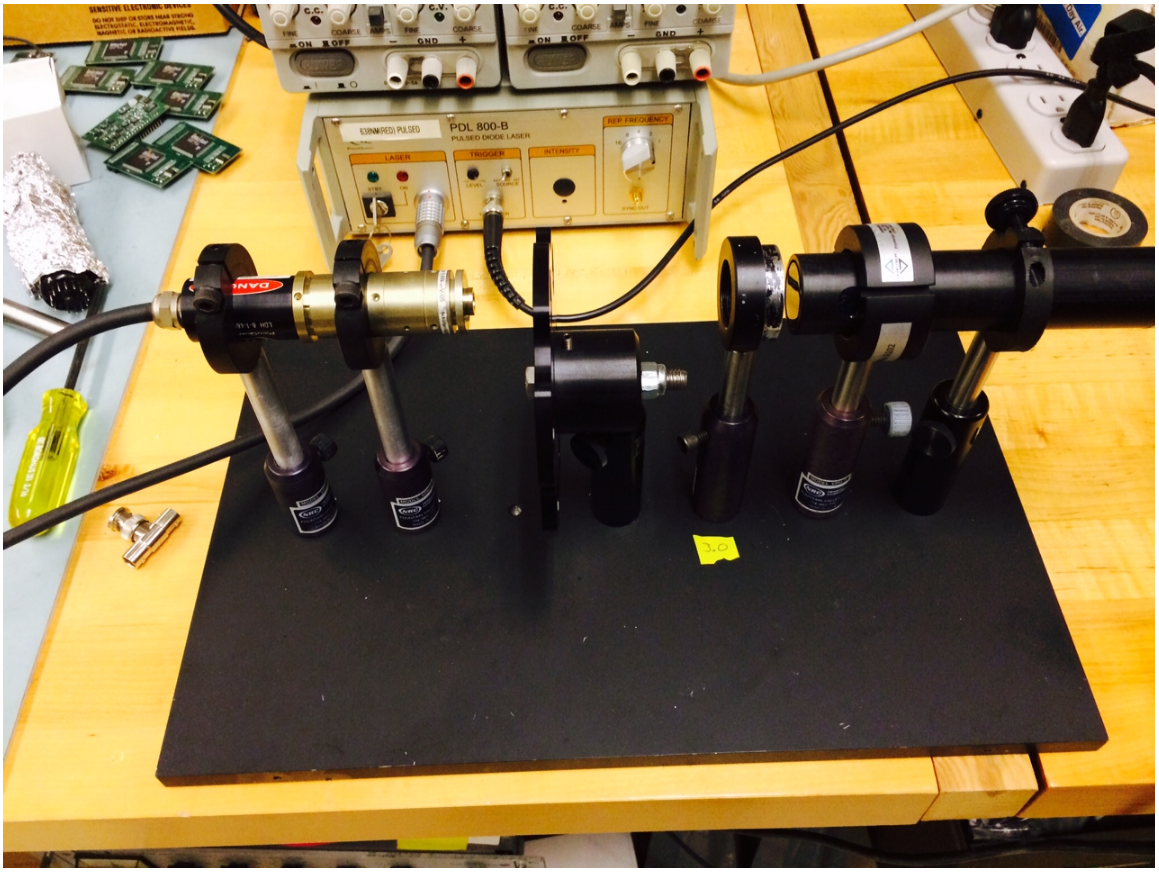

Figure B.1: Laser setup in J. Buckley's lab at Washington Univeristy in St. Louis. Pictured are the PicoQuant pulsed 638 nm laser (*left*), adjustable neutral density filter wheel (*middle-left*), secondary filter holder (*middle-right*), and Hamamatsu PMT (*right*).

B.2 Procedure

Traces from the PMT for each optical density configuration were recorded on the oscilloscope before being recorded in the FADC. Ten traces in the FADC were recorded by hand using the program *testfadc* to dump the raw data to a terminal and copy-pasting to a file; there did not appear to be any evident means to automate this process. A total of 128 samples were read out for each recorded pulse. The average pulse amplitude for each configuration was then calculated by assuming one pulse as a template and then aligning the other pulses for averaging (this eliminates effects due to timing jitter).

B.3 Results

There are two main results that have been better quantified by this study:

- Saturation of pulses at 255 digital counts in the high-gain regime of the FADC
- Nonlinearity in the low-gain regime.

These results are illustrated in Figure B.2 and Figure B.3. Example traces that can be used in a template-matching method in the simulations are shown in Figure B.2, Figure B.3, and Figure B.6.

The results shown here were later improved in work done by former graduate student T. Nguyen (Georgia Tech) using a larger set of OD filters in order to obtain a finer sampling of templates. These templates are now in use in the Camera And Readout Electronics (CARE) simulation package, which is maintained by N. Otte (Georgia Tech) and will improve the energy reconstruction of the VERITAS analysis.

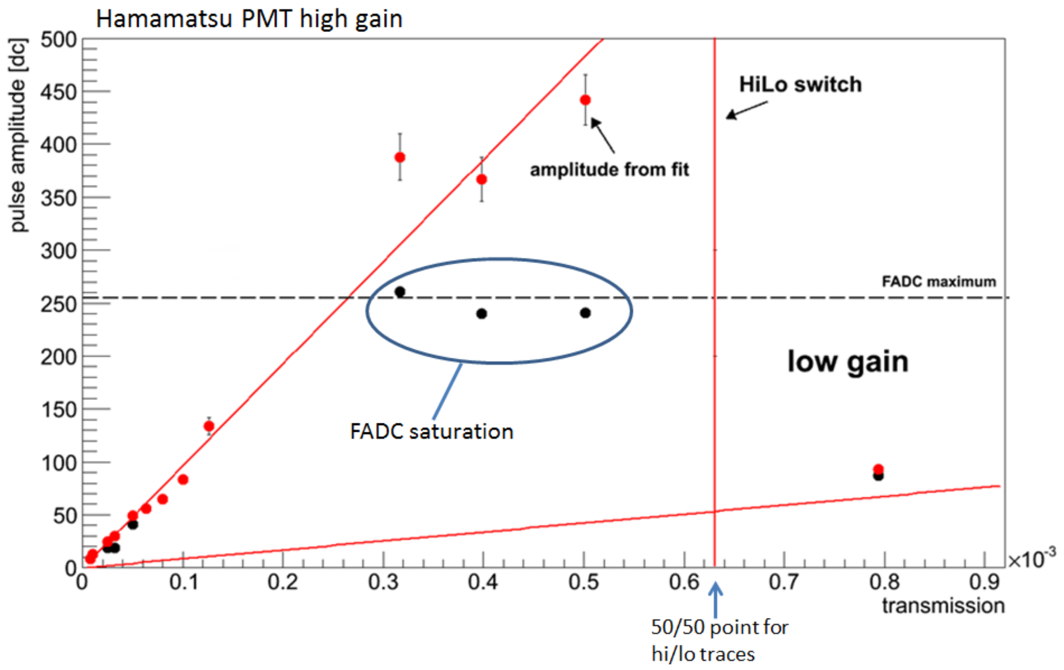

Figure B.2: High-gain amplitude response across varying levels of light for the Hamamatsu PMT. The straight, red lines are linear fits to the data points for high gain (and the same for low gain shown in Figure B.3). The black points are average amplitudes for one light level (or equivalently, one OD value), whereas the red points are computed by adopting one trace as a template, fitting each recorded trace for the given OD with a Gaussian, and time-shifting and amplitude-scaling to best match the template trace before averaging. The FADC maximum is shown as the dashed black line, and note that the red points extend beyond the FADC maximum since the truncated traces are all fit with Gaussian shapes.

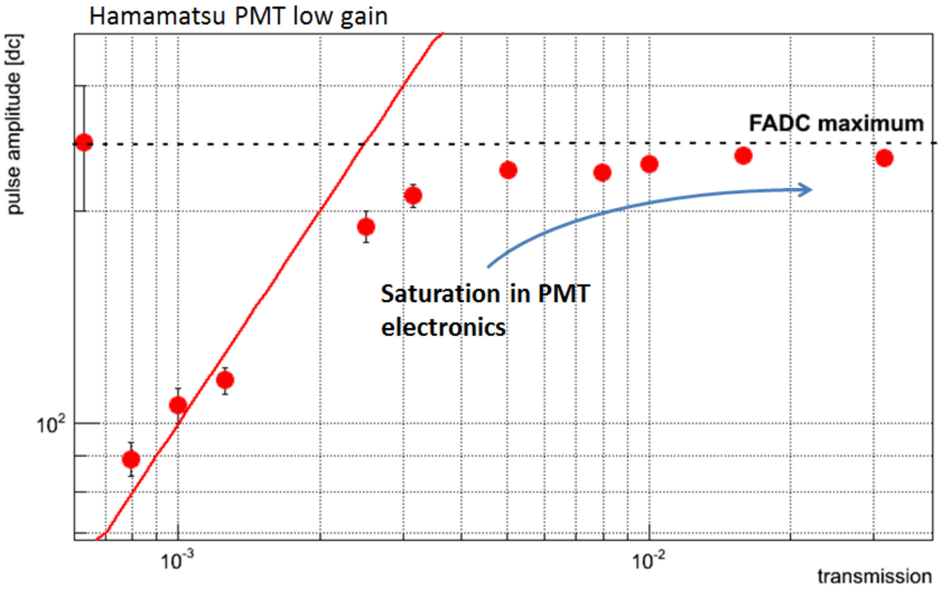

Figure B.3: Low-gain amplitude response across varying levels of light for the Hamamatsu PMT. The red points are computed in the same manner described above. The pulse amplitudes clearly do not follow a linear progression.

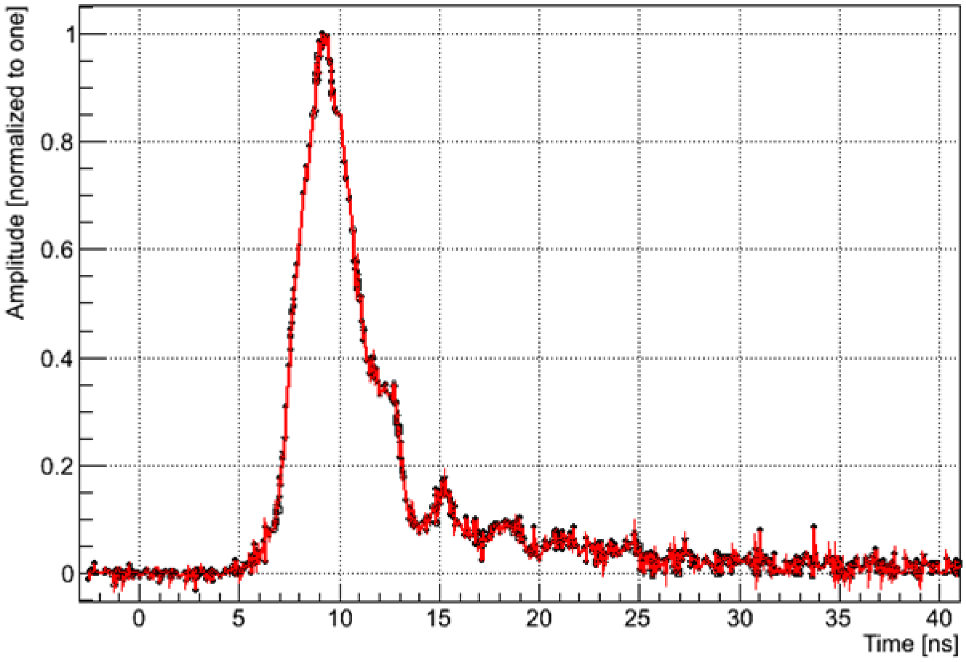

Figure B.4: Average high-gain pulse shape obtained from averaging all recorded traces.

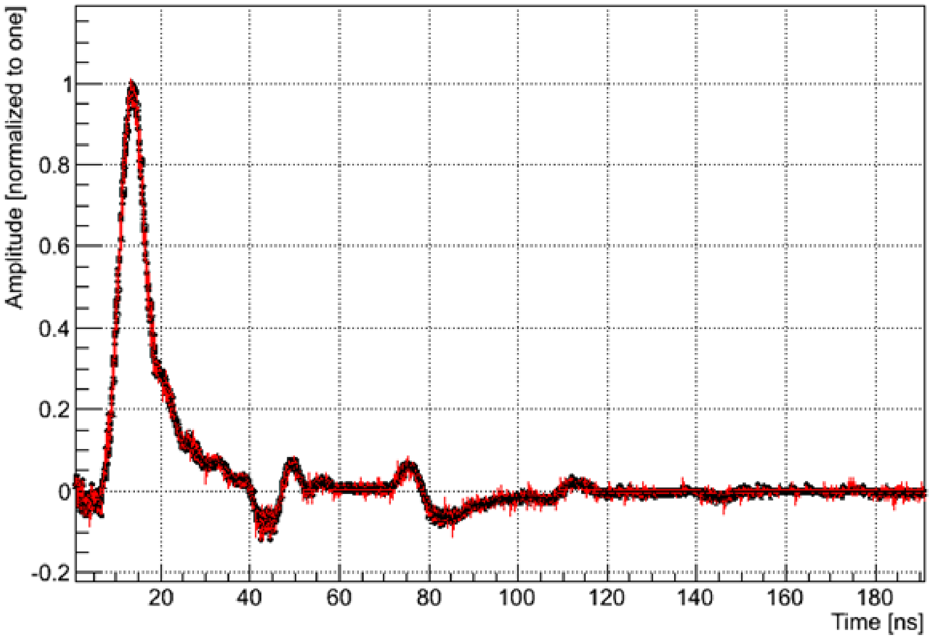

Figure B.5: Average low-gain pulse shape obtained from averaging all recorded traces in the low-gain linear regime.

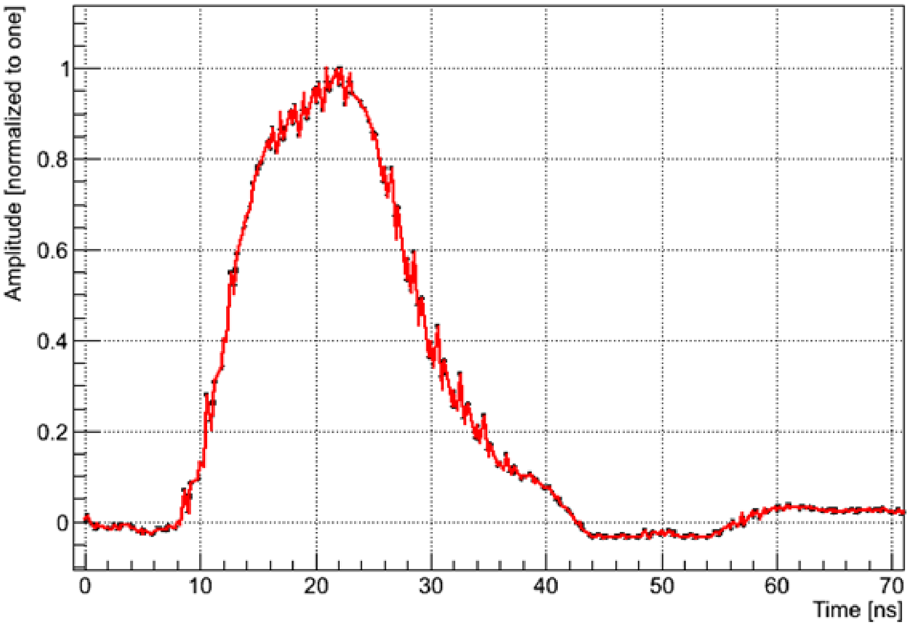

Figure B.6: An example of a low-gain trace in the nonlinear regime where significant pulse broadening can be seen.

REFERENCES

[1] T. C. Weekes, M. F. Cawley, D. J. Fegan, K. G. Gibbs, A. M. Hillas, P. W. Kowk, R. C. Lamb, D. A. Lewis, D. Macomb, N. A. Porter, P. T. Reynolds, and G. Vacanti, "Observation of TeV gamma rays from the Crab nebula using the atmospheric Cerenkov imaging technique," *The Astrophysical Journal*, vol. 342, pp. 379–395, Jul. 1989.

[2] S. P. Wakely and D. Horan, "TeVCat: An online catalog for Very High Energy Gamma-Ray Astronomy," *International Cosmic Ray Conference*, vol. 3, pp. 1341–1344, 2008.

[3] VERITAS Collaboration, E. Aliu, T. Arlen, T. Aune, M. Beilicke, W. Benbow, A. Bouvier, S. M. Bradbury, J. H. Buckley, V. Bugaev, K. Byrum, A. Cannon, A. Cesarini, J. L. Christiansen, L. Ciupik, E. Collins-Hughes, M. P. Connolly, W. Cui, R. Dickherber, C. Duke, M. Errando, A. Falcone, J. P. Finley, G. Finnegan, L. Fortson, A. Furniss, N. Galante, D. Gall, K. Gibbs, G. H. Gillanders, S. Godambe, S. Griffin, J. Grube, R. Guenette, G. Gyuk, D. Hanna, J. Holder, H. Huan, G. Hughes, C. M. Hui, T. B. Humensky, A. Imran, P. Kaaret, N. Karlsson, M. Kertzman, D. Kieda, H. Krawczynski, F. Krennrich, M. J. Lang, M. Lyutikov, A. S. Madhavan, G. Maier, P. Majumdar, S. McArthur, A. McCann, M. McCutcheon, P. Moriarty, R. Mukherjee, P. Nuñez, R. A. Ong, M. Orr, A. N. Otte, N. Park, J. S. Perkins, F. Pizlo, M. Pohl, H. Prokoph, J. Quinn, K. Ragan, L. C. Reyes, P. T. Reynolds, E. Roache, H. J. Rose, J. Ruppel, D. B. Saxon, M. Schroedter, G. H. Sembroski, G. D. Şentürk, A. W. Smith, D. Staszak, G. Tevsić, M. Theiling, S. Thibadeau, K. Tsurusaki, J. Tyler, A. Varlotta, V. V. Vassiliev, S. Vincent, M. Vivier, S. P. Wakely, J. E. Ward, T. C. Weekes, A. Weinstein, T. Weisgarber, D. A. Williams, and B. Zitzer, "Detection of Pulsed Gamma Rays Above 100 GeV from the Crab Pulsar," *Science*, vol. 334, pp. 69–, Oct. 2011. arXiv: `1108.3797 [astro-ph.HE]`.

[4] S. Ansoldi, L. A. Antonelli, P. Antoranz, A. Babic, P. Bangale, U. Barres de Almeida, J. A. Barrio, J. Becerra González, W. Bednarek, E. Bernardini, B. Biasuzzi, A. Biland, O. Blanch, S. Bonnefoy, G. Bonnoli, F. Borracci, T. Bretz, E. Carmona, A. Carosi, P. Colin, E. Colombo, J. L. Contreras, J. Cortina, S. Covino, P. Da Vela, F. Dazzi, A. De Angelis, G. De Caneva, B. De Lotto, E. de Oña Wilhelmi, C. Delgado Mendez, F. Di Pierro, D. Dominis Prester, D. Dorner, M. Doro, S. Einecke, D. Eisenacher Glawion, D. Elsaesser, A. Fernández-Barral, D. Fidalgo, M. V. Fonseca, L. Font, K. Frantzen, C. Fruck, D. Galindo, R. J. García López, M. Garczarczyk, D. Garrido Terrats, M. Gaug, N. Godinović, A. González Muñoz, S. R. Gozzini, Y. Hanabata, M. Hayashida, J. Herrera, K. Hirotani, J. Hose, D. Hrupec, G. Hughes, W. Idec, H. Kellermann, M. L. Knoetig, K. Kodani, Y. Konno, J. Krause, H. Kubo, J. Kushida, A. La Barbera, D. Lelas, N. Lewandowska, E.

Lindfors, S. Lombardi, F. Longo, M. López, R. López-Coto, A. López-Oramas, E. Lorenz, M. Makariev, K. Mallot, G. Maneva, K. Mannheim, L. Maraschi, B. Marcote, M. Mariotti, M. Martínez, D. Mazin, U. Menzel, J. M. Miranda, R. Mirzoyan, A. Moralejo, P. Munar-Adrover, D. Nakajima, V. Neustroev, A. Niedzwiecki, M. Nevas Rosillo, K. Nilsson, K. Nishijima, K. Noda, R. Orito, A. Overkemping, S. Paiano, M. Palatiello, D. Paneque, R. Paoletti, J. M. Paredes, X. Paredes-Fortuny, M. Persic, J. Poutanen, P. G. Prada Moroni, E. Prandini, I. Puljak, R. Reinthal, W. Rhode, M. Ribó, J. Rico, J. Rodriguez Garcia, T. Saito, K. Saito, K. Satalecka, V. Scalzotto, V. Scapin, C. Schultz, T. Schweizer, S. N. Shore, A. Sillanpää, J. Sitarek, I. Snidaric, D. Sobczynska, A. Stamerra, T. Steinbring, M. Strzys, L. Takalo, H. Takami, F. Tavecchio, P. Temnikov, T. Terzić, D. Tescaro, M. Teshima, J. Thaele, D. F. Torres, T. Toyama, A. Treves, J. Ward, M. Will, and R. Zanin, "Teraelectronvolt pulsed emission from the Crab Pulsar detected by MAGIC," *Astronomy & Astrophysics*, vol. 585, A133, A133, Jan. 2016. arXiv: `1510.07048 [astro-ph.HE]`.

[5] K. S. Cheng, C. Ho, and M. Ruderman, "Energetic Radiation from Rapidly Spinning Pulsars. II. VELA and Crab," *The Astrophysical Journal*, vol. 300, p. 522, Jan. 1986.

[6] A. A. Abdo, M. Ajello, A. Allafort, L. Baldini, J. Ballet, G. Barbiellini, M. G. Baring, D. Bastieri, A. Belfiore, R. Bellazzini, and et al., "The Second Fermi Large Area Telescope Catalog of Gamma-Ray Pulsars," *The Astrophysical Journal Supplements*, vol. 208, 17, p. 17, Oct. 2013. arXiv: `1305.4385 [astro-ph.HE]`.

[7] E. Aliu, S. Archambault, A. Archer, T. Aune, A. Barnacka, M. Beilicke, W. Benbow, R. Bird, J. H. Buckley, V. Bugaev, K. Byrum, J. V. Cardenzana, M. Cerruti, X. Chen, L. Ciupik, M. P. Connolly, W. Cui, H. J. Dickinson, J. Dumm, J. D. Eisch, M. Errando, A. Falcone, Q. Feng, J. P. Finley, H. Fleischhack, P. Fortin, L. Fortson, A. Furniss, G. H. Gillanders, S. Griffin, S. T. Griffiths, J. Grube, G. Gyuk, N. Håkansson, D. Hanna, J. Holder, T. B. Humensky, C. A. Johnson, P. Kaaret, P. Kar, M. Kertzman, D. Kieda, F. Krennrich, S. Kumar, M. J. Lang, M. Lyutikov, A. S. Madhavan, G. Maier, S. McArthur, A. McCann, K. Meagher, J. Millis, P. Moriarty, R. Mukherjee, D. Nieto, A. O'Faoláin de Bhróithe, R. A. Ong, A. N. Otte, N. Park, M. Pohl, A. Popkow, H. Prokoph, E. Pueschel, J. Quinn, K. Ragan, L. C. Reyes, P. T. Reynolds, G. T. Richards, E. Roache, M. Santander, G. H. Sembroski, K. Shahinyan, A. W. Smith, D. Staszak, I. Telezhinsky, J. V. Tucci, J. Tyler, A. Varlotta, S. Vincent, S. P. Wakely, A. Weinstein, D. A. Williams, A. Zajczyk, and B. Zitzer, "A Search for Pulsations from Geminga above 100 GeV with VERITAS," *The Astrophysical Journal*, vol. 800, 61, p. 61, Feb. 2015. arXiv: `1412.4734 [astro-ph.HE]`.

[8] E. Aliu, S. Archambault, A. Archer, W. Benbow, R. Bird, J. Biteau, M. Buchovecky, J. H. Buckley, V. Bugaev, K. Byrum, J. V. Cardenzana, M. Cerruti, X. Chen, L. Ciupik, M. P. Connolly, W. Cui, H. J. Dickinson, J. D. Eisch, A. Falcone, Q. Feng, J. P. Finley, H. Fleischhack, A. Flinders, P. Fortin, L. Fortson, A. Furniss,

G. H. Gillanders, S. Griffin, J. Grube, G. Gyuk, M. Hütten, N. Håkansson, J. Holder, T. B. Humensky, C. A. Johnson, P. Kaaret, P. Kar, N. Kelley-Hoskins, M. Kertzman, D. Kieda, M. Krause, M. J. Lang, A. Loo, G. Maier, S. McArthur, A. McCann, K. Meagher, P. Moriarty, R. Mukherjee, T. Nguyen, D. Nieto, A. O'Faoláin de Bhróithe, R. A. Ong, A. N. Otte, D. Pandel, N. Park, V. Pelassa, A. Petrashyk, M. Pohl, A. Popkow, E. Pueschel, J. Quinn, K. Ragan, P. T. Reynolds, G. T. Richards, E. Roache, C. Rulten, M. Santander, G. H. Sembroski, K. Shahinyan, A. W. Smith, D. Staszak, I. Telezhinsky, J. V. Tucci, J. Tyler, A. Varlotta, S. Vincent, S. P. Wakely, O. M. Weiner, A. Weinstein, A. Wilhelm, D. A. Williams, B. Zitzer, M. Chernyakova, and M. S. E. Roberts, "A Search for Very High Energy Gamma Rays from the Missing Link Binary Pulsar J1023+0038 with VERITAS," *The Astrophysical Journal*, vol. 831, 193, p. 193, Nov. 2016. arXiv: `1609.01692 [astro-ph.HE]`.

[9] G. Brumfiel, "Air force had early warning of pulsars," *Nature*, vol. 448, pp. 974–975, Aug. 2007.

[10] A. Hewish, S. J. Bell, J. D. H. Pilkington, P. F. Scott, and R. A. Collins, "Observation of a Rapidly Pulsating Radio Source," *Nature*, vol. 217, pp. 709–713, Feb. 1968.

[11] F. Pacini, "Energy Emission from a Neutron Star," *Nature*, vol. 216, pp. 567–568, Nov. 1967.

[12] T. Gold, "Rotating Neutron Stars as the Origin of the Pulsating Radio Sources," *Nature*, vol. 218, pp. 731–732, May 1968.

[13] L. Ferrario, A. Melatos, and J. Zrake, "Magnetic Field Generation in Stars," *Space Science Reviews*, vol. 191, pp. 77–109, Oct. 2015. arXiv: `1504.08074 [astro-ph.SR]`.

[14] R. N. Manchester, G. B. Hobbs, A. Teoh, and M. Hobbs, "The Australia Telescope National Facility Pulsar Catalogue," *The Astronomical Journal*, vol. 129, pp. 1993–2006, Apr. 2005. eprint: `astro-ph/0412641`.

[15] N. Chamel, P. Haensel, J. L. Zdunik, and A. F. Fantina, "On the Maximum Mass of Neutron Stars," *International Journal of Modern Physics E*, vol. 22, 1330018, p. 1 330 018, Jul. 2013. arXiv: `1307.3995 [astro-ph.HE]`.

[16] R. W. Romani, "Gamma-Ray Pulsars: Radiation Processes in the Outer Magnetosphere," *The Astrophysical Journal*, vol. 470, p. 469, Oct. 1996.

[17] A. Lyne and F. Graham-Smith, *Pulsar Astronomy*. Mar. 2012.

[18] A. McCann, "Discovery of Emission above 100 GeV from The Crab Pulsar With VERITAS," PhD thesis, McGill University, 2011.

[19] P. Goldreich and W. H. Julian, “Pulsar Electrodynamics,” *The Astrophysical Journal*, vol. 157, p. 869, Aug. 1969.

[20] J. Pétri, “Theory of pulsar magnetosphere and wind,” *Journal of Plasma Physics*, vol. 82, no. 5, 635820502, p. 635 820 502, Oct. 2016. arXiv: `1608.04895 [astro-ph.HE]`.

[21] E. Aliu, H. Anderhub, L. A. Antonelli, P. Antoranz, M. Backes, C. Baixeras, J. A. Barrio, H. Bartko, D. Bastieri, J. K. Becker, W. Bednarek, K. Berger, E. Bernardini, C. Bigongiari, A. Biland, R. K. Bock, G. Bonnoli, P. Bordas, V. Bosch-Ramon, T. Bretz, I. Britvitch, M. Camara, E. Carmona, A. Chilingarian, S. Commichau, J. L. Contreras, J. Cortina, M. T. Costado, S. Covino, V. Curtef, F. Dazzi, A. De Angelis, E. De Cea del Pozo, R. de los Reyes, B. De Lotto, M. De Maria, F. De Sabata, C. Delgado Mendez, A. Dominguez, D. Dorner, M. Doro, D. Elsässer, M. Errando, M. Fagiolini, D. Ferenc, E. Fernandez, R. Firpo, M. V. Fonseca, L. Font, N. Galante, R. J. Garcia Lopez, M. Garczarczyk, M. Gaug, F. Goebel, D. Hadasch, M. Hayashida, A. Herrero, D. Höhne, J. Hose, C. C. Hsu, S. Huber, T. Jogler, D. Kranich, A. La Barbera, A. Laille, E. Leonardo, E. Lindfors, S. Lombardi, F. Longo, M. Lopez, E. Lorenz, P. Majumdar, G. Maneva, N. Mankuzhiyil, K. Mannheim, L. Maraschi, M. Mariotti, M. Martinez, D. Mazin, M. Meucci, M. Meyer, J. M. Miranda, R. Mirzoyan, M. Moles, A. Moralejo, D. Nieto, K. Nilsson, J. Ninkovic, N. Otte, I. Oya, R. Paoletti, J. M. Paredes, M. Pasanen, D. Pascoli, F. Pauss, R. G. Pegna, M. A. Perez-Torres, M. Persic, L. Peruzzo, A. Piccioli, F. Prada, E. Prandini, N. Puchades, A. Raymers, W. Rhode, M. Ribó, J. Rico, M. Rissi, A. Robert, S. Rügamer, A. Saggion, T. Y. Saito, M. Salvati, M. Sanchez-Conde, P. Sartori, K. Satalecka, V. Scalzotto, V. Scapin, T. Schweizer, M. Shayduk, K. Shinozaki, S. N. Shore, N. Sidro, A. Sierpowska-Bartosik, A. Sillanpää, D. Sobczynska, F. Spanier, A. Stamerra, L. S. Stark, L. Takalo, F. Tavecchio, P. Temnikov, D. Tescaro, M. Teshima, M. Tluczykont, D. F. Torres, N. Turini, H. Vankov, A. Venturini, V. Vitale, R. M. Wagner, W. Wittek, V. Zabalza, F. Zandanel, R. Zanin, J. Zapatero, O. C. de Jager, E. de Ona Wilhelmi, and MAGIC Collaboration, “Observation of Pulsed γ-Rays Above 25 GeV from the Crab Pulsar with MAGIC,” *Science*, vol. 322, p. 1221, Nov. 2008. arXiv: `0809.2998`.

[22] P. A. Sturrock, “A Model of Pulsars,” *The Astrophysical Journal*, vol. 164, p. 529, Mar. 1971.

[23] M. A. Ruderman and P. G. Sutherland, “Theory of pulsars - Polar caps, sparks, and coherent microwave radiation,” *The Astrophysical Journal*, vol. 196, pp. 51–72, Feb. 1975.

[24] A. N. Timokhin and A. K. Harding, “On the Polar Cap Cascade Pair Multiplicity of Young Pulsars,” *The Astrophysical Journal*, vol. 810, 144, p. 144, Sep. 2015. arXiv: `1504.02194 [astro-ph.HE]`.

[25] A. K. Harding and A. G. Muslimov, “Pulsar Polar Cap Heating and Surface Thermal X-Ray Emission. II. Inverse Compton Radiation Pair Fronts,” *The Astrophysical Journal*, vol. 568, pp. 862–877, Apr. 2002. eprint: `astro-ph/0112392`.

[26] A. K. Harding, M. G. Baring, and P. L. Gonthier, “Photon-Splitting Cascades in Gamma-Ray Pulsars and the Spectrum of PSR 1509-58,” *The Astrophysical Journal*, vol. 476, pp. 246–260, Feb. 1997. eprint: `astro-ph/9609167`.

[27] J. Arons, “Pair creation above pulsar polar caps - Geometrical structure and energetics of slot gaps,” *The Astrophysical Journal*, vol. 266, pp. 215–241, Mar. 1983.

[28] J. K. Daugherty and A. K. Harding, “Gamma-Ray Pulsars: Emission from Extended Polar CAP Cascades,” *The Astrophysical Journal*, vol. 458, p. 278, Feb. 1996. eprint: `astro-ph/9508155`.

[29] A. G. Muslimov and A. K. Harding, “Extended Acceleration in Slot Gaps and Pulsar High-Energy Emission,” *The Astrophysical Journal*, vol. 588, pp. 430–440, May 2003. eprint: `astro-ph/0301023`.

[30] ——, “High-Altitude Particle Acceleration and Radiation in Pulsar Slot Gaps,” *The Astrophysical Journal*, vol. 606, pp. 1143–1153, May 2004. eprint: `astro-ph/0402462`.

[31] K. S. Cheng, C. Ho, and M. Ruderman, “Energetic radiation from rapidly spinning pulsars. I - Outer magnetosphere gaps. II - VELA and Crab,” *The Astrophysical Journal*, vol. 300, pp. 500–539, Jan. 1986.

[32] Y. Chai, K.-S. Cheng, and J. Takata, “Probing Gamma-ray Emission of Geminga and Vela with Non-stationary Models,” *Journal of Astronomy and Space Sciences*, vol. 33, pp. 75–92, Jun. 2016.

[33] K. Chen and M. Ruderman, “Pulsar death lines and death valley,” *The Astrophysical Journal*, vol. 402, pp. 264–270, Jan. 1993.

[34] K. P. Watters, R. W. Romani, P. Weltevrede, and S. Johnston, “An Atlas for Interpreting γ-Ray Pulsar Light Curves,” *The Astrophysical Journal*, vol. 695, pp. 1289–1301, Apr. 2009. arXiv: `0812.3931`.

[35] M. Pierbattista, A. K. Harding, I. A. Grenier, T. J. Johnson, P. A. Caraveo, M. Kerr, and P. L. Gonthier, “Light-curve modelling constraints on the obliquities and aspect angles of the young Fermi pulsars,” *Astronomy & Astrophysics*, vol. 575, A3, A3, Mar. 2015. arXiv: `1403.3849 [astro-ph.HE]`.

[36] G. C. K. Leung, J. Takata, C. W. Ng, A. K. H. Kong, P. H. T. Tam, C. Y. Hui, and K. S. Cheng, “Fermi-LAT Detection of Pulsed Gamma-Rays above 50 GeV from

the Vela Pulsar," *The Astrophysical Journal Letters*, vol. 797, L13, p. L13, Dec. 2014. arXiv: `1410.5208 [astro-ph.HE]`.

[37] A. A. Abdo, M. Ackermann, M. Ajello, A. Allafort, W. B. Atwood, L. Baldini, J. Ballet, G. Barbiellini, M. G. Baring, D. Bastieri, B. M. Baughman, K. Bechtol, R. Bellazzini, B. Berenji, R. D. Blandford, E. D. Bloom, E. Bonamente, A. W. Borgland, A. Bouvier, J. Bregeon, A. Brez, M. Brigida, P. Bruel, T. H. Burnett, S. Buson, G. A. Caliandro, R. A. Cameron, P. A. Caraveo, S. Carrigan, J. M. Casandjian, C. Cecchi, Ö. Çelik, A. Chekhtman, C. C. Cheung, J. Chiang, S. Ciprini, R. Claus, J. Cohen-Tanugi, J. Conrad, C. D. Dermer, A. de Luca, F. de Palma, M. Dormody, E. d. C. e. Silva, P. S. Drell, R. Dubois, D. Dumora, C. Farnier, C. Favuzzi, S. J. Fegan, W. B. Focke, P. Fortin, M. Frailis, Y. Fukazawa, S. Funk, P. Fusco, F. Gargano, D. Gasparrini, N. Gehrels, S. Germani, G. Giavitto, B. Giebels, N. Giglietto, F. Giordano, T. Glanzman, G. Godfrey, I. A. Grenier, M.-H. Grondin, J. E. Grove, L. Guillemot, S. Guiriec, D. Hadasch, A. K. Harding, E. Hays, G. Hobbs, D. Horan, R. E. Hughes, M. S. Jackson, G. Jóhannesson, A. S. Johnson, T. J. Johnson, W. N. Johnson, T. Kamae, H. Katagiri, J. Kataoka, N. Kawai, M. Kerr, J. Knödlseder, M. Kuss, J. Lande, L. Latronico, S.-H. Lee, M. Lemoine-Goumard, M. Llena Garde, F. Longo, F. Loparco, B. Lott, M. N. Lovellette, P. Lubrano, A. Makeev, R. N. Manchester, M. Marelli, M. N. Mazziotta, W. McConville, J. E. McEnery, S. McGlynn, C. Meurer, P. F. Michelson, W. Mitthumsiri, T. Mizuno, A. A. Moiseev, C. Monte, M. E. Monzani, A. Morselli, I. V. Moskalenko, S. Murgia, T. Nakamori, P. L. Nolan, J. P. Norris, A. Noutsos, E. Nuss, T. Ohsugi, N. Omodei, E. Orlando, J. F. Ormes, M. Ozaki, D. Paneque, J. H. Panetta, D. Parent, V. Pelassa, M. Pepe, M. Pesce-Rollins, M. Pierbattista, F. Piron, T. A. Porter, S. Rainò, R. Rando, P. S. Ray, M. Razzano, A. Reimer, O. Reimer, T. Reposeur, S. Ritz, L. S. Rochester, A. Y. Rodriguez, R. W. Romani, M. Roth, F. Ryde, H. F.-W. Sadrozinski, A. Sander, P. M. Saz Parkinson, C. Sgrò, E. J. Siskind, D. A. Smith, P. D. Smith, G. Spandre, P. Spinelli, J.-L. Starck, M. S. Strickman, D. J. Suson, H. Takahashi, T. Takahashi, T. Tanaka, J. B. Thayer, J. G. Thayer, D. J. Thompson, L. Tibaldo, D. F. Torres, G. Tosti, A. Tramacere, T. L. Usher, A. Van Etten, V. Vasileiou, C. Venter, N. Vilchez, V. Vitale, A. P. Waite, P. Wang, K. Watters, P. Weltevrede, B. L. Winer, K. S. Wood, T. Ylinen, and M. Ziegler, "The Vela Pulsar: Results from the First Year of Fermi LAT Observations," *The Astrophysical Journal*, vol. 713, pp. 154–165, Apr. 2010. arXiv: `1002.4050 [astro-ph.HE]`.

[38] A. A. Abdo, M. Ackermann, M. Ajello, W. B. Atwood, M. Axelsson, L. Baldini, J. Ballet, G. Barbiellini, M. G. Baring, D. Bastieri, K. Bechtol, R. Bellazzini, B. Berenji, R. D. Blandford, E. D. Bloom, E. Bonamente, A. W. Borgland, J. Bregeon, A. Brez, M. Brigida, P. Bruel, T. H. Burnett, G. A. Caliandro, R. A. Cameron, F. Camilo, P. A. Caraveo, J. M. Casandjian, C. Cecchi, Ö. Çelik, A. Chekhtman, C. C. Cheung, J. Chiang, S. Ciprini, R. Claus, I. Cognard, J. Cohen-Tanugi, L. R. Cominsky, J. Conrad, C. D. Dermer, A. de Angelis, A. de Luca, F. de Palma, S. W. Digel, E. d. C. e. Silva, P. S. Drell, R. Dubois, D. Dumora, C. Espinoza, C. Farnier, C. Favuzzi, S. J. Fegan, E. C. Ferrara, W. B. Focke, M. Frailis, P. C. C. Freire, Y.

Fukazawa, S. Funk, P. Fusco, F. Gargano, D. Gasparrini, N. Gehrels, S. Germani, G. Giavitto, B. Giebels, N. Giglietto, F. Giordano, T. Glanzman, G. Godfrey, I. A. Grenier, M.-H. Grondin, J. E. Grove, L. Guillemot, S. Guiriec, Y. Hanabata, A. K. Harding, M. Hayashida, E. Hays, R. E. Hughes, G. Jóhannesson, A. S. Johnson, R. P. Johnson, T. J. Johnson, W. N. Johnson, S. Johnston, T. Kamae, H. Katagiri, J. Kataoka, N. Kawai, M. Kerr, J. Knödlseder, M. L. Kocian, M. Kramer, F. Kuehn, M. Kuss, J. Lande, L. Latronico, S.-H. Lee, M. Lemoine-Goumard, F. Longo, F. Loparco, B. Lott, M. N. Lovellette, P. Lubrano, A. G. Lyne, A. Makeev, M. Marelli, M. N. Mazziotta, J. E. McEnery, C. Meurer, P. F. Michelson, W. Mitthumsiri, T. Mizuno, A. A. Moiseev, C. Monte, M. E. Monzani, E. Moretti, A. Morselli, I. V. Moskalenko, S. Murgia, T. Nakamori, P. L. Nolan, J. P. Norris, A. Noutsos, E. Nuss, T. Ohsugi, N. Omodei, E. Orlando, J. F. Ormes, M. Ozaki, D. Paneque, J. H. Panetta, D. Parent, V. Pelassa, M. Pepe, M. Pesce-Rollins, M. Pierbattista, F. Piron, T. A. Porter, S. Rainò, R. Rando, P. S. Ray, M. Razzano, A. Reimer, O. Reimer, T. Reposeur, S. Ritz, L. S. Rochester, A. Y. Rodriguez, R. W. Romani, M. Roth, F. Ryde, H. F.-W. Sadrozinski, D. Sanchez, A. Sander, P. M. Saz Parkinson, J. D. Scargle, C. Sgrò, E. J. Siskind, D. A. Smith, P. D. Smith, G. Spandre, P. Spinelli, B. W. Stappers, M. S. Strickman, D. J. Suson, H. Tajima, H. Takahashi, T. Tanaka, J. B. Thayer, J. G. Thayer, G. Theureau, D. J. Thompson, S. E. Thorsett, L. Tibaldo, D. F. Torres, G. Tosti, A. Tramacere, Y. Uchiyama, T. L. Usher, A. Van Etten, V. Vasileiou, N. Vilchez, V. Vitale, A. P. Waite, E. Wallace, P. Wang, K. Watters, P. Weltevrede, B. L. Winer, K. S. Wood, T. Ylinen, and M. Ziegler, "Fermi Large Area Telescope Observations of the Crab Pulsar And Nebula," *The Astrophysical Journal*, vol. 708, pp. 1254–1267, Jan. 2010. arXiv: `0911.2412 [astro-ph.HE]`.

[39] A. N. Otte, E. Aliu, J. L. Contreras, M. Gaug, M. Lopez, and P. Majumdar, "Observation of the Crab Nebula with the MAGIC telescope," *International Cosmic Ray Conference*, vol. 2, pp. 827–830, 2008.

[40] O. C. de Jager, B. C. Raubenheimer, and J. W. H. Swanepoel, "A poweful test for weak periodic signals with unknown light curve shape in sparse data," *Astronomy & Astrophysics*, vol. 221, pp. 180–190, Aug. 1989.

[41] J. Aleksić, E. A. Alvarez, L. A. Antonelli, P. Antoranz, M. Asensio, M. Backes, J. A. Barrio, D. Bastieri, J. Becerra González, W. Bednarek, A. Berdyugin, K. Berger, E. Bernardini, A. Biland, O. Blanch, R. K. Bock, A. Boller, G. Bonnoli, D. Borla Tridon, I. Braun, T. Bretz, A. Cañellas, E. Carmona, A. Carosi, P. Colin, E. Colombo, J. L. Contreras, J. Cortina, L. Cossio, S. Covino, F. Dazzi, A. De Angelis, G. De Caneva, E. De Cea del Pozo, B. De Lotto, C. Delgado Mendez, A. Diago Ortega, M. Doert, A. Domínguez, D. Dominis Prester, D. Dorner, M. Doro, D. Eisenacher, D. Elsaesser, D. Ferenc, M. V. Fonseca, L. Font, C. Fruck, R. J. García López, M. Garczarczyk, D. Garrido, G. Giavitto, N. Godinović, D. Hadasch, D. Häfner, A. Herrero, D. Hildebrand, D. Höhne-Mönch, J. Hose, D. Hrupec, T. Jogler, H. Kellermann, S. Klepser, T. Krähenbühl, J. Krause, J. Kushida, A. La Barbera, D. Lelas, E. Leonardo, E. Lindfors, S. Lombardi, M. López, A. López-

Oramas, E. Lorenz, M. Makariev, G. Maneva, N. Mankuzhiyil, K. Mannheim, L. Maraschi, B. Marcote, M. Mariotti, M. Martínez, D. Mazin, M. Meucci, J. M. Miranda, R. Mirzoyan, J. Moldón, A. Moralejo, P. Munar-Adrover, D. Nieto, K. Nilsson, R. Orito, N. Otte, I. Oya, D. Paneque, R. Paoletti, S. Pardo, J. M. Paredes, S. Partini, M. A. Perez-Torres, M. Persic, L. Peruzzo, M. Pilia, J. Pochon, F. Prada, P. G. Prada Moroni, E. Prandini, I. Puerto Gimenez, I. Puljak, I. Reichardt, R. Reinthal, W. Rhode, M. Ribó, J. Rico, M. Rissi, S. Rügamer, A. Saggion, K. Saito, T. Y. Saito, M. Salvati, K. Satalecka, V. Scalzotto, V. Scapin, C. Schultz, T. Schweizer, M. Shayduk, S. N. Shore, A. Sillanpää, J. Sitarek, I. Snidaric, D. Sobczynska, F. Spanier, S. Spiro, V. Stamatescu, A. Stamerra, B. Steinke, J. Storz, N. Strah, T. Surić, L. Takalo, H. Takami, F. Tavecchio, P. Temnikov, T. Terzić, D. Tescaro, M. Teshima, O. Tibolla, D. F. Torres, A. Treves, M. Uellenbeck, H. Vankov, P. Vogler, R. M. Wagner, Q. Weitzel, V. Zabalza, F. Zandanel, R. Zanin, and K. Hirotani, "Observations of the Crab Pulsar between 25 and 100 GeV with the MAGIC I Telescope," *The Astrophysical Journal*, vol. 742, 43, p. 43, Nov. 2011. arXiv: `1108.5391 [astro-ph.HE]`.

[42] J. Aleksić, S. Ansoldi, L. A. Antonelli, P. Antoranz, A. Babic, P. Bangale, U. Barres de Almeida, J. A. Barrio, J. Becerra González, W. Bednarek, E. Bernardini, B. Biasuzzi, A. Biland, O. Blanch, S. Bonnefoy, G. Bonnoli, F. Borracci, T. Bretz, E. Carmona, A. Carosi, P. Colin, E. Colombo, J. L. Contreras, J. Cortina, S. Covino, P. Da Vela, F. Dazzi, A. De Angelis, G. De Caneva, B. De Lotto, C. Delgado Mendez, M. Doert, D. Dominis Prester, D. Dorner, M. Doro, S. Einecke, D. Eisenacher, D. Elsaesser, E. Farina, D. Ferenc, D. Fidalgo, M. V. Fonseca, L. Font, K. Frantzen, C. Fruck, R. J. García López, M. Garczarczyk, D. Garrido Terrats, M. Gaug, N. Godinović, A. González Muñoz, S. R. Gozzini, D. Hadasch, M. Hayashida, J. Herrera, A. Herrero, D. Hildebrand, K. Hirotani, J. Hose, D. Hrupec, W. Idec, V. Kadenius, H. Kellermann, K. Kodani, Y. Konno, J. Krause, H. Kubo, J. Kushida, A. La Barbera, D. Lelas, N. Lewandowska, E. Lindfors, S. Lombardi, M. López, R. López-Coto, A. López-Oramas, E. Lorenz, I. Lozano, M. Makariev, K. Mallot, G. Maneva, N. Mankuzhiyil, K. Mannheim, L. Maraschi, B. Marcote, M. Mariotti, M. Martínez, D. Mazin, U. Menzel, J. M. Miranda, R. Mirzoyan, A. Moralejo, P. Munar-Adrover, D. Nakajima, A. Niedzwiecki, K. Nilsson, K. Nishijima, K. Noda, N. Nowak, R. Orito, A. Overkemping, S. Paiano, M. Palatiello, D. Paneque, R. Paoletti, J. M. Paredes, X. Paredes-Fortuny, S. Partini, M. Persic, P. G. Prada Moroni, E. Prandini, S. Preziuso, I. Puljak, R. Reinthal, W. Rhode, M. Ribó, J. Rico, J. Rodriguez Garcia, S. Rügamer, A. Saggion, T. Y. Saito, K. Saito, K. Satalecka, V. Scalzotto, V. Scapin, C. Schultz, T. Schweizer, S. N. Shore, A. Sillanpää, J. Sitarek, I. Snidaric, D. Sobczynska, F. Spanier, V. Stamatescu, A. Stamerra, T. Steinbring, J. Storz, M. Strzys, S. Sun, T. Surić, L. Takalo, H. Takami, F. Tavecchio, P. Temnikov, T. Terzić, D. Tescaro, M. Teshima, J. Thaele, O. Tibolla, D. F. Torres, T. Toyama, A. Treves, M. Uellenbeck, P. Vogler, R. M. Wagner, and R. Zanin, "Detection of bridge emission above 50 GeV from the Crab pulsar with the MAGIC telescopes," *Astronomy & Astrophysics*, vol. 565, L12, p. L12, May 2014. arXiv: `1402.4219 [astro-ph.HE]`.

[43] G. F. Bignami and P. A. Caraveo, “Geminga: Its Phenomenology, Its Fraternity, and Its Physics,” *Annual Review of Astronomy and Astrophysics*, vol. 34, pp. 331–382, 1996.

[44] J. Faherty, F. M. Walter, and J. Anderson, “The trigonometric parallax of the neutron star Geminga,” *Astrophysics and Space Science*, vol. 308, pp. 225–230, Apr. 2007.

[45] D. L. Bertsch, K. T. S. Brazier, C. E. Fichtel, R. C. Hartman, S. D. Hunter, G. Kanbach, D. A. Kniffen, P. W. Kwok, Y. C. Lin, and J. R. Mattox, “Pulsed high-energy gamma-radiation from Geminga (1E0630 + 178),” *Nature*, vol. 357, p. 306, May 1992.

[46] M. Lyutikov, N. Otte, and A. McCann, “The Very High Energy Emission from Pulsars: A Case for Inverse Compton Scattering,” *The Astrophysical Journal*, vol. 754, 33, p. 33, Jul. 2012. arXiv: `1108.3824 [astro-ph.HE]`.

[47] M. L. Ahnen, S. Ansoldi, L. A. Antonelli, P. Antoranz, A. Babic, B. Banerjee, P. Bangale, U. Barres de Almeida, J. A. Barrio, J. Becerra González, W. Bednarek, E. Bernardini, A. Berti, B. Biasuzzi, A. Biland, O. Blanch, S. Bonnefoy, G. Bonnoli, F. Borracci, T. Bretz, S. Buson, A. Carosi, A. Chatterjee, R. Clavero, P. Colin, E. Colombo, J. L. Contreras, J. Cortina, S. Covino, P. Da Vela, F. Dazzi, A. De Angelis, B. De Lotto, E. de Oña Wilhelmi, F. Di Pierro, M. Doert, A. Domínguez, D. Dominis Prester, D. Dorner, M. Doro, S. Einecke, D. Eisenacher Glawion, D. Elsaesser, V. Fallah Ramazani, A. Fernández-Barral, D. Fidalgo, M. V. Fonseca, L. Font, K. Frantzen, C. Fruck, D. Galindo, R. J. García López, M. Garczarczyk, D. Garrido Terrats, M. Gaug, P. Giammaria, N. Godinović, A. González Muñoz, D. Gora, D. Guberman, D. Hadasch, A. Hahn, Y. Hanabata, M. Hayashida, J. Herrera, J. Hose, D. Hrupec, G. Hughes, W. Idec, K. Kodani, Y. Konno, H. Kubo, J. Kushida, A. La Barbera, D. Lelas, E. Lindfors, S. Lombardi, F. Longo, M. López, R. López-Coto, P. Majumdar, M. Makariev, K. Mallot, G. Maneva, M. Manganaro, K. Mannheim, L. Maraschi, B. Marcote, M. Mariotti, M. Martínez, D. Mazin, U. Menzel, J. M. Miranda, R. Mirzoyan, A. Moralejo, E. Moretti, D. Nakajima, V. Neustroev, A. Niedzwiecki, M. Nievas Rosillo, K. Nilsson, K. Nishijima, K. Noda, L. Nogués, A. Overkemping, S. Paiano, J. Palacio, M. Palatiello, D. Paneque, R. Paoletti, J. M. Paredes, X. Paredes-Fortuny, G. Pedaletti, M. Peresano, L. Perri, M. Persic, J. Poutanen, P. G. Prada Moroni, E. Prandini, I. Puljak, I. Reichardt, W. Rhode, M. Ribó, J. Rico, J. Rodriguez Garcia, T. Saito, K. Satalecka, C. Schultz, T. Schweizer, S. N. Shore, A. Sillanpää, J. Sitarek, I. Snidaric, D. Sobczynska, A. Stamerra, T. Steinbring, M. Strzys, T. Surić, L. Takalo, F. Tavecchio, P. Temnikov, T. Terzić, D. Tescaro, M. Teshima, J. Thaele, D. F. Torres, T. Toyama, A. Treves, G. Vanzo, V. Verguilov, I. Vovk, J. E. Ward, M. Will, M. H. Wu, and R. Zanin, “Search for VHE gamma-ray emission from Geminga pulsar and nebula with the MAGIC telescopes,” *Astronomy & Astrophysics*, vol. 591, A138, A138, Jun. 2016. arXiv: `1603.00730 [astro-ph.HE]`.

[48] R. Dodson, D. Legge, J. E. Reynolds, and P. M. McCulloch, “The Vela Pulsar’s Proper Motion and Parallax Derived from VLBI Observations,” *The Astrophysical Journal*, vol. 596, pp. 1137–1141, Oct. 2003. eprint: `astro-ph/0302374`.

[49] A. A. Abdo, M. Ackermann, W. B. Atwood, R. Bagagli, L. Baldini, J. Ballet, D. L. Band, G. Barbiellini, M. G. Baring, J. Bartelt, and et al., “Fermi Large Area Telescope Observations of the Vela Pulsar,” *The Astrophysical Journal*, vol. 696, pp. 1084–1093, May 2009. arXiv: `0812.2960`.

[50] A. Djannati-Ata, G. Giavitto, M. Holler, B. Rudak, C. Venter, and T. H.E.S. S. Collaboration, “Probing vela pulsar down to 20 gev with h.e.s.s. ii observations,” *AIP Conference Proceedings*, vol. 1792, no. 1, p. 040 028, 2017. eprint: `http://aip.scitation.org/doi/pdf/10.1063/1.4968932`.

[51] R. W. Romani and K. P. Watters, “Constraining Pulsar Magnetosphere Geometry with γ-ray Light Curves,” *The Astrophysical Journal*, vol. 714, pp. 810–824, May 2010. arXiv: `0912.3845 [astro-ph.HE]`.

[52] R.-B. Wang and K. Hirotani, “Death Line of Gamma-Ray Pulsars with Outer Gaps,” *The Astrophysical Journal*, vol. 736, 127, p. 127, Aug. 2011. arXiv: `1105.3030 [astro-ph.HE]`.

[53] J. Takata, Y. Wang, and K. S. Cheng, “Pulsar High Energy Emissions from Outer Gap Accelerator Closed by a Magnetic Pair-creation Process,” *The Astrophysical Journal*, vol. 715, pp. 1318–1326, Jun. 2010. arXiv: `1004.1243 [astro-ph.HE]`.

[54] A. K. Harding and C. Kalapotharakos, “Synchrotron Self-Compton Emission from the Crab and Other Pulsars,” *The Astrophysical Journal*, vol. 811, 63, p. 63, Sep. 2015. arXiv: `1508.06251 [astro-ph.HE]`.

[55] F. A. Aharonian, S. V. Bogovalov, and D. Khangulyan, “Abrupt acceleration of a ‘cold’ ultrarelativistic wind from the Crab pulsar,” *Nature*, vol. 482, pp. 507–509, Feb. 2012.

[56] S. V. Bogovalov and F. A. Aharonian, “Very-high-energy gamma radiation associated with the unshocked wind of the Crab pulsar,” *Monthly Notices of the Royal Astronomical Society*, vol. 313, pp. 504–514, Apr. 2000. eprint: `astro-ph/0003157`.

[57] I. Mochol and J. Pétri, “Very high energy emission as a probe of relativistic magnetic reconnection in pulsar winds,” *Monthly Notices of the Royal Astronomical Society*, vol. 449, pp. L51–L55, Apr. 2015. arXiv: `1501.07123 [astro-ph.HE]`.

[58] R. Zanin, “The Crab pulsar at VHE,” in *European Physical Journal Web of Conferences*, ser. European Physical Journal Web of Conferences, vol. 136, Mar. 2017, p. 03 003. arXiv: `1701.07364 [astro-ph.HE]`.

[59] T. C. Weekes, *Very high energy gamma-ray astronomy*. 2003.

[60] W.-M. Yao, C. Amsler, D. Asner, R. M. Barnett, J. Beringer, P. R. Burchat, C. D. Carone, C. Caso, O. Dahl, G. D’Ambrosio, A. De Gouvea, M. Doser, S. Eidelman, J. L. Feng, T. Gherghetta, M. Goodman, C. Grab, D. E. Groom, A. Gurtu, K. Hagiwara, K. G. Hayes, J. J. Hernández-Rey, K. Hikasa, H. Jawahery, C. Kolda, Y. Kwon, M. L. Mangano, A. V. Manohar, A. Masoni, R. Miquel, K. Mönig, H. Murayama, K. Nakamura, S. Navas, K. A. Olive, L. Pape, C. Patrignani, A. Piepke, G. Punzi, G. Raffelt, J. G. Smith, M. Tanabashi, J. Terning, N. A. Törnqvist, T. G. sTrippe, P. Vogel, T. Watari, C. G. Wohl, R. L. Workman, P. A. Zyla, B. Armstrong, G. Harper, V. S. Lugovsky, P. Schaffner, M. Artuso, K. S. Babu, H. R. Band, E. Barberio, M. Battaglia, H. Bichsel, O. Biebel, P. Bloch, E. Blucher, R. N. Cahn, D. Casper, A. Cattai, A. Ceccucci, D. Chakraborty, R. S. Chivukula, G. Cowan, T. Damour, T. DeGrand, K. Desler, M. A. Dobbs, M. Drees, A. Edwards, D. A. Edwards, V. D. Elvira, J. Erler, V. V. Ezhela, W. Fetscher, B. D. Fields, B. Foster, D. Froidevaux, T. K. Gaisser, L. Garren, H.-J. Gerber, G. Gerbier, L. Gibbons, F. J. Gilman, G. F. Giudice, A. V. Gritsan, M. Grünewald, H. E. Haber, C. Hagmann, I. Hinchliffe, A. Höcker, P. Igo-Kemenes, J. D. JAckson, K. F. Johnson, D. Karlen, B. Kayser, D. Kirkby, S. R. Klein, K. Kleinknecht, I. G. Knowles, R. V. Kowalewski, P. Kreitz, B. Kursche, Y. V. Kuyanov, O. Lahav, P. Langacker, A. Liddle, Z. Ligeti, T. M. Liss, L. Littenberg, J. C. Liu, K. S. Lugovsky, s. B. Lugovsky, T. Mannel, D. M. Manley, W. J. Marciano, A. D. Martin, D. Milstead, M. Narain, P. Nason, Y. Nir, J. A. Peacock, S. A. Prell, A. Quadt, S. Raby, B. N. Ratcliff, E. A. Razuvaev, B. Renk, P. Richardson, S. Roesler, G. Rolandi, M. T. Ronan, L. J. Rosenberg, C. T. Sachrajda, Y. Sakai, S. Sarkar, M. Schmitt, O. Schneider, D. Scott, T. Sjöstrand, G. F. Smoot, P. Sokolsky, S. Spanier, H. Spieler, A. Stahl, T. Stanev, R. E. Streitmatter, T. Sumiyoshi, N. P. Tkachenko, G. H. Trilling, G. Valencia, K. van Bibber, M. G. Vincter, D. R. Ward, B. R. Webber, J. D. Wells, M. Whalley, L. Wolfenstsein, J. Womersley, C. L. Woody, A. Yamamoto, O. V. Zenin, J. Zhang, and R.-Y. Zhu, “Review of Particle Physics,” *Journal of Physics G Nuclear Physics*, vol. 33, pp. 1–1232, Jul. 2006.

[61] A. Bonardi, G. Pühlhofer, S. Hermanutz, and A. Santangelo, “A new solution for mirror coating in γ-ray Cherenkov astronomy,” *Experimental Astronomy*, vol. 38, pp. 1–9, Nov. 2014. arXiv: `1406.0622 [astro-ph.IM]`.

[62] A. N. Otte, “Observation of VHE gamma rays from the vicinity of magnetized neutron stars and development of new photon-detectors for future ground based gamma-ray detectors,” PhD thesis, Technische Universität München, 2007.

[63] J. Holder, R. W. Atkins, H. M. Badran, G. Blaylock, S. M. Bradbury, J. H. Buckley, K. L. Byrum, D. A. Carter-Lewis, O. Celik, Y. C. K. Chow, P. Cogan, W. Cui, M. K. Daniel, I. de la Calle Perez, C. Dowdall, P. Dowkontt, C. Duke, A. D. Falcone, S. J. Fegan, J. P. Finley, P. Fortin, L. F. Fortson, K. Gibbs, G. Gillanders, O. J. Glidewell, J. Grube, K. J. Gutierrez, G. Gyuk, J. Hall, D. Hanna, E. Hays, D. Horan, S. B. Hughes, T. B. Humensky, A. Imran, I. Jung, P. Kaaret, G. E. Kenny, D. Kieda, J. Kildea, J. Knapp, H. Krawczynski, F. Krennrich, M. J. Lang, S. LeBohec, E. Linton, E. K. Little, G. Maier, H. Manseri, A. Milovanovic, P. Moriarty, R. Mukherjee, P. A. Ogden, R. A. Ong, D. Petry, J. S. Perkins, F. Pizlo, M. Pohl, J. Quinn, K. Ragan, P. T. Reynolds, E. T. Roache, H. J. Rose, M. Schroedter, G. H. Sembroski, G. Sleege, D. Steele, S. P. Swordy, A. Syson, J. A. Toner, L. Valcarcel, V. V. Vassiliev, S. P. Wakely, T. C. Weekes, R. J. White, D. A. Williams, and R. Wagner, "The first VERITAS telescope," *Astroparticle Physics*, vol. 25, pp. 391–401, Jul. 2006. eprint: `astro-ph/0604119`.

[64] J. Holder, V. A. Acciari, E. Aliu, T. Arlen, M. Beilicke, W. Benbow, S. M. Bradbury, J. H. Buckley, V. Bugaev, Y. Butt, K. L. Byrum, A. Cannon, O. Celik, A. Cesarini, L. Ciupik, Y. C. K. Chow, P. Cogan, P. Colin, W. Cui, M. K. Daniel, T. Ergin, A. D. Falcone, S. J. Fegan, J. P. Finley, G. Finnegan, P. Fortin, L. F. Fortson, A. Furniss, G. H. Gillanders, J. Grube, R. Guenette, G. Gyuk, D. Hanna, E. Hays, D. Horan, C. M. Hui, T. B. Humensky, A. Imran, P. Kaaret, N. Karlsson, M. Kertzman, D. B. Kieda, J. Kildea, A. Konopelko, H. Krawczynski, F. Krennrich, M. J. Lang, S. Lebohec, G. Maier, A. McCann, M. McCutcheon, P. Moriarty, R. Mukherjee, T. Nagai, J. Niemiec, R. A. Ong, D. Pandel, J. S. Perkins, M. Pohl, J. Quinn, K. Ragan, L. C. Reyes, P. T. Reynolds, H. J. Rose, M. Schroedter, G. H. Sembroski, A. W. Smith, D. Steele, S. P. Swordy, J. A. Toner, L. Valcarcel, V. V. Vassiliev, R. Wagner, S. P. Wakely, J. E. Ward, T. C. Weekes, A. Weinstein, R. J. White, D. A. Williams, S. A. Wissel, M. Wood, and B. Zitzer, "Status of the VERITAS Observatory," in *American Institute of Physics Conference Series*, F. A. Aharonian, W. Hofmann, and F. Rieger, Eds., ser. American Institute of Physics Conference Series, vol. 1085, Dec. 2008, pp. 657–660. arXiv: `0810.0474`.

[65] J. M. Davies and E. S. Cotton, "Design of the quartermaster solar furnace," *Solar Energy*, vol. 1, pp. 16–22, Apr. 1957.

[66] D. B. Kieda for the VERITAS Collaboration, "The Gamma Ray Detection sensitivity of the upgraded VERITAS Observatory," *ArXiv e-prints*, Aug. 2013. arXiv: `1308.4849 [astro-ph.IM]`.

[67] R. Mirzoyan, M. Garczarczyk, J. Hose, and D. Paneque, "A method to measure the mirror reflectivity of a prime focus telescope," *Astroparticle Physics*, vol. 27, pp. 509–511, Jul. 2007. eprint: `astro-ph/0703174`.

[68] G. B. Hobbs, R. T. Edwards, and R. N. Manchester, “TEMPO2, a new pulsar-timing package - I. An overview,” *Monthly Notices of the Royal Astronomical Society*, vol. 369, pp. 655–672, Jun. 2006. eprint: `astro-ph/0603381`.

[69] E. M. Standish, “An approximation to the errors in the planetary ephemerides of the Astronomical Almanac,” *Astronomy & Astrophysics*, vol. 417, pp. 1165–1171, Apr. 2004.

[70] W. B. Atwood, A. A. Abdo, M. Ackermann, W. Althouse, B. Anderson, M. Axelsson, L. Baldini, J. Ballet, D. L. Band, G. Barbiellini, and et al., “The Large Area Telescope on the Fermi Gamma-Ray Space Telescope Mission,” *The Astrophysical Journal*, vol. 697, pp. 1071–1102, Jun. 2009. arXiv: `0902.1089 [astro-ph.IM]`.

[71] M. Ackermann, M. Ajello, A. Albert, A. Allafort, W. B. Atwood, M. Axelsson, L. Baldini, J. Ballet, G. Barbiellini, D. Bastieri, K. Bechtol, R. Bellazzini, E. Bissaldi, R. D. Blandford, E. D. Bloom, J. R. Bogart, E. Bonamente, A. W. Borgland, E. Bottacini, A. Bouvier, T. J. Brandt, J. Bregeon, M. Brigida, P. Bruel, R. Buehler, T. H. Burnett, S. Buson, G. A. Caliandro, R. A. Cameron, P. A. Caraveo, J. M. Casandjian, E. Cavazzuti, C. Cecchi, Ö. Çelik, E. Charles, R. C. G. Chaves, A. Chekhtman, C. C. Cheung, J. Chiang, S. Ciprini, R. Claus, J. Cohen-Tanugi, J. Conrad, R. Corbet, S. Cutini, F. D’Ammando, D. S. Davis, A. de Angelis, M. DeKlotz, F. de Palma, C. D. Dermer, S. W. Digel, E. d. C. e. Silva, P. S. Drell, A. Drlica-Wagner, R. Dubois, C. Favuzzi, S. J. Fegan, E. C. Ferrara, W. B. Focke, P. Fortin, Y. Fukazawa, S. Funk, P. Fusco, F. Gargano, D. Gasparrini, N. Gehrels, B. Giebels, N. Giglietto, F. Giordano, M. Giroletti, T. Glanzman, G. Godfrey, I. A. Grenier, J. E. Grove, S. Guiriec, D. Hadasch, M. Hayashida, E. Hays, D. Horan, X. Hou, R. E. Hughes, M. S. Jackson, T. Jogler, G. Jóhannesson, R. P. Johnson, T. J. Johnson, W. N. Johnson, T. Kamae, H. Katagiri, J. Kataoka, M. Kerr, J. Knödlseder, M. Kuss, J. Lande, S. Larsson, L. Latronico, C. Lavalley, M. Lemoine-Goumard, F. Longo, F. Loparco, B. Lott, M. N. Lovellette, P. Lubrano, M. N. Mazziotta, W. McConville, J. E. McEnery, J. Mehault, P. F. Michelson, W. Mitthumsiri, T. Mizuno, A. A. Moiseev, C. Monte, M. E. Monzani, A. Morselli, I. V. Moskalenko, S. Murgia, M. Naumann-Godo, R. Nemmen, S. Nishino, J. P. Norris, E. Nuss, M. Ohno, T. Ohsugi, A. Okumura, N. Omodei, M. Orienti, E. Orlando, J. F. Ormes, D. Paneque, J. H. Panetta, J. S. Perkins, M. Pesce-Rollins, M. Pierbattista, F. Piron, G. Pivato, T. A. Porter, J. L. Racusin, S. Rainò, R. Rando, M. Razzano, S. Razzaque, A. Reimer, O. Reimer, T. Reposeur, L. C. Reyes, S. Ritz, L. S. Rochester, C. Romoli, M. Roth, H. F.-W. Sadrozinski, D. A. Sanchez, P. M. Saz Parkinson, C. Sbarra, J. D. Scargle, C. Sgrò, J. Siegal-Gaskins, E. J. Siskind, G. Spandre, P. Spinelli, T. E. Stephens, D. J. Suson, H. Tajima, H. Takahashi, T. Tanaka, J. G. Thayer, J. B. Thayer, D. J. Thompson, L. Tibaldo, M. Tinivella, G. Tosti, E. Troja, T. L. Usher, J. Vandenbroucke, B. Van Klaveren, V. Vasileiou, G. Vianello, V. Vitale, A. P. Waite, E. Wallace, B. L. Winer, D. L. Wood, K. S. Wood, M. Wood, Z. Yang, and S. Zimmer, “The Fermi Large Area Telescope on Orbit: Event Classifica-

tion, Instrument Response Functions, and Calibration," *The Astrophysical Journal Supplements*, vol. 203, 4, p. 4, Nov. 2012. arXiv: `1206.1896 [astro-ph.IM]`.

[72] P. L. Nolan, A. A. Abdo, M. Ackermann, M. Ajello, A. Allafort, E. Antolini, W. B. Atwood, M. Axelsson, L. Baldini, J. Ballet, and et al., "Fermi Large Area Telescope Second Source Catalog," *The Astrophysical Journal Supplements*, vol. 199, 31, p. 31, Apr. 2012. arXiv: `1108.1435 [astro-ph.HE]`.

[73] F. Acero, M. Ackermann, M. Ajello, A. Albert, W. B. Atwood, M. Axelsson, L. Baldini, J. Ballet, G. Barbiellini, D. Bastieri, A. Belfiore, R. Bellazzini, E. Bissaldi, R. D. Blandford, E. D. Bloom, J. R. Bogart, R. Bonino, E. Bottacini, J. Bregeon, R. J. Britto, P. Bruel, R. Buehler, T. H. Burnett, S. Buson, G. A. Caliandro, R. A. Cameron, R. Caputo, M. Caragiulo, P. A. Caraveo, J. M. Casandjian, E. Cavazzuti, E. Charles, R. C. G. Chaves, A. Chekhtman, C. C. Cheung, J. Chiang, G. Chiaro, S. Ciprini, R. Claus, J. Cohen-Tanugi, L. R. Cominsky, J. Conrad, S. Cutini, F. D'Ammando, A. de Angelis, M. DeKlotz, F. de Palma, R. Desiante, S. W. Digel, L. Di Venere, P. S. Drell, R. Dubois, D. Dumora, C. Favuzzi, S. J. Fegan, E. C. Ferrara, J. Finke, A. Franckowiak, Y. Fukazawa, S. Funk, P. Fusco, F. Gargano, D. Gasparrini, B. Giebels, N. Giglietto, P. Giommi, F. Giordano, M. Giroletti, T. Glanzman, G. Godfrey, I. A. Grenier, M.-H. Grondin, J. E. Grove, L. Guillemot, S. Guiriec, D. Hadasch, A. K. Harding, E. Hays, J. W. Hewitt, A. B. Hill, D. Horan, G. Iafrate, T. Jogler, G. Jóhannesson, R. P. Johnson, A. S. Johnson, T. J. Johnson, W. N. Johnson, T. Kamae, J. Kataoka, J. Katsuta, M. Kuss, G. La Mura, D. Landriu, S. Larsson, L. Latronico, M. Lemoine-Goumard, J. Li, L. Li, F. Longo, F. Loparco, B. Lott, M. N. Lovellette, P. Lubrano, G. M. Madejski, F. Massaro, M. Mayer, M. N. Mazziotta, J. E. McEnery, P. F. Michelson, N. Mirabal, T. Mizuno, A. A. Moiseev, M. Mongelli, M. E. Monzani, A. Morselli, I. V. Moskalenko, S. Murgia, E. Nuss, M. Ohno, T. Ohsugi, N. Omodei, M. Orienti, E. Orlando, J. F. Ormes, D. Paneque, J. H. Panetta, J. S. Perkins, M. Pesce-Rollins, F. Piron, G. Pivato, T. A. Porter, J. L. Racusin, R. Rando, M. Razzano, S. Razzaque, A. Reimer, O. Reimer, T. Reposeur, L. S. Rochester, R. W. Romani, D. Salvetti, M. Sánchez-Conde, P. M. Saz Parkinson, A. Schulz, E. J. Siskind, D. A. Smith, F. Spada, G. Spandre, P. Spinelli, T. E. Stephens, A. W. Strong, D. J. Suson, H. Takahashi, T. Takahashi, Y. Tanaka, J. G. Thayer, J. B. Thayer, D. J. Thompson, L. Tibaldo, O. Tibolla, D. F. Torres, E. Torresi, G. Tosti, E. Troja, B. Van Klaveren, G. Vianello, B. L. Winer, K. S. Wood, M. Wood, S. Zimmer, and Fermi-LAT Collaboration, "Fermi Large Area Telescope Third Source Catalog," *The Astrophysical Journal Supplements*, vol. 218, 23, p. 23, Jun. 2015. arXiv: `1501.02003 [astro-ph.HE]`.

[74] A. M. Hillas, "Cerenkov light images of EAS produced by primary gamma," *International Cosmic Ray Conference*, vol. 3, pp. 445–448, Aug. 1985.

[75] D. J. Fegan, "TOPICAL REVIEW: gamma/hadron separation at TeV energies," *Journal of Physics G Nuclear Physics*, vol. 23, pp. 1013–1060, Sep. 1997.

[76] M. K. Daniel, "The VERITAS standard data analysis," *International Cosmic Ray Conference*, vol. 3, pp. 1325–1328, 2008. arXiv: `0709.4006`.

[77] V. P. Fomin, A. A. Stepanian, R. C. Lamb, D. A. Lewis, M. Punch, and T. C. Weekes, "New methods of atmospheric Cherenkov imaging for gamma-ray astronomy. I. The false source method," *Astroparticle Physics*, vol. 2, pp. 137–150, May 1994.

[78] D. Berge, S. Funk, and J. Hinton, "Background modelling in very-high-energy γ-ray astronomy," *Astronomy & Astrophysics*, vol. 466, pp. 1219–1229, May 2007. eprint: `astro-ph/0610959`.

[79] W. A. Rolke and A. M. López, "Confidence intervals and upper bounds for small signals in the presence of background noise," *Nuclear Instruments and Methods in Physics Research A*, vol. 458, pp. 745–758, Feb. 2001. eprint: `hep-ph/0005187`.

[80] O. Helene, "Determination of the upper limit of a peak area," *Nuclear Instruments and Methods in Physics Research A*, vol. 300, pp. 132–136, Jan. 1991.

[81] T.-P. Li and Y.-Q. Ma, "Analysis methods for results in gamma-ray astronomy," *The Astrophysical Journal*, vol. 272, pp. 317–324, Sep. 1983.

[82] R. Buccheri, K. Bennett, G. F. Bignami, J. B. G. M. Bloemen, V. Boriakoff, P. A. Caraveo, W. Hermsen, G. Kanbach, R. N. Manchester, J. L. Masnou, H. A. Mayer-Hasselwander, M. E. Özel, J. A. Paul, B. Sacco, L. Scarsi, and A. W. Strong, "Search for pulsed gamma-ray emission from radio pulsars in the COS-B data," *Astronomy & Astrophysics*, vol. 128, pp. 245–251, Nov. 1983.

[83] J. D. Hart, "On the Choice of a Truncation Point in Fourier Series Density Estimation," *J. Stat. Comp.*, vol. 21, pp. 95–116, 1985.

[84] O. C. de Jager, "On periodicity tests and flux limit calculations for gamma-ray pulsars," *The Astrophysical Journal*, vol. 436, pp. 239–248, Nov. 1994.

[85] D. J. Thompson, D. L. Bertsch, and R. H. O'Neal Jr., "The Highest-Energy Photons Seen by the Energetic Gamma Ray Experiment Telescope (EGRET) on the Compton Gamma Ray Observatory," *The Astrophysical Journal Supplements*, vol. 157, pp. 324–334, Apr. 2005. eprint: `astro-ph/0412376`.

[86] P. A. Caraveo, "Gamma-Ray Pulsar Revolution," *Annual Review of Astronomy and Astrophysics*, vol. 52, pp. 211–250, Aug. 2014. arXiv: `1312.2913 [astro-ph.HE]`.

[87] P. M. Saz Parkinson and Fermi-LAT Collaboration, "Fermi-LAT detection of gamma-ray pulsars above 10 GeV," in *American Institute of Physics Conference Series*, F. A. Aharonian, W. Hofmann, and F. M. Rieger, Eds., ser. American Institute

of Physics Conference Series, vol. 1505, Dec. 2012, pp. 293–296. arXiv: `1210.7525 [astro-ph.HE]`.

[88] M. Ackermann, M. Ajello, A. Allafort, W. B. Atwood, L. Baldini, J. Ballet, G. Barbiellini, D. Bastieri, K. Bechtol, A. Belfiore, R. Bellazzini, E. Bernieri, E. Bissaldi, E. D. Bloom, E. Bonamente, T. J. Brandt, J. Bregeon, M. Brigida, P. Bruel, R. Buehler, T. H. Burnett, S. Buson, G. A. Caliandro, R. A. Cameron, R. Campana, P. A. Caraveo, J. M. Casandjian, E. Cavazzuti, C. Cecchi, E. Charles, R. C. G. Chaves, A. Chekhtman, C. C. Cheung, J. Chiang, G. Chiaro, S. Ciprini, R. Claus, J. Cohen-Tanugi, L. R. Cominsky, J. Conrad, S. Cutini, F. D'Ammando, A. de Angelis, F. de Palma, C. D. Dermer, R. Desiante, S. W. Digel, L. Di Venere, P. S. Drell, A. Drlica-Wagner, C. Favuzzi, S. J. Fegan, E. C. Ferrara, W. B. Focke, P. Fortin, A. Franckowiak, S. Funk, P. Fusco, F. Gargano, D. Gasparrini, N. Gehrels, S. Germani, N. Giglietto, P. Giommi, F. Giordano, M. Giroletti, G. Godfrey, G. A. Gomez-Vargas, I. A. Grenier, S. Guiriec, D. Hadasch, Y. Hanabata, A. K. Harding, M. Hayashida, E. Hays, J. Hewitt, A. B. Hill, D. Horan, R. E. Hughes, T. Jogler, G. Jóhannesson, A. S. Johnson, T. J. Johnson, W. N. Johnson, T. Kamae, J. Kataoka, T. Kawano, J. Knödlseder, M. Kuss, J. Lande, S. Larsson, L. Latronico, M. Lemoine-Goumard, F. Longo, F. Loparco, B. Lott, M. N. Lovellette, P. Lubrano, E. Massaro, M. Mayer, M. N. Mazziotta, J. E. McEnery, J. Mehault, P. F. Michelson, T. Mizuno, A. A. Moiseev, M. E. Monzani, A. Morselli, I. V. Moskalenko, S. Murgia, R. Nemmen, E. Nuss, T. Ohsugi, A. Okumura, M. Orienti, J. F. Ormes, D. Paneque, J. S. Perkins, M. Pesce-Rollins, F. Piron, G. Pivato, T. A. Porter, S. Rainò, M. Razzano, A. Reimer, O. Reimer, T. Reposeur, S. Ritz, R. W. Romani, M. Roth, P. M. Saz Parkinson, A. Schulz, C. Sgrò, E. J. Siskind, D. A. Smith, G. Spandre, P. Spinelli, Ł. Stawarz, A. W. Strong, D. J. Suson, H. Takahashi, J. G. Thayer, J. B. Thayer, D. J. Thompson, L. Tibaldo, M. Tinivella, D. F. Torres, G. Tosti, E. Troja, Y. Uchiyama, T. L. Usher, J. Vandenbroucke, V. Vasileiou, G. Vianello, V. Vitale, M. Werner, B. L. Winer, K. S. Wood, and M. Wood, "The First Fermi-LAT Catalog of Sources above 10 GeV," *The Astrophysical Journal Supplements*, vol. 209, 34, p. 34, Dec. 2013. arXiv: `1306.6772 [astro-ph.IM]`.

[89] J. Aleksić, E. A. Alvarez, L. A. Antonelli, P. Antoranz, M. Asensio, M. Backes, J. A. Barrio, D. Bastieri, J. Becerra González, W. Bednarek, A. Berdyugin, K. Berger, E. Bernardini, A. Biland, O. Blanch, R. K. Bock, A. Boller, G. Bonnoli, D. Borla Tridon, I. Braun, T. Bretz, A. Cañellas, E. Carmona, A. Carosi, P. Colin, E. Colombo, J. L. Contreras, J. Cortina, L. Cossio, S. Covino, F. Dazzi, A. de Angelis, G. de Caneva, E. de Cea Del Pozo, B. de Lotto, C. Delgado Mendez, A. Diago Ortega, M. Doert, A. Domínguez, D. Dominis Prester, D. Dorner, M. Doro, D. Eisenacher, D. Elsaesser, D. Ferenc, M. V. Fonseca, L. Font, C. Fruck, R. J. García López, M. Garczarczyk, D. Garrido, G. Giavitto, N. Godinović, D. Hadasch, D. Häfner, A. Herrero, D. Hildebrand, D. Höhne-Mönch, J. Hose, D. Hrupec, T. Jogler, H. Kellermann, S. Klepser, T. Krähenbühl, J. Krause, J. Kushida, A. La Barbera, D. Lelas, E. Leonardo, N. Lewandowska, E. Lindfors, S. Lombardi, M. López, A. López-Oramas, E. Lorenz, M. Makariev, G. Maneva, N. Mankuzhiyil,

K. Mannheim, L. Maraschi, M. Mariotti, M. Martínez, D. Mazin, M. Meucci, J. M. Miranda, R. Mirzoyan, J. Moldón, A. Moralejo, P. Munar-Adrover, A. Niedzwiecki, D. Nieto, K. Nilsson, N. Nowak, R. Orito, D. Paneque, R. Paoletti, S. Pardo, J. M. Paredes, S. Partini, M. A. Perez-Torres, M. Persic, L. Peruzzo, M. Pilia, J. Pochon, F. Prada, P. G. Prada Moroni, E. Prandini, I. Puerto Gimenez, I. Puljak, I. Reichardt, R. Reinthal, W. Rhode, M. Ribó, J. Rico, S. Rügamer, A. Saggion, K. Saito, T. Y. Saito, M. Salvati, K. Satalecka, V. Scalzotto, V. Scapin, C. Schultz, T. Schweizer, M. Shayduk, S. N. Shore, A. Sillanpää, J. Sitarek, I. **v**Snidarić, D. Sobczynska, F. Spanier, S. Spiro, V. Stamatescu, A. Stamerra, B. Steinke, J. Storz, N. Strah, T. Surić, L. Takalo, H. Takami, F. Tavecchio, P. Temnikov, T. Terzić, D. Tescaro, M. Teshima, O. Tibolla, D. F. Torres, A. Treves, M. Uellenbeck, H. Vankov, P. Vogler, R. M. Wagner, Q. Weitzel, V. Zabalza, F. Zandanel, R. Zanin, and K. Hirotani, "Phase-resolved energy spectra of the Crab pulsar in the range of 50-400 GeV measured with the MAGIC telescopes," *Astronomy & Astrophysics*, vol. 540, A69, A69, Apr. 2012. arXiv: `1109.6124 [astro-ph.HE]`.

[90] W. Bednarek, "On the origin of sub-TeV gamma-ray pulsed emission from rotating neutron stars," *Monthly Notices of the Royal Astronomical Society*, vol. 424, pp. 2079–2085, Aug. 2012. arXiv: `1205.4855 [astro-ph.HE]`.

[91] Y. J. Du, G. J. Qiao, and W. Wang, "Radio-to-TeV Phase-resolved Emission from the Crab Pulsar: The Annular Gap Model," *The Astrophysical Journal*, vol. 748, 84, p. 84, Apr. 2012. arXiv: `1202.1096 [astro-ph.HE]`.

[92] M. Lyutikov, "The γ-Ray Spectrum of Geminga and the Inverse Compton Model of Pulsar High-energy Emission," *The Astrophysical Journal*, vol. 757, 88, p. 88, Sep. 2012. arXiv: `1203.1860 [astro-ph.HE]`.

[93] J. Pétri, "High-energy emission from the pulsar striped wind: a synchrotron model for gamma-ray pulsars," *Monthly Notices of the Royal Astronomical Society*, vol. 424, pp. 2023–2027, Aug. 2012. arXiv: `1205.5101 [astro-ph.HE]`.

[94] P. A. Caraveo, G. F. Bignami, R. Mignani, and L. G. Taff, "Parallax Observations with the Hubble Space Telescope Yield the Distance to Geminga," *The Astrophysical Journal Letters*, vol. 461, p. L91, Apr. 1996.

[95] G. F. Bignami and P. A. Caraveo, "Geminga: Its Phenomenology, Its Fraternity, and Its Physics," *Annual Review of Astronomy and Astrophysics*, vol. 34, pp. 331–382, 1996.

[96] C. E. Fichtel, R. C. Hartman, D. A. Kniffen, D. J. Thompson, H. Ogelman, M. E. Ozel, T. Tumer, and G. F. Bignami, "High-energy gamma-ray results from the second small astronomy satellite," *The Astrophysical Journal*, vol. 198, pp. 163–182, May 1975.

[97] K. Bennett, G. F. Bignami, M. Bonnardeau, R. Buccheri, W. Hermsen, G. Kanbach, G. G. Lichti, H. A. Mayer-Hasselwander, J. A. Paul, L. Scarsi, R. Stiglitz, B. N. Swanenburg, and R. D. Wills, “COS-B observations of localised high-energy gamma-ray emission from the anticentre region of the galactic disc,” *Astronomy & Astrophysics*, vol. 56, pp. 469–471, Apr. 1977.

[98] J. P. Halpern and S. S. Holt, “Discovery of soft X-ray pulsations from the gamma-ray source Geminga,” *Nature*, vol. 357, pp. 222–224, May 1992.

[99] G. F. Blgnami and P. A. Caraveo, “Geminga: new period, old γ-rays,” *Nature*, vol. 357, p. 287, May 1992.

[100] J. R. Mattox, D. L. Bertsch, C. E. Fichtel, R. C. Hartman, D. A. Kniffen, and D. J. Thompson, “SAS 2 observation of pulsed high-energy gamma radiation from Geminga,” *The Astrophysical Journal Letters*, vol. 401, pp. L23–L26, Dec. 1992.

[101] P. A. Caraveo, A. De Luca, S. Mereghetti, A. Pellizzoni, and G. F. Bignami, “Phase-Resolved Spectroscopy of Geminga Shows Rotating Hot Spot(s),” *Science*, vol. 305, pp. 376–380, Jul. 2004. eprint: `astro-ph/0407402`.

[102] H. A. Mayer-Hasselwander, D. L. Bertsch, K. T. S. Brazier, J. Chiang, C. E. Fichtel, J. M. Fierro, R. C. Hartman, S. D. Hunter, G. Kanbach, P. W. Kwok, D. A. Kniffen, Y. C. Lin, J. R. Mattox, P. F. Michelson, P. L. Nolan, K. Pinkau, H. Rothermel, E. J. Schneid, M. Sommer, P. Sreekumar, D. J. Thompson, and C. von Montigny, “High-energy gamma radiation from Geminga observed by EGRET,” *The Astrophysical Journal*, vol. 421, pp. 276–283, Jan. 1994.

[103] J. M. Fierro, P. F. Michelson, P. L. Nolan, and D. J. Thompson, “Phase-resolved Studies of the High-Energy Gamma-Ray Emission from the Crab, Geminga, and VELA Pulsars,” *The Astrophysical Journal*, vol. 494, pp. 734–746, Feb. 1998. eprint: `astro-ph/9709123`.

[104] A. Pellizzoni, M. Pilia, A. Possenti, F. Fornari, P. Caraveo, E. del Monte, S. Mereghetti, M. Tavani, A. Argan, A. Trois, M. Burgay, A. Chen, I. Cognard, E. Costa, N. D’Amico, P. Esposito, Y. Evangelista, M. Feroci, F. Fuschino, A. Giuliani, J. Halpern, G. Hobbs, A. Hotan, S. Johnston, M. Kramer, F. Longo, R. N. Manchester, M. Marisaldi, J. Palfreyman, P. Weltevrede, G. Barbiellini, F. Boffelli, A. Bulgarelli, P. W. Cattaneo, V. Cocco, F. D’Ammando, G. DeParis, G. Di Cocco, I. Donnarumma, M. Fiorini, T. Froysland, M. Galli, F. Gianotti, A. Harding, C. Labanti, I. Lapshov, F. Lazzarotto, P. Lipari, F. Mauri, A. Morselli, L. Pacciani, F. Perotti, P. Picozza, M. Prest, G. Pucella, M. Rapisarda, A. Rappoldi, P. Soffitta, M. Trifoglio, E. Vallazza, S. Vercellone, V. Vittorini, A. Zambra, D. Zanello, C. Pittori, F. Verrecchia, B. Preger, P. Santolamazza, P. Giommi, and L. Salotti, “High-Resolution Timing Observations of Spin-Powered Pulsars with the AGILE Gamma-Ray Tele-

scope," *The Astrophysical Journal*, vol. 691, pp. 1618–1633, Feb. 2009. arXiv: `0810.1516`.

[105] A. A. Abdo, M. Ackermann, M. Ajello, L. Baldini, J. Ballet, G. Barbiellini, D. Bastieri, B. M. Baughman, K. Bechtol, R. Bellazzini, B. Berenji, G. F. Bignami, R. D. Blandford, E. D. Bloom, E. Bonamente, A. W. Borgland, J. Bregeon, A. Brez, M. Brigida, P. Bruel, T. H. Burnett, G. A. Caliandro, R. A. Cameron, P. A. Caraveo, J. M. Casandjian, C. Cecchi, Ö. Çelik, E. Charles, A. Chekhtman, C. C. Cheung, J. Chiang, S. Ciprini, R. Claus, J. Cohen-Tanugi, J. Conrad, C. D. Dermer, F. de Palma, M. Dormody, E. d. C. e. Silva, P. S. Drell, R. Dubois, D. Dumora, Y. Edmonds, C. Farnier, C. Favuzzi, S. J. Fegan, W. B. Focke, P. Fortin, M. Frailis, Y. Fukazawa, S. Funk, P. Fusco, F. Gargano, D. Gasparrini, N. Gehrels, S. Germani, G. Giavitto, N. Giglietto, F. Giordano, T. Glanzman, G. Godfrey, I. A. Grenier, M.-H. Grondin, J. E. Grove, L. Guillemot, S. Guiriec, D. Hadasch, A. K. Harding, E. Hays, R. E. Hughes, G. Jóhannesson, A. S. Johnson, T. J. Johnson, W. N. Johnson, T. Kamae, H. Katagiri, J. Kataoka, N. Kawai, M. Kerr, J. Knödlseder, M. Kuss, J. Lande, L. Latronico, M. Lemoine-Goumard, F. Longo, F. Loparco, B. Lott, M. N. Lovellette, P. Lubrano, A. Makeev, M. Marelli, M. N. Mazziotta, J. E. McEnery, C. Meurer, P. F. Michelson, W. Mitthumsiri, T. Mizuno, A. A. Moiseev, C. Monte, M. E. Monzani, A. Morselli, I. V. Moskalenko, S. Murgia, P. L. Nolan, J. P. Norris, E. Nuss, T. Ohsugi, N. Omodei, E. Orlando, J. F. Ormes, M. Ozaki, D. Paneque, J. H. Panetta, D. Parent, V. Pelassa, M. Pepe, M. Pesce-Rollins, F. Piron, T. A. Porter, S. Rainò, R. Rando, P. S. Ray, M. Razzano, A. Reimer, O. Reimer, T. Reposeur, L. S. Rochester, A. Y. Rodriguez, R. W. Romani, M. Roth, F. Ryde, H. F.-W. Sadrozinski, A. Sander, P. M. Saz Parkinson, J. D. Scargle, C. Sgrò, E. J. Siskind, D. A. Smith, P. D. Smith, G. Spandre, P. Spinelli, M. S. Strickman, D. J. Suson, H. Takahashi, T. Takahashi, T. Tanaka, J. B. Thayer, J. G. Thayer, D. J. Thompson, L. Tibaldo, D. F. Torres, G. Tosti, A. Tramacere, T. L. Usher, A. Van Etten, V. Vasileiou, C. Venter, N. Vilchez, V. Vitale, A. P. Waite, P. Wang, K. Watters, B. L. Winer, K. S. Wood, T. Ylinen, and M. Ziegler, "Fermi-LAT Observations of the Geminga Pulsar," *The Astrophysical Journal*, vol. 720, pp. 272–283, Sep. 2010. arXiv: `1007.1142 [astro-ph.HE]`.

[106] R. Ramachandran, A. A. Deshpande, and C. Indrani, "Upper limits on the pulsed radio emission from the Geminga pulsar at 35 & 327 MHz," *Astronomy & Astrophysics*, vol. 339, pp. 787–790, Nov. 1998. eprint: `astro-ph/9808234`.

[107] M. A. McLaughlin, J. M. Cordes, T. H. Hankins, and D. A. Moffett, "A VLA Search for the Geminga Pulsar: A Bayesian Limit on a Scintillating Source," *The Astrophysical Journal*, vol. 512, pp. 929–941, Feb. 1999. eprint: `astro-ph/9912410`.

[108] A. Shearer, A. Golden, S. Harfst, R. Butler, R. M. Redfern, C. M. M. O'Sullivan, G. M. Beskin, S. I. Neizvestny, V. V. Neustroev, V. L. Plokhotnichenko, M. Cullum,

and A. Danks, “Possible pulsed optical emission from Geminga,” *Astronomy & Astrophysics*, vol. 335, pp. L21–L24, Jul. 1998. eprint: `astro-ph/9802225`.

[109] O. Y. Kargaltsev, G. G. Pavlov, V. E. Zavlin, and R. W. Romani, “Ultraviolet, X-Ray, and Optical Radiation from the Geminga Pulsar,” *The Astrophysical Journal*, vol. 625, pp. 307–323, May 2005. eprint: `astro-ph/0502076`.

[110] C. W. Akerlof, A. C. Breslin, M. F. Cawley, M. Chantell, D. J. Fegan, S. Fennell, J. A. Gaidos, J. Hagan, A. M. Hillas, A. D. Kerrick, R. C. Lamb, M. A. Lawrence, D. A. Lewis, D. I. Meyer, G. Mohanty, K. S. O’Flaherty, M. Punch, P. T. Reynolds, A. C. Rovero, M. S. Schubnell, G. Sembrowski, T. C. Weekes, M. West, T. Whitaker, and C. Wilson, “Search for Tev Gamma-Rays from Geminga,” *Astronomy & Astrophysics*, vol. 274, p. L17, Jul. 1993.

[111] F. Aharonian, A. G. Akhperjanian, J. A. Barrio, K. Bernlöhr, H. Bojahr, J. L. Contreras, J. Cortina, A. Daum, T. Deckers, S. Denninghoff, V. Fonseca, J. C. Gonzalez, G. Heinzelmann, M. Hemberger, G. Hermann, M. Heß, A. Heusler, W. Hofmann, H. Hohl, D. Horns, A. Ibarra, R. Kankanyan, M. Kestel, O. Kirstein, C. Köhler, A. Konopelko, H. Kornmeyer, D. Kranich, H. Krawczynski, H. Lampeitl, A. Lindner, E. Lorenz, N. Magnussen, H. Meyer, R. Mirzoyan, A. Moralejo, L. Padilla, M. Panter, D. Petry, R. Plaga, A. Plyasheshnikov, J. Prahl, G. Pühlhofer, G. Rauterberg, C. Renault, W. Rhode, A. Röhring, V. Sahakian, M. Samorski, D. Schmele, F. Schröder, W. Stamm, H. Völk, B. Wiebel-Sooth, C. Wiedner, M. Willmer, and H. Wirth, “Phase-resolved TeV gamma-ray characteristics of the Crab and Geminga pulsars,” *Astronomy & Astrophysics*, vol. 346, pp. 913–921, Jun. 1999.

[112] B. B. Singh, V. R. Chitnis, D. Bose, M. A. Rahman, S. S. Upadhya, K. S. Gothe, B. K. Nagesh, P. N. Purohit, S. K. Rao, K. K. Rao, S. K. Sharma, P. V. Sudersan, B. L. Venkateshmurthy, P. R. Vishwanath, and B. S. Acharya, “Search for TeV gamma-rays from Geminga pulsar,” *Astroparticle Physics*, vol. 32, pp. 120–128, Sep. 2009.

[113] P. R. Vishwanath, G. P. Sathyanarayana, P. V. Ramanamurthy, and P. N. Bhat, “Search for TeV gamma rays from Geminga,” *Astronomy & Astrophysics*, vol. 267, pp. L5–L7, Jan. 1993.

[114] C. C. G. Bowden, S. M. Bradbury, P. M. Chadwick, J. E. Dickinson, N. A. Dipper, T. J. L. McComb, K. J. Orford, S. M. Rayner, and K. E. Turver, “TeV gamma rays from Geminga,” *Journal of Physics G Nuclear Physics*, vol. 19, pp. L29–L31, Feb. 1993.

[115] Y. I. Neshpor, A. A. Stepanyan, Y. L. Zyskin, O. R. Kalekin, V. P. Fomin, N. N. Chalenko, and V. G. Shitov, “Ultrahigh-Energy Gamma-Ray Emission from the Geminga Pulsar,” *Astronomy Letters*, vol. 27, pp. 228–232, Apr. 2001.

[116] P. A. Caraveo, G. F. Bignami, A. De Luca, S. Mereghetti, A. Pellizzoni, R. Mignani, A. Tur, and W. Becker, "Geminga's Tails: A Pulsar Bow Shock Probing the Interstellar Medium," *Science*, vol. 301, pp. 1345–1348, Sep. 2003.

[117] A. A. Abdo, B. Allen, D. Berley, S. Casanova, C. Chen, D. G. Coyne, B. L. Dingus, R. W. Ellsworth, L. Fleysher, R. Fleysher, M. M. Gonzalez, J. A. Goodman, E. Hays, C. M. Hoffman, B. Hopper, P. H. Hüntemeyer, B. E. Kolterman, C. P. Lansdell, J. T. Linnemann, J. E. McEnery, A. I. Mincer, P. Nemethy, D. Noyes, J. M. Ryan, P. M. Saz Parkinson, A. Shoup, G. Sinnis, A. J. Smith, G. W. Sullivan, V. Vasileiou, G. P. Walker, D. A. Williams, X. W. Xu, and G. B. Yodh, "TeV Gamma-Ray Sources from a Survey of the Galactic Plane with Milagro," *The Astrophysical Journal Letters*, vol. 664, pp. L91–L94, Aug. 2007. arXiv: `0705.0707`.

[118] A. A. Abdo, B. T. Allen, T. Aune, D. Berley, C. Chen, G. E. Christopher, T. DeYoung, B. L. Dingus, R. W. Ellsworth, M. M. Gonzalez, J. A. Goodman, E. Hays, C. M. Hoffman, P. H. Hüntemeyer, B. E. Kolterman, J. T. Linnemann, J. E. McEnery, T. Morgan, A. I. Mincer, P. Nemethy, J. Pretz, J. M. Ryan, P. M. Saz Parkinson, A. Shoup, G. Sinnis, A. J. Smith, V. Vasileiou, G. P. Walker, D. A. Williams, and G. B. Yodh, "Milagro Observations of Multi-TeV Emission from Galactic Sources in the Fermi Bright Source List," *The Astrophysical Journal Letters*, vol. 700, pp. L127–L131, Aug. 2009. arXiv: `0904.1018 [astro-ph.HE]`.

[119] M. Amenomori, X. J. Bi, D. Chen, S. W. Cui, Danzengluobu, L. K. Ding, X. H. Ding, C. Fan, C. F. Feng, Z. Feng, Z. Y. Feng, X. Y. Gao, Q. X. Geng, Q. B. Gou, H. W. Guo, H. H. He, M. He, K. Hibino, N. Hotta, H. Hu, H. B. Hu, J. Huang, Q. Huang, H. Y. Jia, L. Jiang, F. Kajino, K. Kasahara, Y. Katayose, C. Kato, K. Kawata, Labaciren, G. M. Le, A. F. Li, H. C. Li, J. Y. Li, C. Liu, Y.-Q. Lou, H. Lu, X. R. Meng, K. Mizutani, J. Mu, K. Munakata, H. Nanjo, M. Nishizawa, M. Ohnishi, I. Ohta, S. Ozawa, T. Saito, T. Y. Saito, M. Sakata, T. K. Sako, M. Shibata, A. Shiomi, T. Shirai, H. Sugimoto, M. Takita, Y. H. Tan, N. Tateyama, S. Torii, H. Tsuchiya, S. Udo, B. Wang, H. Wang, Y. Wang, Y. G. Wang, H. R. Wu, L. Xue, Y. Yamamoto, C. T. Yan, X. C. Yang, S. Yasue, Z. H. Ye, G. C. Yu, A. F. Yuan, T. Yuda, H. M. Zhang, J. L. Zhang, N. J. Zhang, X. Y. Zhang, Y. Zhang, Y. Zhang, Y. Zhang, Zhaxisangzhu, X. X. Zhou, and Tibet ASγ Collaboration, "Observation of TeV Gamma Rays from the Fermi Bright Galactic Sources with the Tibet Air Shower Array," *The Astrophysical Journal Letters*, vol. 709, pp. L6–L10, Jan. 2010. arXiv: `0912.0386 [astro-ph.HE]`.

[120] P. S. Ray, M. Kerr, D. Parent, A. A. Abdo, L. Guillemot, S. M. Ransom, N. Rea, M. T. Wolff, A. Makeev, M. S. E. Roberts, F. Camilo, M. Dormody, P. C. C. Freire, J. E. Grove, C. Gwon, A. K. Harding, S. Johnston, M. Keith, M. Kramer, P. F. Michelson, R. W. Romani, P. M. Saz Parkinson, D. J. Thompson, P. Weltevrede, K. S. Wood, and M. Ziegler, "Precise γ-ray Timing and Radio Observations of 17 Fermi γ-ray Pulsars," *The Astrophysical Journal Supplements*, vol. 194, 17, p. 17, Jun. 2011. arXiv: `1011.2468 [astro-ph.HE]`.

[121] O. Helene, “Upper limit of peak area,” *Nuclear Instruments and Methods in Physics Research*, vol. 212, pp. 319–322, Jul. 1983.

[122] K. Bernlöhr, A. Barnacka, Y. Becherini, O. Blanch Bigas, E. Carmona, P. Colin, G. Decerprit, F. Di Pierro, F. Dubois, C. Farnier, S. Funk, G. Hermann, J. A. Hinton, T. B. Humensky, B. Khélifi, T. Kihm, N. Komin, J.-P. Lenain, G. Maier, D. Mazin, M. C. Medina, A. Moralejo, S. J. Nolan, S. Ohm, E. de Oña Wilhelmi, R. D. Parsons, M. Paz Arribas, G. Pedaletti, S. Pita, H. Prokoph, C. B. Rulten, U. Schwanke, M. Shayduk, V. Stamatescu, P. Vallania, S. Vorobiov, R. Wischnewski, T. Yoshikoshi, A. Zech, and CTA Consortium, “Monte Carlo design studies for the Cherenkov Telescope Array,” *Astroparticle Physics*, vol. 43, pp. 171–188, Mar. 2013. arXiv: `1210.3503 [astro-ph.IM]`.

[123] M. A. Alpar, A. F. Cheng, M. A. Ruderman, and J. Shaham, “A new class of radio pulsars,” *Nature*, vol. 300, pp. 728–730, Dec. 1982.

[124] P. S. Ray, A. A. Abdo, D. Parent, D. Bhattacharya, B. Bhattacharyya, F. Camilo, I. Cognard, G. Theureau, E. C. Ferrara, A. K. Harding, D. J. Thompson, P. C. C. Freire, L. Guillemot, Y. Gupta, J. Roy, J. W. T. Hessels, S. Johnston, M. Keith, R. Shannon, M. Kerr, P. F. Michelson, R. W. Romani, M. Kramer, M. A. McLaughlin, S. M. Ransom, M. S. E. Roberts, P. M. Saz Parkinson, M. Ziegler, D. A. Smith, B. W. Stappers, P. Weltevrede, and K. S. Wood, “Radio Searches of Fermi LAT Sources and Blind Search Pulsars: The Fermi Pulsar Search Consortium,” *ArXiv e-prints*, May 2012. arXiv: `1205.3089 [astro-ph.HE]`.

[125] M. S. E. Roberts, “New Black Widows and Redbacks in the Galactic Field,” in *American Institute of Physics Conference Series*, M. Burgay, N. D’Amico, P. Esposito, A. Pellizzoni, and A. Possenti, Eds., ser. American Institute of Physics Conference Series, vol. 1357, Aug. 2011, pp. 127–130. arXiv: `1103.0819 [astro-ph.HE]`.

[126] A. M. Archibald, I. H. Stairs, S. M. Ransom, V. M. Kaspi, V. I. Kondratiev, D. R. Lorimer, M. A. McLaughlin, J. Boyles, J. W. T. Hessels, R. Lynch, J. van Leeuwen, M. S. E. Roberts, F. Jenet, D. J. Champion, R. Rosen, B. N. Barlow, B. H. Dunlap, and R. A. Remillard, “A Radio Pulsar/X-ray Binary Link,” *Science*, vol. 324, p. 1411, Jun. 2009. arXiv: `0905.3397 [astro-ph.HE]`.

[127] C. G. Bassa, A. Patruno, J. W. T. Hessels, E. F. Keane, B. Monard, E. K. Mahony, S. Bogdanov, S. Corbel, P. G. Edwards, A. M. Archibald, G. H. Janssen, B. W. Stappers, and S. Tendulkar, “A state change in the low-mass X-ray binary XSS J12270-4859,” *Monthly Notices of the Royal Astronomical Society*, vol. 441, pp. 1825–1830, Jun. 2014. arXiv: `1402.0765 [astro-ph.HE]`.

[128] J. Roy, P. S. Ray, B. Bhattacharyya, B. Stappers, J. N. Chengalur, J. Deneva, F. Camilo, T. J. Johnson, M. Wolff, J. W. T. Hessels, C. G. Bassa, E. F. Keane, E. C. Ferrara, A. K. Harding, and K. S. Wood, “Discovery of Psr J1227-4853: A Tran-

sition from a Low-mass X-Ray Binary to a Redback Millisecond Pulsar," *The Astrophysical Journal Letters*, vol. 800, L12, p. L12, Feb. 2015. arXiv: `1412.4735 [astro-ph.HE]`.

[129] A. Papitto, C. Ferrigno, E. Bozzo, N. Rea, L. Pavan, L. Burderi, M. Burgay, S. Campana, T. di Salvo, M. Falanga, M. D. Filipović, P. C. C. Freire, J. W. T. Hessels, A. Possenti, S. M. Ransom, A. Riggio, P. Romano, J. M. Sarkissian, I. H. Stairs, L. Stella, D. F. Torres, M. H. Wieringa, and G. F. Wong, "Swings between rotation and accretion power in a binary millisecond pulsar," *Nature*, vol. 501, pp. 517–520, Sep. 2013. arXiv: `1305.3884 [astro-ph.HE]`.

[130] S. Bogdanov, "A NuSTAR Observation of the Gamma-ray-emitting X-ray Binary and Transitional Millisecond Pulsar Candidate 1RXS J154439.4-112820," *The Astrophysical Journal*, vol. 826, 28, p. 28, Jul. 2016. arXiv: `1508.05844 [astro-ph.HE]`.

[131] A. K. Harding, V. V. Usov, and A. G. Muslimov, "High-Energy Emission from Millisecond Pulsars," *The Astrophysical Journal*, vol. 622, pp. 531–543, Mar. 2005. eprint: `astro-ph/0411805`.

[132] F. Aharonian, A. G. Akhperjanian, K.-M. Aye, A. R. Bazer-Bachi, M. Beilicke, W. Benbow, D. Berge, P. Berghaus, K. Bernlöhr, C. Boisson, O. Bolz, I. Braun, F. Breitling, A. M. Brown, J. Bussons Gordo, P. M. Chadwick, L.-M. Chounet, R. Cornils, L. Costamante, B. Degrange, A. Djannati-Ataï, L. O'C. Drury, G. Dubus, D. Emmanoulopoulos, P. Espigat, F. Feinstein, P. Fleury, G. Fontaine, Y. Fuchs, S. Funk, Y. A. Gallant, B. Giebels, S. Gillessen, J. F. Glicenstein, P. Goret, C. Hadjichristidis, M. Hauser, G. Heinzelmann, G. Henri, G. Hermann, J. A. Hinton, W. Hofmann, M. Holleran, D. Horns, O. C. de Jager, S. Johnston, B. Khélifi, J. G. Kirk, N. Komin, A. Konopelko, I. J. Latham, R. Le Gallou, A. Lemière, M. Lemoine-Goumard, N. Leroy, O. Martineau-Huynh, T. Lohse, A. Marcowith, C. Masterson, T. J. L. McComb, M. de Naurois, S. J. Nolan, A. Noutsos, K. J. Orford, J. L. Osborne, M. Ouchrif, M. Panter, G. Pelletier, S. Pita, G. Pühlhofer, M. Punch, B. C. Raubenheimer, M. Raue, J. Raux, S. M. Rayner, I. Redondo, A. Reimer, O. Reimer, J. Ripken, L. Rob, L. Rolland, G. Rowell, V. Sahakian, L. Saugé, S. Schlenker, R. Schlickeiser, C. Schuster, U. Schwanke, M. Siewert, O. Skjæraasen, H. Sol, R. Steenkamp, C. Stegmann, J.-P. Tavernet, R. Terrier, C. G. Théoret, M. Tluczykont, G. Vasileiadis, C. Venter, P. Vincent, H. J. Völk, and S. J. Wagner, "Discovery of the binary pulsar PSR B1259-63 in very-high-energy gamma rays around periastron with HESS," *Astronomy & Astrophysics*, vol. 442, pp. 1–10, Oct. 2005. eprint: `astro-ph/0506280`.

[133] M. Tavani, J. Arons, and V. M. Kaspi, "Regimes of high-energy shock emission from the Be star/pulsar system PSR 1259-63," *The Astrophysical Journal Letters*, vol. 433, pp. L37–L40, Sep. 1994.

[134] J. Arons and M. Tavani, “High-energy emission from the eclipsing millisecond pulsar PSR 1957+20,” *The Astrophysical Journal*, vol. 403, pp. 249–255, Jan. 1993.

[135] H.E.S.S. Collaboration, A. Abramowski, F. Acero, F. Aharonian, A. G. Akhperjanian, G. Anton, A. Balzer, A. Barnacka, U. Barres de Almeida, Y. Becherini, J. Becker, B. Behera, K. Bernlöhr, A. Bochow, C. Boisson, J. Bolmont, P. Bordas, J. Brucker, F. Brun, P. Brun, T. Bulik, I. Büsching, S. Carrigan, S. Casanova, M. Cerruti, P. M. Chadwick, A. Charbonnier, R. C. G. Chaves, A. Cheesebrough, L.-M. Chounet, A. C. Clapson, G. Coignet, G. Cologna, J. Conrad, M. Dalton, M. K. Daniel, I. D. Davids, B. Degrange, C. Deil, H. J. Dickinson, A. Djannati-Ataï, W. Domainko, L. O. Drury, F. Dubois, G. Dubus, K. Dutson, J. Dyks, M. Dyrda, K. Egberts, P. Eger, P. Espigat, L. Fallon, C. Farnier, S. Fegan, F. Feinstein, M. V. Fernandes, A. Fiasson, G. Fontaine, A. Förster, M. Füßling, Y. A. Gallant, H. Gast, L. Gérard, D. Gerbig, B. Giebels, J. F. Glicenstein, B. Glück, P. Goret, D. Göring, S. Häffner, J. D. Hague, D. Hampf, M. Hauser, S. Heinz, G. Heinzelmann, G. Henri, G. Hermann, J. A. Hinton, A. Hoffmann, W. Hofmann, P. Hofverberg, M. Holler, D. Horns, A. Jacholkowska, O. C. de Jager, C. Jahn, M. Jamrozy, I. Jung, M. A. Kastendieck, K. Katarzyński, U. Katz, S. Kaufmann, D. Keogh, D. Khangulyan, B. Khélifi, D. Klochkov, W. Kluźniak, T. Kneiske, N. Komin, K. Kosack, R. Kossakowski, H. Laffon, G. Lamanna, D. Lennarz, T. Lohse, A. Lopatin, C.-C. Lu, V. Marandon, A. Marcowith, J. Masbou, D. Maurin, N. Maxted, T. J. L. McComb, M. C. Medina, J. Méhault, R. Moderski, E. Moulin, C. L. Naumann, M. Naumann-Godo, M. de Naurois, D. Nedbal, D. Nekrassov, N. Nguyen, B. Nicholas, J. Niemiec, S. J. Nolan, S. Ohm, D. de Oña Wilhelmi, B. Opitz, M. Ostrowski, I. Oya, M. Panter, M. Paz Arribas, G. Pedaletti, G. Pelletier, P.-O. Petrucci, S. Pita, G. Pühlhofer, M. Punch, A. Quirrenbach, M. Raue, S. M. Rayner, A. Reimer, O. Reimer, M. Renaud, R. de los Reyes, F. Rieger, J. Ripken, L. Rob, S. Rosier-Lees, G. Rowell, B. Rudak, C. B. Rulten, J. Ruppel, F. Ryde, V. Sahakian, A. Santangelo, R. Schlickeiser, F. M. Schöck, A. Schulz, U. Schwanke, S. Schwarzburg, S. Schwemmer, M. Sikora, J. L. Skilton, H. Sol, G. Spengler, Ł. Stawarz, R. Steenkamp, C. Stegmann, F. Stinzing, K. Stycz, I. Sushch, A. Szostek, J.-P. Tavernet, R. Terrier, M. Tluczykont, K. Valerius, C. van Eldik, G. Vasileiadis, C. Venter, J. P. Vialle, A. Viana, P. Vincent, H. J. Völk, F. Volpe, S. Vorobiov, M. Vorster, S. J. Wagner, M. Ward, R. White, A. Wierzcholska, M. Zacharias, A. Zajczyk, A. A. Zdziarski, A. Zech, and H.-S. Zechlin, “Very-high-energy gamma-ray emission from the direction of the Galactic globular cluster Terzan 5,” *Astronomy & Astrophysics*, vol. 531, L18, p. L18, Jul. 2011. arXiv: `1106.4069 [astro-ph.HE]`.

[136] S. M. Ransom, “Pulsars in Globular Clusters,” in *Dynamical Evolution of Dense Stellar Systems*, E. Vesperini, M. Giersz, and A. Sills, Eds., ser. IAU Symposium, vol. 246, May 2008, pp. 291–300.

[137] W. Bednarek and T. Sobczak, "Misaligned TeV γ-ray sources in the vicinity of globular clusters," *Monthly Notices of the Royal Astronomical Society*, vol. 445, pp. 2842–2847, Dec. 2014. arXiv: `1409.7921 [astro-ph.HE]`.

[138] F. Aharonian, A. G. Akhperjanian, G. Anton, U. Barres de Almeida, A. R. Bazer-Bachi, Y. Becherini, B. Behera, K. Bernlöhr, C. Boisson, A. Bochow, V. Borrel, I. Braun, E. Brion, J. Brucker, P. Brun, R. Bühler, T. Bulik, I. Büsching, T. Boutelier, P. M. Chadwick, A. Charbonnier, R. C. G. Chaves, A. Cheesebrough, L.-M. Chounet, A. C. Clapson, G. Coignet, M. Dalton, M. K. Daniel, I. D. Davids, B. Degrange, C. Deil, H. J. Dickinson, A. Djannati-Ataï, W. Domainko, L. O'C. Drury, F. Dubois, G. Dubus, J. Dyks, M. Dyrda, K. Egberts, D. Emmanoulopoulos, P. Espigat, C. Farnier, F. Feinstein, A. Fiasson, A. Förster, G. Fontaine, M. Füßling, S. Gabici, Y. A. Gallant, L. Gérard, B. Giebels, J. F. Glicenstein, B. Glück, P. Goret, D. Hauser, M. Hauser, S. Heinz, G. Heinzelmann, G. Henri, G. Hermann, J. A. Hinton, A. Hoffmann, W. Hofmann, M. Holleran, S. Hoppe, D. Horns, A. Jacholkowska, O. C. de Jager, I. Jung, K. Katarzyński, U. Katz, S. Kaufmann, E. Kendziorra, M. Kerschhaggl, D. Khangulyan, B. Khélifi, D. Keogh, N. Komin, K. Kosack, G. Lamanna, J.-P. Lenain, T. Lohse, V. Marandon, J. M. Martin, O. Martineau-Huynh, A. Marcowith, D. Maurin, T. J. L. McComb, M. C. Medina, R. Moderski, E. Moulin, M. Naumann-Godo, M. de Naurois, D. Nedbal, D. Nekrassov, J. Niemiec, S. J. Nolan, S. Ohm, J.-F. Olive, E. de Oña Wilhelmi, K. J. Orford, M. Ostrowski, M. Panter, M. Paz Arribas, G. Pedaletti, G. Pelletier, P.-O. Petrucci, S. Pita, G. Pühlhofer, M. Punch, A. Quirrenbach, B. C. Raubenheimer, M. Raue, S. M. Rayner, O. Reimer, M. Renaud, F. Rieger, J. Ripken, L. Rob, S. Rosier-Lees, G. Rowell, B. Rudak, C. B. Rulten, J. Ruppel, V. Sahakian, A. Santangelo, R. Schlickeiser, F. M. Schöck, R. Schröder, U. Schwanke, S. Schwarzburg, S. Schwemmer, A. Shalchi, J. L. Skilton, H. Sol, D. Spangler, Ł. Stawarz, R. Steenkamp, C. Stegmann, G. Superina, A. Szostek, P. H. Tam, J.-P. Tavernet, R. Terrier, O. Tibolla, C. van Eldik, G. Vasileiadis, C. Venter, L. Venter, J. P. Vialle, P. Vincent, M. Vivier, H. J. Völk, F. Volpe, S. J. Wagner, M. Ward, A. A. Zdziarski, and A. Zech, "HESS upper limit on the very high energy γ-ray emission from the globular cluster 47 Tucanae," *Astronomy & Astrophysics*, vol. 499, pp. 273–277, May 2009. arXiv: `0904.0361 [astro-ph.HE]`.

[139] M. McCutcheon and for the VERITAS Collaboration, "VERITAS Observations of Globular Clusters," *ArXiv e-prints*, Jul. 2009. arXiv: `0907.4974 [astro-ph.HE]`.

[140] H. Anderhub, L. A. Antonelli, P. Antoranz, M. Backes, C. Baixeras, S. Balestra, J. A. Barrio, D. Bastieri, J. Becerra González, J. K. Becker, W. Bednarek, K. Berger, E. Bernardini, A. Biland, R. K. Bock, G. Bonnoli, P. Bordas, D. Borla Tridon, V. Bosch-Ramon, D. Bose, I. Braun, T. Bretz, I. Britvitch, M. Camara, E. Carmona, S. Commichau, J. L. Contreras, J. Cortina, M. T. Costado, S. Covino, V. Curtef, F. Dazzi, A. DeAngelis, E. DeCea del Pozo, R. de los Reyes, B. DeLotto, M. DeMaria, F. DeSabata, C. Delgado Mendez, A. Dominguez, D. Dorner, M. Doro, D. Elsaesser, M. Errando, D. Ferenc, E. Fernández, R. Firpo, M. V. Fonseca, L.

Font, N. Galante, R. J. García López, M. Garczarczyk, M. Gaug, F. Goebel, D. Hadasch, M. Hayashida, A. Herrero, D. Hildebrand, D. Höhne-Mönch, J. Hose, C. C. Hsu, T. Jogler, D. Kranich, A. La Barbera, A. Laille, E. Leonardo, E. Lindfors, S. Lombardi, F. Longo, M. López, E. Lorenz, P. Majumdar, G. Maneva, N. Mankuzhiyil, K. Mannheim, L. Maraschi, M. Mariotti, M. Martínez, D. Mazin, M. Meucci, M. Meyer, J. M. Miranda, R. Mirzoyan, H. Miyamoto, J. Moldón, M. Moles, A. Moralejo, D. Nieto, K. Nilsson, J. Ninkovic, N. Otte, I. Oya, R. Paoletti, J. M. Paredes, M. Pasanen, D. Pascoli, F. Pauss, R. G. Pegna, M. A. Perez-Torres, M. Persic, L. Peruzzo, F. Prada, E. Prandini, N. Puchades, I. Reichardt, W. Rhode, M. Ribó, J. Rico, M. Rissi, A. Robert, S. Rügamer, A. Saggion, T. Y. Saito, M. Salvati, M. Sanchez-Conde, K. Satalecka, V. Scalzotto, V. Scapin, T. Schweizer, M. Shayduk, S. N. Shore, N. Sidro, A. Sierpowska-Bartosik, A. Sillanpää, J. Sitarek, D. Sobczynska, F. Spanier, A. Stamerra, L. S. Stark, L. Takalo, F. Tavecchio, P. Temnikov, D. Tescaro, M. Teshima, M. Tluczykont, D. F. Torres, N. Turini, H. Vankov, R. M. Wagner, W. Wittek, V. Zabalza, F. Zandanel, R. Zanin, and J. Zapatero, "Search for VHE γ-ray Emission from the Globular Cluster M13 with the Magic Telescope," *The Astrophysical Journal*, vol. 702, pp. 266–269, Sep. 2009. arXiv: `0905.2427 [astro-ph.HE]`.

[141] M. W. McCutcheon, "Search for VHE gamma-ray emission from the globular cluster M13 with VERITAS," PhD thesis, McGill University (Canada, 2012.

[142] N. Wex, S. Johnston, R. N. Manchester, A. G. Lyne, B. W. Stappers, and M. Bailes, "Timing models for the long orbital period binary pulsar PSR B1259-63," *Monthly Notices of the Royal Astronomical Society*, vol. 298, pp. 997–1004, Aug. 1998. eprint: `astro-ph/9803182`.

[143] S. Bogdanov, A. M. Archibald, J. W. T. Hessels, V. M. Kaspi, D. Lorimer, M. A. McLaughlin, S. M. Ransom, and I. H. Stairs, "A Chandra X-Ray Observation of the Binary Millisecond Pulsar PSR J1023+0038," *The Astrophysical Journal*, vol. 742, 97, p. 97, Dec. 2011. arXiv: `1108.5753 [astro-ph.HE]`.

[144] H.E.S.S. Collaboration, A. Abramowski, F. Acero, F. Aharonian, A. G. Akhperjanian, G. Anton, S. Balenderan, A. Balzer, A. Barnacka, Y. Becherini, J. Becker Tjus, K. Bernlöhr, E. Birsin, J. Biteau, C. Boisson, J. Bolmont, P. Bordas, J. Brucker, F. Brun, P. Brun, T. Bulik, S. Carrigan, S. Casanova, M. Cerruti, P. M. Chadwick, R. C. G. Chaves, A. Cheesebrough, S. Colafrancesco, G. Cologna, J. Conrad, C. Couturier, M. Dalton, M. K. Daniel, I. D. Davids, B. Degrange, C. Deil, P. deWilt, H. J. Dickinson, A. Djannati-Ataï, W. Domainko, L. O. Drury, G. Dubus, K. Dutson, J. Dyks, M. Dyrda, K. Egberts, P. Eger, P. Espigat, L. Fallon, C. Farnier, S. Fegan, F. Feinstein, M. V. Fernandes, D. Fernandez, A. Fiasson, G. Fontaine, A. Förster, M. Füßling, M. Gajdus, Y. A. Gallant, T. Garrigoux, H. Gast, B. Giebels, J. F. Glicenstein, B. Glück, D. Göring, M.-H. Grondin, M. Grudzińska, S. Häer, J. D. Hague, J. Hahn, D. Hampf, J. Harris, S. Heinz, G. Heinzelmann, G. Henri, G. Hermann, A. Hillert, J. A. Hinton, W. Hofmann, P. Hofverberg, M. Holler,

D. Horns, A. Jacholkowska, C. Jahn, M. Jamrozy, I. Jung, M. A. Kastendieck, K. Katarzyński, U. Katz, S. Kaufmann, B. Khélifi, S. Klepser, D. Klochkov, W. Kluźniak, T. Kneiske, D. Kolitzus, N. Komin, K. Kosack, R. Kossakowski, F. Krayzel, P. P. Krüger, H. Lan, G. Lamanna, J. Lefaucheur, M. Lemoine-Goumard, J.-P. Lenain, D. Lennarz, T. Lohse, A. Lopatin, C.-C. Lu, V. Marandon, A. Marcowith, J. Masbou, G. Maurin, N. Maxted, M. Mayer, T. J. L. McComb, M. C. Medina, J. Méhault, U. Menzler, R. Moderski, M. Mohamed, E. Moulin, C. L. Naumann, M. Naumann-Godo, M. de Naurois, D. Nedbal, N. Nguyen, J. Niemiec, S. J. Nolan, L. Oakes, S. Ohm, E. de Oña Wilhelmi, B. Opitz, M. Ostrowski, I. Oya, M. Panter, R. D. Parsons, M. Paz Arribas, N. W. Pekeur, G. Pelletier, J. Perez, P.-O. Petrucci, B. Peyaud, S. Pita, G. Pühlhofer, M. Punch, A. Quirrenbach, S. Raab, M. Raue, A. Reimer, O. Reimer, M. Renaud, R. de los Reyes, F. Rieger, J. Ripken, L. Rob, S. Rosier-Lees, G. Rowell, B. Rudak, C. B. Rulten, V. Sahakian, D. A. Sanchez, A. Santangelo, R. Schlickeiser, A. Schulz, U. Schwanke, S. Schwarzburg, S. Schwemmer, F. Sheidaei, J. L. Skilton, H. Sol, G. Spengler, Ł. Stawarz, R. Steenkamp, C. Stegmann, F. Stinzing, K. Stycz, I. Sushch, A. Szostek, J.-P. Tavernet, R. Terrier, M. Tluczykont, C. Trichard, K. Valerius, C. van Eldik, G. Vasileiadis, C. Venter, A. Viana, P. Vincent, H. J. Völk, F. Volpe, S. Vorobiov, M. Vorster, S. J. Wagner, M. Ward, R. White, A. Wierzcholska, P. Willmann, D. Wouters, M. Zacharias, A. Zajczyk, A. A. Zdziarski, A. Zech, and H.-S. Zechlin, "H.E.S.S. observations of the binary system PSR B1259-63/LS 2883 around the 2010/2011 periastron passage," *Astronomy & Astrophysics*, vol. 551, A94, A94, Mar. 2013. arXiv: `1301.3930 [astro-ph.HE]`.

[145] A. T. Deller, J. Moldon, J. C. A. Miller-Jones, A. Patruno, J. W. T. Hessels, A. M. Archibald, Z. Paragi, G. Heald, and N. Vilchez, "Radio Imaging Observations of PSR J1023+0038 in an LMXB State," *The Astrophysical Journal*, vol. 809, 13, p. 13, Aug. 2015. arXiv: `1412.5155 [astro-ph.SR]`.

[146] A. M. Archibald, V. M. Kaspi, S. Bogdanov, J. W. T. Hessels, I. H. Stairs, S. M. Ransom, and M. A. McLaughlin, "X-ray Variability and Evidence for Pulsations from the Unique Radio Pulsar/X-ray Binary Transition Object FIRST J102347.6+003841," *The Astrophysical Journal*, vol. 722, pp. 88–95, Oct. 2010. arXiv: `1008.1068 [astro-ph.HE]`.

[147] P. H. T. Tam, C. Y. Hui, R. H. H. Huang, A. K. H. Kong, J. Takata, L. C. C. Lin, Y. J. Yang, K. S. Cheng, and R. E. Taam, "Evidence for Gamma-ray Emission from the Low-mass X-ray Binary System First J102347.6+003841," *The Astrophysical Journal Letters*, vol. 724, pp. L207–L211, Dec. 2010. arXiv: `1010.4311 [astro-ph.HE]`.

[148] A. M. Archibald, V. M. Kaspi, J. W. T. Hessels, B. Stappers, G. Janssen, and A. Lyne, "Long-Term Radio Timing Observations of the Transition Millisecond Pulsar PSR˜J1023+0038," *ArXiv e-prints*, Nov. 2013. arXiv: `1311.5161 [astro-ph.HE]`.

[149] B. W. Stappers, A. Archibald, C. Bassa, J. Hessels, G. Janssen, V. Kaspi, A. Lyne, A. Patruno, and A. B. Hill, "State-change in the "transition" binary millisecond pulsar J1023+0038," *The Astronomer's Telegram*, vol. 5513, Oct. 2013.

[150] J. P. Halpern, E. Gaidos, A. Sheffield, A. M. Price-Whelan, and S. Bogdanov, "Optical Observations of the Binary MSP J1023+0038 in a New Accreting State," *The Astronomer's Telegram*, vol. 5514, Oct. 2013.

[151] P. Szkody, O. Fraser, N. Silvestri, A. Henden, S. F. Anderson, J. Frith, B. Lawton, E. Owens, S. Raymond, G. Schmidt, M. Wolfe, J. Bochanski, K. Covey, H. Harris, S. Hawley, G. R. Knapp, B. Margon, W. Voges, L. Walkowicz, J. Brinkmann, and D. Q. Lamb, "Cataclysmic Variables from the Sloan Digital Sky Survey. II. The Second Year," *The Astronomical Journal*, vol. 126, pp. 1499–1514, Sep. 2003. eprint: `astro-ph/0306269`.

[152] A. K. H. Kong, "Enhanced X-ray emission of the binary millisecond pulsar J1023+0038," *The Astronomer's Telegram*, vol. 5515, Oct. 2013.

[153] A. Patruno, A. Archibald, S. Bogdanov, V. Kaspi, S. Tendulkar, C. Bassa, G. Janssen, B. Stappers, and A. Lyne, "X-Ray and UV/Optical Variability of the Missing Link Binary Pulsar PSR J1023+0038," *The Astronomer's Telegram*, vol. 5516, Oct. 2013.

[154] A. M. Archibald, S. Bogdanov, A. Patruno, J. W. T. Hessels, A. T. Deller, C. Bassa, G. H. Janssen, V. M. Kaspi, A. G. Lyne, B. W. Stappers, S. P. Tendulkar, C. R. D'Angelo, and R. Wijnands, "Accretion-powered Pulsations in an Apparently Quiescent Neutron Star Binary," *The Astrophysical Journal*, vol. 807, 62, p. 62, Jul. 2015. arXiv: `1412.1306 [astro-ph.HE]`.

[155] B. W. Stappers, A. M. Archibald, J. W. T. Hessels, C. G. Bassa, S. Bogdanov, G. H. Janssen, V. M. Kaspi, A. G. Lyne, A. Patruno, S. Tendulkar, A. B. Hill, and T. Glanzman, "A State Change in the Missing Link Binary Pulsar System PSR J1023+0038," *The Astrophysical Journal*, vol. 790, 39, p. 39, Jul. 2014. arXiv: `1311.7506 [astro-ph.HE]`.

[156] W. A. Rolke, A. M. López, and J. Conrad, "Limits and confidence intervals in the presence of nuisance parameters," *Nuclear Instruments and Methods in Physics Research A*, vol. 551, pp. 493–503, Oct. 2005. eprint: `physics/0403059`.

[157] J. Takata, K. L. Li, G. C. K. Leung, A. K. H. Kong, P. H. T. Tam, C. Y. Hui, E. M. H. Wu, Y. Xing, Y. Cao, S. Tang, Z. Wang, and K. S. Cheng, "Multi-wavelength Emissions from the Millisecond Pulsar Binary PSR J1023+0038 during an Accretion Active State," *The Astrophysical Journal*, vol. 785, 131, p. 131, Apr. 2014. arXiv: `1312.0605 [astro-ph.HE]`.

[158] J. R. Thorstensen and E. Armstrong, “Is FIRST J102347.6+003841 Really a Cataclysmic Binary?” *The Astronomical Journal*, vol. 130, pp. 759–766, Aug. 2005. eprint: `astro-ph/0504523`.

[159] L. Homer, P. Szkody, B. Chen, A. Henden, G. Schmidt, S. F. Anderson, N. M. Silvestri, and J. Brinkmann, “XMM-Newton and Optical Follow-up Observations of SDSS J093249.57+472523.0 and SDSS J102347.67+003841.2,” *The Astronomical Journal*, vol. 131, pp. 562–570, Jan. 2006. eprint: `astro-ph/0509802`.

[160] S. P. Tendulkar, C. Yang, H. An, V. M. Kaspi, A. M. Archibald, C. Bassa, E. Bellm, S. Bogdanov, F. A. Harrison, J. W. T. Hessels, G. H. Janssen, A. G. Lyne, A. Patruno, B. Stappers, D. Stern, J. A. Tomsick, S. E. Boggs, D. Chakrabarty, F. E. Christensen, W. W. Craig, C. A. Hailey, and W. Zhang, “NuSTAR Observations of the State Transition of Millisecond Pulsar Binary PSR J1023+0038,” *The Astrophysical Journal*, vol. 791, 77, p. 77, Aug. 2014. arXiv: `1406.7009 [astro-ph.HE]`.

[161] A. T. Deller, A. M. Archibald, W. F. Brisken, S. Chatterjee, G. H. Janssen, V. M. Kaspi, D. Lorimer, A. G. Lyne, M. A. McLaughlin, S. Ransom, I. H. Stairs, and B. Stappers, “A Parallax Distance and Mass Estimate for the Transitional Millisecond Pulsar System J1023+0038,” *The Astrophysical Journal Letters*, vol. 756, L25, p. L25, Sep. 2012. arXiv: `1207.5670 [astro-ph.SR]`.

[162] C. M. Espinoza, L. Guillemot, Ö. Çelik, P. Weltevrede, B. W. Stappers, D. A. Smith, M. Kerr, V. E. Zavlin, I. Cognard, R. P. Eatough, P. C. C. Freire, G. H. Janssen, F. Camilo, G. Desvignes, J. W. Hewitt, X. Hou, S. Johnston, M. Keith, M. Kramer, A. Lyne, R. N. Manchester, S. M. Ransom, P. S. Ray, R. Shannon, G. Theureau, and N. Webb, “Six millisecond pulsars detected by the Fermi Large Area Telescope and the radio/gamma-ray connection of millisecond pulsars,” *Monthly Notices of the Royal Astronomical Society*, vol. 430, pp. 571–587, Mar. 2013. arXiv: `1212.4360 [astro-ph.HE]`.

[163] M. S. Longair, *High Energy Astrophysics*. Feb. 2011.

[164] S. Corbel, G. Dubus, J. A. Tomsick, A. Szostek, R. H. D. Corbet, J. C. A. Miller-Jones, J. L. Richards, G. Pooley, S. Trushkin, R. Dubois, A. B. Hill, M. Kerr, W. Max-Moerbeck, A. C. S. Readhead, A. Bodaghee, V. Tudose, D. Parent, J. Wilms, and K. Pottschmidt, “A giant radio flare from Cygnus X-3 with associated γ-ray emission,” *Monthly Notices of the Royal Astronomical Society*, vol. 421, pp. 2947–2955, Apr. 2012. arXiv: `1201.3356 [astro-ph.HE]`.

[165] D. Malyshev, A. A. Zdziarski, and M. Chernyakova, “High-energy gamma-ray emission from Cyg X-1 measured by Fermi and its theoretical implications,” *Monthly Notices of the Royal Astronomical Society*, vol. 434, pp. 2380–2389, Sep. 2013. arXiv: `1305.5920 [astro-ph.HE]`.

[166] F. Coti Zelati, M. C. Baglio, S. Campana, P. D'Avanzo, P. Goldoni, N. Masetti, T. Muñoz-Darias, S. Covino, R. P. Fender, E. Jiménez Bailón, H. Otí-Floranes, E. Palazzi, and F. G. Ramón-Fox, "Engulfing a radio pulsar: the case of PSR J1023+0038," *Monthly Notices of the Royal Astronomical Society*, vol. 444, pp. 1783–1792, Oct. 2014. arXiv: `1409.0427 [astro-ph.HE]`.

[167] K. L. Li, A. K. H. Kong, J. Takata, K. S. Cheng, P. H. T. Tam, C. Y. Hui, and R. Jin, "NuSTAR Observations and Broadband Spectral Energy Distribution Modeling of the Millisecond Pulsar Binary PSR J1023+0038," *The Astrophysical Journal*, vol. 797, 111, p. 111, Dec. 2014. arXiv: `1410.4563 [astro-ph.HE]`.

[168] A. Papitto and D. F. Torres, "A Propeller Model for the Sub-luminous State of the Transitional Millisecond Pulsar PSR J1023+0038," *The Astrophysical Journal*, vol. 807, 33, p. 33, Jul. 2015. arXiv: `1504.05029 [astro-ph.HE]`.

[169] J. Morin, "Magnetic Fields from Low-Mass Stars to Brown Dwarfs," in *EAS Publications Series*, C. Reylé, C. Charbonnel, and M. Schultheis, Eds., ser. EAS Publications Series, vol. 57, Nov. 2012, pp. 165–191. arXiv: `1208.3363 [astro-ph.SR]`.

[170] S. Pineault, T. L. Landecker, B. Madore, and S. Gaumont-Guay, "The supernova remnant CTA1 and the surrounding interstellar medium," *The Astronomical Journal*, vol. 105, pp. 1060–1073, Mar. 1993.

[171] Y. Xu, M. J. Reid, X. W. Zheng, and K. M. Menten, "The Distance to the Perseus Spiral Arm in the Milky Way," *Science*, vol. 311, pp. 54–57, Jan. 2006. eprint: `astro-ph/0512223`.

[172] G. Theureau, D. Parent, I. Cognard, G. Desvignes, D. A. Smith, J. M. Casandjian, C. C. Cheung, H. A. Craig, D. Donato, R. Foster, L. Guillemot, A. K. Harding, J.-F. Lestrade, P. S. Ray, R. W. Romani, D. J. Thompson, W. W. Tian, and K. Watters, "PSRs J0248+6021 and J2240+5832: young pulsars in the northern Galactic plane. Discovery, timing, and gamma-ray observations," *Astronomy & Astrophysics*, vol. 525, A94, A94, Jan. 2011. arXiv: `1010.4230 [astro-ph.HE]`.

[173] M. Marelli, A. De Luca, D. Salvetti, N. Sartore, A. Sartori, P. Caraveo, F. Pizzolato, P. M. Saz Parkinson, and A. Belfiore, "PSR J0357+3205: The Tail of the Turtle," *The Astrophysical Journal*, vol. 765, 36, p. 36, Mar. 2013. arXiv: `1212.6664 [astro-ph.HE]`.

[174] A. Zepka, J. M. Cordes, I. Wasserman, and S. C. Lundgren, "Discovery of Three Radio Pulsars from an X-Ray–selected Sample," *The Astrophysical Journal*, vol. 456, p. 305, Jan. 1996.

[175] A. A. Abdo, M. Ackermann, M. Ajello, L. Baldini, J. Ballet, G. Barbiellini, D. Bastieri, B. M. Baughman, K. Bechtol, R. Bellazzini, B. Berenji, R. D. Blandford,

E. D. Bloom, E. Bonamente, A. W. Borgland, J. Bregeon, A. Brez, M. Brigida, P. Bruel, T. H. Burnett, S. Buson, G. A. Caliandro, R. A. Cameron, F. Camilo, P. A. Caraveo, J. M. Casandjian, C. Cecchi, Ö. Çelik, A. Chekhtman, C. C. Cheung, J. Chiang, S. Ciprini, R. Claus, I. Cognard, J. Cohen-Tanugi, L. R. Cominsky, J. Conrad, S. Cutini, A. de Angelis, F. de Palma, S. W. Digel, B. L. Dingus, M. Dormody, E. d. C. e. Silva, P. S. Drell, R. Dubois, D. Dumora, C. Farnier, C. Favuzzi, S. J. Fegan, W. B. Focke, P. Fortin, M. Frailis, P. C. C. Freire, Y. Fukazawa, S. Funk, P. Fusco, F. Gargano, D. Gasparrini, N. Gehrels, S. Germani, G. Giavitto, B. Giebels, N. Giglietto, F. Giordano, T. Glanzman, G. Godfrey, I. A. Grenier, M.-H. Grondin, J. E. Grove, L. Guillemot, S. Guiriec, Y. Hanabata, A. K. Harding, E. Hays, R. E. Hughes, M. S. Jackson, G. Jóhannesson, A. S. Johnson, T. J. Johnson, W. N. Johnson, S. Johnston, T. Kamae, H. Katagiri, J. Kataoka, N. Kawai, M. Kerr, J. Knödlseder, M. L. Kocian, M. Kuss, J. Lande, L. Latronico, M. Lemoine-Goumard, F. Longo, F. Loparco, B. Lott, M. N. Lovellette, P. Lubrano, A. Makeev, M. Marelli, M. N. Mazziotta, J. E. McEnery, C. Meurer, P. F. Michelson, W. Mitthumsiri, T. Mizuno, A. A. Moiseev, C. Monte, M. E. Monzani, A. Morselli, I. V. Moskalenko, S. Murgia, P. L. Nolan, J. P. Norris, E. Nuss, T. Ohsugi, N. Omodei, E. Orlando, J. F. Ormes, D. Paneque, D. Parent, V. Pelassa, M. Pepe, M. Pesce-Rollins, F. Piron, T. A. Porter, S. Rainò, R. Rando, P. S. Ray, M. Razzano, A. Reimer, O. Reimer, T. Reposeur, S. Ritz, M. S. E. Roberts, L. S. Rochester, A. Y. Rodriguez, R. W. Ro'mani, M. Roth, F. Ryde, H. F.-W. Sadrozinski, D. Sanchez, A. Sander, P. M. Saz Parkinson, J. D. Scargle, C. Sgrò, E. J. Siskind, D. A. Smith, P. D. Smith, G. Spandre, P. Spinelli, M. S. Strickman, D. J. Suson, H. Tajima, H. Takahashi, T. Tanaka, J. B. Thayer, J. G. Thayer, G. Theureau, D. J. Thompson, L. Tibaldo, O. Tibolla, D. F. Torres, G. Tosti, A. Tramacere, Y. Uchiyama, T. L. Usher, A. Van Etten, V. Vasileiou, C. Venter, N. Vilchez, V. Vitale, A. P. Waite, P. Wang, K. Watters, B. L. Winer, M. T. Wolff, K. S. Wood, T. Ylinen, and M. Ziegler, "PSR J1907+0602: A Radio-Faint Gamma-Ray Pulsar Powering a Bright TeV Pulsar Wind Nebula," *The Astrophysical Journal*, vol. 711, pp. 64–74, Mar. 2010. arXiv: `1001.0792 [astro-ph.HE]`.

[176] A. Kirichenko, A. Danilenko, P. Shternin, Y. Shibanov, E. Ryspaeva, D. Zyuzin, M. Durant, O. Kargaltsev, G. Pavlov, and A. Cabrera-Lavers, "Optical Observations of Psr J2021+3651 in the Dragonfly Nebula With the GTC," *The Astrophysical Journal*, vol. 802, 17, p. 17, Mar. 2015. arXiv: `1501.04594 [astro-ph.SR]`.

[177] T. L. Landecker, R. S. Roger, and L. A. Higgs, "Atomic hydrogen in a field in Cygnus X containing the supernova remnant G78.2+2.1," *Astronomy & Astrophysics, Supplement*, vol. 39, pp. 133–151, Feb. 1980.

[178] F. Camilo, P. S. Ray, S. M. Ransom, M. Burgay, T. J. Johnson, M. Kerr, E. V. Gotthelf, J. P. Halpern, J. Reynolds, R. W. Romani, P. Demorest, S. Johnston, W. van Straten, P. M. Saz Parkinson, M. Ziegler, M. Dormody, D. J. Thompson, D. A. Smith, A. K. Harding, A. A. Abdo, F. Crawford, P. C. C. Freire, M. Keith, M. Kramer, M. S. E. Roberts, P. Weltevrede, and K. S. Wood, "Radio Detection of

LAT PSRs J1741-2054 and J2032+4127: No Longer Just Gamma-ray Pulsars," *The Astrophysical Journal*, vol. 705, pp. 1–13, Nov. 2009. arXiv: `0908.2626`.

[179] R. Kothes, B. Uyaniker, and S. Pineault, "The Supernova Remnant G106.3+2.7 and Its Pulsar-Wind Nebula: Relics of Triggered Star Formation in a Complex Environment," *The Astrophysical Journal*, vol. 560, pp. 236–243, Oct. 2001. eprint: `astro-ph/0106270`.

[180] J. P. Halpern, E. V. Gotthelf, F. Camilo, D. J. Helfand, and S. M. Ransom, "X-Ray, Radio, and Optical Observations of the Putative Pulsar in the Supernova Remnant CTA 1," *The Astrophysical Journal*, vol. 612, pp. 398–407, Sep. 2004. eprint: `astro-ph/0404312`.

[181] E. Aliu, S. Archambault, T. Arlen, T. Aune, M. Beilicke, W. Benbow, A. Bouvier, J. H. Buckley, V. Bugaev, A. Cesarini, L. Ciupik, E. Collins-Hughes, M. P. Connolly, W. Cui, R. Dickherber, C. Duke, J. Dumm, V. V. Dwarkadas, M. Errando, A. Falcone, S. Federici, Q. Feng, J. P. Finley, G. Finnegan, L. Fortson, A. Furniss, N. Galante, D. Gall, G. H. Gillanders, S. Godambe, E. V. Gotthelf, S. Griffin, J. Grube, G. Gyuk, D. Hanna, J. Holder, G. Hughes, T. B. Humensky, P. Kaaret, O. Kargaltsev, N. Karlsson, Y. Khassen, D. Kieda, H. Krawczynski, F. Krennrich, M. J. Lang, K. Lee, A. S. Madhavan, G. Maier, P. Majumdar, S. McArthur, A. McCann, P. Moriarty, R. Mukherjee, T. Nelson, A. O'Faoláin de Bhróithe, R. A. Ong, M. Orr, A. N. Otte, N. Park, J. S. Perkins, M. Pohl, H. Prokoph, J. Quinn, K. Ragan, L. C. Reyes, P. T. Reynolds, E. Roache, M. Roberts, D. B. Saxon, M. Schroedter, G. H. Sembroski, P. Slane, A. W. Smith, D. Staszak, I. Telezhinsky, G. Tevsić, M. Theiling, S. Thibadeau, K. Tsurusaki, J. Tyler, A. Varlotta, V. V. Vassiliev, S. Vincent, M. Vivier, S. P. Wakely, T. C. Weekes, A. Weinstein, R. Welsing, D. A. Williams, and B. Zitzer, "Discovery of TeV Gamma-Ray Emission from CTA 1 by VERITAS," *The Astrophysical Journal*, vol. 764, 38, p. 38, Feb. 2013. arXiv: `1212.4739 [astro-ph.HE]`.

[182] J. Aleksić, S. Ansoldi, L. A. Antonelli, P. Antoranz, A. Babic, P. Bangale, J. A. Barrio, J. Becerra González, W. Bednarek, E. Bernardini, B. Biasuzzi, A. Biland, O. Blanch, S. Bonnefoy, G. Bonnoli, F. Borracci, T. Bretz, E. Carmona, A. Carosi, P. Colin, E. Colombo, J. L. Contreras, J. Cortina, S. Covino, P. Da Vela, F. Dazzi, A. De Angelis, G. De Caneva, B. De Lotto, E. de Oña Wilhelmi, C. Delgado Mendez, D. Dominis Prester, D. Dorner, M. Doro, S. Einecke, D. Eisenacher, D. Elsaesser, M. V. Fonseca, L. Font, K. Frantzen, C. Fruck, D. Galindo, R. J. García López, M. Garczarczyk, D. Garrido Terrats, M. Gaug, N. Godinović, A. González Muñoz, S. R. Gozzini, D. Hadasch, Y. Hanabata, M. Hayashida, J. Herrera, D. Hildebrand, J. Hose, D. Hrupec, W. Idec, V. Kadenius, H. Kellermann, K. Kodani, Y. Konno, J. Krause, H. Kubo, J. Kushida, A. La Barbera, D. Lelas, N. Lewandowska, E. Lindfors, S. Lombardi, M. López, R. López-Coto, A. López-Oramas, E. Lorenz, I. Lozano, M. Makariev, K. Mallot, G. Maneva, N. Mankuzhiyil, K. Mannheim, L. Maraschi, B. Marcote, M. Mariotti, M. Martínez, D. Mazin, U. Menzel, J. M. Mi-

randa, R. Mirzoyan, A. Moralejo, P. Munar-Adrover, D. Nakajima, A. Niedzwiecki, K. Nilsson, K. Nishijima, K. Noda, R. Orito, A. Overkemping, S. Paiano, M. Palatiello, D. Paneque, R. Paoletti, J. M. Paredes, X. Paredes-Fortuny, M. Persic, P. G. Prada Moroni, E. Prandini, I. Puljak, R. Reinthal, W. Rhode, M. Ribó, J. Rico, J. Rodriguez Garcia, S. Rügamer, T. Saito, K. Saito, K. Satalecka, V. Scalzotto, V. Scapin, C. Schultz, T. Schweizer, S. N. Shore, A. Sillanpää, J. Sitarek, I. Snidaric, D. Sobczynska, F. Spanier, V. Stamatescu, A. Stamerra, T. Steinbring, J. Storz, M. Strzys, L. Takalo, H. Takami, F. Tavecchio, P. Temnikov, T. Terzić, D. Tescaro, M. Teshima, J. Thaele, O. Tibolla, D. F. Torres, T. Toyama, A. Treves, M. Uellenbeck, P. Vogler, and R. Zanin, "Discovery of TeV γ-ray emission from the pulsar wind nebula 3C 58 by MAGIC," *Astronomy & Astrophysics*, vol. 567, L8, p. L8, Jul. 2014. arXiv: `1405.6074 [astro-ph.HE]`.

[183] A. De Luca, M. Marelli, R. P. Mignani, P. A. Caraveo, W. Hummel, S. Collins, A. Shearer, P. M. Saz Parkinson, A. Belfiore, and G. F. Bignami, "Discovery of a Faint X-Ray Counterpart and a Parsec-long X-Ray Tail for the Middle-aged, γ-Ray-only Pulsar PSR J0357+3205," *The Astrophysical Journal*, vol. 733, 104, p. 104, Jun. 2011. arXiv: `1102.3278 [astro-ph.HE]`.

[184] A. A. Abdo, M. Ackermann, M. Ajello, B. Anderson, W. B. Atwood, M. Axelsson, L. Baldini, J. Ballet, G. Barbiellini, M. G. Baring, D. Bastieri, B. M. Baughman, K. Bechtol, R. Bellazzini, B. Berenji, G. F. Bignami, R. D. Blandford, E. D. Bloom, E. Bonamente, A. W. Borgland, J. Bregeon, A. Brez, M. Brigida, P. Bruel, T. H. Burnett, G. A. Caliandro, R. A. Cameron, P. A. Caraveo, J. M. Casandjian, C. Cecchi, Ö. Çelik, A. Chekhtman, C. C. Cheung, J. Chiang, S. Ciprini, R. Claus, J. Cohen-Tanugi, J. Conrad, S. Cutini, C. D. Dermer, A. de Angelis, A. de Luca, F. de Palma, S. W. Digel, M. Dormody, E. do Couto e Silva, P. S. Drell, R. Dubois, D. Dumora, C. Farnier, C. Favuzzi, S. J. Fegan, Y. Fukazawa, S. Funk, P. Fusco, F. Gargano, D. Gasparrini, N. Gehrels, S. Germani, B. Giebels, N. Giglietto, P. Giommi, F. Giordano, T. Glanzman, G. Godfrey, I. A. Grenier, M.-H. Grondin, J. E. Grove, L. Guillemot, S. Guiriec, C. Gwon, Y. Hanabata, A. K. Harding, M. Hayashida, E. Hays, R. E. Hughes, G. Jóhannesson, R. P. Johnson, T. J. Johnson, W. N. Johnson, T. Kamae, H. Katagiri, J. Kataoka, N. Kawai, M. Kerr, J. Knödlseder, M. L. Kocian, M. Kuss, J. Lande, L. Latronico, M. Lemoine-Goumard, F. Longo, F. Loparco, B. Lott, M. N. Lovellette, P. Lubrano, G. M. Madejski, A. Makeev, M. Marelli, M. N. Mazziotta, W. McConville, J. E. McEnery, C. Meurer, P. F. Michelson, W. Mitthumsiri, T. Mizuno, C. Monte, M. E. Monzani, A. Morselli, I. V. Moskalenko, S. Murgia, P. L. Nolan, J. P. Norris, E. Nuss, T. Ohsugi, N. Omodei, E. Orlando, J. F. Ormes, D. Paneque, D. Parent, V. Pelassa, M. Pepe, M. Pesce-Rollins, M. Pierbattista, F. Piron, T. A. Porter, J. R. Primack, S. Rainò, R. Rando, P. S. Ray, M. Razzano, N. Rea, A. Reimer, O. Reimer, T. Reposeur, S. Ritz, L. S. Rochester, A. Y. Rodriguez, R. W. Romani, F. Ryde, H. F.-W. Sadrozinski, D. Sanchez, A. Sander, P. M. S. Parkinson, J. D. Scargle, C. Sgrò, E. J. Siskind, D. A. Smith, P. D. Smith, G. Spandre, P. Spinelli, J.-L. Starck, M. S. Strickman, D. J. Suson, H. Tajima, H. Takahashi, T. Takahashi, T. Tanaka, J. G. Thayer, D. J. Thompson, L. Tibaldo, O.

Tibolla, D. F. Torres, G. Tosti, A. Tramacere, Y. Uchiyama, T. L. Usher, A. Van Etten, V. Vasileiou, N. Vilchez, V. Vitale, A. P. Waite, P. Wang, K. Watters, B. L. Winer, M. T. Wolff, K. S. Wood, T. Ylinen, M. Ziegler, and Fermi LAT Collaboration, "Detection of 16 Gamma-Ray Pulsars Through Blind Frequency Searches Using the Fermi LAT," *Science*, vol. 325, p. 840, Aug. 2009. arXiv: `1009.0748 [astro-ph.GA]`.

[185] Y. Ladouceur and S. Pineault, "New perspectives on the supernova remnant G78.2+2.1," *Astronomy & Astrophysics*, vol. 490, pp. 197–211, Oct. 2008.

[186] E. Aliu, S. Archambault, T. Arlen, T. Aune, M. Beilicke, W. Benbow, R. Bird, A. Bouvier, S. M. Bradbury, J. H. Buckley, V. Bugaev, K. Byrum, A. Cannon, A. Cesarini, L. Ciupik, E. Collins-Hughes, M. P. Connolly, W. Cui, R. Dickherber, C. Duke, J. Dumm, V. V. Dwarkadas, M. Errando, A. Falcone, S. Federici, Q. Feng, J. P. Finley, G. Finnegan, L. Fortson, A. Furniss, N. Galante, D. Gall, G. H. Gillanders, S. Godambe, E. V. Gotthelf, S. Griffin, J. Grube, G. Gyuk, D. Hanna, J. Holder, H. Huan, G. Hughes, T. B. Humensky, P. Kaaret, N. Karlsson, M. Kertzman, Y. Khassen, D. Kieda, H. Krawczynski, F. Krennrich, M. J. Lang, K. Lee, A. S. Madhavan, G. Maier, P. Majumdar, S. McArthur, A. McCann, J. Millis, P. Moriarty, R. Mukherjee, T. Nelson, A. O'Faoláin de Bhróithe, R. A. Ong, M. Orr, A. N. Otte, D. Pandel, N. Park, J. S. Perkins, M. Pohl, A. Popkow, H. Prokoph, J. Quinn, K. Ragan, L. C. Reyes, P. T. Reynolds, E. Roache, H. J. Rose, J. Ruppel, D. B. Saxon, M. Schroedter, G. H. Sembroski, G. D. Şentürk, C. Skole, I. Telezhinsky, G. Tevsić, M. Theiling, S. Thibadeau, K. Tsurusaki, J. Tyler, A. Varlotta, V. V. Vassiliev, S. Vincent, S. P. Wakely, J. E. Ward, T. C. Weekes, A. Weinstein, T. Weisgarber, R. Welsing, D. A. Williams, and B. Zitzer, "Discovery of TeV Gamma-Ray Emission toward Supernova Remnant SNR G78.2+2.1," *The Astrophysical Journal*, vol. 770, 93, p. 93, Jun. 2013. arXiv: `1305.6508 [astro-ph.HE]`.

[187] A. Allafort, L. Baldini, J. Ballet, G. Barbiellini, M. G. Baring, D. Bastieri, R. Bellazzini, E. Bonamente, E. Bottacini, T. J. Brandt, J. Bregeon, P. Bruel, R. Buehler, S. Buson, G. A. Caliandro, R. A. Cameron, P. A. Caraveo, C. Cecchi, R. C. G. Chaves, A. Chekhtman, J. Chiang, G. Chiaro, S. Ciprini, R. Claus, F. D'Ammando, F. de Palma, S. W. Digel, L. Di Venere, P. S. Drell, C. Favuzzi, E. C. Ferrara, A. Franckowiak, P. Fusco, F. Gargano, D. Gasparrini, N. Giglietto, M. Giroletti, T. Glanzman, G. Godfrey, I. A. Grenier, S. Guiriec, D. Hadasch, A. K. Harding, M. Hayashida, K. Hayashi, E. Hays, J. Hewitt, A. B. Hill, D. Horan, X. Hou, T. Jogler, A. S. Johnson, T. J. Johnson, M. Kerr, J. Knödlseder, M. Kuss, J. Lande, S. Larsson, L. Latronico, M. Lemoine-Goumard, F. Longo, F. Loparco, P. Lubrano, D. Malyshev, M. Marelli, M. Mayer, M. N. Mazziotta, J. Mehault, T. Mizuno, M. E. Monzani, A. Morselli, S. Murgia, R. Nemmen, E. Nuss, T. Ohsugi, N. Omodei, M. Orienti, E. Orlando, D. Paneque, M. Pesce-Rollins, M. Pierbattista, F. Piron, G. Pivato, T. A. Porter, S. Rainò, R. Rando, P. S. Ray, M. Razzano, O. Reimer, T. Reposeur, R. W. Romani, A. Sartori, P. M. Saz Parkinson, C. Sgrò, E. J. Siskind, D. A. Smith, P. Spinelli, A. W. Strong, H. Takahashi, J. B. Thayer, D. J. Thompson,

L. Tibaldo, M. Tinivella, D. F. Torres, G. Tosti, Y. Uchiyama, T. L. Usher, J. Vandenbroucke, V. Vasileiou, C. Venter, G. Vianello, V. Vitale, B. L. Winer, and K. S. Wood, "PSR J2021+4026 in the Gamma Cygni Region: The First Variable γ-Ray Pulsar Seen by the Fermi LAT," *The Astrophysical Journal Letters*, vol. 777, L2, p. L2, Nov. 2013. arXiv: `1308.0358 [astro-ph.HE]`.

[188] W. C. G. Ho, C.-Y. Ng, A. G. Lyne, B. W. Stappers, M. J. Coe, J. P. Halpern, T. J. Johnson, and I. A. Steele, "Multiwavelength monitoring and X-ray brightening of Be X-ray binary PSR J2032+4127/MT91 213 on its approach to periastron," *Monthly Notices of the Royal Astronomical Society*, vol. 464, pp. 1211–1219, Jan. 2017. arXiv: `1609.06328 [astro-ph.SR]`.

[189] A. G. Lyne, B. W. Stappers, M. J. Keith, P. S. Ray, M. Kerr, F. Camilo, and T. J. Johnson, "The binary nature of PSR J2032+4127," *Monthly Notices of the Royal Astronomical Society*, vol. 451, pp. 581–587, Jul. 2015. arXiv: `1502.01465 [astro-ph.HE]`.

[190] M. M. Hohle, R. Neuhäuser, and B. F. Schutz, "Masses and luminosities of O- and B-type stars and red supergiants," *Astronomische Nachrichten*, vol. 331, p. 349, Apr. 2010. arXiv: `1003.2335 [astro-ph.SR]`.

[191] E. Aliu, T. Aune, B. Behera, M. Beilicke, W. Benbow, K. Berger, R. Bird, J. H. Buckley, V. Bugaev, J. V. Cardenzana, M. Cerruti, X. Chen, L. Ciupik, M. P. Connolly, W. Cui, C. Duke, J. Dumm, M. Errando, A. Falcone, S. Federici, Q. Feng, J. P. Finley, P. Fortin, L. Fortson, A. Furniss, N. Galante, G. H. Gillanders, S. Griffin, S. T. Griffiths, J. Grube, G. Gyuk, D. Hanna, J. Holder, G. Hughes, T. B. Humensky, P. Kaaret, O. Kargaltsev, M. Kertzman, Y. Khassen, D. Kieda, H. Krawczynski, M. J. Lang, A. S. Madhavan, G. Maier, P. Majumdar, A. McCann, P. Moriarty, R. Mukherjee, D. Nieto, A. O'Faoláin de Bhróithe, R. A. Ong, A. N. Otte, D. Pandel, J. S. Perkins, M. Pohl, A. Popkow, H. Prokoph, J. Quinn, K. Ragan, J. Rajotte, L. C. Reyes, P. T. Reynolds, G. T. Richards, E. Roache, G. H. Sembroski, C. Skole, D. Staszak, I. Telezhinsky, M. Theiling, J. V. Tucci, J. Tyler, A. Varlotta, S. Vincent, S. P. Wakely, T. C. Weekes, A. Weinstein, R. Welsing, D. A. Williams, and B. Zitzer, "Observations of the Unidentified Gamma-Ray Source TeV J2032+4130 by VERITAS," *The Astrophysical Journal*, vol. 783, 16, p. 16, Mar. 2014. arXiv: `1401.2828 [astro-ph.HE]`.

[192] J. Albert, E. Aliu, H. Anderhub, P. Antoranz, A. Armada, C. Baixeras, J. A. Barrio, H. Bartko, D. Bastieri, J. K. Becker, W. Bednarek, K. Berger, C. Bigongiari, A. Biland, R. K. Bock, P. Bordas, V. Bosch-Ramon, T. Bretz, I. Britvitch, M. Camara, E. Carmona, A. Chilingarian, J. A. Coarasa, S. Commichau, J. L. Contreras, J. Cortina, M. T. Costado, V. Curtef, V. Danielyan, F. Dazzi, A. De Angelis, C. Delgado, R. de los Reyes, B. De Lotto, E. Domingo-Santamaría, D. Dorner, M. Doro, M. Errando, M. Fagiolini, D. Ferenc, E. Fernández, R. Firpo, J. Flix, M. V. Fonseca, L. Font, M. Fuchs, N. Galante, R. García-López, M. Garczarczyk, M. Gaug, M. Giller, F.

Goebel, D. Hakobyan, M. Hayashida, T. Hengstebeck, A. Herrero, D. Höhne, J. Hose, C. C. Hsu, P. Jacon, T. Jogler, R. Kosyra, D. Kranich, R. Kritzer, A. Laille, E. Lindfors, S. Lombardi, F. Longo, J. López, M. López, E. Lorenz, P. Majumdar, G. Maneva, K. Mannheim, O. Mansutti, M. Mariotti, M. Martínez, D. Mazin, C. Merck, M. Meucci, M. Meyer, J. M. Miranda, R. Mirzoyan, S. Mizobuchi, A. Moralejo, D. Nieto, K. Nilsson, J. Ninkovic, E. Oña-Wilhelmi, N. Otte, I. Oya, D. Paneque, M. Panniello, R. Paoletti, J. M. Paredes, M. Pasanen, D. Pascoli, F. Pauss, R. Pegna, M. Persic, L. Peruzzo, A. Piccioli, M. Poller, E. Prandini, N. Puchades, A. Raymers, W. Rhode, M. Ribó, J. Rico, M. Rissi, A. Robert, S. Rügamer, A. Saggion, A. Sánchez, P. Sartori, V. Scalzotto, V. Scapin, R. Schmitt, T. Schweizer, M. Shayduk, K. Shinozaki, S. N. Shore, N. Sidro, A. Sillanpää, D. Sobczynska, A. Stamerra, L. S. Stark, L. Takalo, P. Temnikov, D. Tescaro, M. Teshima, N. Tonello, D. F. Torres, N. Turini, H. Vankov, V. Vitale, R. M. Wagner, T. Wibig, W. Wittek, F. Zandanel, R. Zanin, and J. Zapatero, "VHE γ-Ray Observation of the Crab Nebula and its Pulsar with the MAGIC Telescope," *The Astrophysical Journal*, vol. 674, 1037-1055, pp. 1037–1055, Feb. 2008. arXiv: `0705.3244`.

[193] J. P. W. Verbiest, J. M. Weisberg, A. A. Chael, K. J. Lee, and D. R. Lorimer, "On Pulsar Distance Measurements and Their Uncertainties," *The Astrophysical Journal*, vol. 755, 39, p. 39, Aug. 2012. arXiv: `1206.0428 [astro-ph.GA]`.

[194] E. Aliu, S. Archambault, T. Aune, W. Benbow, K. Berger, R. Bird, A. Bouvier, J. H. Buckley, V. Bugaev, K. Byrum, M. Cerruti, X. Chen, L. Ciupik, M. P. Connolly, W. Cui, J. Dumm, M. Errando, A. Falcone, S. Federici, Q. Feng, J. P. Finley, P. Fortin, L. Fortson, A. Furniss, N. Galante, G. H. Gillanders, S. Griffin, S. T. Griffiths, J. Grube, G. Gyuk, D. Hanna, J. Holder, G. Hughes, T. B. Humensky, P. Kaaret, M. Kertzman, Y. Khassen, D. Kieda, F. Krennrich, S. Kumar, M. J. Lang, M. Lyutikov, G. Maier, S. McArthur, A. McCann, K. Meagher, J. Millis, P. Moriarty, R. Mukherjee, A. O'Faoláin de Bhróithe, R. A. Ong, A. N. Otte, N. Park, J. S. Perkins, M. Pohl, A. Popkow, J. Quinn, K. Ragan, J. Rajotte, L. C. Reyes, P. T. Reynolds, G. T. Richards, E. Roache, G. H. Sembroski, F. Sheidaei, A. W. Smith, D. Staszak, I. Telezhinsky, M. Theiling, J. V. Tucci, J. Tyler, A. Varlotta, S. P. Wakely, T. C. Weekes, A. Weinstein, R. Welsing, D. A. Williams, A. Zajczyk, and B. Zitzer, "A Search for Enhanced Very High Energy Gamma-Ray Emission from the 2013 March Crab Nebula Flare," *The Astrophysical Journal Letters*, vol. 781, L11, p. L11, Jan. 2014. arXiv: `1309.5949 [astro-ph.HE]`.

[195] J. J. Hester, "The Crab Nebula: An Astrophysical Chimera," *Annual Review of Astronomy and Astrophysics*, vol. 46, pp. 127–155, Sep. 2008.

[196] R. J. Gould, "High-Energy Photons from the Compton-Synchrotron Process in the Crab Nebula," *Physical Review Letters*, vol. 15, pp. 577–579, Oct. 1965.

[197] T. C. Weekes, M. F. Cawley, D. J. Fegan, K. G. Gibbs, A. M. Hillas, P. W. Kowk, R. C. Lamb, D. A. Lewis, D. Macomb, N. A. Porter, P. T. Reynolds, and G. Va-

canti, "Observation of TeV gamma rays from the Crab nebula using the atmospheric Cerenkov imaging technique," *The Astrophysical Journal*, vol. 342, pp. 379–395, Jul. 1989.

[198] O. C. de Jager and A. K. Harding, "The expected high-energy to ultra-high-energy gamma-ray spectrum of the Crab Nebula," *The Astrophysical Journal*, vol. 396, pp. 161–172, Sep. 1992.

[199] F. Aharonian, A. Akhperjanian, M. Beilicke, K. Bernlöhr, H.-G. Börst, H. Bojahr, O. Bolz, T. Coarasa, J. L. Contreras, J. Cortina, S. Denninghoff, M. V. Fonseca, M. Girma, N. Götting, G. Heinzelmann, G. Hermann, A. Heusler, W. Hofmann, D. Horns, I. Jung, R. Kankanyan, M. Kestel, A. Kohnle, A. Konopelko, D. Kranich, H. Lampeitl, M. Lopez, E. Lorenz, F. Lucarelli, O. Mang, D. Mazin, H. Meyer, R. Mirzoyan, A. Moralejo, E. Oña-Wilhelmi, M. Panter, A. Plyasheshnikov, G. Pühlhofer, R. de los Reyes, W. Rhode, J. Ripken, G. Rowell, V. Sahakian, M. Samorski, M. Schilling, M. Siems, D. Sobzynska, W. Stamm, M. Tluczykont, V. Vitale, H. J. Völk, C. A. Wiedner, and W. Wittek, "The Crab Nebula and Pulsar between 500 GeV and 80 TeV: Observations with the HEGRA Stereoscopic Air Cerenkov Telescopes," *The Astrophysical Journal*, vol. 614, pp. 897–913, Oct. 2004. eprint: `astro-ph/0407118`.

[200] D. H. Staelin and E. C. Reifenstein III, "Pulsating Radio Sources near the Crab Nebula," *Science*, vol. 162, pp. 1481–1483, Dec. 1968.

[201] M. J. Rees and J. E. Gunn, "The origin of the magnetic field and relativistic particles in the Crab Nebula," *Monthly Notices of the Royal Astronomical Society*, vol. 167, pp. 1–12, Apr. 1974.

[202] C. F. Kennel and F. V. Coroniti, "Magnetohydrodynamic model of Crab nebula radiation," *The Astrophysical Journal*, vol. 283, pp. 710–730, Aug. 1984.

[203] M. Tavani, A. Bulgarelli, V. Vittorini, A. Pellizzoni, E. Striani, P. Caraveo, M. C. Weisskopf, A. Tennant, G. Pucella, A. Trois, E. Costa, Y. Evangelista, C. Pittori, F. Verrecchia, E. Del Monte, R. Campana, M. Pilia, A. De Luca, I. Donnarumma, D. Horns, C. Ferrigno, C. O. Heinke, M. Trifoglio, F. Gianotti, S. Vercellone, A. Argan, G. Barbiellini, P. W. Cattaneo, A. W. Chen, T. Contessi, F. D'Ammando, G. DeParis, G. Di Cocco, G. Di Persio, M. Feroci, A. Ferrari, M. Galli, A. Giuliani, M. Giusti, C. Labanti, I. Lapshov, F. Lazzarotto, P. Lipari, F. Longo, F. Fuschino, M. Marisaldi, S. Mereghetti, E. Morelli, E. Moretti, A. Morselli, L. Pacciani, F. Perotti, G. Piano, P. Picozza, M. Prest, M. Rapisarda, A. Rappoldi, A. Rubini, S. Sabatini, P. Soffitta, E. Vallazza, A. Zambra, D. Zanello, F. Lucarelli, P. Santolamazza, P. Giommi, L. Salotti, and G. F. Bignami, "Discovery of Powerful Gamma-Ray Flares from the Crab Nebula," *Science*, vol. 331, pp. 736–, Feb. 2011. arXiv: `1101.2311 [astro-ph.HE]`.

[204] A. A. Abdo, M. Ackermann, M. Ajello, A. Allafort, L. Baldini, J. Ballet, G. Barbiellini, D. Bastieri, K. Bechtol, R. Bellazzini, B. Berenji, R. D. Blandford, E. D. Bloom, E. Bonamente, A. W. Borgland, A. Bouvier, T. J. Brandt, J. Bregeon, A. Brez, M. Brigida, P. Bruel, R. Buehler, S. Buson, G. A. Caliandro, R. A. Cameron, A. Cannon, P. A. Caraveo, J. M. Casandjian, Ö. Çelik, E. Charles, A. Chekhtman, C. C. Cheung, J. Chiang, S. Ciprini, R. Claus, J. Cohen-Tanugi, L. Costamante, S. Cutini, F. D'Ammando, C. D. Dermer, A. de Angelis, A. de Luca, F. de Palma, S. W. Digel, E. do Couto e Silva, P. S. Drell, A. Drlica-Wagner, R. Dubois, D. Dumora, C. Favuzzi, S. J. Fegan, E. C. Ferrara, W. B. Focke, P. Fortin, M. Frailis, Y. Fukazawa, S. Funk, P. Fusco, F. Gargano, D. Gasparrini, N. Gehrels, S. Germani, N. Giglietto, F. Giordano, M. Giroletti, T. Glanzman, G. Godfrey, I. A. Grenier, M.-H. Grondin, J. E. Grove, S. Guiriec, D. Hadasch, Y. Hanabata, A. K. Harding, K. Hayashi, M. Hayashida, E. Hays, D. Horan, R. Itoh, G. Jóhannesson, A. S. Johnson, T. J. Johnson, D. Khangulyan, T. Kamae, H. Katagiri, J. Kataoka, M. Kerr, J. Knödlseder, M. Kuss, J. Lande, L. Latronico, S.-H. Lee, M. Lemoine-Goumard, F. Longo, F. Loparco, P. Lubrano, G. M. Madejski, A. Makeev, M. Marelli, M. N. Mazziotta, J. E. McEnery, P. F. Michelson, W. Mitthumsiri, T. Mizuno, A. A. Moiseev, C. Monte, M. E. Monzani, A. Morselli, I. V. Moskalenko, S. Murgia, T. Nakamori, M. Naumann-Godo, P. L. Nolan, J. P. Norris, E. Nuss, T. Ohsugi, A. Okumura, N. Omodei, J. F. Ormes, M. Ozaki, D. Paneque, D. Parent, V. Pelassa, M. Pepe, M. Pesce-Rollins, M. Pierbattista, F. Piron, T. A. Porter, S. Rainò, R. Rando, P. S. Ray, M. Razzano, A. Reimer, O. Reimer, T. Reposeur, S. Ritz, R. W. Romani, H. F.-W. Sadrozinski, D. Sanchez, P. M. S. Parkinson, J. D. Scargle, T. L. Schalk, C. Sgrò, E. J. Siskind, P. D. Smith, G. Spandre, P. Spinelli, M. S. Strickman, D. J. Suson, H. Takahashi, T. Takahashi, T. Tanaka, J. B. Thayer, D. J. Thompson, L. Tibaldo, D. F. Torres, G. Tosti, A. Tramacere, E. Troja, Y. Uchiyama, J. Vandenbroucke, V. Vasileiou, G. Vianello, V. Vitale, P. Wang, K. S. Wood, Z. Yang, and M. Ziegler, "Gamma-Ray Flares from the Crab Nebula," *Science*, vol. 331, pp. 739–, Feb. 2011. arXiv: `1011.3855 [astro-ph.HE]`.

[205] M. Balbo, R. Walter, C. Ferrigno, and P. Bordas, "Twelve-hour spikes from the Crab Pevatron," *Astronomy & Astrophysics*, vol. 527, L4, p. L4, Mar. 2011. arXiv: `1012.3397 [astro-ph.HE]`.

[206] R. Buehler, J. D. Scargle, R. D. Blandford, L. Baldini, M. G. Baring, A. Belfiore, E. Charles, J. Chiang, F. D'Ammando, C. D. Dermer, S. Funk, J. E. Grove, A. K. Harding, E. Hays, M. Kerr, F. Massaro, M. N. Mazziotta, R. W. Romani, P. M. Saz Parkinson, A. F. Tennant, and M. C. Weisskopf, "Gamma-Ray Activity in the Crab Nebula: The Exceptional Flare of 2011 April," *The Astrophysical Journal*, vol. 749, 26, p. 26, Apr. 2012. arXiv: `1112.1979 [astro-ph.HE]`.

[207] E. Clausen-Brown and M. Lyutikov, "Crab nebula gamma-ray flares as relativistic reconnection minijets," *Monthly Notices of the Royal Astronomical Society*, vol. 426, pp. 1374–1384, Oct. 2012. arXiv: `1205.5094 [astro-ph.HE]`.

[208] M. Lyutikov, D. Balsara, and C. Matthews, “Crab GeV flares from the corrugated termination shock,” *Monthly Notices of the Royal Astronomical Society*, vol. 422, pp. 3118–3129, Jun. 2012. arXiv: `1109.1204 [astro-ph.HE]`.

[209] W. Bednarek and W. Idec, “On the variability of the GeV and multi-TeV gamma-ray emission from the Crab nebula,” *Monthly Notices of the Royal Astronomical Society*, vol. 414, pp. 2229–2234, Jul. 2011. arXiv: `1011.4176 [astro-ph.HE]`.

[210] E. Striani, M. Tavani, G. Piano, I. Donnarumma, G. Pucella, V. Vittorini, A. Bulgarelli, A. Trois, C. Pittori, F. Verrecchia, E. Costa, M. Weisskopf, A. Tennant, A. Argan, G. Barbiellini, P. Caraveo, M. Cardillo, P. W. Cattaneo, A. W. Chen, G. De Paris, E. Del Monte, G. Di Cocco, Y. Evangelista, A. Ferrari, M. Feroci, F. Fuschino, M. Galli, F. Gianotti, A. Giuliani, C. Labanti, I. Lapshov, F. Lazzarotto, F. Longo, M. Marisaldi, S. Mereghetti, A. Morselli, L. Pacciani, A. Pellizzoni, F. Perotti, P. Picozza, M. Pilia, M. Rapisarda, A. Rappoldi, S. Sabatini, P. Soffitta, M. Trifoglio, S. Vercellone, F. Lucarelli, P. Santolamazza, and P. Giommi, “The Crab Nebula Super-flare in 2011 April: Extremely Fast Particle Acceleration and Gamma-Ray Emission,” *The Astrophysical Journal Letters*, vol. 741, L5, p. L5, Nov. 2011. arXiv: `1105.5028 [astro-ph.HE]`.

[211] E. Striani, M. Tavani, V. Vittorini, I. Donnarumma, A. Giuliani, G. Pucella, A. Argan, A. Bulgarelli, S. Colafrancesco, M. Cardillo, E. Costa, E. Del Monte, A. Ferrari, S. Mereghetti, L. Pacciani, A. Pellizzoni, G. Piano, C. Pittori, M. Rapisarda, S. Sabatini, P. Soffitta, M. Trifoglio, A. Trois, S. Vercellone, and F. Verrecchia, “Variable Gamma-Ray Emission from the Crab Nebula: Short Flares and Long “Waves”,” *The Astrophysical Journal*, vol. 765, 52, p. 52, Mar. 2013. arXiv: `1302.4342 [astro-ph.HE]`.

[212] D. Horns, A. Tennant, C. Ferrigno, M. C. Weisskopf, A. Neronov, M. Tavani, E. Costa, and P. Caraveo, “Chandra follow-up observation of the Crab nebula after the high energy flare,” *The Astronomer’s Telegram*, vol. 3058, p. 1, Nov. 2010.

[213] M. C. Weisskopf, “Monitoring the Crab Nebula with Chandra . A search for the location of the gamma -ray flares,” *Memorie della Societa Astronomica Italiana*, vol. 84, p. 582, 2013. arXiv: `1211.7109 [astro-ph.HE]`.

[214] M. Mariotti, “No significant enhancement in the VHE gamma-ray flux of the Crab Nebula measured by MAGIC in September 2010,” *The Astronomer’s Telegram*, vol. 2967, Oct. 2010.

[215] R. A. Ong, “Search for an Enhanced TeV Gamma-Ray Flux from the Crab Nebula with VERITAS,” *The Astronomer’s Telegram*, vol. 2968, Oct. 2010.

[216] G. Aielli, P. Camarri, R. Iuppa, R. Santonico, C. Bacci, P. Branchini, A. Budano, S. Bussino, P. Celio, M. de Vincenzi, I. James, S. M. Mari, P. Montini, P. Pis-

tilli, B. Bartoli, S. Catalanotti, B. D'Ettorre Piazzoli, T. di Girolamo, M. Iacovacci, L. Saggese, P. Bernardini, C. Bleve, I. de Mitri, G. Mancarella, G. Marsella, D. Martello, M. Panareo, L. Perrone, X. J. Bi, Z. Cao, S. Z. Chen, Y. Chen, Z. Feng, Q. B. Gou, Y. Q. Guo, H. H. He, H. Hu, X. X. Li, C. Liu, H. Lu, X. H. Ma, P. R. Shen, X. D. Sheng, F. Shi, Y. H. Tan, B. Wang, H. Wang, C. Y. Wu, H. R. Wu, Z. G. Yao, M. Zha, H. M. Zhang, J. Zhang, J. Zhang, Y. Zhang, Q. Q. Zhu, A. K. Calabrese Melcarne, G. Zizzi, A. Cappa, P. Vallania, S. Vernetto, R. Cardarelli, G. di Sciascio, B. Liberti, C. Cattaneo, P. Salvini, P. Creti, A. Surdo, S. W. Cui, B. Z. Dai, C. Q. Liu, J. Liu, Q. Y. Yang, X. C. Yang, L. Zhang, P. Zhang, G. D'Ali'Staiti, T. L. Chen, Danzengluobu, X. H. Ding, H. Hu, Labaciren, H. J. Li, M. Y. Liu, C. C. Ning, A. F. Yuan, Zhaxisangzhu, Zhaxiciren, M. Dattoli, C. Vigorito, C. F. Feng, J. Y. Li, X. B. Qu, L. Xue, X. Y. Zhang, Z. Feng, Q. Huang, H. Y. Jia, B. Xu, X. X. Zhou, F. R. Zhu, F. Galeazzi, R. Gargana, F. Ruggieri, C. Stanescu, P. Galeotti, E. Giroletti, G. Liguori, S. Mastroianni, E. Rossi, and A. Pagliaro, "Enhanced TeV gamma ray flux from the Crab Nebula observed," *The Astronomer's Telegram*, vol. 2921, Oct. 2010.

[217] B. Bartoli, P. Bernardini, X. J. Bi, I. Bolognino, P. Branchini, A. Budano, A. K. C. Melcarne, P. Camarri, Z. Cao, R. Cardarelli, S. Catalanotti, C. Cattaneo, S. Z. Chen, T. L. Chen, Y. Chen, P. Creti, S. W. Cui, B. Z. Dai, G. D. Staiti, A. D'Amone, Danzengluobu, I. De Mitri, B. D'Ettorre Piazzoli, T. Di Girolamo, X. H. Ding, G. Di Sciascio, C. F. Feng, Z. Feng, Z. Feng, F. Galeazzi, E. Giroletti, Q. B. Gou, Y. Q. Guo, H. H. He, H. Hu, H. Hu, Q. Huang, M. Iacovacci, R. Iuppa, I. James, H. Y. Jia, Labaciren, H. J. Li, J. Y. Li, X. X. Li, G. Liguori, C. Liu, C. Q. Liu, J. Liu, M. Y. Liu, H. Lu, L. L. Ma, X. H. Ma, G. Mancarella, S. M. Mari, G. Marsella, D. Martello, S. Mastroianni, P. Montini, C. C. Ning, A. Pagliaro, M. Panareo, B. Panico, L. Perrone, P. Pistilli, F. Ruggieri, P. Salvini, R. Santonico, S. N. Sbano, P. R. Shen, X. D. Sheng, F. Shi, A. Surdo, Y. H. Tan, P. Vallania, S. Vernetto, C. Vigorito, B. Wang, H. Wang, C. Y. Wu, H. R. Wu, B. Xu, L. Xue, Q. Y. Yang, X. C. Yang, Z. G. Yao, A. F. Yuan, M. Zha, H. M. Zhang, J. Zhang, J. Zhang, L. Zhang, P. Zhang, X. Y. Zhang, Y. Zhang, J. Zhao, Zhaxiciren, Zhaxisangzhu, X. X. Zhou, F. R. Zhu, Q. Q. Zhu, and G. Zizzi, "Enhanced TeV gamma ray flux from the Crab Nebula observed by the ARGO-YBJ experiment," *The Astronomer's Telegram*, vol. 4258, Jul. 2012.

[218] S. Vernetto and for the ARGO-YBJ collaboration, "Study of the Crab Nebula TeV emission variability during five years with ARGO-YBJ," *ArXiv e-prints*, Jul. 2013. arXiv: `1307.7041 [astro-ph.HE]`.

[219] M. Errando, "Target of opportunity observations of flaring blazars with VERITAS," *International Cosmic Ray Conference*, vol. 8, p. 133, 2011. arXiv: `1110.1028 [astro-ph.HE]`.

[220] R. Ojha, E. Hays, R. Buehler, and M. Dutka, “Fermi LAT detection of a new gamma-ray flare from the Crab Nebula region,” *The Astronomer’s Telegram*, vol. 4855, Mar. 2013.

[221] F. Aharonian, A. Akhperjanian, J. Barrio, K. Bernlöhr, H. Börst, H. Bojahr, O. Bolz, J. Contreras, J. Cortina, S. Denninghoff, V. Fonseca, J. Gonzalez, N. Götting, G. Heinzelmann, G. Hermann, A. Heusler, W. Hofmann, D. Horns, A. Ibarra, C. Iserlohe, I. Jung, R. Kankanyan, M. Kestel, J. Kettler, A. Kohnle, A. Konopelko, H. Kornmeyer, D. Kranich, H. Krawczynski, H. Lampeitl, M. Lopez, E. Lorenz, F. Lucarelli, N. Magnussen, O. Mang, H. Meyer, R. Mirzoyan, A. Moralejo, E. Ona, L. Padilla, M. Panter, R. Plaga, A. Plyasheshnikov, J. Prahl, G. Pühlhofer, G. Rauterberg, A. Röhring, W. Rhode, G. P. Rowell, V. Sahakian, M. Samorski, M. Schilling, F. Schröder, M. Siems, W. Stamm, M. Tluczykont, H. J. Völk, C. A. Wiedner, and W. Wittek, “Evidence for TeV gamma ray emission from Cassiopeia A,” *Astronomy & Astrophysics*, vol. 370, pp. 112–120, Apr. 2001. eprint: `astro-ph/0102391`.

[222] D. Hanna, A. McCann, M. McCutcheon, and L. Nikkinen, “An LED-based flasher system for VERITAS,” *Nuclear Instruments and Methods in Physics Research A*, vol. 612, pp. 278–287, Jan. 2010. arXiv: `0911.2015 [astro-ph.IM]`.

[223] A. K. Konopelko, “Stereo imaging of the VHE γ-rays with HEGRA & H.E.S.S.,” in *American Institute of Physics Conference Series*, F. A. Aharonian and H. J. Völk, Eds., ser. American Institute of Physics Conference Series, vol. 558, Apr. 2001, pp. 569–573. eprint: `astro-ph/0011214`.

[224] A. G. Lyne, R. S. Pritchard, and F. Graham-Smith, “Twenty-Three Years of Crab Pulsar Rotational History,” *Monthly Notices of the Royal Astronomical Society*, vol. 265, p. 1003, Dec. 1993.

[225] T. Alexander, “Is AGN Variability Correlated with Other AGN Properties? ZDCF Analysis of Small Samples of Sparse Light Curves,” in *Astronomical Time Series*, D. Maoz, A. Sternberg, and E. M. Leibowitz, Eds., ser. Astrophysics and Space Science Library, vol. 218, 1997, p. 163.

[226] ——, “Improved AGN light curve analysis with the z-transformed discrete correlation function,” *ArXiv e-prints*, Feb. 2013. arXiv: `1302.1508 [astro-ph.IM]`.

[227] P. L. Marsden, F. C. Gillett, R. E. Jennings, J. P. Emerson, T. de Jong, and F. M. Olnon, “Far-infrared observations of the Crab nebula,” *The Astrophysical Journal Letters*, vol. 278, pp. L29–L32, Mar. 1984.